Accelerated Stokesian Dynamics: Development and application to sheared non-Brownian suspensions

Thesis by
Asimina Sierou

In Partial Fulfillment of the Requirements
for the Degree of
Doctor of Philosophy

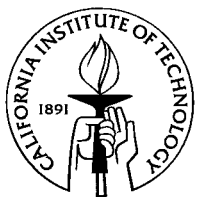

California Institute of Technology
Pasadena, California

2002

(Defended July 27, 2001)

Acknowledgements

What a great surprise!!!!
I would like to thank the Academy for this great honor... This is really unexpected—I never expected to win and I am honestly in shock...
There are so many people I would like to thank and so little time...

First of all, of course, my deep gratitude to my producer and director, John Brady. His dream and vision made this work possible and his guidance and encouragement made me the performer I now am—this Oscar belongs to him as much as it belongs to me...

Very special thanks to co-producers Melany Hunt, Julie Kornfield and Zhen-Gang Wang for their interest in my performance and the completion of this movie and to all the executive producers that made sure that funding never ran out...

I would like to thank all the other members of the cast for their love and support—working with all of you has been a lot of fun, and I wish I had the time to name you all here (please forgive me)!

My parents (I love you Mom and Dad!), my brother, my friends here (Pete and Amy, Rob and Ann, Chris and Shaney and everybody else who I am now forgetting) and back home (especially Zaira), the technical and executive supervisors and everyone that helped to make this dream come true...

My hairdresser, my stuffed animals, Ernie for the flautas, my kindergarten teacher, my first-grade teacher, my second grade teacher, all the Diet-Coke® vending machines in America for very valuable service, Zeus and Hera for their divine interventions during

bad times, minor deities for minor interventions (especially Dionysos for some fun afternoons), and last but not least the devil for not crashing the computers those last days of production...

Thank you, thank you all very-very much and right now... ...I am king of the world!

Pasadena, July 2001
(somewhere near Hollywood)

PS. In Oscar tradition, I forgot to thank my best friend and husband, Jeff... He will be thanked separately during the press conference and in private when I get home...

Guide:
The Academy: Caltech
director/producer: advisor/mentor
co-producers: members of the committee
executive-producer: funding partially provided by a Dow Graduate fellowship
Supporting cast: Members of the Brady group, past and present
Technical supervisors: Suresh and the people over at CACR
Executive supervisors: Margie and Kathy
movie/oscar/performance/performer: work/thesis/science/scientist

Accelerated Stokesian Dynamics: Development and application to sheared non-Brownian suspensions

by

Asimina Sierou

In Partial Fulfillment of the
Requirements for the Degree of
Doctor of Philosophy

Abstract

A new implementation of the conventional Stokesian Dynamics (SD) algorithm, called Accelerated Stokesian Dynamics (ASD), is presented. The equations governing the motion of N particles suspended in a viscous fluid at low particle Reynolds number are solved accurately and efficiently, including all hydrodynamic interactions, but with a significantly lower computational cost of $O(N \ln N)$. The main differences from the conventional SD method lie in the calculation of the many-body long-range interactions, where the Ewald-summed wave-space contribution is calculated as a Fourier Transform sum, and in the iterative inversion of the now sparse resistance matrix. The ASD method opens up an entire new class of suspension problems that can be investigated, including particles of non-spherical shape and a distribution of sizes, and can be readily extended to other low-Reynolds-number flow problems. The new method is applied to the study of sheared non-Brownian suspensions.

The rheological behavior of a monodisperse suspension of non-Brownian particles in simple shear flow in the presence of a weak interparticle force is studied first. The availability of a faster numerical algorithm permits the investigation of larger systems (typically of $N = 512 - 1000$ particles) and accurate results for the suspension viscosity, first and second normal stress differences and the particle pressure are determined as a function of the volume fraction. The system microstructure, expressed through the pair-distribution function, is also studied and it is demonstrated how the resulting anisotropy in the mi-

crostructure is correlated with the suspension non-Newtonian behavior. The ratio of the normal to excess shear stress is found to be an increasing function of the volume fraction, suggesting different volume fraction scalings for different elements of the stress tensor. The relative strength and range of the interparticle force is varied and its effect on the shear and normal stresses is analyzed. Volume fractions above the equilibrium freezing volume fraction ($\phi \approx 0.494$) are also studied, and it is found that the system exhibits a strong tendency to order under flow for volume fractions below the hard-sphere glass transition; limited results for $\phi = 0.60$, however, show that the system is again disordered under shear.

Self-diffusion is subsequently studied and accurate results for the complete tensor of the shear-induced self-diffusivities are determined. The finite, and oftentimes large, autocorrelation time requires the mean-square displacement curves to be followed for longer times than was previously thought necessary. Results determined from either the mean-square displacement or the velocity autocorrelation function are in excellent agreement. The longitudinal (in the flow direction) self-diffusion coefficient is also determined, and it is shown that the finite autocorrelation time introduces an additional coupled term to the longitudinal self-diffusivity, a term which previous theoretical and numerical results omitted. The longitudinal self-diffusivities for a system of non-Brownian particles are calculated for the first time as a function of the volume fraction.

Contents

List of Figures

List of Tables

Chapter 1

Introduction

Suspensions are important in a large number of applications and in a variety of natural and industrial settings. Examples include handling and transportation of solid particulate materials and manufacturing processes of many products (e.g., ceramics, paints and food). The flow behavior of these suspensions is often complex and a more fundamental understanding of their properties is of great interest. In such systems the suspending particles interact through hydrodynamic, interparticle and Brownian (or thermal forces). The properties of the suspending particles and the nature of the fluid medium determine the relative importance of the above forces and the balance of these forces determines the suspension's macroscopic behavior. This work will concentrate on non-Brownian, or non-colloidal, suspensions at low particle-Reynolds number. Non-Brownian implies that thermal forces giving rise to Brownian motion are negligible (generally for particles of order 10μm or larger), while low particle Reynolds number means that the inertial forces are negligible and that the fluid motion is governed by the Stokes equation.

Since Einstein (1906) developed a theoretical expression for the viscosity of a dilute suspension of such non-Brownian spheres, a large number of studies have concentrated on the theoretical prediction of the macroscopic transport properties of suspensions. For the most part, theoretical studies are limited to dilute concentrations where single- or two-body interactions dominate and exact solutions are often possible. The determination of hydrodynamic interactions among many particles, however, can be complicated mainly due to the long-range nature of the interactions and the presence of strong lubrication

effects when particles are in close proximity to each other. The fluid velocity disturbance caused by a particle on which a net external force acts decays as $1/r$, where r is the distance from the particle, and therefore the hydrodynamic interactions cannot be truncated and no simple pairwise-additive approximation can be made. In addition, the presence of lubrication effects makes conventional numerical techniques (such as the boundary-integral technique) expensive computationally when two particles approach each other.

Durlofsky, Brady & Bossis (1987) developed a method that successfully accounts for both the many-body interactions and the near-field lubrication effects by splitting the hydrodynamic interactions into a far-field mobility calculation and a pair-wise additive resistance calculation. The main advantage of the method is that a relatively small number of unknowns per particle is sufficient to adequately solve many dynamic simulation problems. The main disadvantage of the method, however, is that it requires inverting a far-field mobility matrix with at least $(11N)^2$ elements (N being the number of particles in the system), with a computational cost that limits the method to N on the order of a hundred.

The method of Durlofsky, Brady & Bossis (1987) and its extension to infinite suspensions by Phillips *et al.* (1988) is known as Stokesian Dynamics and has been used successfully for the study of many problems over the past decade. The limitation on the system size, however, generates the need for a new algorithm that maintains a high level of accuracy with a more favorable computational cost. The first part of this thesis will concentrate on the development of such an algorithm. This new algorithm, referred to as Accelerated Stokesian Dynamics (ASD), will be presented in detail and validated for some test problems. The costly construction and inversion of the far-field mobility matrix is now avoided and replaced by a Particle-Mesh-Ewald approach (Darden *et al.* 1993) and as a result the computational cost is reduced to scale as only $O(N \ln N)$. Access to larger systems allows the study of a variety of problems where the system size effects can be significant. The high-frequency dynamic viscosity and short-time self-diffusivity of suspensions for volume fractions above the freezing point (along the metastable fluid-phase branch) are thus calculated. This is a case where a large number of particles is necessary to capture the correct behavior, since a macroscopic system at these high volume frac-

tions will undoubtedly have clusters in some regions and freely mobile particles in others, a structure which is difficult to model unless the unit cell is sufficiently large.

The second part of this thesis utilizes the ASD algorithm to study the rheological behavior of non-colloidal suspensions. Over the last years significant research effort has focused on such systems of non-Brownian particles and in particular on their non-Newtonian behavior (finite normal stress differences and a particle phase contribution to the isotropic stress). Gadala-Maria (1979) reported normal stress differences that scale as $\eta\dot{\gamma}$, where η is the viscosity of the solvent and $\dot{\gamma}$ the shear rate. Experiments by Singh (2000) and Zarraga *et al.* (2000) followed and confirmed the presence of finite normal stress differences for such systems. Stokesian Dynamics simulation results for Brownian systems at high values of the Péclet number also demonstrated a similar behavior (Phung 1996, Foss & Brady 2000).

Singh (2000) and Zarraga *et al.* (2000) also evaluated the isotropic contribution to the particle stress, referred to as the particle pressure, from a combination of experimental measurements of all normal stress components. This particle pressure is a consequence of the hydrodynamic (and interparticle force) interactions among particles as opposed to the thermally induced "osmotic" pressure in colloidal systems. Its theoretical calculation became possible only recently after Jeffrey, Morris & Brady (1993) calculated the necessary hydrodynamic two-body functions.

The impact of the suspension microstructure on its non-Newtonian rheological properties has also been the subject of a number of theoretical studies. Brady & Morris (1997) analytically calculated the viscosity and normal stress differences for a dilute suspension of particles taking into account hydrodynamic interactions and the presence of a hard-sphere-type pairwise interparticle force, which prevented particles from approaching one another beyond a minimum separation $b > a$. This force breaks the fore-aft symmetry and thus leads to a viscosity correction and finite normal stress-differences. By studying the balance between hydrodynamic and interparticle forces in a boundary layer near particle-particle contact, Brady & Morris (1997) proposed a scaling for the particle stress that incorporates the effect of the particle volume fraction, the range of the interparticle force, and the resulting microstructure.

In this work we study the structure, rheology and self-diffusion of sheared monodisperse non-Brownian suspensions in the presence of a weak repulsive interparticle force. Access to a faster algorithm allows the simulation of much larger systems, typically of $N = 512-1000$ particles. Larger systems allow a more accurate calculation of all rheological properties, and in particular of the normal stresses which are often subject to large fluctuations. The microstructure is investigated with the help of the pair-distribution function, $g(\boldsymbol{r})$, and the examination of its angular and radial dependence. The resulting microstructure is studied in comparison with the changes in the rheological properties and the scaling theory of Brady & Morris (1997) is utilized.

The third part of this thesis applies the ASD methodology to the study of the fluctuating motion of non-colloidal suspensions (described as shear-induced diffusion). The first direct experimental observation of shear-induced diffusion dates back to Eckstein *et al.* (1977) who studied the fluctuating motion of individual tracer particles in a Couette flow. The nature of the phenomenon is quite different from the more familiar concept of Brownian diffusion which is caused by thermal fluctuations and which is negligible for non-colloidal particles. Shear-induced diffusion (or hydrodynamic diffusion, as it is sometimes referred to) is the result of the fluctuating motion of the particles due to the presence of neighboring particles and the hydrodynamic interactions among them. The work of Eckstein *et al.* (1977) was followed by experiments by Leighton & Acrivos (1987) and Phan & Leighton (1999), and more recently by Breedveld *et al.* (1998, 2001). Theoretical work on self-diffusion has focused on the dilute limit, where only interactions between two or three particles are taken into account. In the presence of only hydrodynamic interactions a two-particle collision introduces no net displacement (for the motion in the velocity gradient and vorticity directions). Da Cuncha & Hinch (1996) introduced asymmetry by studying the motion of two rough particles, while Wang *et al.* (1996) introduced a third particle to break the symmetry. Brady & Morris (1997) calculated the diffusion coefficient for dilute systems in the presence of weak residual Brownian motion and a hard-sphere interparticle force, which also breaks the symmetry of the two-particle limit and leads to diffusive motion.

The self-diffusivities are also calculated and are found to be significantly affected by

the system size (in particular for small number of particles); large systems are therefore necessary in order to obtain quantitatively accurate results. Emphasis is placed on the calculation of the longitudinal (in the flow direction) self-diffusivity, for which very limited results are available. The coupling of the advective flow with the diffusive motion in the velocity-gradient direction introduces further difficulties which are addressed in detail. The importance of a finite correlation time for the diffusive motion is also addressed and it is demonstrated how previous studies (Breedveld *et al.* 1998, 2000; Foss & Brady 1999) did not use long enough strains for the diffusive regime to be established.

The thesis is organized as follows: The principles of the new method (ASD) are described in chapter 2 along with validation of the method for some test problems (mainly results for cubic arrays) and demonstration of the total operation cost. The high-frequency dynamic viscosity and short-time self-diffusivity are also presented and results are expanded to volume fractions very near close packing.

The new method is used in chapter 3 for the calculation of the rheology and microstructure under simple shear of suspensions of non-Brownian particles. The effect of the interparticle force is discussed and very concentrated systems are briefly studied.

In chapter 4 the complete self-diffusion tensor is calculated for the same system of non-Brownian particles and presented as a function of the volume fraction. The effect of the system size is investigated and some limitations for the calculation of the longitudinal self-diffusivity are addressed.

All three appendices serve mostly as a companion to chapter 2 and to the new method. In Appendix A an overview of ASD is presented and some practical considerations are addressed. Appendix B presents in some detail the distribution of the force from the particle's center to a fixed grid (used for the wave-space part of the Ewald sums), while Appendix C presents the formulae for the real-space parts of the Ewald sums.

Finally, it is noted that chapters 2, 3 and 4 are self-contained and have been (or will be) published independently in scientific journals.

References

BRADY, J. F. & MORRIS, J. F. 1997 Microstructure of strongly sheared suspensions and its impact on rheology and diffusion. *J Fluid Mech.* **348**, 103.

BREEDVELD, V., VAN DEN ENDE, D., TRIPATHI, A. & ACRIVOS, A. 1998 The measurement of the shear-induced particle and fluid tracer diffusivities by a novel method. *J Fluid Mech.* **375**, 297.

BREEDVELD, V., VAN DEN ENDE, D., BOSSCHER, M., JONGSCHAAP, R. J. J. & MELLEMA, J. 2001 Measuring shear-induced self-diffusion in a counter-rotating geometry. *Phys. Rev. E* **63**, 1403.

DA CUNHA, F. R. & HINCH, E. J. 1996 Shear-induced dispersion in a dilute suspension of rough spheres. *J. Fluid Mech.* **309**, 211.

DARDEN, T., YORK, D. & PEDERSEN, L. 1993 Particle Mesh Ewald: An $n \log(n)$ method for Ewald sums in large systems. *J. Chem. Phys.* **98**, 10089.

DURLOFSKY, L. J., BRADY, J. F. & BOSSIS, G. 1987 Dynamic simulations of hydrodynamically interacting particles. *J. Fluid Mech.* **180**, 21.

EINSTEIN, A. 1906 Eine neue bestimmung der molekuldimensionen. *Ann. Phys.* **19**, 289.

FOSS, D. R. & BRADY, J. F. 1999 Self-diffusion in sheared suspensions by dynamic simulation. *J. Fluid Mech.* **401**, 243.

FOSS, D. R. & BRADY, J. F. 2000 Structure, diffusion and rheology of Brownian suspensions by Stokesian Dynamics simulation. *J. Fluid Mech.* **407**, 167.

GADALA-MARIA, F. 1979 The rheology of concentrated suspensions, PhD Thesis, Stanford University.

JEFFREY, D. J., MORRIS, J. F. & BRADY, J. F. 1993 The pressure moments for two spheres in low-Reynolds-number flow. *Phys. Fluids A* **5**, 2317.

LEIGHTON, D. & ACRIVOS, A. 1987 Measurement of shear-induced migration of particles in concentrated suspensions. *J. Fluid Mech.* **177**, 109.

PHAN, S. E. & LEIGHTON, D. 1999 Measurement of the shear-induced tracer diffusivity in concentrated suspensions. *J. Fluid Mech.* (submitted).

PHILLIPS, R. J., BRADY, J. F. & BOSSIS, G. 1988 Hydrodynamic transport properties of hard-sphere dispersions. I. Suspensions of freely mobile particles. *Phys. Fluids* **31**, 3462.

PHUNG, T. N., BRADY, J. F. & BOSSIS, G. 1996 Stokesian Dynamics simulations of Brownian suspensions. *J. Fluid Mech.* **313**, 181.

SINGH, A. 2000 Rheology of non-colloidal suspensions. PhD Thesis, Indian Institute of Science, Bangalore, India.

WANG, Y., MAURI, R. & ACRIVOS, A. 1996 Transverse shear-induced liquid and particle tracer diffusivities of a dilute suspension of spheres undergoing a simple shear flow. *J. Fluid Mech.* **327**, 255.

ZARRAGA, I. E., HILL, D. A. & LEIGHTON, D. T. 2000 The characterization of the total stress of concentrated suspensions of non-colloidal spheres in Newtonian fluids. *J. Rheol.* **44**, 185.

Chapter 2

Accelerated Stokesian Dynamics Simulations

2.1 Introduction

Numerical simulations of the behavior of suspensions of particles provide a valuable tool for understanding many complex rheological phenomena. Through simulations both the macroscopic suspension properties and the suspension microstructure have been studied, and insight into structure-property relationships has been obtained (Brady & Bossis 1988, Foss & Brady 2000). Determining the hydrodynamic interactions among particles in Stokes flow (small Reynolds number), however, can be a complicated and computationally expensive task, mainly due to the long-range nature of the interactions and the presence of strong lubrication effects when particles are in close proximity to each other. The fluid velocity disturbance caused by a particle on which a net external force acts decays as $1/r$, where r is the distance from the particle, and therefore the hydrodynamic interactions cannot be truncated and no simple pairwise-additive approximation can be made. In addition, the presence of lubrication effects makes conventional numerical techniques (such as the boundary-integral technique) expensive computationally when two particles approach each other.

Durlofsky, Brady & Bossis (1987) developed a method that successfully accounts for both the many-body interactions and the near-field lubrication effects by splitting the hydrodynamic interactions into a far-field mobility calculation and a pair-wise additive resistance calculation. The main advantage of the method is that a relatively small num-

ber of unknowns per particle is sufficient to adequately solve many dynamic simulation problems. The main disadvantage of the method, however, is that it requires inverting a far-field mobility matrix with at least $(11N)^2$ elements (N being the number of particles in the system), with a computational cost that limits the method to N on the order of a hundred.

The method of Durlofsky, Brady & Bossis (1987) and its extension to infinite suspensions by Phillips *et al.* (1988) is known as Stokesian Dynamics (Brady & Bossis 1988; hereafter referred to as SD) and has been used successfully over the last decade to give accurate results for many problems where the system size is of relatively little importance. For a variety of problems, however, it is desirable to simulate systems containing a much larger number of particles in order to eliminate any system size effects. For example, in the simulation of very dense suspensions, large-scale simulations are often needed to capture the microstructure correctly; in addition, most commonly used Monte Carlo algorithms cannot even generate particle configurations above the freezing point of hard spheres ($\phi > 0.49$) for $N < 500 - 1000$ as the small system size causes very rapid crystallization. Similarly, problems involving fiber suspensions require large-scale simulations to assure that the simulation box size is significantly larger than the length of each fiber.

In order to address problems where the system size is important and larger systems are therefore necessary, we present a new method that maintains the same level of accuracy as conventional Stokesian Dynamics but with a computational cost that scales only as $N \ln N$. Our main objective is to avoid both the costly construction of the far-field mobility matrix and its inversion. Before going into the details of our new approach, it is worth making some general observations to see how one might construct a more efficient algorithm.

Iterative schemes can replace $O(N^3)$ inversions with potentially less costly $O(N^2)$ multiplications, and when applied to "special" matrices—sparse, positive-definite, well-conditioned—iterative schemes can result in $O(N)$ operations. As we shall see in the next section, for most applications of hydrodynamic interactions in Stokes flow, the far-field resistance matrix usually appears as a product with a velocity and the knowledge of the far-field hydrodynamic force (and not the elements of the matrix itself) is sufficient for the iterative calculation of the particle velocities. It is therefore feasible to attempt a

method that would only calculate $6N$ far-field hydrodynamic force/torques as opposed to the full far-field mobility matrix. In addition, with this approach only the near-field contribution to the hydrodynamic interactions remains in a matrix-like form; a matrix that is now sparse and can be manipulated easily in $O(N)$ operations. This approach leads again to a system of linear equations of the form $\boldsymbol{A} \cdot \boldsymbol{x} = \boldsymbol{b}$, where now $\boldsymbol{x}$ is the vector representing the translational and rotational velocities of all particles, $\boldsymbol{A}$ is a sparse matrix representing the near-field part of the resistance matrix with only $O(N)$ non-zero elements, and $\boldsymbol{b}$ represents the shearing and non-hydrodynamic force/torques on the particles and, in addition, includes all the far-field physics. We use a particle-mesh approach (Hockney & Eastwood 1988) in combination with the Ewald summation technique to generate the far-field part of $\boldsymbol{b}$ in $O(N \ln N)$, an approach based on newly developed Particle-Mesh-Ewald algorithms (Darden *et al.* 1993). Lubrication interactions are treated as in conventional SD, taking special care to store the now sparse resistance matrix in a computationally efficient manner. The linear system is solved iteratively and, with proper preconditioning, very few iterations are necessary to achieve convergence.

We should also mention here the existence of other $O(N)$ algorithms, developed by Ladd (1994a,b) and by Sangani & Mo (1996), that attempt to address similar problems. Ladd's method is based on the lattice-Boltzmann technique—the fluid continuum is replaced by a lattice-Boltzmann gas, while the behavior of the rigid particles is simulated with the use of suitable rules for the momentum and position exchange between the lattice-gas particles. Ladd (1994a,b) also used continuum Stokes flow lubrication results to reduce the number of lattice gas points between near touching particles. Sangani & Mo's algorithm follows a more traditional approach by calculating the full resistance matrix through a fast multipole summation technique and inverting the resulting matrix iteratively. The fast multipole method is a widely used approach to performing fast summations in a number of fields. This method is in principle $O(N)$, although the iterative solution technique employed by Sangani & Mo appears to perform poorly, at least in their published results. The calculation of the far-field hydrodynamic interactions presented in the following sections was inspired by the work of Higdon and coworkers (private communication, Guckel 1999). Higdon applied a Particle-Mesh-Ewald-sum (PME) technique (Darden *et al.* 1993)

for the calculation of the far-field hydrodynamic force/torques; the problem of solving the resulting system of equations efficiently, however, was never fully addressed.

The basic method is presented in §2.2 where we describe in detail both the calculation of the far-field interactions and the iterative scheme for the solution of the resulting linear system. In §2.3 we test the accuracy of our method by performing calculations for simple cubic arrays—cases that have been studied extensively in the past and for which both analytical and simulation results are available for comparison. In §2.4 we calculate properties of random suspensions and document results where the system size is indeed important, e.g., for very concentrated suspensions. We conclude in §2.5 with remarks on how this method can be extended to other problems in Stokes flow and the analogous problems in electrostatics and elasticity theory.

2.2 Method

Before proceeding with the presentation of the new method, we give a brief overview of the conventional Stokesian Dynamics technique. For N rigid particles suspended in an incompressible Newtonian fluid of viscosity η and density ρ, the motion of the fluid is governed by the Navier-Stokes equations, while the motion of the particles is described by the coupled N-body equation of motion:

$$\boldsymbol{m} \cdot \frac{\mathrm{d}\boldsymbol{U}_p}{\mathrm{d}t} = \boldsymbol{F}^h + \boldsymbol{F}^p, \tag{2.1}$$

which simply states that the mass times the acceleration equals the sum of the forces. In (2.1) $\boldsymbol{m}$ is the generalized mass/moment-of-inertia matrix of dimensions $6N \times 6N$, $\boldsymbol{U}_p$ is the particle translational/rotational velocity vector of dimension $6N$, and $\boldsymbol{F}^h$ and $\boldsymbol{F}^p$ are the hydrodynamic and external force-torque vectors acting on the particles. Although the Stokesian Dynamics method can also be applied to problems where Brownian motion is important, here we only consider non-Brownian systems (infinite Péclet number); extension to include Brownian motion in ASD is possible, however (Banchio & Brady 2001). When the motion on the particle scale is such that the particle Reynolds number is small, the fluid equation of motion becomes linear (Stokes equation) and the hydrodynamic forces

and torques acting on the particles in a suspension undergoing a bulk linear flow are given by:

$$\boldsymbol{F}^h = -\boldsymbol{R}_{FU} \cdot (\boldsymbol{U}_p - \boldsymbol{u}^\infty) + \boldsymbol{R}_{FE} : \boldsymbol{E}. \tag{2.2}$$

Here, $\boldsymbol{u}^\infty$ is the velocity of the bulk linear flow evaluated at the particle center, $\boldsymbol{E}$ is the externally imposed rate of strain tensor, and $\boldsymbol{R}_{FU}(\boldsymbol{x})$ and $\boldsymbol{R}_{FE}(\boldsymbol{x})$ are the configuration-dependent resistance matrices that give the hydrodynamic force/torques on the particles due to their motion relative to the fluid and due to the imposed shear flow, respectively; the vector $\boldsymbol{x}$ denotes the configuration—position and orientation—of the particles.

The combination of the resistance matrices is denoted the grand resistance matrix:

$$\mathcal{R} = \begin{bmatrix} \boldsymbol{R}_{FU} & \boldsymbol{R}_{FE} \\ \boldsymbol{R}_{SU} & \boldsymbol{R}_{SE} \end{bmatrix}, \tag{2.3}$$

where $\boldsymbol{R}_{SU}$ and $\boldsymbol{R}_{SE}$ are similar to $\boldsymbol{R}_{FU}$ and $\boldsymbol{R}_{FE}$ and relate the particle stresslet, $\boldsymbol{S}^h$—the symmetric first moment of the force density on a particle—to the velocity and the rate of strain. The inverse of the resistance matrix is known as the mobility matrix $\boldsymbol{M}$ and gives the particle velocities ($\boldsymbol{U}_p - \boldsymbol{u}^\infty$, $-\boldsymbol{E}$) in terms of the forces ($\boldsymbol{F}^h$ and $\boldsymbol{S}^h$). Conventional SD exploits the fact that hydrodynamic interactions among particles can be decomposed into long-range mobility interactions and short-range lubrication interactions. The long-range interactions are computed by expanding the force density on the surface of each particle in a series of moments. The zeroth moment is simply the net force acting on a particle (plus, for a spherical particle, a potential dipole), the first moment can be decomposed into the torque and the stresslet, while higher moments are neglected. There is no fundamental reason that higher moments cannot and should not be included, and indeed there are problems where higher moments are significant (Ladd, 1990). But, the first two moments, when combined with the near-field lubrication interactions, are the minimum set needed and require the least computational effort. Furthermore, this level of truncation has been shown to give very accurate results for many hydrodynamic problems.

This truncated multipole expansion, in combination with Faxén's laws, is used to

form the grand mobility matrix $\mathcal{M}^{\infty}$. Once constructed, the grand mobility matrix is inverted to yield a far-field approximation to the grand resistance matrix. While $\mathcal{M}^{\infty}$ is pair-wise additive, on inversion infinite reflections among all moments and all particles are computed, and thus the far-field resistance matrix is a true many-body interaction. Finally, since the many-body approximation to the resistance matrix still lacks lubrication, which would only be reproduced upon inversion of the mobility matrix if all multipole moments were included, the near-field interactions are introduced into the resistance tensor in a pair-wise additive fashion. The exact two-body resistance interactions (Jeffrey & Onishi 1984), $\mathcal{R}_{2B}$, are added to $(\mathcal{M}^{\infty})^{-1}$, but since the far-field two-particle resistance interactions have already been included upon the inversion of $\mathcal{M}^{\infty}$ special care is needed in order not to count these interactions twice. Thus, the two-body interactions already included in $(\mathcal{M}^{\infty})^{-1}$, denoted as $\mathcal{R}_{2B}^{\infty}$, are subtracted (Durlofsky, Brady & Bossis, 1987), and the approximation to the grand resistance matrix becomes:

$$\mathcal{R} = (\mathcal{M}^{\infty})^{-1} + \mathcal{R}_{2B} - \mathcal{R}_{2B}^{\infty}. \tag{2.4}$$

Once the grand resistance matrix is known, from (2.1) and (2.2) the particle velocities can be obtained if the forces are known or vice versa. From the particle velocities new configurations are obtained, the resistance tensors are computed anew and the procedure repeated. This method captures both the near- and far-field physics and has given excellent results for many problems. Unfortunately, the direct solution of equation (2.1) as implemented in conventional Stokesian Dynamics is computationally expensive since it involves the costly $O(N^2)$ calculation of the far-field mobility matrix and its costly $O(N^3)$ inversion. We now present an alternate approach in an attempt to minimize the computational cost and devise a method with a more favorable scaling.

As in conventional SD, we split the hydrodynamic force into a far-field and a near-field

part:

$$\begin{aligned} \boldsymbol{F}^h &= \boldsymbol{F}^h_{ff} + \boldsymbol{F}^h_{nf} \\ &= -\boldsymbol{R}_{FU,ff} \cdot (\boldsymbol{U}_p - \boldsymbol{u}^\infty) + \boldsymbol{R}_{FE,ff} : \boldsymbol{E} \\ &\quad - \boldsymbol{R}_{FU,nf} \cdot (\boldsymbol{U}_p - \boldsymbol{u}^\infty) + \boldsymbol{R}_{FE,nf} : \boldsymbol{E}. \end{aligned} \tag{2.5}$$

The near-field resistance matrix in the above equation corresponds simply to the proper component of $\mathcal{R}_{2B} - \mathcal{R}^\infty_{2B}$ in (2.4), while the far-field resistance matrix is the corresponding part of $(\mathcal{M}^\infty)^{-1}$. Instead of calculating $(\mathcal{M}^\infty)^{-1}$ directly as was done before, however, we now calculate the far-field hydrodynamic force instead. Although this approach does result in some loss of information (compared to the calculation of the full matrix), it allows us to calculate only $6N$ hydrodynamic forces/torques, a procedure with a significantly smaller computational cost. In the following subsections, we discuss in detail how this calculation is done, along with a discussion of iterative techniques that further reduce the computational cost of the inversion of the remaining near-field matrix.

2.2.1 Calculation of the far-field interactions

As was already mentioned, in order to avoid the expensive construction of the far-field resistance matrix we calculate the far-field hydrodynamic force directly—that is, the product of the resistance matrix with a known velocity. In order to clarify the most important features of the new approach, we first use a simple schematic description. In Stokes flow the velocity at any point in the fluid can be expressed in a number of equivalent ways—integral representations of Green functions, multipole expansions of force moments, etc. In the following paragraphs we will present the multipole expansion approach in detail, but for the moment we use a very general functional form:

$$u_i(\boldsymbol{x}) - u_i^\infty(\boldsymbol{x}) = \sum_n G_{ij}(\boldsymbol{x}, \boldsymbol{x}_n) F_j^n, \tag{2.6}$$

where $u_i(\boldsymbol{x}) - u_i^\infty(\boldsymbol{x})$ is the i-component of the velocity disturbance in the fluid at any position $\boldsymbol{x}$, F_j^n is the j-component of the hydrodynamic force, torque, stresslet (or even

higher moments) on each particle n, and G_{ij} corresponds to the appropriate solution function. To determine the motion of a particle immersed in a flow field given by (2.6), we make use of the Faxén formulae that relate the force (and higher moments) on a particle n to the particle velocity $U^n_{p,i}$ and the fluid velocity at the particle center, $u_i(\boldsymbol{x}_n)$:

$$F^n_i = (U^n_{p,i} - u^\infty_i(\boldsymbol{x}_n)) + H(u_i(\boldsymbol{x}_n) - u^\infty_i(\boldsymbol{x}_n)), \tag{2.7}$$

where H represents a known functional operation. (A scalar operator multiplying the particle velocity, e.g., $6\pi\eta a$ for a sphere of radius a in a fluid with viscosity η, can be included in the non-dimensionalization of the force and therefore has been omitted here.) It should be clear that by combining equations (2.6) and (2.7) one can eliminate the fluid velocity $u_i(\boldsymbol{x}_n)$ and construct a mobility matrix relating the velocity of each particle to the forces on all of the particles. It should also be obvious that the mobility formulation is the most straightforward to calculate, since $U^n_{p,i}$ is only present in equation (2.7); such a mobility formulation then needs to be inverted to give the resistance formulation.

An alternative approach is to never calculate the mobility matrix and calculate F^n_i directly in an iterative manner. Assuming that all the particle velocities are known (either as a nested iterative procedure, or more simply as the velocities of the previous time step), an initial value is assumed for the hydrodynamic forces, equation (2.6) is solved for the corresponding fluid velocities, u_i, and then with application of Faxén's laws (2.7) the initial forces are corrected and the process repeated until convergence. The computational cost of such a procedure is dominated by the $O(N^2)$ calculation of $\sum_n G_{ij}(\boldsymbol{x}, \boldsymbol{x}_n)F^n_j$—a sum over the forces of all the other particles. However, the calculation of these sums can be accelerated significantly with the use of recently developed methods, like the Particle-Mesh-Ewald (referred to as PME hereafter) technique. The ideas of particle-mesh techniques (Hockney & Eastwood 1986) are used to assign particles to a mesh according to their positions and then fast Fourier transform (FFT) techniques are used to evaluate the wave-space part of the Ewald sum on this mesh. The fast evaluation of the wave-space sum is then used to set the parameters to allow an $O(N)$ evaluation of the real-space sum. PME algorithms have been successfully applied to the calculation of Coulombic interactions (Darden *et al.* 1993,

1997, Essmann *et al.* 1995, Petersen 1995) and recently have been formulated for the case of hydrodynamic interactions by Higdon & coworkers (Guckel 1999); this formulation will be described here in detail.

Our starting point is Hasimoto's solution (1959) of the Stokes equations for the flow past a periodic array of spheres. Hasimoto's solution is exactly equivalent to that given by Beenaker (1986); however, because a regular grid of points is used for the calculation of the Fourier space sum, Hasimoto's approach is preferred. Note also that all of the following analysis refers to periodic systems; the subject of convergence of the resulting infinite sums will not be discussed since it has been resolved in the past (see Brady *et al.* 1988). Following Hasimoto, the fluid velocity in the presence of a periodic array of N suspended particles at positions $\boldsymbol{r}_n$, represented as point forces $\boldsymbol{F}^n$ (with F_j^n, the j-component of the force that the fluid exerts on particle n), in a periodic unit cell of volume V_0 can be expressed as:

$$u_j(\boldsymbol{x}) = \frac{1}{4\pi\eta}\left(S_j^1 - \frac{\partial^2 S_l^2}{\partial x_l \partial x_j}\right), \tag{2.8}$$

where

$$S_l^2 = -\frac{1}{4\pi^3 V_0}\sum_{\boldsymbol{k}\neq 0}\frac{\mathrm{e}^{-2\pi \mathrm{i}(\boldsymbol{k}\cdot\boldsymbol{r})}}{k^4}\hat{F}_l^k, \tag{2.9}$$

and

$$S_j^1 = \nabla^2 S_j^2. \tag{2.10}$$

Here, $\boldsymbol{k}$ is the reciprocal lattice vector (corresponding to the real space vector $\boldsymbol{r}$), and $\hat{F}_j^k$ is the j-component of the Fourier transform of the real-space lattice point force $\boldsymbol{F}^n$.

The above sum, which simply represents the contribution to the fluid velocity of all the "particle-point-forces", can be evaluated efficiently with the introduction of Ewald's summation technique. We start with an integral representation for $1/k^{2m}$:

$$\frac{1}{k^{2m}} = \frac{\pi^m}{\Gamma(m)}\int_0^\infty \mathrm{e}^{-\pi k^2 \beta}\beta^{m-1}d\beta. \tag{2.11}$$

Then

$$\sigma_j^m = \sum_{\boldsymbol{k}\neq 0} \frac{\mathrm{e}^{-2\pi \mathrm{i}(\boldsymbol{k}\cdot\boldsymbol{r})}}{k^{2m}} \hat{F}_j^k = \frac{\pi^m}{\Gamma(m)} \sum_{\boldsymbol{k}\neq 0} \int_0^\infty \mathrm{e}^{-\pi k^2\beta - 2\pi \mathrm{i}(\boldsymbol{k}\cdot\boldsymbol{r})} \hat{F}_j^k \beta^{m-1} d\beta$$
$$= \frac{\pi^m}{\Gamma(m)} \int_0^\infty \beta^{m-1} \left[\sum_{\boldsymbol{k}} \hat{F}_j^k \mathrm{e}^{-\pi k^2\beta - 2\pi \mathrm{i}(\boldsymbol{k}\cdot\boldsymbol{r})} - \hat{F}_j^0 \right] d\beta. \tag{2.12}$$

A splitting parameter α is introduced and the integral in (2.12) is split into two parts, one from 0 to α, and the other from α to ∞. Ewald's theta transformation formula

$$\sum_{\boldsymbol{k}} \hat{F}_j^k \mathrm{e}^{-\pi k^2\beta - 2\pi \mathrm{i}(\boldsymbol{k}\cdot\boldsymbol{r})} = \frac{V_0}{\beta^{\frac{3}{2}}} \sum_n \mathrm{e}^{-\pi(\boldsymbol{r}-\boldsymbol{r}_n)/\beta} F_j^n \tag{2.13}$$

is then applied to the integral from 0 to α.

The general formula for the evaluation of S_j^1 or S_j^2 is then:

$$\sigma_j^m = \sum_{\boldsymbol{k}\neq 0} \frac{\mathrm{e}^{-2\pi \mathrm{i}(\boldsymbol{k}\cdot\boldsymbol{r})}}{k^{2m}} \hat{F}_j^k$$
$$= \frac{\pi^m \alpha^m}{\Gamma(m)} \left[V_0 \alpha^{-\frac{3}{2}} \sum_n \phi_{-m+\frac{1}{2}} \left(\frac{\pi(\boldsymbol{r}-\boldsymbol{r}_n)^2}{\alpha} \right) F_j^n - \frac{\hat{F}_j^0}{m} \right]$$
$$+ \frac{\pi^m \alpha^m}{\Gamma(m)} \left[\sum_{\boldsymbol{k}\neq 0} \mathrm{e}^{-2\pi \mathrm{i}(\boldsymbol{k}\cdot\boldsymbol{r})} \phi_{m-1}(\pi\alpha k^2) \hat{F}_j^k \right], \tag{2.14}$$

where we have replaced $\beta = \alpha/\xi$ in the first integral and $\beta = \alpha\xi$ in the second. The first sum and the constant term correspond to the real-space sum contribution from the presence of all particles (including the self-term), while the second sum is the wave-space sum excluding the $\boldsymbol{k} = 0$ term. The function ϕ_ν is the incomplete Γ-function:

$$\phi_\nu(x) = \int_1^\infty \xi^\nu \mathrm{e}^{-x\xi} d\xi, \tag{2.15}$$

and can easily be evaluated since it satisfies simple recurrence formulae (see Hasimoto (1958) for more detail).

Using (2.14) and substituting the expressions (2.9) and (2.10) for S_1 and S_2 into (2.8)

for the fluid velocity, we obtain:

$$u_j(\boldsymbol{x}) = \frac{1}{4\pi\eta}\left(\sum_n F_l^n\left[\left(-\frac{\pi}{\alpha^{\frac{3}{2}}}\right) r^2\phi_{\frac{1}{2}}\delta_{jl} + \alpha^{-\frac{1}{2}}\delta_{jl} + \left(\frac{\pi}{\alpha^{\frac{3}{2}}}\right) x_l x_j \phi_{\frac{1}{2}}\right]\right)$$
$$+ \frac{1}{4\pi\eta}\left(\frac{1}{\pi V_0}\sum_{\boldsymbol{k}\neq 0} \mathrm{e}^{-2\pi\mathrm{i}(\boldsymbol{k}\cdot\boldsymbol{r})}\left(\frac{\hat{F}_j^k}{k^2} - \frac{\hat{F}_l^k k_l k_j}{k^4}\right)\mathrm{e}^{-\pi\alpha k^2}\left(1+\pi\alpha k^2\right)\right). \qquad (2.16)$$

This is the exact result for Stokes flow in a periodic array of point forces. We shall now show how this result can be generalized for the case of a random distribution of particles, to include higher moments (torque, stresslet, etc.) in order to account for the finite size of the particles in different types of flows, and we shall demonstrate an efficient way to calculate the above sums numerically.

The incomplete Γ-functions $\phi_\nu(x)$ tend rapidly to zero as $x \to \infty$. Therefore, as $\alpha \to 0$, $\phi_{-m+\frac{1}{2}}\left(\frac{\pi(\boldsymbol{r}-\boldsymbol{r}_n)^2}{\alpha}\right) \to 0$ and the velocity is represented as a pure wave-space sum. On the other hand, for large values of α the wave-space sum contribution vanishes and the velocity is represented as a real-space sum. The choice of α and the optimum efficiency of balancing the computational work for the evaluation of the two sums is one of the main issues of the algorithm.

2.2.2 Wave-space sum contribution

The wave-space sum contribution to the fluid velocity given by

$$WS = \frac{1}{4\pi\eta}\left[\frac{1}{\pi V_0}\sum_{\boldsymbol{k}\neq 0} \mathrm{e}^{-2\pi\mathrm{i}(\boldsymbol{k}\cdot\boldsymbol{r})}\left(\frac{\hat{F}_j^k}{k^2} - \frac{\hat{F}_l^k k_l k_j}{k^4}\right)\mathrm{e}^{-\pi\alpha k^2}\left(1+\pi\alpha k^2\right)\right], \qquad (2.17)$$

can be evaluated efficiently as the inverse Fourier transform of the expression

$$\left(\frac{F_j^n}{k^2} - \frac{F_l^n k_l k_j}{k^4}\right)\mathrm{e}^{-\pi\alpha k^2}\left(1+\pi\alpha k^2\right). \qquad (2.18)$$

In order to do so, some further analysis of the meaning and calculation of $\hat{F}_j^k$ is necessary. Let us consider again the flow past a periodic array of spheres. If the spheres are sufficiently small, then the force acting on the surface of each sphere can be simply assumed to be a

point force acting on its center. The position of sphere n can then be specified either in the real-space ($\boldsymbol{r}$) or in the reciprocal-space ($\boldsymbol{k}$). For the case of a real-space simple cubic lattice, the reciprocal space lattice is also simple cubic. Then if F_j^n is the j component of the point-force representing particle n at position $\boldsymbol{r}_n$, $\hat{F}_j^k$ is simply its Fourier transform (on the same position, since both the real and reciprocal lattices are simple-cubic). For the case of a cubic array of point forces, the above description is all that is needed to evaluate the wave sum using conventional FFT methods. In order to address more realistic cases though, e.g., finite sized particles in random configurations and in different external fields, while still maintaining the "lattice-point-force" approach, we need to implement a more general particle and grid representation.

Let us now consider the case of a random distribution of spheres in a periodic computational domain where the particles are no longer part of a periodic array. Although the positions of the spheres no longer define a lattice, we can still define an artificial rectangular grid over the computational domain (see figure 2.1); the positions of the particles, however, no longer coincide with the grid-points. It is nevertheless possible to transfer the force acting on the center of each sphere to a collection of forces acting on the grid-points located in the sphere's vicinity. This is done by following well-known particle-mesh algorithms (Eastwood & Hockney 1988). It is desirable that the transition from the particle center to the grid involve only a relatively small number of grid points, be a smooth function of the location of the particle and capture the correct long-range physics for distances far away from the force center. Here, we perform the force assignment by the use of matched Taylor series expansions. For example, for the point force we require:

$$F_j^0 \mathrm{e}^{-2\pi \mathrm{i}(\boldsymbol{k}\cdot\boldsymbol{r}^0)} = \sum_{nodes\ \gamma} f_j^\gamma \mathrm{e}^{-2\pi \mathrm{i}(\boldsymbol{k}\cdot\boldsymbol{r}^\gamma)}, \tag{2.19}$$

or, after Taylor series expansion:

$$\begin{aligned} F_j^0 \left(1 + 2\pi \mathrm{i} k_l x_l^0 - 2\pi^2 k_l k_m x_l^0 x_m^0 + ..\right) = \\ \sum_{nodes} f_j^\gamma \left(1 + 2\pi \mathrm{i} k_l x_l^\gamma - 2\pi^2 k_l k_m x_l^\gamma x_n^\gamma + ..\right), \end{aligned} \tag{2.20}$$

where x_l^0 is the l-coordinate of the actual position of the particle and x_l^γ is the l-coordinate of the grid-point positions γ. Equations (2.19) and (2.20) simply state that when a force is transfered to the grid from a particle center, all its moments are also preserved. It is of course not possible to retain infinite terms in (2.20) and a truncated version is used.

The above analysis was limited to the case of point-forces; in most practical applications, however, we need to take into account the particle size and represent the particles more accurately. Following the conventional Stokesian Dynamics approach, each particle is represented as an expansion of the force density on its surface in a series of moments at its center. Using the same level of accuracy as in conventional SD, each spherical particle is represented as a point force $\boldsymbol{F}$, a doublet $\boldsymbol{D}$ (corresponding to the torque and stresslet), a potential dipole $\boldsymbol{d}$ (which is simply equal to $-a^2\boldsymbol{F}/6\eta$, where a is the particle radius), and a potential quadrupole $\boldsymbol{L}$ (which simply equals $-a^4\boldsymbol{S}/10\eta$, where $\boldsymbol{S}$ is the particle stresslet), while higher moments are neglected. The redistribution of the potential doublet, dipole, etc., follows the exact same procedure as for the force since they are just higher moments of the force singularity, and formulae equivalent to (2.20) can be derived. These formulae simply state, as was the case with (2.20), that the net force, torque, stresslet, etc., is conserved when transferred from the particle to the grid. The number of moments retained depends on the desired accuracy, and for this work an $O(k^3)$ matching is used, which means that the potential quadrupole is distributed to the grid with a leading error of $O(dx)$. To obtain that level of accuracy, the force moments need to be distributed as equivalent forces on a $5\times5\times5$ set of grid points centered at the node closest to the particle center. Higher accuracy can be obtained with an increased number of matched terms (corresponding to increased number of grid points upon which the force is distributed), but the computational cost increases accordingly. The formulae for the moment distribution on the grid can be found in Appendix B.

To summarize, the wave sum is calculated through the following steps: (a) each particle's force/torque/stresslet/etc. is distributed on a regular mesh over the computational domain, (b) the FFT of the distributed forces is calculated and the expression in equation (2.18) is evaluated, (c) the inverse FFT of step (b) is calculated, which simply gives the wave-space sum of equation (2.17). Thus, at the end, for a *given* set of forces and higher

moments on the particles, the contribution to the fluid velocity due to the wave-space sum is calculated. This contribution is a far-field contribution. The distribution of the forces on the grid and the simultaneous solution for all grid points includes effects from all particles.

This velocity corresponds to the fluid velocity on the given grid of nodes and not to the velocity at the particle centers, which is needed for Faxén's laws. The fluid velocity at a particle's center is obtained by interpolating from the grid to the particle position by a simple Lagrangian interpolation with a $5 \times 5 \times 5$ set of grid points for each particle. The general form of the Lagrangian interpolation is

$$\boldsymbol{u}(\boldsymbol{x}_0) = \sum_{i=1}^{5}\sum_{j=1}^{5}\sum_{k=1}^{5} h_i(x)h_j(y)h_k(z)\boldsymbol{u}_{i,j,k}, \tag{2.21}$$

where $\boldsymbol{u}(\boldsymbol{x}_0)$ is the interpolated velocity at position $\boldsymbol{x}_0$ and $\boldsymbol{u}_{i,j,k}$ are the velocities at a given grid point (i,j,k) (the indices i, j, k now correspond to local nodes around each particle's center). The interpolating polynomials are of the form:

$$h_i(x_0) = \frac{\prod_{j,j\neq i}(x_0 - x_j)}{\prod_{j,j\neq i}(x_i - x_j)}, \tag{2.22}$$

where x_i are the positions of the interpolation grid points in one dimension. The derivatives of the interpolants are then used to calculate the derivatives of the fluid velocity at the particle's center.

2.2.3 Real-space sum contribution

In addition to the wave-space sum contribution, the real-space sum expression

$$RS = \frac{1}{4\pi\eta}\sum_n F_l^n \left[\left(-\frac{\pi}{\alpha^{\frac{3}{2}}}\right)\phi_{\frac{1}{2}} r^2\delta_{jl} + \alpha^{-\frac{1}{2}}\delta_{jl} + \left(\frac{\pi}{\alpha^{\frac{3}{2}}}\right)\phi_{\frac{1}{2}} x_l x_j\right], \tag{2.23}$$

needs to be evaluated. This equation gives the velocity at any point in the fluid due to the presence of an array of point forces at distances $\boldsymbol{r}_n$; similar expressions can be obtained in a straightforward manner for the velocity and any number of higher derivatives of the velocity due to the presence of a torque, stresslet, etc. Equation (2.23) suggests that the

calculation of the real-space sum requires $O(N^2)$ operations, since the calculation of the velocity at each particle center requires the sum over all particles (including a self-term). The incomplete Γ-function, ϕ_ν, however, decays very fast, so that for small enough α the contribution of particle-pairs that are not near-neighbors will be very small and can be neglected without significant error. The elementary way to evaluate this sum is to sweep through all the particles, test whether their separation is less than a "cut-off separation", r_c, and if so compute the two particle contribution according to (2.23). Such an approach is clearly impractical, however, since it also gives an operation count that scales as N^2.

To reduce the computational cost, we arrange the particles in such a way that the tests for locating the neighboring particles are only performed over a small subset N_n of the total number of particles N. This is accomplished by introducing a "chaining mesh" (Hockney & Eastwood, 1986), which is a regular lattice of $(M_x \times M_y \times M_z)$ cells covering the computational periodic box; the number of the cells in each direction is such that the lengths of each side of each cell is always greater or equal to the aforementioned cut-off radius. Those particles that have non-zero contributions to the real-space sum of the hydrodynamic force must lie either in the same cell as any given particle, or in one of the 27 neighboring cells, and therefore one only needs to sweep through those neighboring cells in search for a particle's nearest neighbors. The calculation of the infinite real-space sum is thus reduced to the calculation of the sum locally over only a small number of neighboring particles—those particles that are closer than the chosen value of the cut-off radius, r_c. (The choice of r_c and its effect on the accuracy of the calculation will be discussed in detail in the following section.) The real-space sum calculation can thus be done analytically in a straightforward manner; the detailed formulae corresponding to the contributions of higher moments are presented in Appendix C. Note that according to (2.23), when calculating the real-space correction to the fluid velocity at the center of a particle, the real-space sum is performed over all neighboring particles, including the reference particle, and thus a self-term contribution also needs to be calculated. After the completion of the real-space sum step for every neighboring particle pair, a correction to the fluid velocity at the particle center is evaluated, which is added to the already evaluated fluid velocity from the wave-space sum.

As a final note, in a sheared suspension the unit cell and FFT grid points must deform along with the shear rate until the lattice repeats itself, typically at the end of one strain for simple shear flow.

2.2.4 Force laws

With the fluid velocity determined at each particle center, the far-field force, torque and stresslet exerted on each particle are calculated from Faxén's laws:

$$\boldsymbol{F}_{ff} = -6\pi\eta a\left(\boldsymbol{U}_p - \boldsymbol{u}^{\infty}(\boldsymbol{x})\right) + 6\pi\eta a(1 + \frac{a^2}{6}\nabla^2)(\boldsymbol{u}_{ff}), \tag{2.24a}$$

$$\boldsymbol{T}_{ff} = -8\pi\eta a^3\left(\boldsymbol{\Omega}_p - \boldsymbol{\omega}^{\infty}(\boldsymbol{x})\right) + 4\pi\eta a^3\nabla\times(\boldsymbol{u}_{ff}), \tag{2.24b}$$

$$\boldsymbol{S}_{ff} = \frac{20}{3}\pi\eta a^3\boldsymbol{E} + \frac{20}{3}\pi\eta a^3(1 + \frac{a^2}{10}\nabla^2)(\boldsymbol{e}_{ff}), \tag{2.24c}$$

where $\boldsymbol{u}_{ff}$ corresponds to the far-field fluid velocity evaluated at the center of the particle, $\boldsymbol{U}_p$, $\boldsymbol{\Omega}_p$ are the particle translational and angular velocities, $\boldsymbol{u}^{\infty}$, $\boldsymbol{\omega}^{\infty}$ and $\boldsymbol{E}$, are the bulk velocity, angular velocity and rate of strain, respectively, and $\boldsymbol{e}_{ff}$ is the rate of strain of the far-field velocity.

The scheme described above corresponds to a prediction-correction method where the hydrodynamic forces on the particles are first used as input to calculate both the wave- and real-space contributions to the fluid velocity and then the forces are calculated again from the far-field velocities with the assistance of Faxén's laws. Determining the forces is the resistance formulation of the problem—for a given configuration of particles and particle velocities, the particle forces and force moments are calculated. It has recently been shown (Ichiki & Brady 2001) that the method of reflections (which corresponds to the simplest iterative scheme for the inversion of the mobility matrix) can be divergent when more than two particles are present.

An alternative way to invert the mobility matrix, which is still largely based on the method of reflections, is to use a simple underrelaxation scheme and replace (2.24) by

$$\boldsymbol{F}_{ff} = \left[-6\pi\eta a\left(\boldsymbol{U}_p - \boldsymbol{u}^{\infty}(\boldsymbol{x})\right) + 6\pi\eta a(1 + \frac{a^2}{6}\nabla^2)(\boldsymbol{u}_{ff})\right]\omega + \boldsymbol{F}_{ff}^{old}(1-\omega), \tag{2.25}$$

where ω is the relaxation parameter, and $\boldsymbol{F}_{ff}^{old}$ is the previous guess for $\boldsymbol{F}_{ff}$. In practice, however, values of ω as low as 0.05 may be necessary for very large, or very dense systems, which leads to a large number of iterations when the initial guess is poor. The relaxation parameter ω appears to have no significant effect on the dynamics of the system after the system is relaxed to a quasi-steady state (typically after the particles have moved the length of the unit cell). For a fixed geometry, as in the lattice calculations described in §2.3, the relaxation parameter has no effect. As suggested by Ichiki & Brady (2001), the breakdown of the method of reflections can also be overcome by the use of a conjugate-gradient-type iterative method. The generalized minimum residual method (GMRES) was used here, and it was found that very accurate results can always be obtained with very few iterations. (It should be noted that the fact that the mobility matrix is never constructed does not introduce any further difficulties since in most iterative methods matrices only appear as products with vectors.)

We also briefly note here that the particle pressure (Jeffrey, Morris & Brady 1993) can be readily calculated following the same procedure. The wave-space contribution is obtained as part of the FFT procedure since it simply corresponds to the fluid pressure at the center of each particle, while the real-space sum part is calculated analytically.

2.2.5 Near-field interactions

Lubrication interactions are included in a manner very similar to conventional SD. The two-body resistance matrix $\boldsymbol{R}_{2B}$ of equation (2.4) is calculated from the known exact results, and the part of the two-body interactions already included in the far-field ($\boldsymbol{R}_{2B}^{\infty}$) is subtracted as in conventional SD. The chaining mesh is again utilized so that only interactions between neighboring particles will be included, thus reducing the computational cost from N^2 to NN_n, where N_n is now the number of particles closer to the cut-off radius for lubrication, which is $4a$. To further reduce both the computational cost and the memory requirements, the near field resistance matrices are stored in a sparse form, i.e., for each particle only the non-zero contributions from neighboring particles are stored, reducing the dimensions of $\boldsymbol{R}_{FU}$ from $6N \times 6N$ to $6N \times 6N_n$. This procedure allows every multiplication with any of the near-field resistance matrices to be an $O(N)$ operation.

2.2.6 Time integration

After both the far-field force and the near-field resistance matrices are calculated, the new particle velocities need to be calculated from (2.1), which, in the absence of particle inertia, gives

$$0 = -\boldsymbol{R}_{FU,nf} \cdot (\boldsymbol{U}_p - \boldsymbol{u}^{\infty}(\boldsymbol{x})) + \boldsymbol{R}_{FE,nf} : \boldsymbol{E}^{\infty} + \boldsymbol{F}^p + \boldsymbol{F}_{ff}, \tag{2.26}$$

where now $\boldsymbol{R}_{FU,nf}$ is a sparse, symmetric, positive-definite matrix. Note that since the far-field interactions are not included in the resistance matrix, the unit tensor $\boldsymbol{I}$ is added to $\boldsymbol{R}_{FU,nf}$ and subtracted from equation (2.26) to assure positive definiteness. The most efficient way to solve a sparse symmetric positive-definite system is by an iterative method, where the computational times can scale linearly with the matrix size since the sparse matrix multiplications required for an iterative method scale as N. However, a carefully designed iterative method needs to be applied since the number of iterations can increase significantly with increasing N. It is also worth noting that in (2.26) the far-field force is considered known, implying that the previous step velocities have been used for its calculation; alternatively an additional iterative scheme can be employed such that the velocities used in the far-field calculation are also updated. In most problems either the far-field force is small in magnitude (e.g., sheared systems) or it does not change rapidly with time (e.g., sedimenting systems), and in both cases the two approaches give results that are statistically indistinguishable; the simpler approach is therefore used hereafter.

Conjugate gradient methods provide a quite general means of solving the $N \times N$ linear system

$$\boldsymbol{A} \cdot \boldsymbol{y} = \boldsymbol{b}. \tag{2.27}$$

The advantage of these methods is that they reference matrix $\boldsymbol{A}$ only through its product with a vector, an operation that can be very efficient for properly stored matrices. The basic idea behind them for the simplest case of a symmetric positive-definite matrix is

minimizing the function

$$f(\boldsymbol{y}) = \frac{1}{2}\boldsymbol{y} \cdot \boldsymbol{A} \cdot \boldsymbol{y} - \boldsymbol{b} \cdot \boldsymbol{y}, \tag{2.28}$$

which is equivalent to its gradient $\nabla f = \boldsymbol{A} \cdot \boldsymbol{y} - \boldsymbol{b}$ being zero, thus giving the solution to (2.27). The minimization proceeds by generating a succession of search directions and improved minimizers until the required accuracy is reached. The ordinary conjugate gradient method works well—the number of iterations required for convergence is reasonably small—for matrices that are well-conditioned, i.e., matrices with eigenvalues that are tightly clustered. This suggests using these methods on a preconditioned form of equation (2.27):

$$\left(\tilde{\boldsymbol{A}}^{-1} \cdot \boldsymbol{A}\right) \cdot \boldsymbol{y} = \tilde{\boldsymbol{A}}^{-1} \cdot \boldsymbol{b}. \tag{2.29}$$

The matrix $\tilde{\boldsymbol{A}}$ is called a preconditioner and its purpose is that now the matrix $\left(\tilde{\boldsymbol{A}}^{-1} \cdot \boldsymbol{A}\right)$ will be well-conditioned, i.e., "close" to the identity matrix.

Torres & Gibson (1996) applied the conjugate gradient method for the sparse positive-definite near-field hydrodynamic resistance matrix $\boldsymbol{R}_{FU,nf}$ for different preconditioners and established that good convergence rates are possible when an incomplete Cholesky preconditioner is used. The incomplete Cholesky factor $\boldsymbol{L}_0$ is constructed following the same algorithm as for the calculation for the complete Cholesky factor, except that a specific element $\boldsymbol{L}_{0,ij}$ is only calculated when the corresponding element $R_{FU,ij}$ is non-zero and is otherwise set equal to zero. Thus, for each $i = 1, 2, ..., 6N$

$$L_{0,ii} = \left(R_{FU,ii} - \sum_{k=1}^{i-1} L_{0,ik}^2\right)^{1/2}, \tag{2.30}$$

and then for $j = i+1, i+2, ..., 6N$

$$L_{0,ji} = \begin{cases} \dfrac{1}{L_{0,ii}}\left(R_{FU,ij} - \displaystyle\sum_{k=1}^{i-1} L_{0,ik}L_{0,jk}\right) & \text{for} \quad R_{FU,ij} \neq 0 \\ 0 & \text{for} \quad R_{FU,ij} = 0. \end{cases} \tag{2.31}$$

The main advantage of the incomplete Cholesky preconditioner is that it captures the essential physics of the lubrication forces between two nearly touching particles while remaining as sparse as the initial $\boldsymbol{R}_{FU}$. If only the non-zero elements of $\boldsymbol{L}_0$ are computed and unnecessary operations with zero-valued elements are avoided, the preconditioning step remains an $O(N)$ operation.

Following Torres & Gibson (1996) a variation of the incomplete Cholesky factor is used where "blocks" of the matrix $\boldsymbol{L}_0$ are handled as opposed to individual elements. Since the resistance matrix consists of 6×6 blocks that map the velocity of one particle to the force/torque on another particle, the entire corresponding block of $\boldsymbol{L}_0$ is computed if any of the elements in the corresponding $\boldsymbol{R}_{FU}$ block are non-zero. Furthermore, they suggest a particle re-ordering according to each particle's proximity to one another so that a more "ordered" form of the resistance matrix can be used. The reverse Cuthill-McKee method (Cuthill & McKee 1967, George & Liu 1981) was found to achieve the best overall results, and we use this approach in our method. The benefit of particle reordering is both a more rapid convergence and a minimization of the breakdowns of the Cholesky preconditioner. Since an incomplete version of the Cholesky factor is calculated there is no guarantee, even for a symmetric positive-definite matrix, that square roots of negative numbers will not occur. To solve this problem $q\boldsymbol{I}$, where q a positive number large enough so that positive definiteness is obtained, is added to $\boldsymbol{R}_{FU}$. Although this addition solves the problem it increases the number of iterations required for convergence, and it was empirically observed by Torres & Gibson that the reordering of the particles reduces significantly the number of factorization break-downs.

We should emphasize here that the use of the preconditioner has a very important effect on the number of iterations required for convergence, especially for dense sheared systems. In the absence of preconditioning the number of iterations can be on the order of $100 - 200$ when particle clusters are forming and the interparticle separations become very small. Sangani & Mo (1996) also report iterations of the same order for their non-preconditioned system. The use of the preconditioner, however, decreases the number of iterations dramatically and most systems, including dense sheared suspensions, can be solved in less than 10 iterations. Figure 2.2 demonstrates the effect of the preconditioner

for a sheared system of $N = 512$ particles at volume fraction $\phi = 0.45$; the necessary number of iterations to achieve an accuracy of 10^{-4} in the residual calculation is significantly smaller for the preconditioned case. The effect of the preconditioner becomes even more significant with increasing strain; as the particles move closer together and form clusters, the non-preconditioned iterative procedure requires consistently more than 100 iterations for convergence.

The iterative procedure works well when the near-field lubrication matrix is reasonably well-behaved—in practice, when the interparticle distances are no less than $(10^{-5}-10^{-6})a$. In order to assure these minimum separations in a dynamic simulation, a repulsive interparticle force is generally needed. When shearing a dense suspension in the absence of Brownian and/or interparticle forces, particle overlaps can occur even for extremely small time-steps (Dratler & Schowalter 1996). The presence of an interparticle force can have a significant effect on the properties of some systems (e.g., sheared dense suspensions) and its impact is a matter for a separate study. The main point that we wish to make here is that our new method does not impose any more restrictions on the minimum interparticle separation compared to conventional SD, because the implicit inversion of the near-field resistance matrix captures the same physics as the inversion of the full resistance matrix. Since we shall validate the method only with non-dynamic results where the interparticle force will always be zero, the issue of the interparticle force will not be mentioned further.

2.2.7 Total operations count for each time step

The most time consuming parts of our algorithm are the calculation of the far-field and near-field interactions and the inversion of the resistance matrix. The inversion of the resistance matrix, when done iteratively as described in the previous section, can be an $O(N)$ operation depending on the preconditioner. The near-field interactions and the real-space contribution to the far-field, as was already discussed, can be calculated in $O(N)$ operations with the introduction of a chaining mesh. The wave-space contribution of the far-field interactions, on the other hand, is calculated in $O(N_m^3 \ln N_m)$, where N_m is the total number of mesh points in each-direction. In order for this part of the calculation to be $O(N)$, N_m must scale as $N^{1/3}$. The number of mesh points N_m determines the

accuracy of the wave-space sum calculation, and therefore our choice of N_m should be a compromise between desired accuracy and computational cost. This is where the choice of the splitting parameter α becomes important.

For small values of α, the wave-space sum constitutes the largest part of the contribution, and therefore a large number of FFT points per particle are necessary for an acceptable degree of accuracy. But if a large value of α is used, then the wave-space sum contribution is small and even low accuracy in its calculation leads to an acceptable overall error. The real-space sum on the other hand, requires a small value of α to minimize its error since only a few neighboring particles are used for the calculation of the real-space sum. By balancing those two requirements an optimum value of α can be found that will give both acceptable accuracy and reasonable computational cost.

To demonstrate the effect of the method parameters—splitting parameter α, cut-off radius for the calculation of the real-space sum r_c, and number of mesh-points N_m for the FFT calculation—on the Ewald-sum calculation, we study the following problem: A small number of particles ($N = 30$) is placed randomly in a unit cell of length $L = 16a$, corresponding to a volume fraction of 3%. An external force is imposed on all particles and the resulting far-field fluid velocities at the center of each particle are calculated according to (2.16). The same calculation is repeated by using the exact formulation of the Ewald sum of (2.16); this is done by including the interactions between all the particles not only in the unit cell, but also in 10 neighboring cells in each direction. The relative error between the exact Ewald-sum calculation and the PME calculation is then determined as $(u_{fluid,PME} - u_{fluid,exact})/u_{fluid,exact}$ and averaged over all the positions of the particles. Figure 2.3 shows this relative error for different values of α, wave-space sum discretization dx ($= L/N_m$, where L is the length of the unit cell and N_m is the number of FFT points in each direction) and cut-off radius r_c. It can clearly be seen that for every choice of dx and real-space sum cut-off radius, an optimum α exists. This is expected since, as was already mentioned, for increasing α the error in the wave-space sum calculation decreases, while the error in the real-space sum calculation increases. For a given dx the error decreases with increasing r_c, while the optimum choice of α increases with increasing r_c. In other words, for a fixed accuracy of the wave-space sum calculation, corresponding to fixed

number of FFT points, the overall accuracy will increase as the accuracy of the real-space sum calculation increases (cut-off radius for the real-space sum increases). In addition, the increased accuracy of the real-space sum calculation is more important for larger values of the splitting parameter α; for small values of α the real-sum contribution is very small and its accuracy does not affect the overall accuracy significantly. On the other hand, for a fixed cut-off radius and increasing number of FFT points the optimum value of α now decreases, since increased accuracy in the wave-space sum calculation now allows smaller values of the splitting parameter. It is also worth noting that the minimum error is completely determined by the choice of dx and r_c, and for some cases no choice of α gives acceptable behavior; for example, for the case of $r_c = 2a$, $dx = 1.0a$, the minimum error is close to 30%. For 2 FFT points per particle radius ($dx = 0.5a$, Figure 2.3c) and $r_c = 6 - 7a$, accuracy within 1% can be obtained with a choice of $\alpha \approx 12 - 15$, and for most applications this range of parameters will be used since it was found also to give an acceptable computational cost.

Figure 2.4 shows the computational time (in seconds) for one time step as a function of the number of particles N. The times correspond to a shearing problem at volume fraction $\phi = 0.45$; one iteration is performed for the convergence of the far-field interactions, and the inversion of the near-field matrix takes $8 - 10$ iterations for all numbers of particles shown. All the runs were performed on a single DEC Alpha AXP 21164 processor and the times are given in sec. The data are in good agreement with the proposed $N \ln N$ scaling set by the scaling of the FFT calculations.

2.3 Results—Simple Cubic Arrays

In this section the accuracy of the method is tested for the case of simple cubic arrays of spheres, a case for which a number of analytical and simulation results are available. Different choices for the method parameters are presented, which further demonstrates—this time for a problem with a known solution—that the PME calculation of the far-field contribution can give acceptable accuracy with a low computational cost.

2.3.1 Sedimentation of cubic arrays: sensitivity to method parameters

The first case we consider is a set of 8 particles sedimenting in a simple cubic lattice. Since the system is periodic, the number of particles is not important and our main goal is to check the accuracy of the far-field calculations. It is easy to show that for identical spherical particles on a cubic lattice subject to a constant external force, the pair-wise additive near-field forces will always sum to zero regardless of the volume fraction; therefore, the accuracy of the calculation of the far-field is the only issue. The exact infinite sums presented in § 2.2.1 are expected to give, within the number of moments included, results in exact agreement with the multipole moments analytical results of Zick & Homsy (1982) and the conventional SD results since an equivalent approach is used for their derivation.

The introduction of an FFT method, however, truncates the wave-space sum to the number of mesh points used, while the introduction of a near-field-like approach to the real-space sum truncates it to only the contributions of a few neighboring particles. Nevertheless, with a careful choice of the splitting parameter α, the infinite sums decay rapidly and acceptable accuracy can be obtained.

Figure 2.5 presents the sedimentation velocity for a relatively low volume fraction, $\phi = 0.064$, as a function of both the splitting parameter α and the wave-space sum discretization dx; the cut-off radius for the calculation of the real-space sum is defined so that only one neighbor in each direction is included, $r_c = \sqrt{3} \times 4a \approx 7a$. Good accuracy for the sedimentation velocity is obtained for a wide range of α and a desired plateau is observed for α near the optimum. The plateau in figure 2.5 corresponds to the range of α's where the inclusion of only one neighbor in the real-space sum and the discretization of the wave-space sum provide a nearly exact evaluation of the sums in equations (2.16). Obviously, as the wave-space sum discretization (dx) becomes finer, a wider range of α's (starting from smaller values) can be used with no significant loss of accuracy. Near the optimum value of α, however, values of dx near 0.5, or two points per particle radius, are sufficient for satisfactory accuracy, which allows us to treat large systems using a relatively small number of FFT discretization points.

Figures 2.6 and 2.7 present the same analysis for the case of $\phi = 0.5236$, a close packed simple cubic array. Figure 2.6 corresponds to the inclusion of only one neighbor in the

real-space sum, a cut-off radius of $r_c = \sqrt{3} \times 2a \approx 3.46a$, while figure 2.7 corresponds to the inclusion of two neighbors, $r_c = \sqrt{3} \times 4a \approx 7a$. The case of $r_c \approx 3.46a$ only gives satisfactory results when a fine wave-space discretization is used, in agreement with the observations of figure 2.3. In figure 2.7, on the other hand, the larger value of r_c allows fewer FFT points to be used and permits a greater range of α, in this case going to larger values since more neighboring particles have already been included. It should also be noted that for dense systems the same value of r_c corresponds to a larger number of near neighbors and therefore a larger computational cost in the real-space sum. On the other hand (for the same number of particles) dense systems correspond to much smaller unit cells and therefore the extra computational cost for the inclusion of more near neighbors is counteracted by the need for fewer FFT points for a given discretization (dx) and vice versa.

Figure 2.8 presents the sedimentation velocity for volume fraction $\phi = 0.064$ and $\alpha = 16$ as a function of the wave-space sum discretization parameter, dx, and for two different positions of the particles—on the grid points, and positioned midway between two grid points. This tests both the significance of the discretization in the wave-space sum and the accuracy of the force distribution/interpolation scheme. Again, for the given value of α corresponding to a value near the optimum, no significant loss of accuracy occurs for a wide range of dx. Also, the positions of the particles on or off the FFT grid is of little importance even for the largest values of dx. The same parametric analysis was also conducted for the case of sheared suspensions; the dependence on the far-field method parameters was even less apparent in this case since lubrication is now important and the calculation of the near-field interactions dominates the accuracy of the method.

2.3.2 Sedimentation of cubic arrays: volume fraction dependence

We now discuss the average sedimentation velocity of a simple cubic array of spherical particles as a function of the volume fraction ϕ. As was already mentioned, lubrication plays no role for this problem and the accuracy of the resulting sedimentation velocity is solely determined by the accuracy of the far-field calculation. Since the mobility matrix is never calculated, the sedimentation velocity can be found by simply imposing an external

force (gravity) on all the particles and calculating the resulting steady-state (converged) velocities. Also, since all particles are identical in a periodic lattice they all have the same velocity and therefore the relative distances between particles always remain constant; in other words there is no difference between a dynamic and a static approach to the problem. Figure 2.9 shows a comparison of the non-dimensional sedimentation velocity of a simple-cubic array of spheres obtained by the ASD method with the conventional SD results of Brady *et al.* (1988) and the theoretical calculations by Saffman (1973) and Zick & Homsy (1982). Saffman's calculations are for point-force particles and result in a sedimentation velocity $U/U_0 = 1 - 1.738\phi^{\frac{1}{3}}$, where U_0 is the settling velocity of an isolated particle under the same conditions. Zick & Homsy's results are exact, as they used sufficient moments to achieve convergence to the exact limit. For the same number of moments the SD and ASD results are identical for all volume fractions—the new method has the exact same accuracy as conventional SD.

For low volume fractions all methods give identical results. For high volume fractions ASD overestimates the sedimentation velocities in the exact same manner that conventional SD does. Only the point force and the second moment of that point force have a contribution in this formulation. Odd moments, although included, have no effect on the sedimentation velocity of cubic arrays, and as a result only the second-order method results of Zick & Homsy can be reproduced. For high volume fractions higher moments are needed; the SC results of Zick & Homsy and the random array results of Ladd (1990) indicate that at least four moments are needed for reasonable accuracy near maximum packing. This can easily be done in principle following the methodology outlined above, but at an increased computational cost per particle; the overall method will still scale as $N \ln N$, however.

2.3.3 Shear viscosity of cubic arrays

To calculate the shear viscosity of a cubic array of spheres, the relationship between the bulk stress and the imposed rate of strain is needed. Again, since the far-field mobility or resistance matrices are never calculated, we simply impose an external rate of strain on the particles and calculate the resulting induced far-field hydrodynamic stresslets. To

those values the near-field contribution calculated from the near-field resistance matrix, $\boldsymbol{R}_{SE,nf}$, is added; for a cubic lattice there is no $\boldsymbol{R}_{SU}$ contribution because all the particles move with the velocity of the bulk flow ($\boldsymbol{U}_p = \boldsymbol{u}^\infty$). It should also be noted that the viscosity is calculated for an instantaneous configuration corresponding to a non-distorted cubic lattice. At a later instant in time the cubic lattice will be distorted as the particles move with the bulk flow and a different instantaneous viscosity can be evaluated. It is a straightforward matter to calculate the stresslets at each instant; for both simple shear and planar pure straining motion, the unit cell returns to its non-distorted shape periodically and only a finite number of configurations need to be sampled. Since all analytical results available correspond to the non-distorted cubic cell we present only this case here. The particle stress for a simple cubic array can be described by two independent parameters α and β, which are only functions of the lattice geometry and the particle volume fraction; these two functions correspond to pure straining and simple shear flow, respectively, and the viscosity for any other linear flow can be obtained as a linear combination of these two cases (Zuzovsky *et al.* 1983, Nunan & Keller 1984). (We retain the notation α and β for consistency with previous authors; the viscosity function α is not to be confused with the splitting parameter of the same symbol.)

Figure 2.10 shows a comparison of α and β for a simple cubic lattice obtained by our ASD simulations with the asymptotic and exact results of Hoffman (1999). Hoffman's results reproduce the well-established analytical results of Nunan & Keller for low to intermediate volume fractions, while the high volume fraction asymptotes are generated with higher accuracy. Specifically, Hoffman's asymptotic expansions for high volume fractions can be expressed in terms of $\epsilon = 1 - (\phi/\phi_{max})^{1/3}$, as follows:

$$\alpha = \frac{3}{16}\pi\epsilon^{-1} + \frac{27}{80}\pi \ln\epsilon^{-1} - 2.85 - 1.3\epsilon\ln\epsilon^{-1} + O(\epsilon), \tag{2.32a}$$

$$\beta = \frac{1}{4}\ln\epsilon^{-1} - 0.604 - 0.30\epsilon\ln\epsilon^{-1} + O(\epsilon), \tag{2.32b}$$

where the constant term has been corrected from the Nunan & Keller result (Hoffman claims there is a sign error in those results.) and the coefficient of the next term ($\epsilon\ln\epsilon^{-1}$) is also evaluated. The far-field only (absence of lubrication) results are also presented and

are in exact agreement with the low volume fraction asymptotic behavior. In contrast to sedimentation, the high-volume-fraction asymptote is also reproduced with very good accuracy; for shearing motion lubrication is important and it precisely captures the two-body singular effects described by the high-ϕ asymptotes. The inclusion of higher moments in the far field is not as important as it was in the case of sedimentation, although for intermediate volume fractions our viscosities are slightly larger than the analytical results of Hoffman, as was also the case for the conventional SD algorithm.

2.3.4 Spin viscosity of cubic arrays

The spin viscosity of a cubic array gives the relationship between the torque exerted on each particle $\boldsymbol{T}$ and its angular velocity $\boldsymbol{\omega}$. (Since all particles in a cubic array are identical, no averaging is necessary.) Symmetry of the cubic lattice reduces the calculation of the spin viscosity to the calculation of one scalar, ζ, such that:

$$T_i = -\zeta \omega_i. \tag{2.33}$$

Zuzovsky *et al.* (1983) determined the high- and low-ϕ asymptotes for ζ, while Hoffman (1999) calculated ζ for all volume fractions and improved upon the asymptotic expansions by including higher order terms. Hoffman's asymptotic expansion is: $\zeta = \pi \ln((\phi/\phi_{max})^{-1/3} - 1)^{-1} - 3.15$; the evaluation of the constant term improves the expansion significantly since it is now valid for much lower volume fractions. Figure 2.11 compares the results obtained for the spin viscosity ζ as a function of volume fraction to the exact results of Hoffman. Excellent agreement is observed for all volume fractions, and the low- and high-volume-fraction asymptotic results are reproduced very accurately.

2.4 Results—Random Suspensions

In the following sections we present the results of a series of Monte Carlo simulations from which the hydrodynamic properties of random hard-sphere suspensions can be obtained. The Monte Carlo approach consists of generating several samples, calculating the transport properties of interest for each sample, and then averaging in order to obtain values that

describe the macroscopic behavior of the system. Different sampling techniques were used for different volume fractions; for $\phi < 0.49$ the particles were placed in an arbitrary initial configuration and then moved using a random-stepping routine in order to ensure that the sample was disordered—for $\phi > 0.49$ the sampling technique is discussed in detail in the following sections. We first present the high-frequency dynamic viscosity of random suspensions for volume fractions ranging from infinite dilution up to random close packing along the metastable fluid branch of the hard-sphere system. For volume fractions below the freezing point ($\phi = 0.494$), analytical and other simulation results are available for comparison. For volume fractions above the freezing point the system is maintained in the disordered metastable liquid state, and the singular behavior of the viscosity as ϕ approaches random close packing ($\phi_{rcp} \approx 0.64$) is studied. We next turn briefly to the sedimentation problem. As has been shown in the past for conventional SD, the order of approximation is only accurate for low to intermediate volume fractions, and we therefore simply present the N-dependence of the sedimentation velocity for a given low volume fraction. Finally, we study the short-time self-diffusion coefficient—the mobility of a single particle in a suspension of force-free particles. This is an example of a case where the knowledge of the resistance matrix, and not just the far-field hydrodynamic force, is of importance, and we demonstrate how our method can still determine the short-time self-diffusion coefficient in $O(N \ln N)$ operations.

2.4.1 Viscosity of random suspensions: below the freezing point

The effective viscosity of a random dispersion of hard spheres, which is known as the high-frequency dynamic viscosity, has been studied in the past for volume fractions below the freezing point, and essentially exact, as well as low ϕ asymptotic, results are available (Batchelor & Green 1972, Ladd 1990). The effective viscosity is readily calculated by imposing an external shear flow and converging the far-field contributions and the particle velocities, while keeping the particles at fixed positions. In contrast to the cubic array, the externally imposed stresslet produces non-zero particle velocities that also need to be determined as part of the iterative procedure. The total particle stresslet is then calculated as a sum of the converged far-field contribution, $\boldsymbol{S}_{ff}$, and the near-field contribution

$\boldsymbol{S}_{nf} = \boldsymbol{R}_{SE,nf} : \boldsymbol{E} - \boldsymbol{R}_{SU,nf} \cdot (\boldsymbol{U}_p - \boldsymbol{u}^{\infty})$, which now also contains a non-zero velocity contribution.

Figure 2.12 shows the hydrodynamic viscosity of a random suspension of identical spheres as a function of the volume fraction for different numbers of particles ranging from $N = 125 - 2000$, and averaged over a number of independent configurations ranging from $10 - 100$. Since a much larger number of particles can now be used, fewer independent configurations are needed giving statistical errors that are less than 2% for all volume fractions below the freezing point and all number of particles shown. (The error bars in figure 2.12 are omitted since they are always smaller than the size of the symbols.) The results of Ladd (1990) where up to 7 moments have been included in the calculations are taken to be exact. As was the case for the cubic array, the importance of lubrication is such that very accurate results are obtained even when using a low-order moment approximation to the far-field interactions. (Ladd also observed that the effective viscosity is not sensitive to the inclusion of higher moments.) It is also apparent that the viscosity is insensitive to the system size, since statistically indistinguishable results are obtained for N ranging from 125 to 2000. Also shown are the experimental results of Van der Werff *et al.* (1989) and Shikata & Pearson (1994) obtained from oscillating Couette viscometry with a frequency sufficiently high that the distribution of the solid particles is unaffected by the shear flow and corresponds to the equilibrium hard-sphere structure. Very good agreement is observed, especially for the lower volume fractions (see below for results above the freezing point).

2.4.2 Viscosity of random suspensions: above the freezing point

Although a large number of analytical results exist for the effective viscosity of hard-sphere suspensions for volume fractions in the stable fluid region (below $\phi = 0.494$), very few theoretical or experimental results are available for systems along the metastable extension of the fluid branch. For volume fraction below $\phi = 0.494$ only a single stable fluid (disordered) phase exists; above this point the phase diagram splits into a metastable fluid phase (leading to random close packing) and a stable ordered phase (leading to FCC crystals). This work will only be concerned with the metastable disordered branch of

the phase diagram. This is an example where a large number of particles is necessary to capture the correct behavior, as a macroscopic system at these high volume fractions will undoubtedly have clusters in some regions and freely mobile particles in others, which is difficult to model unless the unit cell is sufficiently large. In addition, even generating such a dense configuration can be challenging since metastable systems have a tendency to crystallize and to introduce order into the structure.

Standard hard-sphere molecular dynamics or Monte Carlo algorithms cannot be used to generate random distributions above the freezing transition. Using a different approach with a large number of particles, however, hard-sphere microstructures at volume fractions up to random close packing can be generated. Although the term random close packing is widely used, it is not always clear whether it is a universal quantity, or whether it depends on the method used to generate any given configuration; the exact value of ϕ_{rcp} is also discussed and the value $\phi_{rcp} = 0.64$ was used here. (See Torquato, Truskett & Debenedetti (2000) for a discussion on whether random close packing is a well defined state.) For the purpose of this work the computational technique suggested by Rintoul & Torquato (1996b) was used to generate the random hard-sphere configurations. Starting from an initial set of random overlapping spheres, the spheres are expanded and simultaneously moved to reduce overlap; if the system becomes jammed (overlapping cannot be reduced) the spheres are shrunk and moved until the system becomes unjammed (see Clarke & Wiley 1986). This process of expansion and contraction is repeated until a desirable volume fraction is obtained. After that, the system is equilibrated using standard hard-sphere molecular dynamics. For volume fractions above the freezing point the equilibration process needs to be closely monitored because there are two phenomena occurring simultaneously—the system moves from a non-equilibrium to an equilibrium state and at the same time it moves from the metastable branch to the stable ordered branch of the phase diagram. By monitoring the system pressure and by utilizing the differences in the time scales between the equilibration and crystallization processes (it usually takes longer for the system to crystallize), it is possible to generate the desired configurations of random hard-spheres for volume fractions very close to random close packing (Rintoul & Torquato 1996a, Speedy 1994). It was observed that small systems had a tendency to

crystallize sooner, and therefore for some volume fractions up to 2000 particles were used. It is worth noting that it is the most difficult to generate non-ordered configurations for volume fractions between 0.52 and 0.58 as the system tends to crystallize very fast. The higher volume fractions correspond to an amorphous glassy state, and the tendency for freezing is less severe. (See Speedy (1994), (1997) for more details on sampling and phase transitions.)

In figure 2.13 and table 2.1 we present the high-frequency dynamic viscosity for volume fractions up to 0.635, along with the experimental results of Van der Werff *et al.* (1989) and Shikata & Pearson (1994). Two extrapolated expressions, one from the experimental results of Van der Werff *et al.* and one derived from the results of Ladd, are also presented. There is significant spread in the experimental data at high volume fraction that might be an indication of some freezing in some of the experimental data or simply represent the difficulty of measuring the volume fraction at high volume fractions. Within the error bars of the experimental data, however, our results are in reasonable agreement with the experiments. It is interesting to note that our results for $\phi < 0.60$ are in good agreement with the fitted curve given by Ladd (1990), which is a simple extrapolation of a semi-empirical fit of Ladd's results from lower volume fractions. This is not surprising; since the metastable branch is the continuous extension of the fluid branch, it is reasonable that the viscosity would also be a continuous extension of the viscosity from below the freezing point and can potentially be described by the same empirical equation. The empirical relation given by Ladd, however, does not predict any singular behavior as maximum packing is approached, and therefore fails at very high volume fractions.

A very sharp increase in the viscosity is observed for volume fractions above 60%, suggesting a singular behavior in the limit of $\phi \to \phi_{rcp}$. The exact form of this singular behavior is not known. Results from lubrication theory for cubic lattices would suggest that the singular form should consist of both $1/\epsilon$ and $\ln \epsilon$ terms (corresponding to α and β of figure 2.10), where $\epsilon = 1-(\phi/\phi_{rcp})^{1/3}$, but the relative amount of each term is unknown. We found the data to be well fit by $\eta_r = 15.78 \ln(1/\epsilon) - 42.47$ as seen in figure 2.14. A similar fit with both $1/\epsilon$ and $\ln \epsilon$ gave a very small coefficient (of order 10^{-2}) for the $1/\epsilon$ term. As far as we are able to tell at this point the $\ln \epsilon$ behavior accurately describes the

numerical data.

2.4.3 Sedimentation velocity: dependence on system size

It is straightforward to calculate the average sedimentation velocity of a random suspension of spheres: after imposing an external force on each particle, the velocity of each particle is converged while the particles remain fixed at their random locations. As was discussed for the sedimentation of the cubic arrays, our method can only predict accurate velocities for low to moderate volume fractions; for higher volume fractions more moments are needed to represent the particles correctly. Since this behavior has been discussed and analyzed in the past for the conventional SD method (Phillips *et al.* 1988), here we restrict ourselves to low volume fractions and demonstrate the dependence of the sedimentation velocity on the system size. Phillips *et al.* (1988) showed that the sedimentation velocity has a strong $N^{-1/3}$ dependence due to the long-range effects of the periodic images of particles outside the unit cell. The motion is in essence a superposition of the sedimentation velocity of the dilute periodic array of images, $(\phi/N)^{1/3}$, with that for the random suspension (which is $O(\phi)$ at low ϕ). Figure 2.15 shows clearly the $N^{-1/3}$ dependence of the sedimentation velocity for a volume fraction of $\phi = 0.05$.

Mo & Sangani (1994) calculated the difference in the velocity induced at the center of a test particle in a periodic suspension and a random suspension to be

$$U_s = U_s(N) + 1.7601(\phi/N)^{1/3}\eta_0/\eta\, S(0)U_0 + O(\phi/N), \tag{2.34}$$

where $S(0)$ is the structure factor, and η and η_0 are the suspension and pure fluid viscosities, respectively (values for the suspension viscosity η are the high-frequency dynamic viscosity and were calculated in the previous section and given in figure 2.12). The structure factor can be estimated for the hard-sphere dispersion from the Carnahan-Starling approximation:

$$S(0) = \frac{(1-\phi)^4}{1+4\phi+4\phi^2-4\phi^3+\phi^4}, \tag{2.35}$$

and the corrected sedimentation velocities can be calculated directly from (2.34). The

corrected velocities are also presented in figure 2.15 and they do indeed give the same value for all N.

2.4.4 Short-time self-diffusion coefficient

The short-time self-diffusion coefficient is defined through the Stokes-Einstein relation:

$$\boldsymbol{D}_0^s = kT\langle trace(\boldsymbol{R}_{FU}^{-1})\rangle, \tag{2.36}$$

where the *trace* operator picks out only the diagonal elements of $\boldsymbol{R}_{FU}^{-1}$, and the angle brackets imply a sum over all particles and an average over all configurations. Since the far-field part of the resistance matrix $\boldsymbol{R}_{FU}$ is never calculated, we need to find a different approach to calculate the self-diffusion coefficient. In addition, we now need to isolate the diagonal elements of the resistance matrix for each particle, and therefore the knowledge of only $\langle \boldsymbol{R}_{FU}^{-1}\rangle$ is not adequate as it was for the calculation of the sedimentation velocity.

A straightforward way to perform this calculation in order N operations is to impose an external force, $\boldsymbol{F}^g$, with a Gaussian distribution on the particles, i.e., $\langle \boldsymbol{F}_g\rangle = 0$ and $\langle F_i^{g,m} F_j^{g,n}\rangle = \delta_{ij}\delta_{mn}$, where $F_i^{g,m}$ is the i-component of the force acting on particle m (superscripts m, n denote particles, while subscripts i and j denote Cartesian coordinates). Following the procedure described above, the resulting particle velocities can be readily calculated in order N. Although the mobility matrix is never calculated, the resulting particle velocities, U_i^n, still satisfy:

$$U_i^n = R_{FU,ijnm}^{-1} F_j^{g,m}. \tag{2.37}$$

Now form the product

$$U_i^n F_i^{g,n} = R_{FU,ijnm}^{-1} F_j^{g,m} F_i^{g,n}, \tag{2.38}$$

which gives after ensemble-averaging

$$\langle U_i^n F_i^{g,n}\rangle = \langle R_{FU,iinn}^{-1}\rangle, \tag{2.39}$$

from which the short-time self-diffusion coefficient can be calculated directly. This approach was successfully employed to calculate the diffusion coefficient and study its dependence on both the number of particles and the volume fraction.

Like the sedimentation velocity, the translational self-diffusivity also shows a strong $N^{-1/3}$ dependence (Brady *et al.* 1988). Ladd (1990) proposed the following expression to extract the infinite system diffusivity from the N-particle periodic diffusion coefficient:

$$D_0^s = D_0^s(N) + (\eta_0/\eta)(kT/6\pi\eta_0 a)\left[1.7601(\phi/N)^{1/3} - \phi/N\right], \tag{2.40}$$

where η and η_0 are the suspension and pure fluid viscosities, respectively. The Stokes-Einstein diffusivity of a single isolated particle is $D_0 = kT/6\pi\eta_0 a$. Figure 2.16 shows the self-diffusion coefficients for $\phi = 0.05$ and N ranging from 16 to 512. The corrected diffusivities, after applying the correction given by (2.40), are also shown verifying both the strong $N^{-1/3}$ dependence of the self-diffusion coefficient on the number of particles and the validity of equation (2.40), since a constant value can indeed be extracted for all N.

Figure 2.17 and table 2.1 presents the short-time self-diffusion coefficients for volume fractions up to 0.635, along with a number of available experimental and simulation data. The self-diffusion coefficients are calculated from 20 realizations of $N = 512$ particles and the values are adjusted to correct for the $N^{1/3}$ dependence (limit for infinite N). Very good agreement is observed between experimental and simulation results for all volume fractions below the freezing point (where experimental results are available). A sharp decrease in the self-diffusion coefficient, in agreement with the sharp increase in the viscosity, is observed for volume fractions above 60%. The self-diffusivity is expected to vanish at random close packing in a manner inversely proportional to the high-frequency dynamic viscosity. In figure 2.18 the self-diffusivity is plotted as a function of the inverse high-frequency dynamic viscosity, resulting in a clear linear scaling and therefore verifying that $D_0^s \approx 1/\eta$, in the limit of $\phi \to \phi_{rcp}$.

We note here that the accuracy of our simulation results is limited by the small number of moments used. It has been suggested in the past (Ladd, 1990) that higher moments

can influence the value of the self-diffusivity, especially for high volume fractions. No attempt has been made to correct for the inclusion of higher moments, although the very good agreement between our results and experimental results would suggest that the magnitude of the correction is indeed small.

2.5 Conclusions

We have described in detail a new method for calculating the hydrodynamic interactions among particles in a suspension at small Reynolds number based on the Stokesian Dynamics method but with a significantly more favorable computational cost of $N \ln N$. The new method avoids the expensive calculation of the far-field mobility matrix in favor of the direct calculation of the far-field hydrodynamic force, and uses a carefully chosen preconditioning scheme to dramatically reduce the computational cost of any iterative matrix inversions. The results of the method are in excellent agreement with those obtained from conventional Stokesian Dynamics, and much larger systems can now be simulated with the same accuracy. The power of the new method is demonstrated in the calculation of the high-frequency dynamic viscosity and short-time self-diffusivity of suspensions for volume fractions above the freezing point, a case where a large number of particles is necessary to capture the correct behavior. This work was limited to the validation and evaluation of the method and to some characteristic results corresponding to static (not evolving in time) systems. This is by no means a restriction of the method; in fact, the method is ideally suited for dynamic simulations where good initial guesses from the previous step in time exist for all the iterative procedures. Results from dynamical studies will be the subject of the next two chapters.

It should also be noted that the same methodology as used here can be applied to other problems in Stokes flow—non-spherical particles, deformable drops, etc.—with the same performance characteristics. There are also analogous problems governed by Laplace's equation (e.g., effective conductivity) or the biharmonic equation (e.g., linear elasticity) that could also be addressed in $O(N \ln N)$ operations using the ASD methodology.

Acknowledgement

This work was supported in part by grants NAG3-2166 and NAG8-1661 from NASA. The authors benefitted greatly from discussions with Prof. J. J. L. Higdon on the PME method for Stokes flow. An anonymous referee is thanked for the suggestion of the random forces to determine the short-time self-diffusivity.

References

BANCHIO, A. & BRADY, J. F. 2001 Accelerated Stokesian Dymamics: Brownian motion (in preparation).

BATCHELOR, G. K. & GREEN, J. T. 1972 The determination of the bulk stress in a suspension of spherical particles to order c^2. *J. Fluid Mech.* **56**, 401.

BEENAKER, C. W. J. 1986 Ewald sum of the Rotne-Prager tensor. *J. Chem. Phys.* **85**, 1581.

BRADY, J. F. & BOSSIS, G. 1988 Stokesian dynamics. *J. Fluid Mech.* **20**, 111.

BRADY, J. F., PHILLIPS, R. J., LESTER, J. C. & BOSSIS, G. 1988 Dynamic simulation of hydrodynamically interacting suspensions. *J Fluid Mech.* **195**, 257.

CLARKE, A. S. & WILEY, J. D. 1987 Numerical Simulation of the dense random packing of a binary mixture of hard spheres: Amorphous metals. *Phys. Rev. B* **35**, 7350.

CUTHILL, E. & MCKEE, J. 1969 Reducing the bandwidth of sparse symmetric matrices. *Proceedings 24th National Conference of the Association for Computing Machinery*, Brandon Press, NJ, 157.

DARDEN, T., YORK, D. & PEDERSEN, L. 1993 Particle Mesh Ewald: An $n \log(n)$ method for Ewald sums in large systems. *J. Chem. Phys.* **98**, 10089.

DARDEN, T., PEDERSEN, L., TOUKMAJI, A., CROWLEY, M. & CHEATHAM, T. 1997 Particle-mesh based methods for fast Ewald summation in molecular dynamics simulations. *Ninth SIAM Conference on Parallel Processing for Scientific Computing*, 1997.

DRATLER, D. I. & SCHOWALTER, W. R. 1996 Dynamic simulations of suspensions of non-Brownian hard spheres. *J. Fluid Mech.* **325**, 53.

DURLOFSKY, L. J., BRADY, J. F. & BOSSIS, G. 1987 Dynamic simulations of hydrodynamically interacting particles. *J. Fluid Mech.* **180**, 21.

ESSMANN, U., PERERA, L., BERKOWITZ, M. L., DARDEN, T., LEE, H. & PEDERSEN, L. G. 1995 A smooth particle mesh Ewald method. *J. Chem. Phys.* **103**, 8577.

FOSS, D. R. & BRADY, J. F. 2000 Structure, diffusion and rheology of Brownian suspensions by Stokesian Dynamics simulations. *J. Fluid Mech.* **407**, 167.

GEORGE, A. & LIU, J. W. 1981 Computer solution of large sparse positive definite systems. Prentice-Hall, Englewood Cliffs, NJ.

GUCKEL, E. K. 1999 Large Simulations of particulate systems using the PME method. PhD thesis, University of Illinois at Urbana-Champaign.

HASIMOTO, H. 1959 On the periodic fundamental solutions of the Stokes equations and their application to viscous flow past a cubic array of spheres. *J. Fluid Mech.* **5**, 317.

HIGDON, J. J. L. 2000 Private communication.

HOCKNEY, R. W. & EASTWOOD, J. W. 1982 Computer simulation using particles. Kluwer, New York.

HOFFMAN, J. M. A. 1999 Hydrodynamic Properties of Dense Colloidal Crystals. PhD thesis, Technische University Eindhoven.

ICHIKI, K. & BRADY, J. F. 2001 Many-body effects and matrix inversion in low-Reynolds-number hydrodynamics. *Phys. Fluids* **13**, 350.

JEFFREY, J. D., MORRIS, J. F. & BRADY, J. F. 1993 The pressure moments for two rigid spheres in low-Reynolds-number flow. *Phys. Fluids A* **5**, 2317.

JEFFREY, D. J. & ONISHI, Y. 1984 Calculation of the resistance and mobility functions for two unequal rigid spheres in low-Reynolds-number flow. *J. Fluid Mech.* **139**, 261.

LADD, A. J. C. 1990 Hydrodynamic transport coefficients of random dispersions of hard spheres. *J. Chem. Phys.* **93**, 3484.

LADD, A. J. C. 1994a Numerical simulations of particulate suspensions via a discretized Boltzmann equation. Part 1. Theoretical foundation. *J. Fluid Mech.* **271**, 285.

LADD, A. J. C. 1994b Numerical simulations of particulate suspensions via a discretized Boltzmann equation. Part 2. Numerical results. *J. Fluid Mech.* **271**, 311.

MO, G. & SANGANI, A. S. 1994 A method for computing Stokes flow interactions among spherical objects and its application to suspensions of drops and porous materials. *Phys. Fluids* **6**, 1637.

NUNAN, K. C. & KELLER, J. B. 1984 Effective viscosity of a periodic suspension. *J. Fluid Mech.* **142**, 269.

OTTEWILL, R. H. & WILLIAMS, N. S. S. 1987 Study of particle motion in concentrated dispersions by tracer diffusion. *Nature* **325**, 232.

PETERSEN, H. G. 1995 Accuracy and efficiency of the particle mesh Ewald method. *J. Chem. Phys.* **103**, 3668.

PHILLIPS, R. J., BRADY, J. F. & BOSSIS, G. 1988 Hydrodynamic transport properties of hard-sphere dispersions. I. Suspensions of freely mobile particles. *Phys. Fluids* **31**, 3462.

PUSEY, P. N. & VANMEGEN, W. 1983 Measurement of the short-time self-mobility of particles in concentrated particle dispersions. *J. Phys. Paris* **44**, 285.

RINTOUL, M. D. & TORQUATO, S. 1996a Metastability and Crystallization in Hard-Sphere Systems. *Phys. Rev. Lett.* **77**, 4198.

RINTOUL, M. D. & TORQUATO, S. 1996b Computer simulations of dense hard-sphere systems. *J. Chem. Phys.* **105**, 9258.

SAFFMAN, P. G. 1973 On the settling speed of free and fixed suspensions. *Stud. Appl. Maths.* **52**, 115.

SANGANI, A. S. & MO, G. 1996 An $O(N)$ algorithm for Stokes and Laplace interactions of particles. *Phys. Fluids* **8**, 1990.

SEGRE, P. N., BEHREND, O. P. & PUSEY, P. N. 1995 Short-time Brownian-Motion in colloidal suspensions: Experiment and simulation. *Phys. Rev. E* **52**, 5070.

SHIKATA, T. & PEARSON, D. S. 1994 Viscoelastic behavior of concentrated spherical suspensions. *J. Rheol.* **38**, 601.

SPEEDY, R. J. 1994 On the reproducibility of glasses. *J. Chem. Phys.* **100**, 6684.

SPEEDY, R. J. 1997 Pressure of the metastable hard-sphere fluid. *J. Phys. Condensed Matter* **9**, 8591.

TORQUATO, S., TRUSKETT, T. M. & DEBENEDETTI, P. G. 2000 Is Random Close Packing of Spheres Well Defined? *Phys. Rev. Lett.* **84**, 2064.

TORRES, F. E. & GILBERT, J. R. 1996 Large scale Stokesian Dynamics simulations of non-Brownian suspensions. Unpublished results.

VANMEGEN, W., OTTEWILL, R. H., OWENS, S. M. & PUSEY, P. N. 1985 Measurement of the wave-vector dependent diffusion coefficient in concentrated particle dispersions. *J. Chem. Phys.* **82**, 508.

VANMEGEN, W., UNDERWOOD, S. M. & SNOOK, I. 1986 Tracer Diffusion in concentrated colloidal dispersions. *J. Chem. Phys.* **85**, 4065.

VANMEGEN, W. & UNDERWOOD, S. M. 1989 Tracer Diffusion in concentrated colloidal dispersions. 3. Mean squared displacements and self-diffusion coefficients. *J. Chem. Phys.* **91**, 552.

VANVELUWEN, A., LEKKERKERKER, H. N. W., KRUIF DE, C. G. & VRIJ, A. 1987 Measurement of the short-time self-diffusion coefficient in dilute and concentrated suspensions—influence of direct particle interactions. *J. Chem. Phys.* **87**, 4783.

VANVELUWEN, A. & LEKKERKERKER, H. N. W. 1988 Non-Gaussian behavior of the displacement statistics of interacting colloidal particles. *Phys. Rev. A* **38**, 3758.

WERFF VAN DER, J. C., KRUIF DE, C. G., BLOM, C. & MELLEMA, J. 1989 Linear viscoelastic behavior of dense hard-sphere dispersions. *Phys. Rev. A* **39**, 795.

ZICK, A. A. & HOMSY, G. M. 1982 Stokes flow through periodic arrays of spheres. *J. Fluid Mech.* **115**, 13.

ZUZOVSKY, M., ADLER, P. M. & BRENNER, H. 1983 Spatially periodic suspensions of convex particles in linear shear flows. III. Dilute arrays of spheres suspended in Newtonian fluids. *Phys. Fluids* **26**, 1714.

ϕ	η'_∞	D_0^s
0.00	1	1
0.05	1.136	0.910
0.10	1.310	0.818
0.15	1.522	0.719
0.20	1.802	0.636
0.25	2.16	0.550
0.30	2.64	0.466
0.35	3.34	0.388
0.40	4.27	0.319
0.45	5.70	0.255
0.52	9.36	0.173
0.56	12.1	0.135
0.60	19.4	0.094
0.61	22.9	0.079
0.62	28.1	0.069
0.63	39.7	0.048
0.635	52.3	0.036

Table 2.1: The high-frequency dynamic viscosity and the short-time self-diffusivity as a function of the volume fraction for volume fractions up to close packing and $N = 512$. The values of the short-time self-diffusivity, D_0^s, are adjusted to correct for the $N^{1/3}$ dependence according to (2.40).

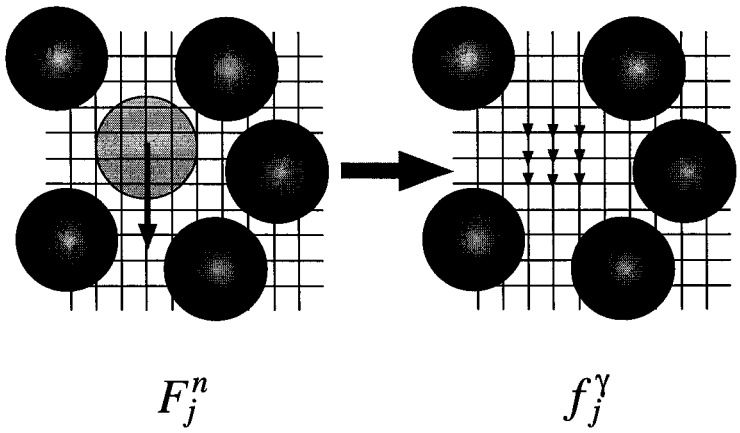

Figure 2.1: The transition from a force acting on a particle's center to a set of forces acting on the grid points γ.

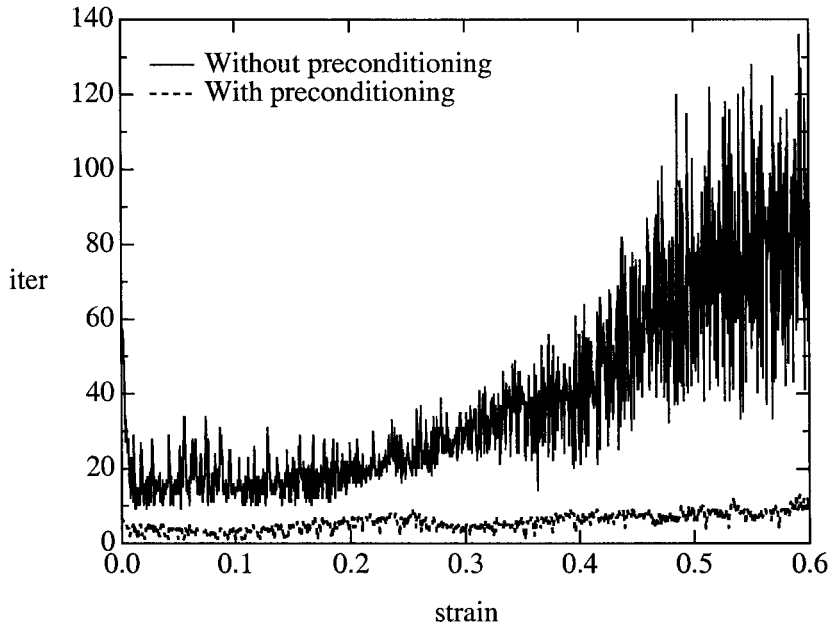

Figure 2.2: The number of iterations required for convergence of 10^{-4} with and without preconditioning ($N = 512$, $\phi = 0.45$, sheared system). The effect of an appropriate preconditioner becomes increasingly important for large strains as particle clusters form and the resulting resistance matrix, $\boldsymbol{R}_{FU,nf}$, becomes increasingly ill-conditioned.

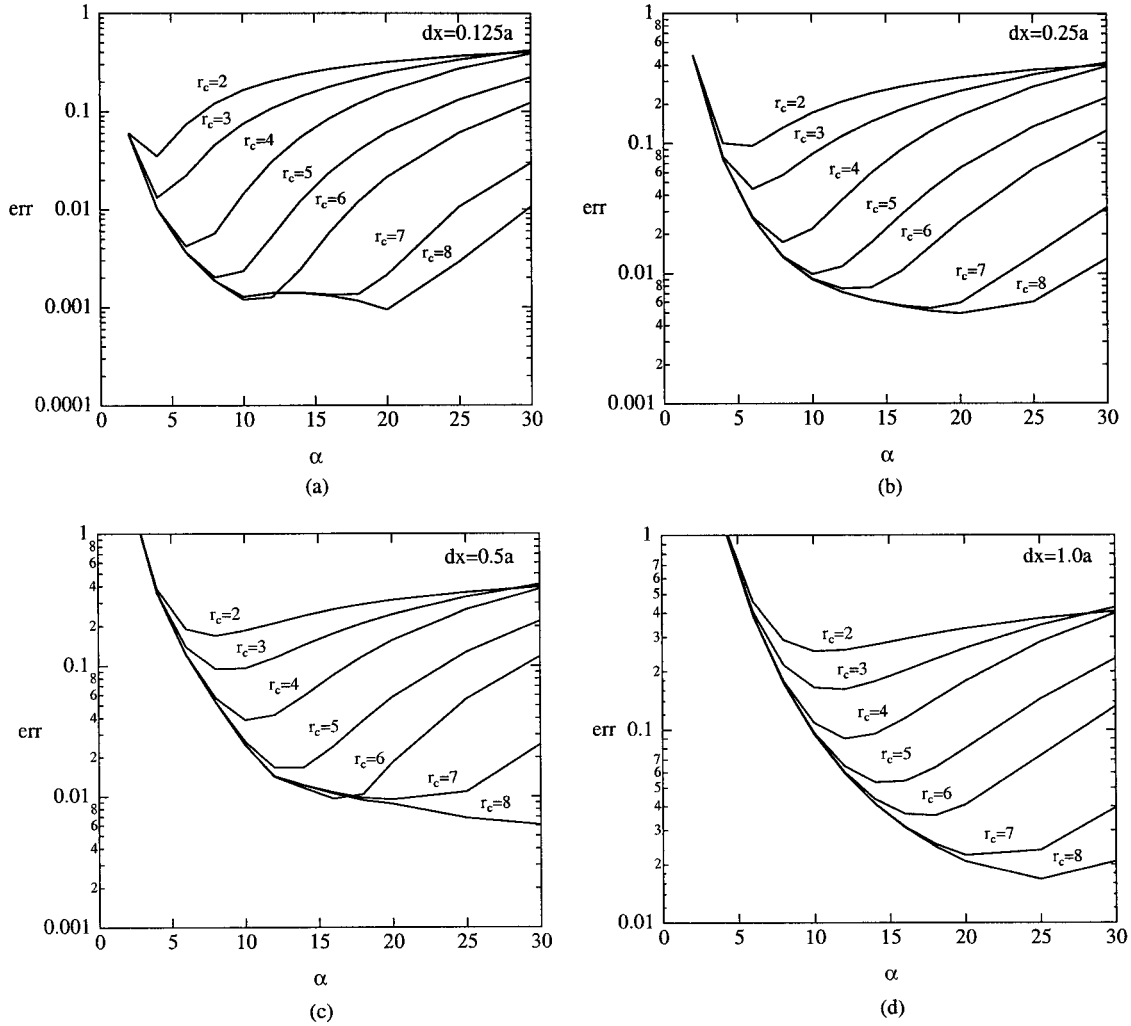

Figure 2.3: The relative error for the calculation of the fluid velocity for a system of $N = 30$ particles in a gravitational field. The error is presented for different values of the wave-space sum discretisation, dx, and different values of the real-space sum cut-off radius, r_c, as a function of the splitting parameter α.

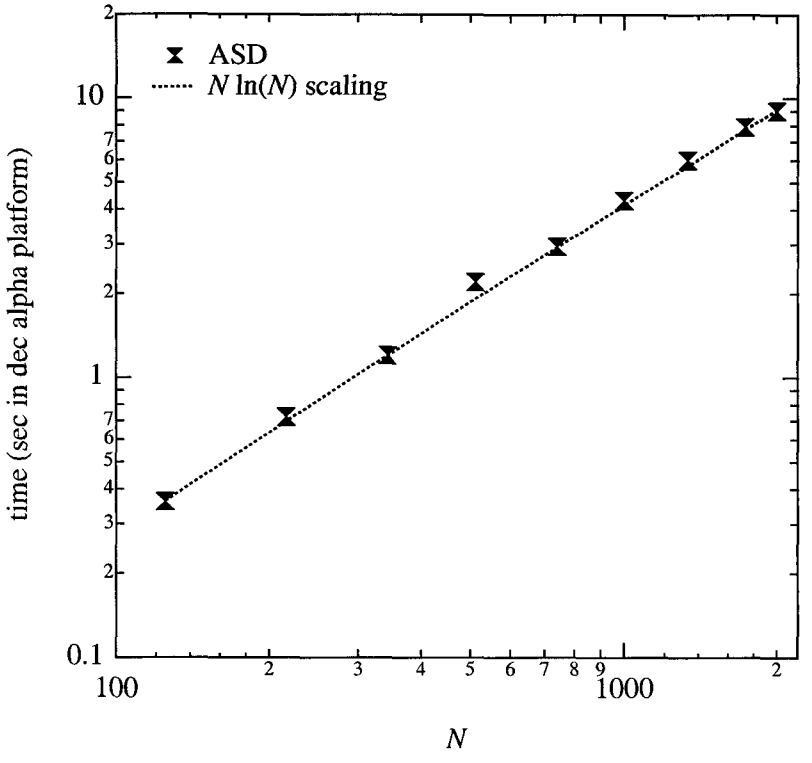

Figure 2.4: The CPU time (in seconds) for one time-step of a shearing simulation as a function of the number of particles N.

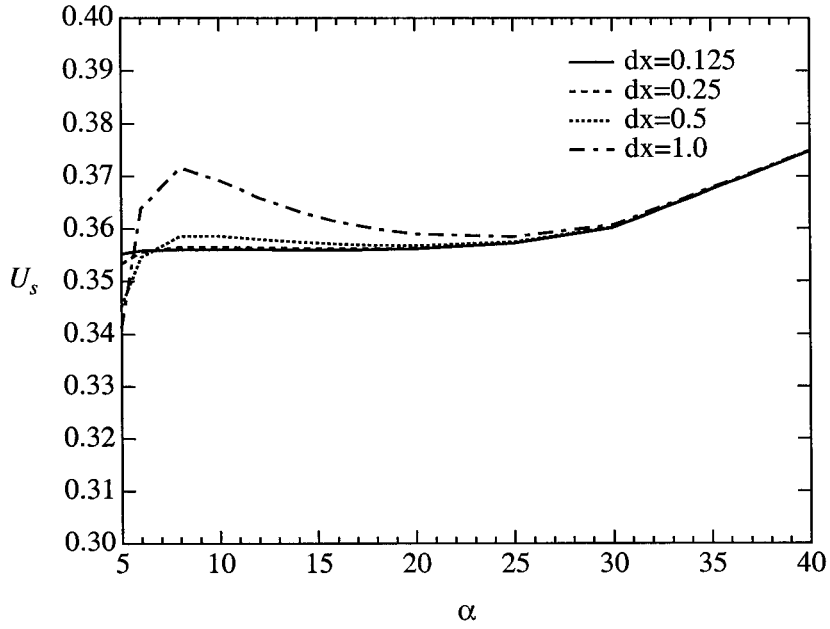

Figure 2.5: The dependence of the sedimentation velocity of a SC array of spheres on α and dx; $N = 8$, $\phi = 0.064$, $L = 8.0$, $r_c = \sqrt{3} \times 4a$.

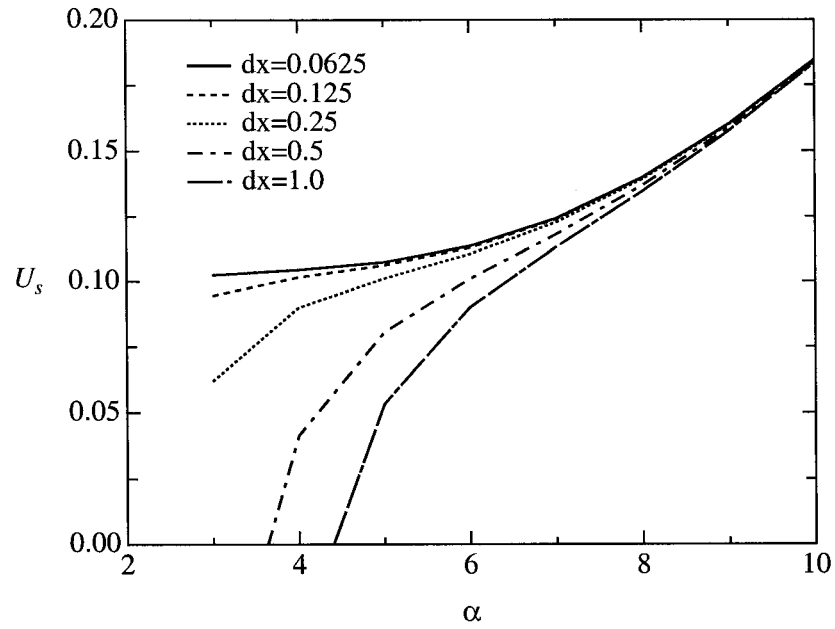

Figure 2.6: The dependence of the sedimentation velocity of a SC array of spheres on α and dx; $N = 8$, $\phi = 0.5236$, $L = 4.0$, $r_c = \sqrt{3} \times 2a$.

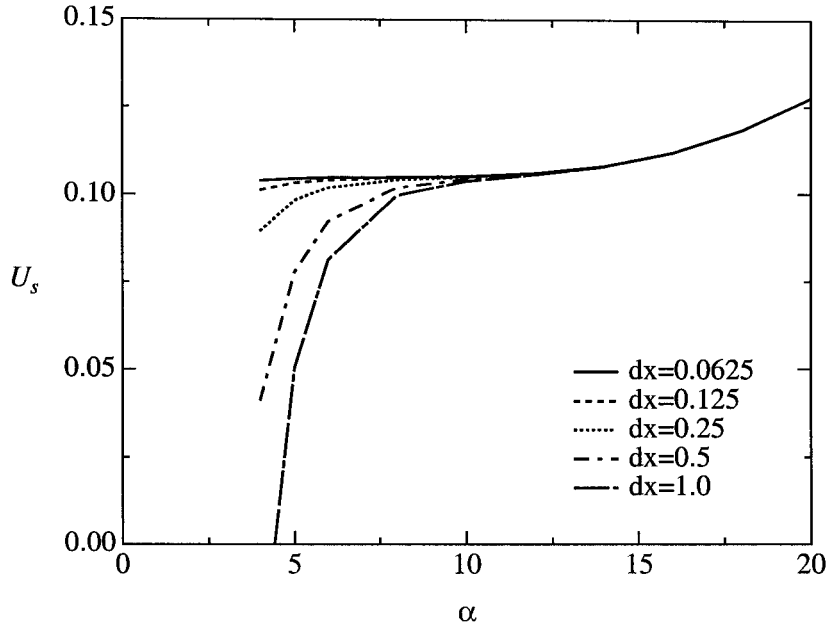

Figure 2.7: The dependence of the sedimentation velocity of a SC array of spheres on α and dx; $N = 8$, $\phi = 0.5236$, $L = 4.0$, $r_c = \sqrt{3} \times 4a$.

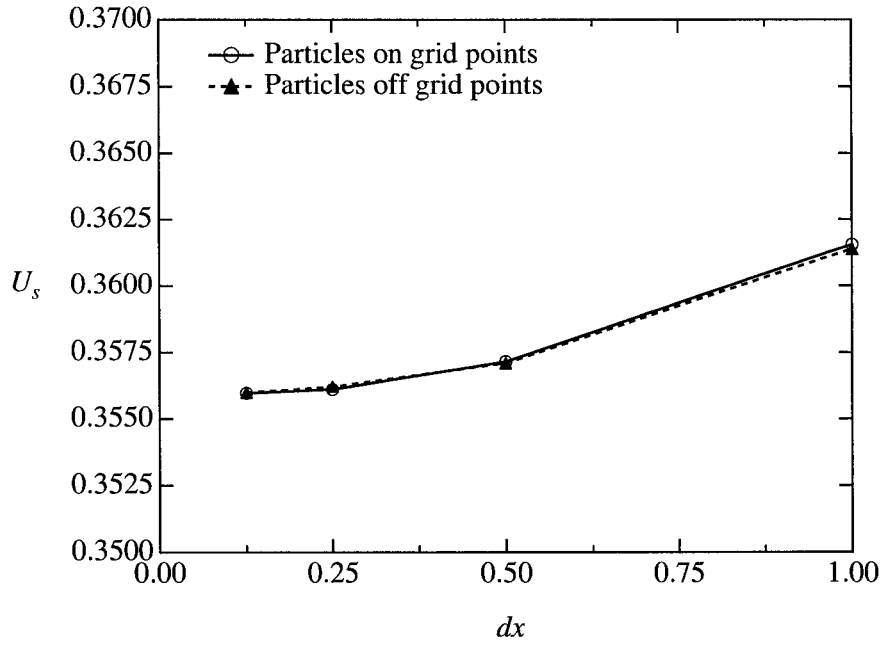

Figure 2.8: The dependence of the sedimentation velocity of a SC array of spheres on particle position and dx; $N = 8$, $\phi = 0.064$, $L = 8.0$, $r_c = \sqrt{3} \times 4a$, $\alpha = 16$.

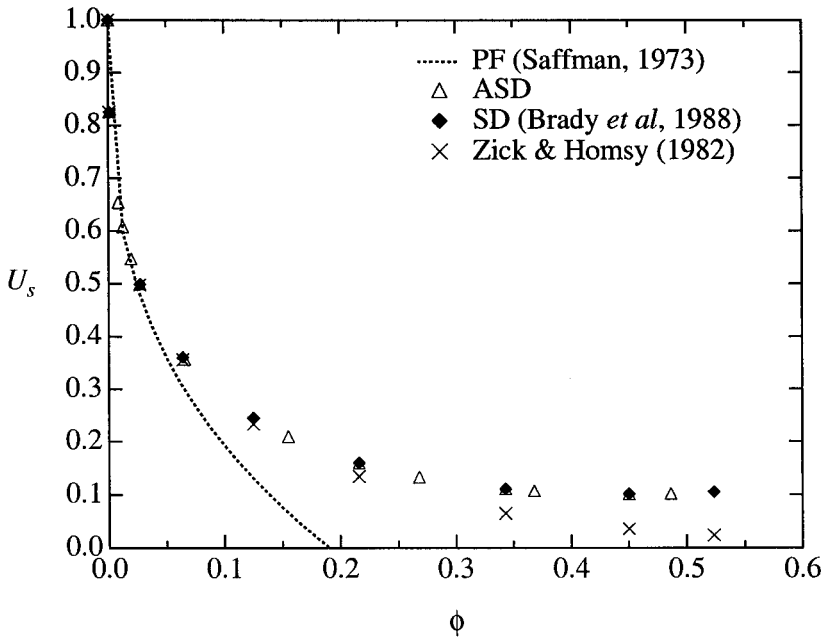

Figure 2.9: The dependence of the sedimentation velocity of a SC array of spheres on the volume fraction. The open triangles are the Accelerated Stokesian Dynamics (ASD) results, the filled diamonds are the Stokesian Dynamics (SD) results (Brady *et al.* 1988), the crosses are the exact results of Zick & Homsy (1982), and the dotted curve is the point-force (PF) solution of Saffman (1973).

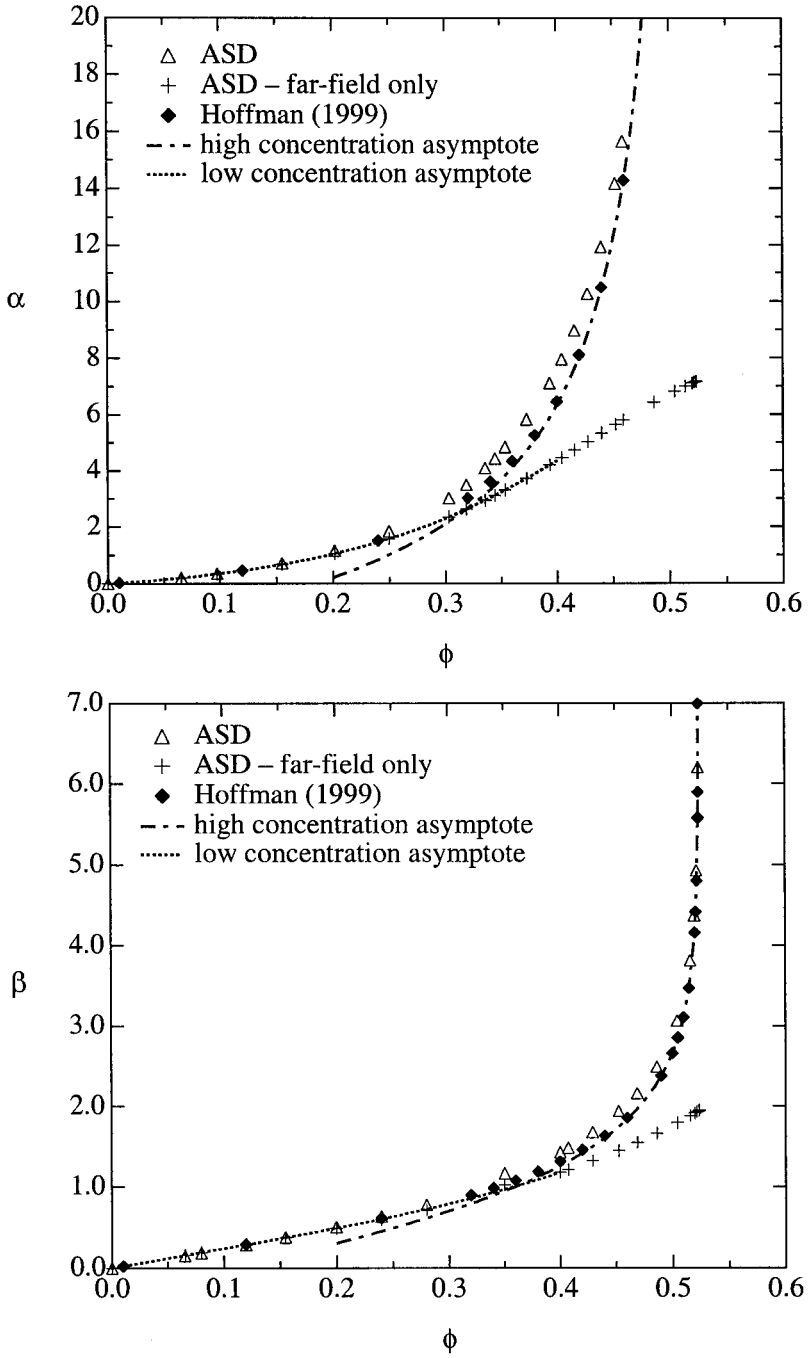

Figure 2.10: The dependence of the shear viscosity functions α and β of a SC array of spheres on the volume fraction. The open triangles are the Accelerated Stokesian Dynamics (ASD) results, the crosses are the ASD results in the absence of lubrication, the filled diamonds are the exact analytical results of Hoffman (1999), and the dotted and dot-dashed curves are the asymptotic results of Hoffman for the $\phi \to 0$ and $\phi \to \phi_{max}$ limits, respectively.

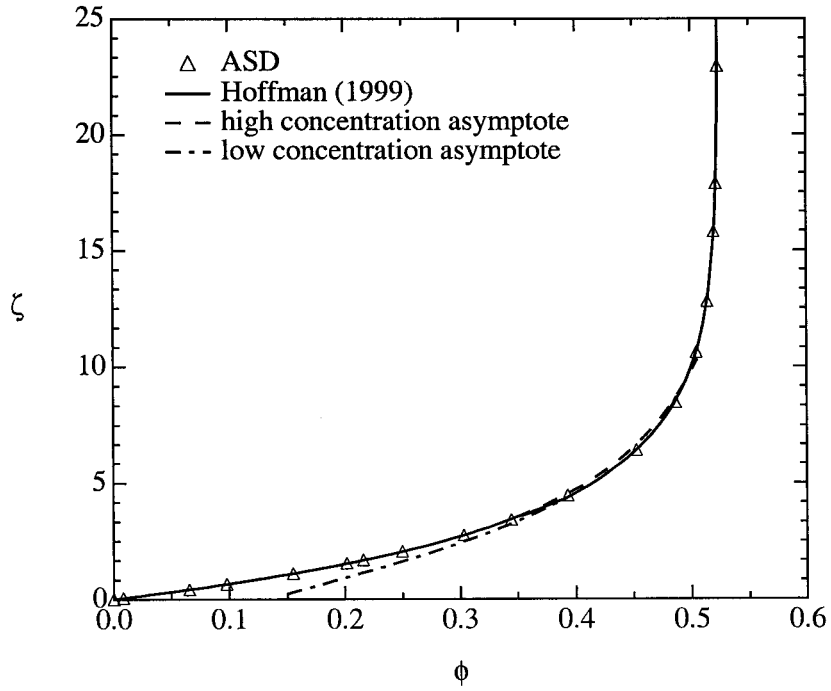

Figure 2.11: The dependence of the spin viscosity ζ of a SC array of spheres on the volume fraction. The open triangles are the Accelerated Stokesian Dynamics (ASD) results, the solid curve is the exact calculation of Hoffman (1999), the dashed curve is Hoffman's low concentration analytical result, and the dot-dashed curve is the singular form as $\phi \to \phi_{max}$.

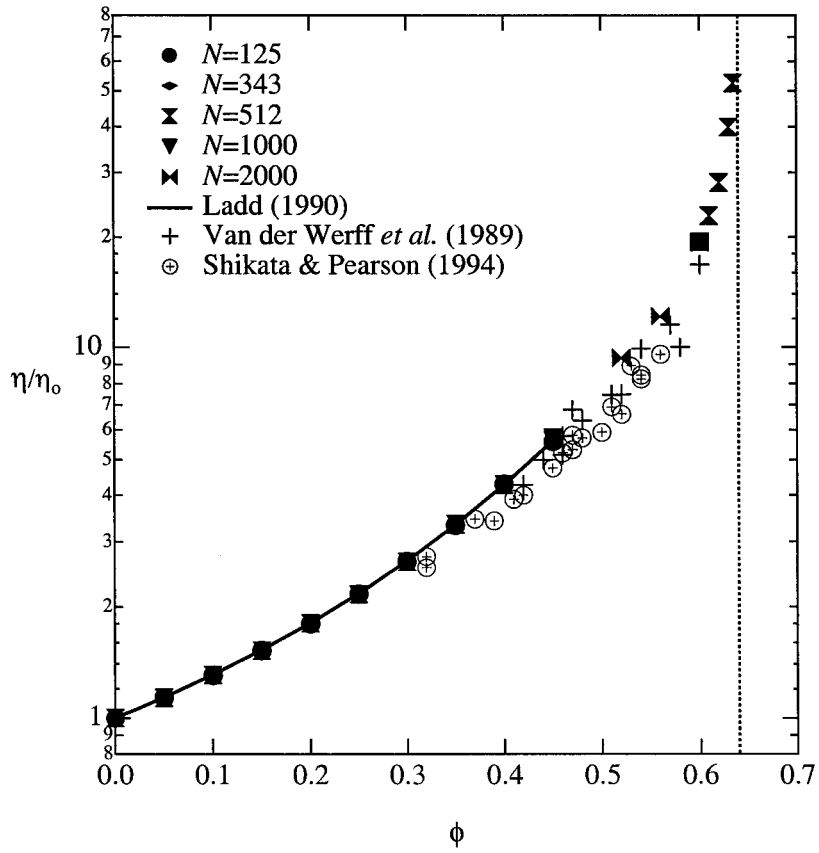

Figure 2.12: The relative viscosity is plotted as a function of the volume fraction for different number of particles ($N = 125 - 2000$) and volume fractions. The solid curve represents the multipole-moment simulation results of Ladd (1990), and the crosses and circles are the experimental results of Van der Werff *et al.* (1989) and Shikata & Pearson (1994), respectively.

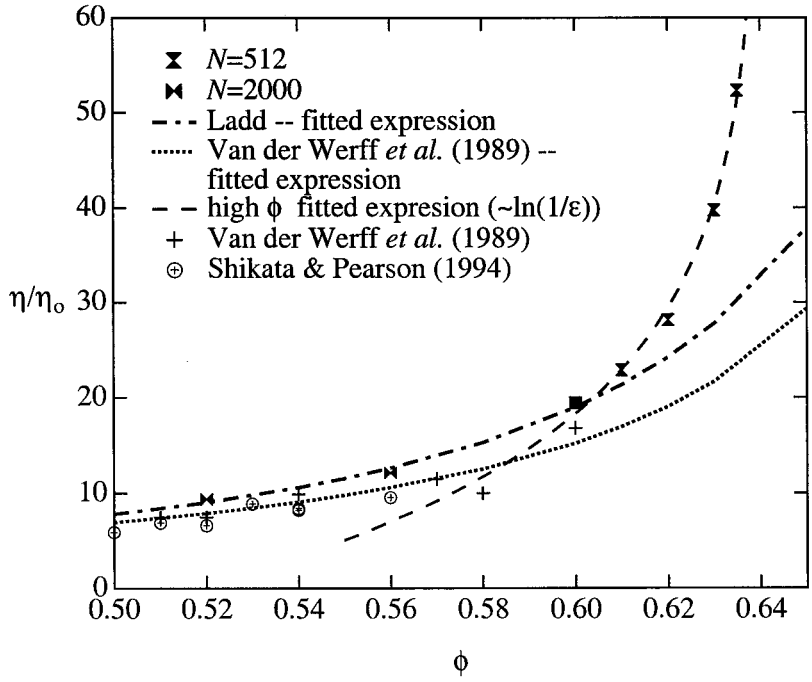

Figure 2.13: The relative viscosity is plotted as a function of the volume fraction for volume fractions above the melting point. The dot-dashed curve is the extension of the empirical fit to Ladd's simulation results below the freezing point, and the dotted curve is the same extension for the curve fitted to the Van der Werff *et al.* (1989) results. The dashed curve is a simple best fit curve of the form $A_1 \ln(1/\epsilon) + A_2$, which accurately represents the results for $\phi > 0.60$.

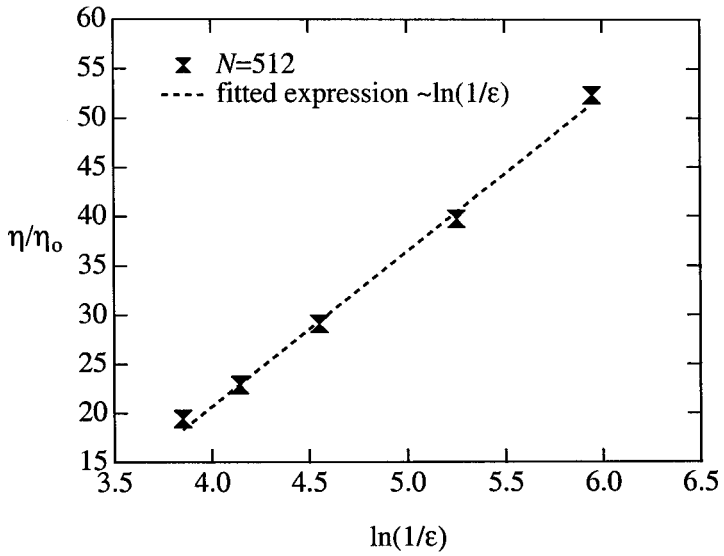

Figure 2.14: The relative viscosity is plotted as a function of $\ln(1/\epsilon)$, where $\epsilon = 1 - \phi/\phi_{rcp}$, for $\phi > 0.60$. A linear best fit is also shown.

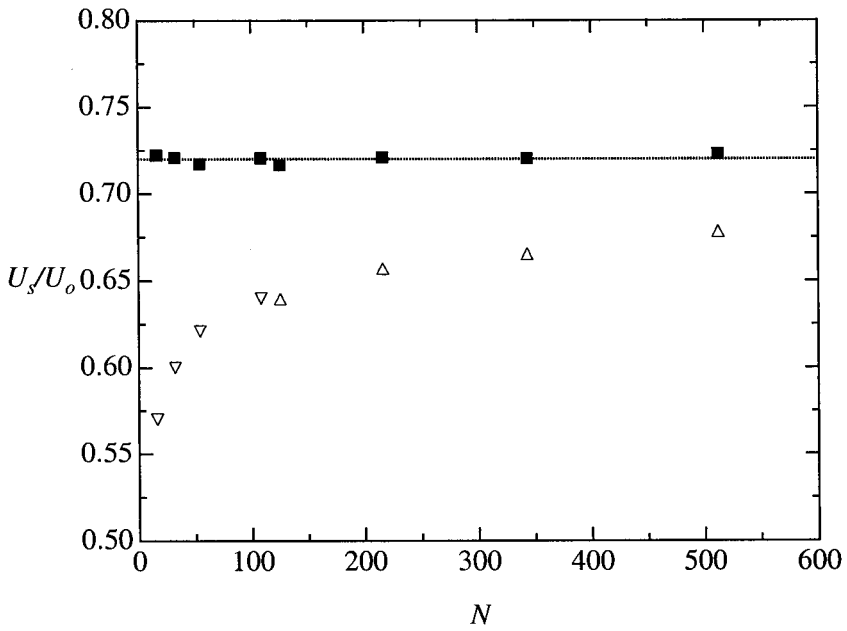

Figure 2.15: The sedimentation velocity of a random suspension of spheres at $\phi = 0.05$ and for different number of particles N. ASD results for N ranging from $125 - 512$ ($\triangle$) are plotted as a continuation of Ladd's (1990) results ($\bigtriangledown$) for smaller systems. The corrected infinite system sedimentation velocity (equation (2.34)) gives a constant value for all N.

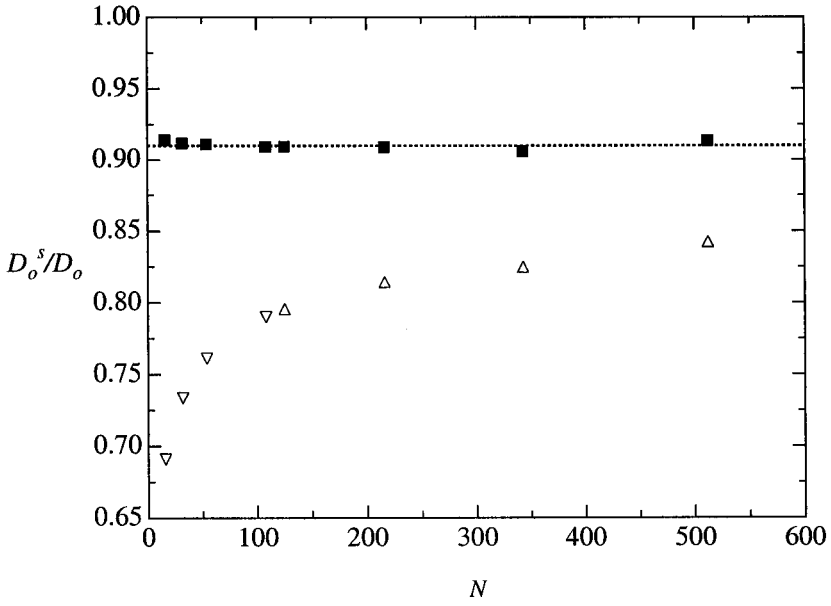

Figure 2.16: The short-time self-diffusion coefficient for a random suspension of spheres at $\phi = 0.05$ and for different number of particles N. ASD results for N ranging from $125-512$ ($\triangle$) are plotted as a continuation of Ladd's (1990) results ($\triangledown$) for smaller systems. The corrected infinite system sedimentation velocity (equation (2.40)) gives a constant value for all N.

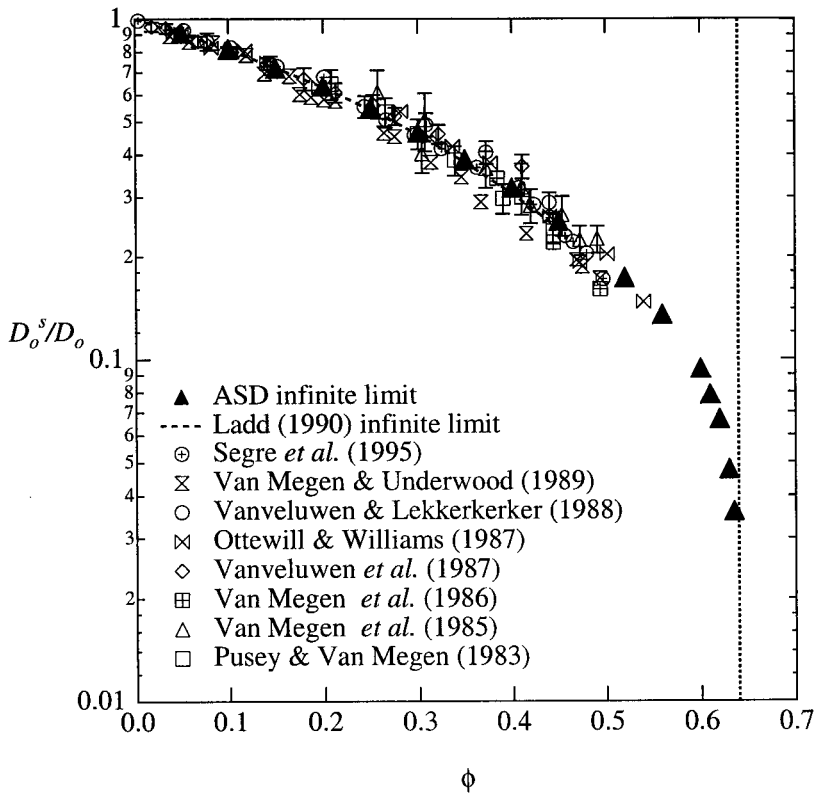

Figure 2.17: The short-time self-diffusion coefficient for an infinite random suspension as a function of the volume fraction ϕ (the values have been corrected according to equation (2.40) from values for $N = 512$). The results are compared with a variety of experimental results for volume fractions below the freezing point.

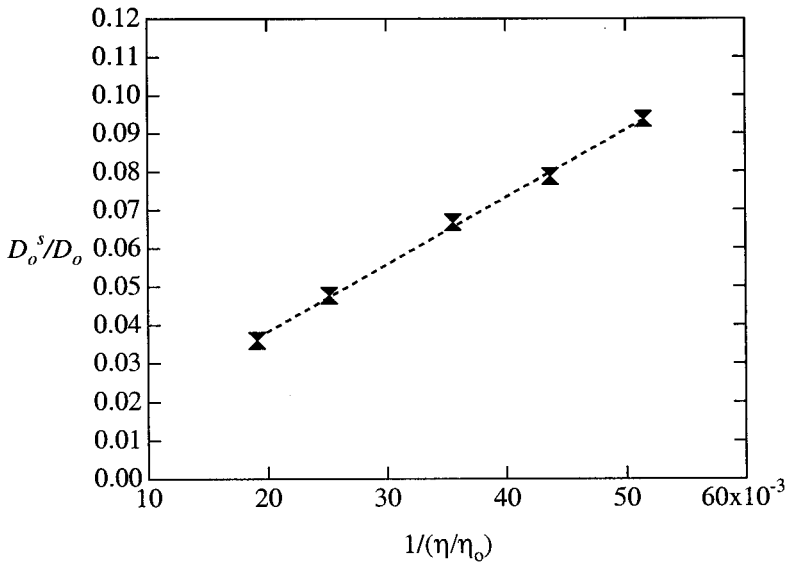

Figure 2.18: The short-time self-diffusion coefficient is plotted as a function of the inverse of the relative viscosity, for $\phi > 0.60$. The solid symbols correspond to the simulation results and the dashed line to a linear best fit.

Chapter 3

Rheology and Microstructure in Concentrated Non-Colloidal Suspensions

3.1 Introduction

Suspensions of non-Brownian particles dispersed in a Newtonian fluid have applications in a variety of natural and industrial settings. The macroscopic behavior of such systems, expressed mainly through their rheological properties and the suspension microstructure, is therefore of extreme importance and has been the subject of numerous theoretical and experimental studies over the last few decades. Our interest is in non-Brownian, or non-colloidal, suspensions at low particle Reynolds number. Non-Brownian implies that the thermal forces giving rise to Brownian motion are negligible (generally for particles of order 10μm or larger), while low particle Reynolds number means that the inertial forces are negligible and that the fluid motion is governed by the Stokes equation. In such systems, the particles interact through hydrodynamic and interparticle forces, and it is the balance of these forces that determines the macroscopic behavior under flow.

The rheological behavior of such a system was initially described by an effective viscosity, and considerable effort was focused on determining this enhanced viscosity as a function of the volume fraction. In recent years, however, a number of studies have demonstrated that the rheological behavior of non-Brownian suspensions is more complicated and non-Newtonian characteristics such as finite normal stress differences and a particle phase contribution to the isotropic stress can be present. Gadala-Maria (1979) first reported

the presence of normal stress differences for a system of polystyrene spheres suspended in water undergoing simple shear flow at small particle Reynolds number. Experiments by Singh (2000) and Zarraga *et al.* (2000) followed, verifying that non-Brownian particles suspended in a Newtonian fluid routinely exhibit non-Newtonian behavior, although the measurement of the resulting normal-stress differences can be difficult and subject to error. Simulations of Brownian systems at very high values of the Péclet number where Brownian motion is almost negligible (Phung 1996, Foss & Brady 2000) also demonstrated the presence of finite normal-stress differences, while recent theoretical work by Brady & Morris (1997) has shown that the high-Pe limit is singular and the residual effect of weak Brownian motion introduces irreversibility, resulting in non-Newtonian behavior (see also Bergenholtz *et al.* 2001). In addition, the presence of an interparticle force also breaks the zero-Reynolds number symmetry and reversibility. By studying the balance between hydrodynamic and interparticle forces in a boundary layer near particle-particle contact, Brady & Morris (1997) proposed a scaling for the particle stress that incorporates the effect of the particle volume fraction, the range of the interparticle force, and the resulting microstructure.

The calculation of the particle pressure—defined as the isotropic component of the particle-induced stress—has also received attention recently. This pressure is a consequence of the hydrodynamic (and interparticle force) interactions among particles, as opposed to the thermally induced "osmotic pressure" in colloidal systems. However, this particle pressure can be viewed as the extension of the osmotic pressure to systems far from equilibrium. Early theoretical studies discarded this isotropic part of the stress; its calculation has only become possible recently after Jeffrey, Morris & Brady (1993) determined the necessary hydrodynamic two-body functions. Singh & Nott (2000) calculated the particle pressure from simulations of a bounded suspension from the normal force on the system's walls. Zarraga *et al.* (2000) and Singh (2000) also attempted a direct evaluation of the particle pressure from experimental measurements of different normal stresses combinations and found the pressure to be a rapidly increasing function of the volume fraction.

In this work we utilize a recently developed algorithm, Accelerated Stokesian Dynamics

(ASD), to study the rheology and microstructure of concentrated monodisperse, non-Brownian, low-Reynolds-number suspensions undergoing simple shear flow in the presence of a short-ranged pairwise repulsive force. The access to a faster simulation method allows the study of much larger systems, typically of $N = 512 - 1000$ particles, and the calculation of the rheological properties, especially the normal stress differences, with improved accuracy. The determination of the particle pressure from the calculation of the full stress tensor is also presented and is found to be in qualitative agreement with experiment. The suspension microstructure is also studied through the determination of the pair-distribution function, and an attempt to connect the microstructure with the measured rheological properties according to the scaling theory of Brady & Morris (1997) is made.

In the next section we outline the Accelerated Stokesian Dynamics method. In §3.3 we present and discuss simulation results for rheology and microstructure in a suspension of non-Brownian particles as a function of the volume fraction. The effect of the interparticle force is discussed in §3.3.5, and systems for volume fractions above $\phi = 0.50$ are briefly studied in §3.3.7. We conclude with a brief summary in §3.4.

3.2 Simulation Method

A new implementation of the conventional Stokesian Dynamics method (SD), called Accelerated Stokesian Dynamics (ASD), is used in our simulations. Since the methodology of ASD has been laid out in a previous work (Sierou & Brady 2001, chapter 2), only a brief account will be presented here. The method combines a Particle-Mesh-Ewald summation technique (Darden *et al.* 1993) with an iterative procedure to solve the equations governing the motion of N particles suspended in a viscous fluid at low particle Reynolds number in $O(N \ln N)$ operations. Following the conventional SD method, the hydrodynamic interactions are split into a far-field many-body part and a pair-wise near-field lubrication part. The near-field interactions can be readily calculated in $O(N)$ operations: The particles are arranged in a chaining mesh (Hockney & Eastwood, 1986) so that each particle's nearest neighbors are easily identified. Since the near-field interactions are short-ranged, the

number of neighboring particles (N_n) is small and the resulting computational cost scales as $N_n N$. To further reduce both the computational cost and the memory requirements, the resulting near-field resistance matrices are stored in a sparse form.

The far-field interactions are calculated in an iterative manner and therefore the far-field mobility matrix is never calculated. A resistance formulation is again followed: From an assumed value for the hydrodynamic forces, the corresponding fluid velocities are calculated and then with application of Faxéns' laws the initial forces are corrected until convergence. The fluid velocity in the presence of N suspended particles (each particle is represented as a series of force multipoles at the particle's center) is calculated following a Particle-Mesh-Ewald approach, i.e., the resulting infinite sums over all the particles are split into a wave-space and a real-space sum with the introduction of a splitting parameter. The resulting wave-space sum contribution is evaluated on a grid as an inverse Fourier transform, while the real-space sum is calculated analytically. The computational cost of the Fourier sums scales as $N_m^3 \ln N_m$, where N_m is the number of mesh points in each direction (for a 3-D problem), and a careful choice of the splitting parameter allows $N_m \approx N^{1/3}$ with no loss in accuracy. The computational cost for the real-space sum scales as NN_l, where N_l is in general the number of all particles influencing the velocity of a given particle. However, for sufficiently small values of the splitting parameter, it can be shown that the contribution of particle pairs that are not near-neighbors is very small and can be ignored without significant error. The same chaining mesh procedure is followed for the calculation of the real-space sums as was used for the near-field interactions at an order N cost.

After both the far-field force and the near-field resistance matrices are calculated, the new particle velocities are calculated from the equation of motion:

$$0 = -\boldsymbol{R}_{FU,nf} \cdot (\boldsymbol{U}_p - \boldsymbol{u}^\infty) + \boldsymbol{R}_{FE,nf} : \boldsymbol{E}^\infty + \boldsymbol{F}^p + \boldsymbol{F}_{ff}, \tag{3.1}$$

where $\boldsymbol{U}_p - \boldsymbol{u}^\infty$ is a $6N$ vector representing the particle non-affine translational and rotational velocities, $\boldsymbol{F}_{ff}$ represents the far-field force/torque, and now $\boldsymbol{R}_{FU,nf}$ is a sparse symmetric positive definite matrix. The imposed flow is a simple shear: $\boldsymbol{u}^\infty(\boldsymbol{x}_p) = \dot{\boldsymbol{\Gamma}} \cdot \boldsymbol{x}_p$,

where $\boldsymbol{x}_p$ is the particle's center, and $\dot{\boldsymbol{\Gamma}} = \boldsymbol{E}^\infty + \boldsymbol{\Omega}^\infty$ is the velocity gradient tensor of the bulk flow; $\boldsymbol{E}^\infty$ and $\boldsymbol{\Omega}^\infty$ are the symmetric and antisymmetric part of $\dot{\boldsymbol{\Gamma}}$, respectively. An iterative conjugate gradient method with an incomplete Cholesky preconditioner is used for the inversion of the sparse near-field resistance matrix. With iterative algorithms the computational time requirement can scale linearly with the matrix size since the sparse matrix multiplications required for an iterative method scale as N; the presence of the preconditioner, however, is necessary for the number of iterations to be relatively small.

We consider the Stokes flow of a suspension of hard spheres in a suspending fluid of viscosity η undergoing simple shear with a shear rate $\dot{\gamma}$ ($\dot{\gamma}$ is the magnitude of $\dot{\boldsymbol{\Gamma}}$). As has been demonstrated in the past (Dratler & Schowalter 1996), in the absence of Brownian motion the presence of a repulsive interparticle force (denoted as $\boldsymbol{F}^p$) is necessary to prevent the system from forming infinite clusters that jam, leading to serious particle overlap. Although the choice of this force is somewhat arbitrary, its introduction captures the behavior of a real physical system, at least qualitatively, since in a real system the presence of residual Brownian forces, or particle roughness, etc., limits the cluster size and prevents overlaps. For most of our simulations (friction is also introduced in §3.3.6), an interparticle force of the form (Bossis & Brady 1984)

$$\boldsymbol{F}^p_{(\alpha\beta)} = F_0 \frac{\tau \exp^{-\tau\epsilon}}{1 - \exp^{-\tau\epsilon}} \boldsymbol{e}_{(\alpha\beta)} \tag{3.2}$$

was used, where $\boldsymbol{F}^p_{(\alpha\beta)}$ is the force exerted on sphere α by sphere β, F_0 represents its magnitude, τ^{-1} is related to the force range, $\epsilon = r - 2$ is the dimensionless spacing between the surfaces of the two spheres and $\boldsymbol{e}_{(\alpha\beta)}$ is the unit vector connecting the centers of the two spheres.

Non-dimensionalizing all lengths by the particle radius a, all times by the characteristic time $\dot{\gamma}^{-1}$, the interparticle force by its magnitude F_0 and the hydrodynamic resistance tensors $\boldsymbol{R}_{FU}$, $\boldsymbol{R}_{FE}$ by $6\pi\eta a$ and $6\pi\eta a^2$, respectively, the equation of motion (3.1) becomes

$$\boldsymbol{R}_{FU,nf} \cdot (\boldsymbol{U}_p - \boldsymbol{u}^\infty) = \boldsymbol{R}_{FE} : \boldsymbol{E}^\infty + \dot{\gamma}^{\star -1} \boldsymbol{F}^p + \boldsymbol{F}_{ff}, \tag{3.3}$$

where $\dot{\gamma}^\star = 6\pi\eta a^2 \dot{\gamma}/F_0$ is the ratio of the shear and interparticle forces.

For the calculation of the rheological properties the bulk stress, $\langle \boldsymbol{\Sigma} \rangle$, is needed; this is defined as an average stress over the volume of the unit cell containing N particles and is given by

$$\langle \boldsymbol{\Sigma} \rangle = -p_f \boldsymbol{I} + 2\eta \boldsymbol{E}^{\infty} + \langle \boldsymbol{\Sigma}_p \rangle \,, \tag{3.4}$$

where p_f is the (constant) pressure in the fluid and $2\eta \boldsymbol{E}^{\infty}$ is the deviatoric contribution from the fluid. The particle contribution to the stress, $\langle \boldsymbol{\Sigma}_p \rangle$, is given by

$$\begin{aligned} \langle \boldsymbol{\Sigma}_p \rangle = & - n \langle \boldsymbol{R}_{SU,nf} \cdot (\boldsymbol{U}_p - \boldsymbol{u}^{\infty}) \rangle \\ & + n \langle \boldsymbol{R}_{SE,nf} : \boldsymbol{E}^{\infty} \rangle + n \langle \boldsymbol{S}_{ff} \rangle \\ & - n \langle \boldsymbol{x} \boldsymbol{F}^p \rangle \,, \end{aligned} \tag{3.5}$$

where n is the particle number density. The contributions from the far-field and the near-field are denoted separately, and the direct interparticle force contribution is $-\langle \boldsymbol{x}\boldsymbol{F}^p \rangle$. We note here that no attempt has been made to separate the particle stress into a hydrodynamic contribution and an interparticle force contribution. As is apparent from (3.3) the particle velocity $(\boldsymbol{U}_p - \boldsymbol{u}^{\infty})$ is a result of both the hydrodynamic and interparticle forces, and, in addition, the resistance matrices depend on the particle configuration, which in turn depends on both the hydrodynamic interactions and the interparticle force, making a separation between various contributions in (3.5) somewhat arbitrary.

The viscosity in a simple shear flow with the flow, velocity-gradient and vorticity directions along the x, y and z axes, respectively, is related to the xy component of the bulk stress and rate of strain in the following manner:

$$\eta_r \equiv \frac{\Sigma_{xy}}{2\eta E_{xy}}, \tag{3.6}$$

which, from (3.4), can be written as

$$\eta_r = 1 + \eta_r^p, \tag{3.7}$$

where η_r^p refers to the particle phase contribution to the viscosity and includes both contributions from the hydrodynamic interactions among the particles and from the interparticle force; the 1 corresponds to the solvent contribution.

The first and second normal stress differences can also be calculated according to their definitions:

$$N_1 \equiv \langle \Sigma_{xx} \rangle - \langle \Sigma_{yy} \rangle \,, \tag{3.8a}$$

$$N_2 \equiv \langle \Sigma_{yy} \rangle - \langle \Sigma_{zz} \rangle \,. \tag{3.8b}$$

Since the pure fluid phase (for a Newtonian fluid) has zero normal stress differences, Σ_{xx}, Σ_{yy} and Σ_{zz} in (3.8) are equal to the particle phase contribution to the normal stresses Σ_{xx}^p, Σ_{yy}^p and Σ_{zz}^p, respectively.

The particle phase suspension pressure is $-1/3$ of the trace of $\langle \boldsymbol{\Sigma}_p \rangle$; i.e., $\Pi = -1/3 \; tr \, \langle \boldsymbol{\Sigma}_p \rangle$. As defined, the resistance tensors and $\langle \boldsymbol{S}_{ff} \rangle$ in (3.5) are not traceless. The trace components are given by the functions $\boldsymbol{R}_{QE,nf}$ and $\boldsymbol{R}_{PU,nf}$ first introduced by Jeffrey *et al.* (1993). The particle-phase pressure also includes the interparticle force contribution $-1/3 \, \langle \boldsymbol{x} \cdot \boldsymbol{F}^p \rangle$. Since the suspension as a whole (fluid plus particles) is incompressible, the arbitrary level of the pressure is set by the fluid contribution p_f.

3.3 Results

A number of simulations were performed for a range of volume fractions between $0.10 \leq \phi \leq 0.50$ and number of particles from $N = 125$ to $N = 1000$, and for a variety of parameters of the interparticle force. In addition, as will be discussed in §3.3.7, volume fractions in the metastable regime ($\phi > 0.50$) were sampled and their microstructure studied. Each long run, typically of $200 - 400$ total strain, was divided into statistically independent subintervals, typically of $10 - 20$ strains, in order to determine the statistical variation of the properties. The resulting statistical errors for all rheological properties were usually less than 5%. All runs were started using hard-sphere equilibrium configurations obtained from a Monte Carlo procedure and the first $10 - 20$ strains were always ignored so that the system is allowed to reach its steady state configuration before computing averages. The

time step used was $\Delta t = 5 \times 10^{-3} - 5 \times 10^{-4}$ depending on the volume fraction (time steps as small as $\Delta t = 10^{-4}$ were necessary to study volume fractions around 60%). A fourth order Adams-Basforth integration scheme was used to update the particle positions.

3.3.1 Dependence on the number of particles N

Systems of $N = 125 - 1000$ were studied for volume fractions between $\phi = 0.10 - 0.50$ and for an interparticle force with $\tau = 1000$ and $\dot{\gamma}^\star = 1000$. The resulting shear viscosities are plotted in figure 3.1. It is apparent that the size of the system has no significant effect on the values of the viscosities for all values of N studied, in agreement with previous studies. Table 3.1 presents the values of the shear-viscosity, first and second normal stress differences and particle pressure for a volume fraction $\phi = 0.40$ and $N = 125$, 256, 512 and 1000. Again, the effect of the system size on all rheological properties is insignificant. Smaller systems were also sampled, and, although the values of the resulting viscosities were always very close and within the statistical error, the errors in the calculation of the normal stress differences increased significantly when very small systems were studied due, no doubt, to the difficulty in accurately determining differences as compared to the viscosity. Unless otherwise noted, for the remainder of this chapter systems of $N = 512$ particles were used.

3.3.2 Shear and normal stresses

In figure 3.2 and tables 3.2 and 3.3 the ϕ-dependence of the suspension relative viscosity, η_r, is shown for a system of $N = 512$ and volume fractions ranging from $\phi = 0.10 - 0.50$ (for completeness the $-\langle \boldsymbol{x}\boldsymbol{F}^p \rangle$ contribution to the stress is also presented in the tables). An interparticle force of the form of (3.2) is also present with $\tau = 1000$ and $\dot{\gamma}^\star = 1000$. A number of experimental results by Zarraga *et al.* (2000), Pätzold (1980), Gadala-Maria (1979) and Rutgers (1962) are also shown. The agreement between simulation and experiment is good for low to moderate volume fractions, while for large volume fractions our viscosities are systematically lower than most of the experimental values. For these high volume fractions, however, the discrepancies between experimental data from different studies are also very large, and it is now recognized (Brady & Morris 1997, Bergenholtz

et al. 2001, Maranzano & Wagner 2001) that repulsive interparticle forces can have a profound impact on the rheology; for example, as we shall see in §3.3.5, reducing the range (increasing τ) or amplitude (increasing $\dot{\gamma}^\star$) can result in a much larger viscosity at high concentrations. Qualitatively, the viscosity is, as expected, a monotonically increasing function of the volume fraction; as the suspension becomes denser, particle clusters form and dominate the macroscopic behavior and the particle stress. It is worth noting here that the experimental measurements of the shear-stress for relatively large non-Brownian particles are subject to a number of limitations that are particularly severe for dense systems. For example, in the experiments of Zarraga *et al.* (2000) the viscosity was found to be a strongly decreasing function of the shear-rate for a large range of shear-rates. A number of factors have been suggested to explain this (and other anomalous) behavior(s) such as the effect of gravity when the particle and fluid phase densities are not perfectly matched, the effect of the walls and the size of the apparatus, etc. The notion of a "universal" viscosity curve is therefore questionable.

In figure 3.3 the high-frequency dynamic viscosity is subtracted from the relative steady-shear viscosity and the resulting quantity is plotted as a function of the volume fraction. The high-frequency dynamic viscosity, η'_∞, which has been obtained by a number of authors—both through simulations and experiments (Sierou & Brady 2001, Foss & Brady 2000, Shikata & Pearson 1994, van der Werff & de Kruif 1989), is purely hydrodynamic in origin and corresponds to the viscous contribution to the stress for a system at equilibrium, i.e., when the system microstructure has not been affected by the flow and is given by the equilibrium hard-sphere distribution. The remaining viscosity $\Delta\eta/\eta = \eta_r - \eta'_\infty$ arises from particle interactions in the non-equilibrium structure induced by the flow. Theories have been advanced (Brady & Morris 1997) that predict this extra particle stress as a function of the distorted microstructure; a detailed discussion will be given in §3.3.4.

The first and second normal stress differences, N_1 and N_2, are presented as a function of the volume fraction in figures 3.4 and 3.5 and tables 3.2 and 3.3 for the same system of $N = 512$. The availability of larger systems allows a much more reliable calculation of the normal stresses than was possible in the past. Limited experimental measurements for the normal-stress differences of non-Brownian systems are also available, but are often

subject to large errors. Zarraga *et al.* (2000) measured the first and second normal stress-differences by combining results from rotating plate and rotating rod experiments, while Singh (2000) obtained the same quantities from a combination of cylindrical Couette and parallel plate experiments. In addition, Zarraga *et al.* (2000) only report the ratio of the normal stresses to the shear stresses, making detailed comparisons even harder. Nevertheless, in figures 3.4 and 3.5 we also report the experimental results of Singh (2000) and Zarraga *et al.* (2000); a fitted expression given by Zarraga is also shown. Since Zarraga *et al.* (2000) only report the ratio of normal to shear stresses, two sets of values are given in the figures. One set, referred to as Z2 on the figure legend, corresponds to using the shear stress calculated from their experiment and the other one, referred to as Z1 on the figure legend, corresponds to using the shear stress calculated from our simulations. Qualitatively, the agreement between the experiments and the simulations is satisfactory—both normal stress differences are negative and are increasing (in absolute value) functions of the volume fraction. The quantitative agreement is also satisfactory between our values for N_1 and those reported by Singh (2000) and our values of N_2 and those reported by Zarraga *et al.* (2000). Contrary to the experimental measurements that have N_2 larger than N_1 (in magnitude), both normal stress differences from our simulations are of the same magnitude for the given interparticle force (the effect of the interparticle force on the normal-stress differences is discussed in more detail in §3.3.5). A negative N_1 implies the rheometer plates would be pulled together. This is a consequence of hydrodynamic interactions—particles must be pulled apart by the shearing motion giving rise to a negative N_1.

Finally, the particle pressure is presented in figure 3.6 and tables 3.2 and 3.3 as a function of the volume fraction. Though very small at small concentrations, it increases rapidly and approaches the values of the shear stress as the volume fraction is further increased, indicating that its experimental measurement should be possible. Zarraga *et al.* (2000) and Singh (2000) both deduced the values for the particle pressure from a combination of the measured normal stresses; these values are also presented in figure 3.6 (for the results of Zarraga *et al.* (2000) only the fitted expression is plotted since the exact values are hard to determine from their plots). The agreement is quite good

both qualitatively, where the pressure appears to be a strongly increasing function of the volume fraction, and quantitatively. Since the pressure corresponds to an average value of the normal stresses, its value is expected to be less sensitive to errors than the normal stress differences, which may explain the better quantitative agreement between all of the results.

Before we proceed to a detailed analysis of the suspension microstructure it is useful to compare the concentration dependence of the normal stresses to the concentration dependence of the shear stresses for our system. It has been suggested by Brady & Morris (1997) that the excess particle contribution to all the elements of the stress tensor should have the same functional dependence on the suspension microstructure and concentration; if this is indeed the case, then the ratio of the normal stresses to the excess shear stress, $\Delta\eta$, should be constant as a function of the volume fraction. This ratio is plotted in figure 3.7 for both the pressure and the sum of the normal stress differences (since the values of N_1 and N_2 were indistinguishable for this set of results, their sum was used for the relative measure). It is apparent from the figure that, while of the same magnitude, the dependence of the normal and shear stresses on the volume fraction is not precisely the same. The magnitude of the pressure increases faster than the excess viscosity, a result in agreement with simulation and experimental observations of Singh & Nott (2000) and Singh (2000). The theoretical analysis of Nott & Brady (1994) also demonstrates that this ratio must be a monotonically increasing function of ϕ for the system to be stable to perturbations in particle concentration. The normal stress differences exhibit a more complicated behavior—for small volume fractions they scale as the particle pressure, while for higher volume fractions they follow the shear stress scaling. In figure 3.8 the ratio of the three individual normal stresses, Σ_{11}, Σ_{22} and Σ_{33}, over the excess viscosity, $\Delta\eta$, is plotted. Although within the statistical errors the three normal stresses have a very similar dependence on both the volume fraction and the shear stress it is nevertheless possible that the normal stress differences can have a qualitatively different behavior from the pressure, since the pressure corresponds to a simple average of the normal stresses and not a difference.

In figures 3.9 (a) and (b) we plot the ratio of the three normal stresses, Σ_{11}, Σ_{22}

and Σ_{33}, and the particle pressure, Π, to the shear-stress. The fitted expressions for the same ratios given by Zarraga *et al.* (2000) are also presented—they correlate their ratio with $\phi^3 \exp^{2.34\phi}$, with different coefficients for each component of the normal stress. The agreement is again quite good for each component of the normal stress, and even better for the pressure; it is noted again that relatively small errors in the calculation of the independent components can give rise to much larger errors in the normal stress differences where the agreement between simulation and experiment is not as good.

A comparison of figures 3.8 and 3.9 shows that the normal stresses are better correlated with the excess viscosity $\Delta\eta$ than with the suspension viscosity η_r; the variation with volume fraction in figure 3.8 is a factor of 6, while that in figure 3.9 is three orders of magnitude. This points to the fact that the origin of the normal stresses and the excess viscosity is the same—the deformed microstructure. The correlation with the excess viscosity in not perfect, however; a perfect correlation would be a constant independent of ϕ. Although both the excess viscosity and the normal stress arise from microstructural deformation due to flow, an excess viscosity would still exist if the microstructure had fore-aft symmetry, while the normal stresses would vanish in this case. A fore-aft symmetric microstructure (see below) is expected in the absence of interparticle forces (or Brownian motion), although it is not possible to steadily shear such a "purely hydrodynamic" system due to the formation of jammed clusters (Melrose & Ball 1995, Dratler & Schowalter 1996).

3.3.3 Microstructure

For a system of non-Brownian particles suspended in a Newtonian fluid, non-Newtonian rheological behavior (i.e., non-zero normal stress differences and a particle pressure) can only result from an anisotropic microstructure which can clearly be seen in the pair-distribution function. Given a particle at the origin, the pair-distribution function, $g(\boldsymbol{r})$, describes the probability density of finding a second particle at distance $\boldsymbol{r}$ normalized by the particle number density in the suspension. The pair-distribution function is determined in the usual manner by discretizing the area around each particle and counting the number of neighboring particles within each discretized area. The manner in which this area is discretized can lead to different representations of the pair-distribution func-

tion. The angularly averaged pair-distribution function contains only information on the relative separation between the particles; the average is over all possible relative particle orientations. The projection of the pair-distribution function onto the plane of shear, xy, (as will be shown later the microstructure is axisymmetric outside the plane of shear), can also be expressed as a function of the relative coordinates, r and θ, as defined in figure 3.10. Here, θ is measured clockwise from the negative x-axis and r is simply the distance from a particle's center. For a given interparticle separation (or range of separations) the angular dependence of the pair-distribution function can be determined from the number of neighboring particles at different values of θ. The angular dependence of $g(\boldsymbol{r})$ can also be illustrated by the projection of the pair-distribution function on all three planes, (x, y), (x, z) and (z, y).

Figure 3.11 shows the angularly averaged radial pair-distribution function for particle to particle distances between 2 and 2.005, where the near-contact particle build-up is expected for the interparticle force used; the interparticle force has a range $1/\tau = 0.001$ and a relative strength $\tau/\dot{\gamma}^{\star} = 1$. In order to correctly capture the particle build-up near contact, especially for the larger volume fractions, very small refinements in the radial coordinate were often necessary (as small as 10^{-6} of the particle radius). A peak in the radial distribution function at position r_{peak} is evident, corresponding to a ring of neighboring particles adjacent to any particle. The values of the pair-distribution function at the peak along with the peak's location are presented in table 3.4 as a function of the volume fraction. It is clear that the magnitude of the peak increases significantly as the particle concentration increases and shifts to closer particle contact. As a result, for high enough concentrations, the radial pair-distribution function resembles the pair-distribution function for a hard-sphere system with a given interparticle separation b, such that $2b/a = r_{peak}$. Particles accumulate near r_{peak} as they would for a hard-sphere system, while their concentration drops significantly for $r < r_{peak}$. For lower concentrations, however, the peak in the pair-distribution function is not as apparent and the probability of finding a particle at distances less than r_{peak} is by comparison high, a behavior characteristic of a soft-interparticle potential. It is interesting to note that for the same values of the interparticle force parameters there is a significant change in the location of the peak as

a function of the volume fraction, which does not occur for a hard-sphere potential.

Figure 3.12 shows the angularly averaged radial distribution function for particle to particle distances between 2 and 7 radii for the same parameters of the interparticle force and for volume fractions $\phi = 0.20$, 0.30, 0.40 and 0.50. The presence of a second peak is apparent and the magnitude of the peak is an increasing function of the volume fraction. This second peak is less pronounced than the first one and is located at distance close to $r = 4$.

We now turn to the angular dependence of the pair-distribution function for particles near contact ($2 < r < 2.001$). Figure 3.13 shows this dependence for the same parameters for the interparticle force and for volume fractions of $\phi = 0.20$, 0.30 and 0.40. The anisotropy in the microstructure is evident: a large particle density exists along the compressional axis and a low density along the extensional axis. We note that the choice of the radial distances within which the angular dependence of the distribution function is calculated can significantly affect representations such as in Figure 3.13. For example, for very low volume fractions and for separations $r < 2.001$, the pair-distribution function would appear to be isotropic and zero everywhere, since the peak of the radial pair distribution function occurs at larger particle-particle separations. On the other hand, for volume fractions near close-packing a much smaller r would be appropriate in order to capture the "maximum" anisotropy. It is also possible that a long-range anisotropy is present, which is not captured in figure 3.13. However, since most of the stress comes from near touching particles, the anisotropy in this region is most important. Increasing the volume fraction increases the anisotropy both in magnitude and also with a shift to smaller θ.

Finally, we present some typical results for the projection of the pair-distribution function onto the xy, xz and zy planes. The case of $N = 512$ and $\phi = 0.40$ is shown in figure 3.14 (a) and (b). The projection of the pair-distribution function on a given plane, e.g., xy, includes contributions from particles at all values of the third coordinate (e.g., z). As a result, the probability of finding a particle at distance $dx = 0$, $dy = 0$ is not zero and the "excluded" volume of the particle is not sharply defined—this is simply a matter of presentation and has no further significance. As was already mentioned, the

microstructure is indeed symmetric on the planes perpendicular to the shear plane, while asymmetry exist in the plane of shear with a build up of particles in the compressional zone and a depletion of particles in the extensional zone (light regions denote high probability and dark low). It is the presence of the asymmetry in the xy plane that leads to the negative normal stress differences. No shear-induced order is present for the values of the interparticle force studied for volume fractions $\phi \leq 0.50$.

3.3.4 Rheology and microstructure

The impact of the suspension microstructure on its non-Newtonian rheological properties has been studied in the past and a number of theoretical predictions are available. Brady & Morris (1997) analytically calculated the viscosity and normal stress differences for a dilute suspension of Brownian particles at high Péclet number, taking into account hydrodynamic interactions and the presence of a hard-sphere-type pairwise interparticle force that prevents particles from approaching one another to less than a minimum separation $b > a$. (Here a always refers to the actual particle radius at which the no-slip hydrodynamic conditions are applied.) This force breaks the fore-aft symmetry and thus leads to a viscosity correction, finite normal stress-differences and a particle pressure. By studying the balance between hydrodynamic and interparticle forces in a boundary layer near particle-particle contact, Brady & Morris (1997) calculated the microstructure, as expressed by the pair-distribution function in the boundary layer, and the resulting contribution to the particle stress. (The boundary layer is a balance of hydrodynamic and weak Brownian motion at the hard-sphere radius b.) Furthermore, they attempted to extend their solution to concentrated suspensions and proposed the following scaling for the leading contribution to the total stress:

$$n\boldsymbol{S}^{H}_{b.l.} \sim \eta\dot{\gamma}\eta'_{\infty}\phi^2 g^{\infty}(2b;\phi)(b/a-1)^{0.22}, \tag{3.9}$$

where $g^{\infty}(2b;\phi)$ is the value of the pair-distribution function (for the given microstructure) at the minimum separation $r = 2b$ and was not calculated in their analysis. We note here that Brady & Morris (1997) split the stress contribution into two parts, one referred

to as the hydrodynamic stress and one referred to as the interparticle force stress; they find that the contribution of the hydrodynamic stress is dominant (the interparticle force contribution is smaller by a factor of $(b/a-1)$) and is the one presented in (3.9). No such splitting was attempted in our calculation and only the total stress was determined in simulation; however, since (3.9) represents the leading contribution to the stress, its scaling should be also valid for the total particle stress.

Equation (3.9) has a simple physical interpretation. It states that the dominant contribution to the stress is simply the number of particle pairs at contact, $\phi^2 g^{\infty}(2b;\ \phi)(b/a-1)^{0.22}$, times the hydrodynamic stress for a pair, $\eta'_{\infty}\eta\dot{\gamma}$. The factor of η'_{∞} arises because particles are being pushed together by shearing in the suspension and resisting this motion by the solvent viscosity that separates near-touching particles. Alternatively, one can simply view η'_{∞} as renormalizing the solvent viscosity with the viscosity of the equilibrium hard-sphere structure. The factor $(b/a-1)^{0.22}$ comes from the asymptotic behavior of the hydrodynamic mobility functions as the particles approach contact.

Although the theory of Brady & Morris (1997) is restricted to the case of a hard-sphere-type interparticle force one can still use the idea that the dominant contribution comes from near-touching pairs—that is, the pairs under the peak in $g(r)$ in figure 3.11—to write:

$$\boldsymbol{\Sigma}_p \approx n^2 \int \boldsymbol{S}(\boldsymbol{r})g(\boldsymbol{r})d\boldsymbol{r} \approx \eta\dot{\gamma}\eta'_{\infty}\phi^2 \int_2^{r^\star} g(\boldsymbol{r})d\boldsymbol{r}, \tag{3.10}$$

where $r^\star$ corresponds roughly to the width of the peak. The location of $r^\star$ is not well-defined since $g(r)$ falls continuously from its peak value as r increases. At the same time the two particle stresslet $\boldsymbol{S}(\boldsymbol{r})$ also drops off rapidly with increasing r. What is needed is an estimate of the number of close pairs, and we have arbitrarily chosen $r^\star$ as the point at which $g(r)$ has dropped to 10% of its peak value, which varies from $r^\star = 2.0009$ at $\phi = 0.50$ to $r^\star = 2.026$ at $\phi = 0.10$. The values of $r^\star$ are given in table 3.4. This scaling relation then suggests that

$$\frac{\eta_r(\phi) - \eta'_{\infty}(\phi)}{\eta'_{\infty}(\phi)\phi^2 \int_2^{r^\star} g(\boldsymbol{r})d\boldsymbol{r}} \tag{3.11}$$

should be independent of volume fraction. This quantity is presented in figure 3.15(a) as a function of the volume fraction; the predicted scaling is indeed quite good, and the excess non-dimensionalized shear-stress appears to be constant with volume fraction.

For comparison, we also attempt to scale the excess shear stress with the hard-sphere scaling of (3.9). Since $g^{\infty}(2b;\phi)$ is not well defined for our soft interparticle potential the value at contact for the equilibrium pair-distribution function, $g^0(2;\phi)$, is used instead. This quantity is a known function of the volume fraction, ϕ, given, for example, from the Carnahan-Stirling equation of state:

$$g^0(2;\phi) = \frac{1-\frac{1}{2}\phi}{(1-\phi)^3}, \quad \phi < 0.50. \tag{3.12}$$

The value of r_{peak} is now used as the corresponding minimum separation distance b, since in the hard-sphere sense it corresponds to where the maximum accumulation of particles is observed. In figure 3.15(b) the excess stress is scaled with $\eta\dot{\gamma}\eta'_{\infty}\phi^2 g^0(2;\phi)(b/a-1)^{0.22}$ and presented as a function of the volume fraction. The scaling is again satisfactory, leading to values independent of the volume fraction. The soft interparticle potential with a given distribution over distance $r^{\star}$ was thus successfully replaced by a hard-sphere interparticle force at distance $2b/a = r_{peak}$. The excess stress scales satisfactory with either approach.

The same scaling is proposed for all the elements of the stress tensor. However, in the absence of any anisotropic microstructure the normal stresses are zero, no equilibrium value needs to be subtracted, and the scaling of (3.10) should apply directly. As was already mentioned, however, the ratio of the normal to the shear stresses is not constant as a function of the volume fraction, and therefore we should expect the same to be the case here. In figure 3.16 the normal stresses, Σ_{11}, Σ_{22} and Σ_{33} are scaled with $\eta\dot{\gamma}\eta'_{\infty}\phi^2 \int_2^{r^{\star}} g(\boldsymbol{r})d\boldsymbol{r}$, while in figure 3.17, the particle pressure and the two normal stress-differences are also plotted with the same scaling. It is again seen that the scaled normal stresses are an increasing function of the volume fraction ϕ. As is apparent from figure 3.17, the normal and excess shear stress are of the same magnitude for all volume fractions studied here. The notion that the dominant contribution to the stress comes from close pairs and can be estimated quite simply is borne out well by the simulation results and

should prove useful in interpreting experimental data.

3.3.5 Effect of the interparticle force

All results presented so far were obtained for the same values of the interparticle force parameters. We now fix the particle volume fraction at $\phi = 0.40$ and number of particles $N = 512$ and vary the range (τ) and the amplitude ($\dot{\gamma}^\star$) of the interparticle force to assess their influence on the rheological behavior.

In table 3.5 we present the values of the relative viscosity and particle pressure for a system at volume fraction $\phi = 0.40$ for different values of the force parameters (the particle pressure is chosen as a characteristic measure of the behavior of the normal stresses in general). While a trend is apparent for the viscosity, the normal stress shows very little variation. The viscosity increases monotonically as the relative strength of the interparticle force decreases; this is apparent both when the range of the interparticle force decreases (increasing τ) and when $\dot{\gamma}^\star$ increases. This behavior is expected because, as the relative importance of the interparticle force decreases, the particles come closer together, larger clusters form and the suspension becomes harder to shear, i.e., it shear thickens. This is completely in keeping with the behavior of Brownian suspensions as $Pe \to \infty$; they too shear thicken. On the other hand, the behavior of the normal stresses is more complicated. In the limit of pure hydrodynamics, the normal stresses should vanish because it is the presence of the interparticle force that breaks the fore-aft symmetry giving rise to normal stresses. At the same time, in the absence of an interparticle force the particles are allowed to come very close together, which generates a large cluster and gives rise to very large lubrication stresses. This competition makes the behavior of the normal stresses difficult to predict, even qualitatively. As is shown in table 3.5, the values of the normal stresses show no systematic variation with τ or $\dot{\gamma}^\star$ and are indistinguishable within the statistical accuracy.

In table 3.6 $\dot{\gamma}^\star$ is varied for a system of $\phi = 0.10$ and 0.30. For these lower volume fractions, the quantitative effect of the interparticle force on the shear stress is not as pronounced as was the case for $\phi = 0.40$. The viscosity, however, again increases as the relative strength of the interparticle force decreases. The magnitude of the particle

pressure is now much smaller, but nevertheless a trend is now evident. The particle pressure decreases as the relative strength of the interparticle force increases. Although the absolute values are very small for $\phi = 0.10$, the change is significant. This is in agreement with the dilute limit results of Zarraga *et al.* (2001) that predict the same behavior with increasing minimum particle to particle separations. For these dilute systems, the formation of dense clusters is of little importance and the behavior is dominated by the decrease in the asymmetry with decreasing importance of the interparticle force.

Quantitative predictions following the scaling of equation (3.10) or (3.9) are difficult to make, primarily because the differences in the rheological properties are not as pronounced (compared to the difference when the volume fraction was varied), and the determination of the appropriate parameters, e.g., $r^\star$, for very different soft potentials is subject to uncertainty. In figure 3.18 we show the change of the angularly averaged radial pair-distribution function for different values of the interparticle force, varying the force magnitude (a) and the force range (b), for a system of $N = 512$ particles at $\phi = 0.40$. It is apparent that by increasing the range $(1/\tau)$, or equivalently increasing the magnitude of the force $(1/\dot{\gamma}^\star)$, the peak in the pair-distribution function decreases in magnitude and shifts to larger particle-particle separations. Although no attempt is made to quantify this behavior, it is worth mentioning that according to the scaling of (3.9), two factors are expected to influence the change in the particle stress: the location of the peak through $(b/a - 1)^{0.22}$ and the magnitude of the peak through $g^\infty(2b)$. As is apparent from figure 3.18, these two factors have qualitatively opposite effects on the value of the stress: as the maximum value of the pair-distribution function is increased (increasing $g^\infty(2b)$), simultaneously its position is shifted to smaller separations (decreasing the value of b/a). For the case of the shear-stress (table 3.5), the overall effect leads to an increase to the value of the viscosity. This is in qualitative agreement with the observation that the dependence on b/a is weak, leading to a behavior dominated by the sharp increase of the value of g at contact. The scaling theory of Brady & Morris (1997) also only takes into account contributions from the boundary layer between the particles—the effect of particles further apart, and the anisotropy possibly associated with their separations is not included; this higher-order effect can be important when the variation in properties is small as is in tables 3.5 and

3.6.

Finally, we remark here that although the shear viscosity at $\phi = 0.40$ in table 3.5 only increased by a factor of 1.2 as $\dot{\gamma}^\star$ varied from 1 to 10^4, at $\phi \approx 0.50$ this same variation in $\dot{\gamma}^\star$ can lead to a doubling of the viscosity (Yurkovetsky 1998), which should be considered in light of the agreement between simulation and experiment in figure 3.2. The rheology is extremely sensitive to the details of near particle-particle interactions at high volume fractions.

3.3.6 Effect of friction

Finally, we have investigated the effect of sliding friction on the rheological behavior. Davis (1992) and Wilson & Davis (2000) first studied the effect of friction for a two-particle system. They considered particles with microscopic surface asperities such that they are able to make contact. When the interparticle surface-surface separation reaches a certain value comparable to the size of the surface asperities, they assumed that the particles were at "contact". The two particles then remain at contact (and at the same minimum separation) for as long as the net hydrodynamic forces acting on them are compressive. While the particles are at contact, the normal (parallel to the line of centers) contact force on each particle is equal and opposite to the normal hydrodynamic force on the particle. In addition, a tangential (tangent to the contact surfaces) force, as a result of solid-solid friction is assumed to exist and its value is a combination of the hydrodynamic force and a friction coefficient, ν. This model is known as the roll-slip model, because for certain magnitudes of the normal force the particles are allowed either to roll around one another, or to slip (see Davis 1992 for a detailed description).

The application of this model to a large number of particles, however, is computationally expensive, since the contact force on each particle depends not only on the particle's position but also on the velocities and hydrodynamic forces exerted on all other particles. To resolve this properly requires solving the complete system of equations for the contact forces. A simpler approach was therefore followed here in order to explore the effect of sliding friction. The interparticle force given by (3.2) was maintained, but it was assumed that the presence of such a normal force between the two particle surfaces would give rise

to a tangential frictional force with its magnitude limited by ν, the friction coefficient. The direction of this frictional force depends on the exact particle velocities, hydrodynamic forces and positions, but for simplicity it was assumed that the frictional force was simply opposing the bulk shearing motion, corresponding to the slipping contact model of Wilson & Davis (2000). Thus the frictional force is given by

$$(\boldsymbol{I}-\boldsymbol{nn})\cdot\boldsymbol{F}^{p}_{fr}=-\nu|\boldsymbol{F}^{p}|\frac{(\boldsymbol{I}-\boldsymbol{nn})\cdot\boldsymbol{E}^{\infty}\cdot\boldsymbol{n}}{|(\boldsymbol{I}-\boldsymbol{nn})\cdot\boldsymbol{E}^{\infty}\cdot\boldsymbol{n}|}, \tag{3.13}$$

where $\boldsymbol{n}$ is center to center unit vector, $\boldsymbol{F}^{p}_{fr}$ is the additional frictional force, $\boldsymbol{E}^{\infty}$ is the bulk rate of strain and $\boldsymbol{F}^{p}$ is the interparticle force of (3.2). We note here that the introduction of a tangential force also generates a torque on the particles that needs to be taken into account in the calculation.

Table 3.7 presents the values of the relative viscosity and normal stresses for different values of the friction coefficient for a system of $N = 512$, $\tau = 1000$, $\dot{\gamma}^{\star} = 1000$ at $\phi = 0.40$. It is apparent that an increase in the friction coefficient gives rise to an increased viscosity. However, the friction results in decreasing values of the first and increasing values of the second normal stress differences (in magnitude). This is an interesting result since the limited experimental studies show the second normal stress difference to be significantly larger than the first normal stress difference, which is the case for increasing friction. This suggests that normal stress differences may be a sensitive meas

It is also interesting that a small change in the suspension microstructure can have a very significant quantitative effect on the rheological behavior. In figure 3.19 the pair-distribution function for $r < 2.0005$ is plotted as a function of the angle θ for $\nu = 0.0$ and $\nu = 0.30$. The effect of the friction is a slight shift of the distribution, and, although small, the effect on the normal stress differences is significant. To further demonstrate this point, we also plot in figure 3.19 the normal stress differences for a system of 2-particles as a function of their relative positions (Nir and Acrivos 1973, Zarraga *et al.* 2001—Zarraga *et al.* (2001) expanded the touching spheres results of Nir & Acrivos (1973) to include particle roughness; for the minimum separations used here, the difference between the two cases is very small, and since only qualitative predictions are made, we only present

the results for touching spheres). The shift in the microstructure corresponds to a larger density of particles that would give rise to a positive N_1 and a smaller density of particle that would give rise to a negative N_1; as a result the values of the first normal stress difference becomes less negative with increasing friction. The opposite effect occurs for N_2; the peak of the pair-distribution function for both curves corresponds to a negative N_2 but the corresponding magnitude of N_2 for the peak for $\nu = 0.30$ is larger. Although it is difficult to make quantitative predictions based only on the microstructure and the 2-body case, it is nevertheless clear how important the details of the interparticle force are on predicting both the microstructure and the resulting rheological properties. The detailed form of the interparticle force is, of course, increasingly important at larger volume fractions, which possibly explains the discrepancies in the rheological properties observed by different researchers at high volume fractions.

3.3.7 Volume fractions above freezing

All the results presented so far correspond to volume fractions below 50% where the suspension remains disordered. Volume fractions above the freezing point were also studied and a number of additional issues were encountered. First of all, the time step necessary to avoid particle overlap becomes increasingly small as the volume fraction increases, even with a repulsive force, making these runs computationally more expensive. In addition, the iterative scheme used for the inversion of the near-field resistance matrix requires a larger number of iterations as the particles get closer together, and the preconditioning is not enough to resolve the ill-conditioning of the near-field lubrication matrix. Nevertheless simulations for volume fractions of 0.52, 0.55 and 0.60 were undertaken for the number of particles ranging from $N = 125 - 512$. The initial random configurations were generated following the technique suggested by Rintoul & Torquato (1996). Figure 3.20 shows the viscosity for all volume fractions up to $\phi = 0.60$, while figure 3.21 shows the corresponding microstructure from the projection of the pair-distribution function onto the yz plane. All runs are for $N = 512$ and $\tau = 1000$, $\dot{\gamma}^\star = 1000$. For volume fractions above 0.50 the system orders into strings. Surprisingly, at even higher volume fractions the system is again disordered. We must mention here that some of the runs were performed for

relatively small strains—on the order of 100—so it is also possible that the system has not yet reached a steady state. For the same strain, however, it was apparent that the denser system of $\phi = 0.60$ showed no signs of order compared to the fully ordered system at $\phi = 0.55$. Order is apparent both in the dramatic change of $g(z, y)$, where the light circles now correspond to particles, and in the drop in the viscosity.

This behavior is reminiscent of molecular dynamics simulations of hard spheres above the freezing point ($\phi \approx 0.494$) and below the glass transition ($\phi \approx 0.58$), where it is observed that in this metastable regime it is impossible to equilibrate the system for long times without some order. Above the glass transition, however, the glassy phase seems to have a much smaller tendency to order for much longer times. Unfortunately, a number of other parameters can also significantly affect the behavior of the system. Different system sizes were tried and, although both the strain necessary and the structure of the ordered phase were affected, all systems for $\phi = 0.52$ and $\phi = 0.55$ eventually ordered. It is also worth mentioning here that for some systems strains of up to 300 were necessary to see the beginning of order, while also for some systems the ordered phase switched after long strains to a different ordered structure, possibly an artifact of the system size and the length of the unit cell. Different values of the interparticle force were also tried but the presence of the ordered phase (at least for $\phi = 0.55$) was persistent. Increasing the value of the friction coefficient also delayed the on-set of order, but did not eliminate it.

The presence of a strong repulsive interparticle force is expected to induce order and it is therefore expected that in the absence of a force (or in the presence of an extremely small force) flow-induced order might not be seen. Unfortunately, it is extremely expensive computationally to decrease the value of the interparticle force since large clusters form and either the system can no longer be sheared, or particle overlaps are unavoidable. The minimum separations obtained for the force used, however, (as is apparent for the values of r_{peak} reported in the previous section) are expected to be sufficiently small since for most experimental situations particle roughness is on the order of $10^{-2} - 10^{-3}$ of the particle radius. Flow-induced order is commonly seen experimentally in electrostatically-stabilized dispersions (Ackerson 1990; Chen, Ackerson & Zukoski 1994) where the presence of a DLVO-type repulsive force between the particles is present. No experimental evidence of

ordering exists for systems of larger non-Brownian particles. However, most studies usually do not examine the particle microstructure when measuring the suspension rheology and therefore the presence of some order cannot be ruled out. In addition, all experimental studies have some polydispersity, and molecular dynamics studies show that relatively small amounts of polydispersity (less than 10% deviation in the particle sizes) can suppress and shift the equilibrium phase transition to higher volume fractions. The effects of polydispersity need to be addressed.

3.4 Conclusions

We have studied the behavior of a suspension of non-Brownian particles undergoing simple shear flow using Accelerated Stokesian Dynamics. Larger systems (typically of $N = 512$ particles) were used and the suspension rheological properties were determined with improved accuracy. The suspension relative viscosity, first and second normal stress differences and particle pressure were studied as a function of the volume fraction and were found to be in satisfactory agreement with experiment, in particular when taking into account the discrepancies between experimental data from different studies. The ratio of the normal to shear stress and the ratio of normal to excess shear stress (defined as the suspension viscosity minus the high-frequency dynamic viscosity) were also determined and it was found that the normal stresses are better correlated with the excess shear stress, pointing to the fact that the origin of both is the deformed microstructure.

The pair-distribution function determined from simulation clearly showed anisotropy in the microstructure, leading to non-Newtonian rheological behavior. The presence of a large particle density along the compressional axis and a low particle density along the extensional axis resulted in negative normal stress differences and a finite particle pressure; the degree of the anisotropy was further increased with increasing volume fraction. Brady & Morris (1997) theoretically calculated the pair-distribution function for a dilute system of Brownian-spheres at high Péclet number by studying the balance between hydrodynamic interactions and a hard-sphere-type pair-wise interparticle force in a boundary layer near particle-particle contact. Furthermore, they suggested that the main

contribution to the particle stress comes from near-touching spheres and as a result the stress should scale with the number of particles near-contact (proportional to the value of the pair-distribution function at contact) and the hydrodynamic stress of each pair (proportional to the high-frequency dynamic viscosity). Although the theory of Brady & Morris (1997) was restricted to the case of a hard-sphere-type interparticle force, the concept that the dominant contribution to the stress comes from near-touching particles can still be used to scale the particle stress for the case of a soft interparticle potential. The resulting scaled shear-stress was successfully reduced to a constant for all volume fractions; the success of this simple scaling in modeling our simulation results should also prove useful in interpreting experimental data.

Different values for the parameters of the repulsive interparticle force were used and the effect of particle-particle friction on the rheological properties was studied. The viscosity increased monotonically as the relative strength of the interparticle force decreased and particles were driven into closer contact where lubrication forces are strong. The behavior of the normal stresses, however, was more complicated: on the one hand, in the pure hydrodynamic limit normal stresses are expected to vanish because of the flow reversal symmetry of the microstructure, and at the same time in the absence of any interparticle force large clusters and consequently large lubrication stresses are generated. Although no quantitative scaling predictions were attempted for the normal stresses, it is nevertheless clear that the presence of a repulsive interparticle force can have a profound impact on the suspension microstructure and the resulting rheology. A broader experimental and theoretical study that investigates the exact nature and detailed functional form of the interparticle force for systems of non-Brownian particles would therefore be of extreme interest and would allow a much better quantitative prediction of the rheological properties of such systems.

No flow-induced ordering was observed for volume fractions below 0.50 and for the range of interparticle force used here. For volume fractions above 0.50 the system ordered into strings, while surprisingly at even higher volume fractions ($\phi = 0.60$) the system was again disordered. This behavior is reminiscent of molecular dynamics simulations of hard-spheres in the metastable regime (above the freezing point $\phi \approx 0.494$ and below the

glass transition $\phi \approx 0.58$) where it is impossible to equilibrate the system for long times without some order. Studying the effect of different interparticle forces and different particle sizes for such dense systems should provide valuable insight into the mechanism of sheared-induced ordering and is left for a future study.

Acknowledgement

This work was supported in part by grant NAG8-1661 from NASA and by a Dow graduate fellowship to AS. Access to an Alpha-based Beowulf cluster located at the California Institute of Technology was provided by the Center for Advanced Computing Research.

References

ACKERSON, B. J. 1990 Shear induced order and shear processing of model hard sphere suspensions. *J. Rheol.* **34**, 553.

BATCHELOR, G. K. 1970 The stress in a suspension of force-free particles. *J Fluid Mech.* **41**, 545.

BERGENHOLTZ, J., BRADY, J. F. & VICIC, M. 2001 The non-Newtonian rheology of dilute colloidal suspensions. *J. Fluid Mech.* (to appear).

BOSSIS, G. & BRADY, J. F. 1984 Dynamic simulation of sheared suspensions. I.General method. *J. Chem. Phys.* **80**, 5141.

BOSSIS, G. & BRADY, J. F. 1985 The rheology of concentrated suspensions of spheres in simple shear flow by numerical simulation. *J. Fluid Mech.* **155**, 105.

BRADY, J. F. & MORRIS, J. F. 1997 Microstructure of strongly sheared suspensions and its impact on rheology and diffusion. *J Fluid Mech.* **348**, 103.

CHEN, L. B., ACKERSON, B. J. & ZUKOSKI, C. F. 1994 Rheological consequences of microstructural transitions in colloidal crystals. *J. Rheol.* **38**, 193.

DARDEN, T., YORK, D. & PEDERSEN, L. 1993 Particle Mesh Ewald: An $n \log(n)$ method for Ewald sums in large systems. *J. Chem. Phys.*, **98**, 10089.

DAVIS, R. H. 1992 Effects of surface roughness on a sphere sedimenting through a dilute suspension of neutrally buoyant spheres. *Phys. Fluids* **4**, 2607.

DRATLER, D. I. & SCHOWALTER, W. R. 1996 Dynamic simulations of suspensions of non-Brownian hard spheres. *J. Fluid Mech.*, **325**, 53.

FOSS, D. R. & BRADY, J. F. 2000 Structure, diffusion and rheology of Brownian suspensions by Stokesian Dynamics simulation. *J. Fluid Mech.* **407**, 167.

GADALA-MARIA, F. 1979 The rheology of concentrated suspensions, PhD Thesis, Stanford University.

HOCKNEY, R. W. & EASTWOOD, J. W. 1982 Computer simulation using particles. Kluwer, New York.

JEFFREY, D. J., MORRIS, J. F. & BRADY, J. F. 1993 The pressure moments for two spheres in low-Reynolds-number flow. *Phys. Fluids A* **5**, 2317.

MARANZANO, B. J. & WAGNER, N. J. 2001 The effects of particle-size on reversible shear thickening of concentrated colloidal dispersions. *J. Chem. Phys.* **114**, 10514.

MELROSE, J. R. & BALL, R. C. 1995 The pathological behavior of sheared hard-spheres with hydrodynamic interactions. *Europhys. Lett.* **32**, 535.

NIR, A. & ACRIVOS, A. 1973 On the creeping motion of two arbitrary-sized touching spheres in a linear shear field. *J. Fluid Mech.* **59**, 209.

NOTT, P. R. & BRADY, J. F. 1994 Pressure driven flow of suspensions: Simulation and theory. *J. Fluid Mech.* **275**, 157.

PÄTZOLD, R. 1980 Die Abhängigkeit des Fließverhaltens konzertierter Kugelsuspensionsionen von der Strömungsform: Ein Vergleich der Viskosität in Scher- und Dehnströmungen. *Rheol. Acta* **19**, 322.

PHUNG, T. N., BRADY, J. F. & BOSSIS, G. 1996 Stokesian Dynamics simulations of Brownian suspensions. *J. Fluid Mech.* **313**, 181.

RINTOUL, M. D. & TORQUATO, S. 1996b Computer simulations of dense hard-sphere systems. *J. Chem. Phys.* **105**, 9258.

RUTGERS, I. R. 1962 Relative viscosity of suspensions of rigid spheres in Newtonian liquids. *Rheol. Acta* **2**, 202.

SHIKATA, T. & PEARSON, D. S. 1994 Viscoelastic behavior of concentrated spherical suspensions. *J. Rheol.* **38**, 601.

SIEROU, A. & BRADY, J. F. 2001 Accelerated Stokesian Dynamics Simulations. *J. Fluid Mech.* (to appear).

SINGH, A. 2000 Rheology of non-colloidal suspensions. PhD Thesis, Indian Institute of Science, Bangalore, India.

SINGH, A., & NOTT, P. R. 2000 Normal stresses and microstructure in bounded sheared suspension via Stokesian Dynamics simulations. *J. Fluid Mech.* **412**, 279.

WERFF VAN DER, J. C. & KRUIF DE, C. G. 1989 Hard-sphere colloidal dispersions: the scaling of rheological properties with particle size, volume fraction, and shear rate. *J. Rheol.* **33**, 421.

WILSON, H. J. & DAVIS, R. H. 2000 The viscosity of a dilute suspension of rough spheres. *J. Fluid Mech.* **421**, 339.

YURKOVETSKY, Y. 1998 I. Statistical mechanics of bubbly liquids. II. Behavior of sheared suspensions of non-Brownian particles. PhD Thesis, California Institute of Technology.

ZARRAGA, I. E., HILL, D. A. & LEIGHTON, D. T. 2000 The characterization of the total stress of concentrated suspensions of non-colloidal spheres in Newtonian fluids. *J. Rheol.* **44**, 185.

ZARRAGA, I. E. & LEIGHTON, D. T. 2001 Normal stress and diffusion in a dilute suspension of hard spheres undergoing simple shear. *Phys. Fluids* **13**, 565.

N	η_r	$-N_1$	$-N_2$	Π
125	6.2180 ± 0.058	0.7830 ± 0.038	0.8656 ± 0.037	1.8903 ± 0.053
256	6.2286 ± 0.072	0.8582 ± 0.074	0.8536 ± 0.150	1.9060 ± 0.050
512	6.2413 ± 0.036	0.8301 ± 0.047	0.8486 ± 0.025	1.9032 ± 0.036
1000	6.2152 ± 0.035	0.8396 ± 0.025	0.8342 ± 0.032	1.8966 ± 0.030

Table 3.1: The dependence of the rheological properties on the number of particles. Simulations are for $\phi = 0.40$, $\tau = 1000$, $\dot{\gamma}^\star = 1000$ and $N = 125 - 1000$. Data are shown for the relative viscosity, η_r, the first, N_1, and second, N_2, normal stress differences and the suspension pressure, Π.

τ	η_r	$-N_1$	$-N_2$	Π
0.10	1.326 ± 0.0015	0.0017 ± 0.0007	0.0019 ± 0.0005	0.0029 ± 0.0004
0.15	1.576 ± 0.0029	0.0083 ± 0.0015	0.0082 ± 0.0012	0.0127 ± 0.0011
0.20	1.917 ± 0.0055	0.025 ± 0.0031	0.0259 ± 0.0029	0.0412 ± 0.0022
0.25	2.408 ± 0.0085	0.063 ± 0.0052	0.068 ± 0.0045	0.117 ± 0.0052
0.30	3.144 ± 0.0120	0.160 ± 0.0072	0.178 ± 0.0057	0.313 ± 0.0454
0.35	4.311 ± 0.0159	0.406 ± 0.0154	0.404 ± 0.0133	0.793 ± 0.0184
0.40	6.24 ± 0.036	0.83 ± 0.047	0.85 ± 0.025	1.90 ± 0.036
0.45	9.40 ± 0.093	1.62 ± 0.109	1.62 ± 0.043	4.32 ± 0.119
0.50	15.07 ± 0.183	2.76 ± 0.152	2.75 ± 0.146	10.15 ± 0.183

Table 3.2: The dependence of the rheological properties on the volume fraction. Simulations are for $N = 512$, $\tau = 1000$ and $\dot{\gamma}^\star = 1000$. The total relative viscosity, η_r, first, N_1, and second, N_2, normal stress differences, and particle pressure, Π, are presented.

τ	η_r^{xF}	$-N_1^{xF}$	$-N_2^{xF}$	Π^{xF}
0.10	0.0018 ± 0.0003	-0.0045 ± 0.0003	0.0041 ± 0.0004	0.0031 ± 0.0003
0.15	0.0087 ± 0.0007	-0.0157 ± 0.0008	0.0154 ± 0.0009	0.0131 ± 0.0006
0.20	0.0287 ± 0.0020	-0.0402 ± 0.0021	0.0409 ± 0.0031	0.0422 ± 0.0023
0.25	0.0834 ± 0.0037	-0.0865 ± 0.0051	0.0915 ± 0.0048	0.119 ± 0.004
0.30	0.226 ± 0.005	-0.150 ± 0.007	0.209 ± 0.006	0.317 ± 0.007
0.35	0.582 ± 0.027	-0.188 ± 0.023	0.430 ± 0.024	0.803 ± 0.037
0.40	1.328 ± 0.037	-0.117 ± 0.046	0.800 ± 0.056	1.910 ± 0.051
0.45	2.826 ± 0.078	0.208 ± 0.099	1.442 ± 0.155	4.336 ± 0.102
0.50	5.993 ± 0.187	0.872 ± 0.119	2.512 ± 0.113	10.114 ± 0.266

Table 3.3: The "force-contribution", $-\boldsymbol{xF}_p$, to the rheological properties as a function of volume fraction. Simulations are for $N = 512$, $\tau = 1000$ and $\dot{\gamma}^\star = 1000$. The $-\boldsymbol{xF}_p$ contribution to the viscosity, η_r^{xF}, first, N_1^{xF}, and second, N_2^{xF}, normal stress differences, and particle pressure, Π^{xF}, are presented.

ϕ	$r_{peak} - 2$	$g(r_{peak})$	$r^\star$
0.10	1.25×10^{-3}	22	2.026
0.15	7.5×10^{-4}	38	2.018
0.20	7.0×10^{-4}	55	2.011
0.25	6.0×10^{-4}	108	2.007
0.30	5.0×10^{-4}	190	2.004
0.35	3.5×10^{-4}	310	2.0026
0.40	2.8×10^{-4}	490	2.0019
0.45	1.7×10^{-4}	803	2.0012
0.50	1.1×10^{-4}	1220	2.0009

Table 3.4: The dependence of the location, r_{peak}, and value, $g(r_{peak})$, of the peak of the pair-distribution function on the volume fraction. The values of $r^\star$ (where the pair-distribution function drops to 10% of its peak value) are also given. Simulations are for $\tau = 1000$, $\dot{\gamma}^\star = 1000$ and $N = 512$.

τ	$\dot{\gamma}^\star$	$F_0\tau/\dot{\gamma}^\star$	η_r	Π
1000	10^4	0.1	6.75 ± 0.060	1.86 ± 0.041
1000	1000	1	6.24 ± 0.036	1.90 ± 0.036
1000	100	10	5.89 ± 0.044	1.93 ± 0.038
1000	10	100	5.66 ± 0.038	1.89 ± 0.044
1000	1	1000	5.55 ± 0.022	1.88 ± 0.047
10000	10^4	1	6.88 ± 0.046	1.87 ± 0.050
1000	1000	1	6.24 ± 0.036	1.90 ± 0.036
100	100	1	5.49 ± 0.037	1.96 ± 0.042

Table 3.5: The dependence of the rheological properties on the parameters of the inter-particle force. Simulations are for $\phi = 0.40$, $N = 512$, $\dot{\gamma}^\star = 1 - 10^4$ and $\tau = 1 - 10^4$. Data are for the relative viscosity, η_r, and the particle pressure, Π.

τ	$\dot{\gamma}^\star$	ϕ	η_r	Π
1000	1000	0.10	1.3265 ± 0.0015	2.99 ± 0.5510^{-3}
1000	100	0.10	1.3241 ± 0.0011	3.70 ± 0.3610^{-3}
1000	10	0.10	1.3236 ± 0.0008	4.50 ± 0.4710^{-3}
1000	1	0.10	1.3232 ± 0.0004	5.13 ± 0.4910^{-3}
1000	10^4	0.30	3.25 ± 0.015	0.256 ± 0.010
1000	1000	0.30	3.14 ± 0.012	0.313 ± 0.007
1000	100	0.30	3.07 ± 0.008	0.342 ± 0.009
1000	10	0.30	3.04 ± 0.010	0.380 ± 0.010
1000	1	0.30	3.02 ± 0.007	0.394 ± 0.008
100	1	0.30	2.86 ± 0.012	0.576 ± 0.012

Table 3.6: The dependence of the rheological properties on the parameters of the inter-particle force. Simulations are for $\phi = 0.10$ and $\phi = 0.30$, $N = 512$, $\tau = 1000$ and $\dot{\gamma}^\star = 1 - 10^4$. Data are for the relative viscosity, η_r and the particle pressure, Π.

N	ν	η_r	$-N_1$	$-N_2$	Π
512	$\nu = 0.0$	6.24 ± 0.036	0.83 ± 0.047	0.85 ± 0.025	1.90 ± 0.036
512	$\nu = 0.1$	6.37 ± 0.038	0.76 ± 0.040	0.97 ± 0.035	1.94 ± 0.039
512	$\nu = 0.2$	6.49 ± 0.041	0.70 ± 0.022	1.07 ± 0.030	2.01 ± 0.042
512	$\nu = 0.3$	6.66 ± 0.043	0.64 ± 0.042	1.19 ± 0.040	2.10 ± 0.037
512	$\nu = 0.5$	6.89 ± 0.042	0.50 ± 0.038	1.49 ± 0.046	2.24 ± 0.045

Table 3.7: The dependence of the rheological properties on the friction coefficient. Simulations are for $\phi = 0.40$, $N = 512$, $\dot{\gamma}^\star = 1000$, $\tau = 1000$, and $\nu = 0.0 - 0.50$. Data for the relative viscosity, η_r, the first, N_1, and second, N_2, normal stress differences and the particle pressure, Π, are shown.

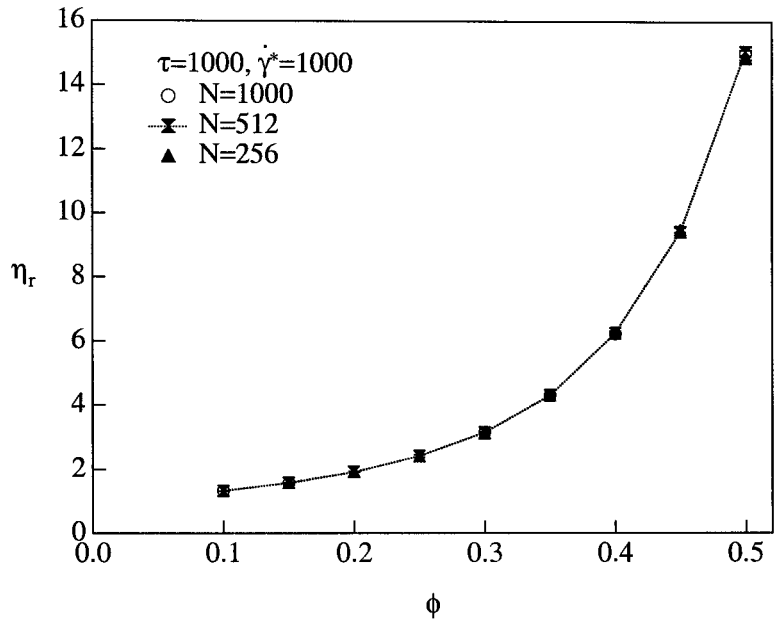

Figure 3.1: The dependence of the suspension viscosity on the number of particles N; $\tau = 1000$, $\dot{\gamma}^\star = 1000$ and $\phi = 0.10 - 0.50$.

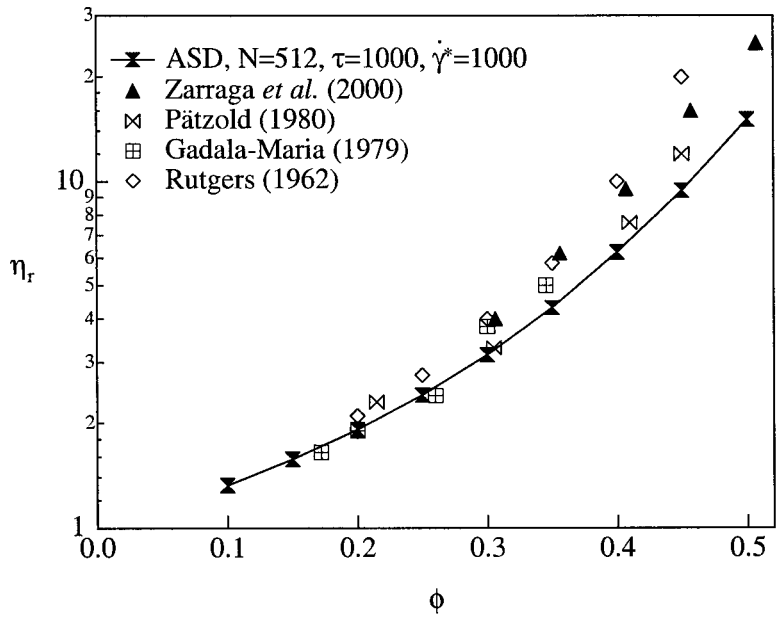

Figure 3.2: The dependence of the suspension relative viscosity, η_r, on the volume fraction. Accelerated Stokesian Dynamics (ASD) results are for $N = 512$, $\tau = 1000$, $\dot{\gamma}^\star = 1000$. A number of experimental results are also shown.

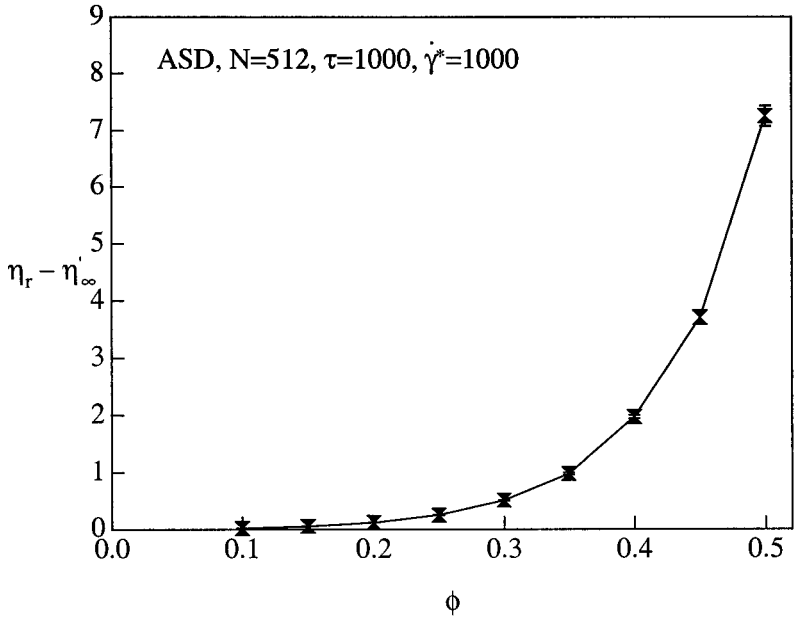

Figure 3.3: The dependence of the suspension excess viscosity, $\eta_r - \eta'_\infty$, on the volume fraction. Accelerated Stokesian Dynamics (ASD) results are for $N = 512$, $\tau = 1000$, $\dot{\gamma}^\star = 1000$. The high-frequency dynamic viscosities, η'_∞, are for the equilibrium hard-sphere microstructures and were determined by Sierou & Brady (2001).

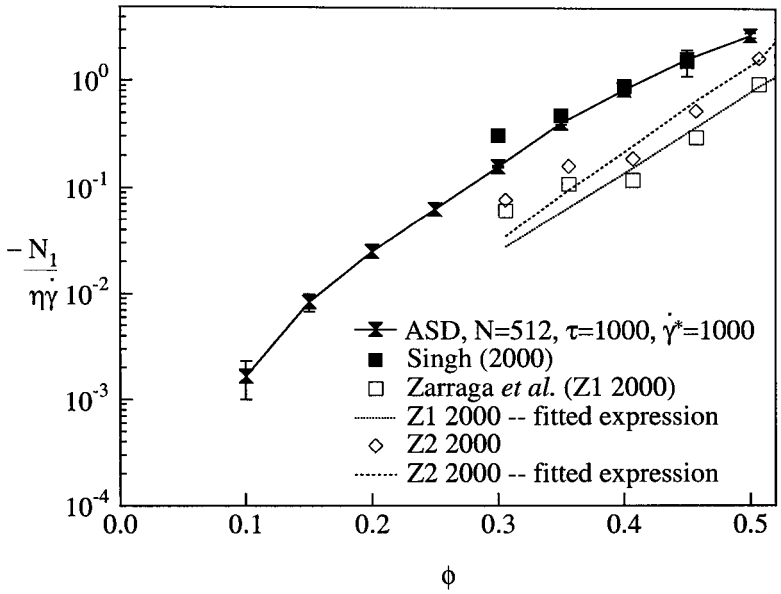

Figure 3.4: The dependence of the first normal stress difference, N_1, on the volume fraction. Accelerated Stokesian Dynamics (ASD) results are for $N = 512$, $\tau = 1000$, $\dot{\gamma}^\star = 1000$. Also shown are the experimental results of Singh (2000) and Zarraga *et al.* (2000).

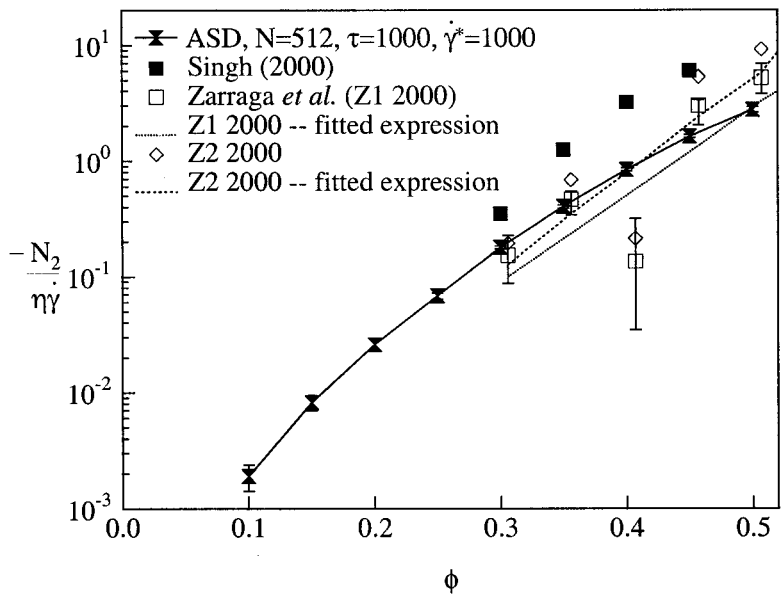

Figure 3.5: The dependence of the second normal stress difference, N_2, on the volume fraction. Accelerated Stokesian Dynamics (ASD) results are for $N = 512$, $\tau = 1000$, $\dot{\gamma}^\star = 1000$. Also shown are the experimental results of Singh (2000) and Zarraga *et al.* (2000).

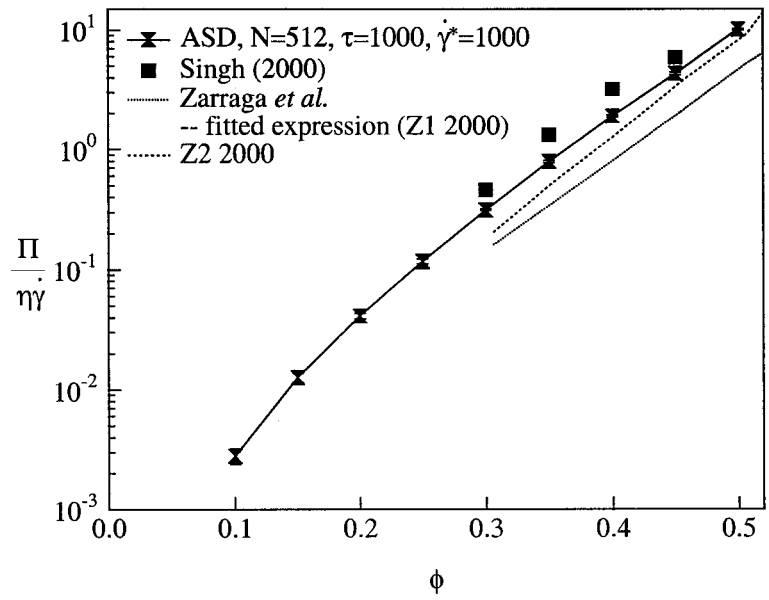

Figure 3.6: The dependence of the particle pressure, Π, on the volume fraction. Accelerated Stokesian Dynamics (ASD) results are for $N = 512$, $\tau = 1000$, $\dot{\gamma}^\star = 1000$. Also shown are the experimental results of Singh (2000) and Zarraga *et al.* (2000).

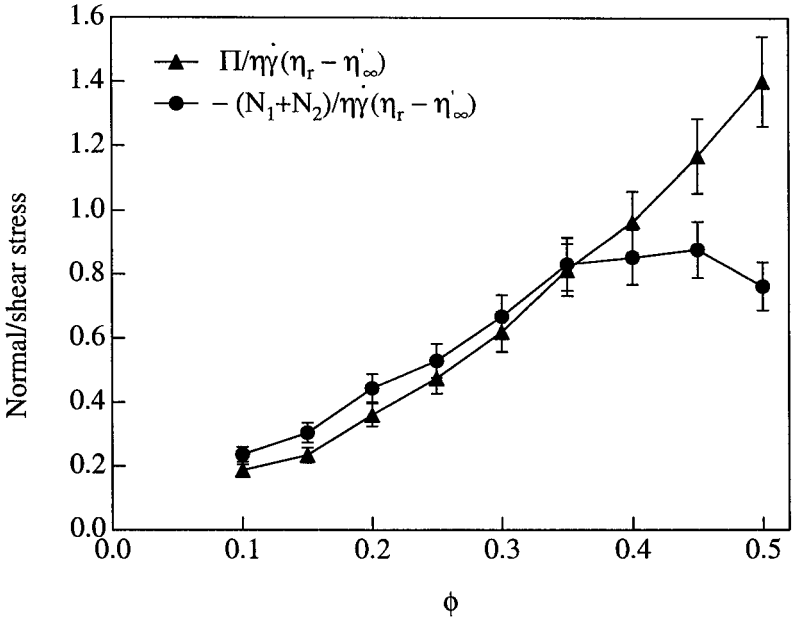

Figure 3.7: The suspension normal stress differences, N_1 and N_2, and the suspension pressure, Π, non-dimensionalized by the excess shear stress, $(\eta_r - \eta'_\infty)\eta\dot{\gamma}$, are shown as a function of the volume fraction. Accelerated Stokesian Dynamics (ASD) results are for $N = 512$, $\tau = 1000$, $\dot{\gamma}^\star = 1000$.

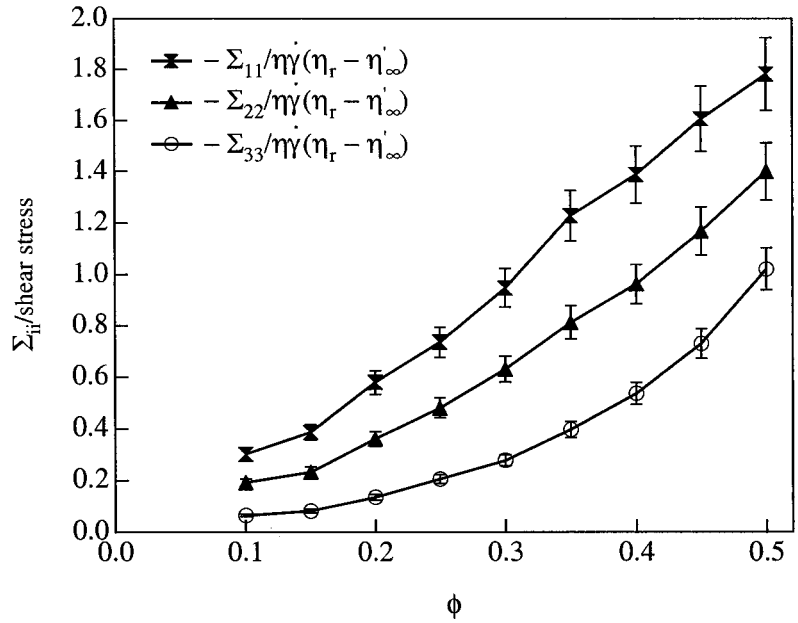

Figure 3.8: The ratios of the suspension normal stresses, Σ_{11}, Σ_{22} and Σ_{33}, to the excess shear stress, $(\eta_r - \eta'_\infty)\eta\dot{\gamma}$, are shown as a function of the volume fraction. Accelerated Stokesian Dynamics (ASD) results are for $N = 512$, $\tau = 1000$, $\dot{\gamma}^\star = 1000$.

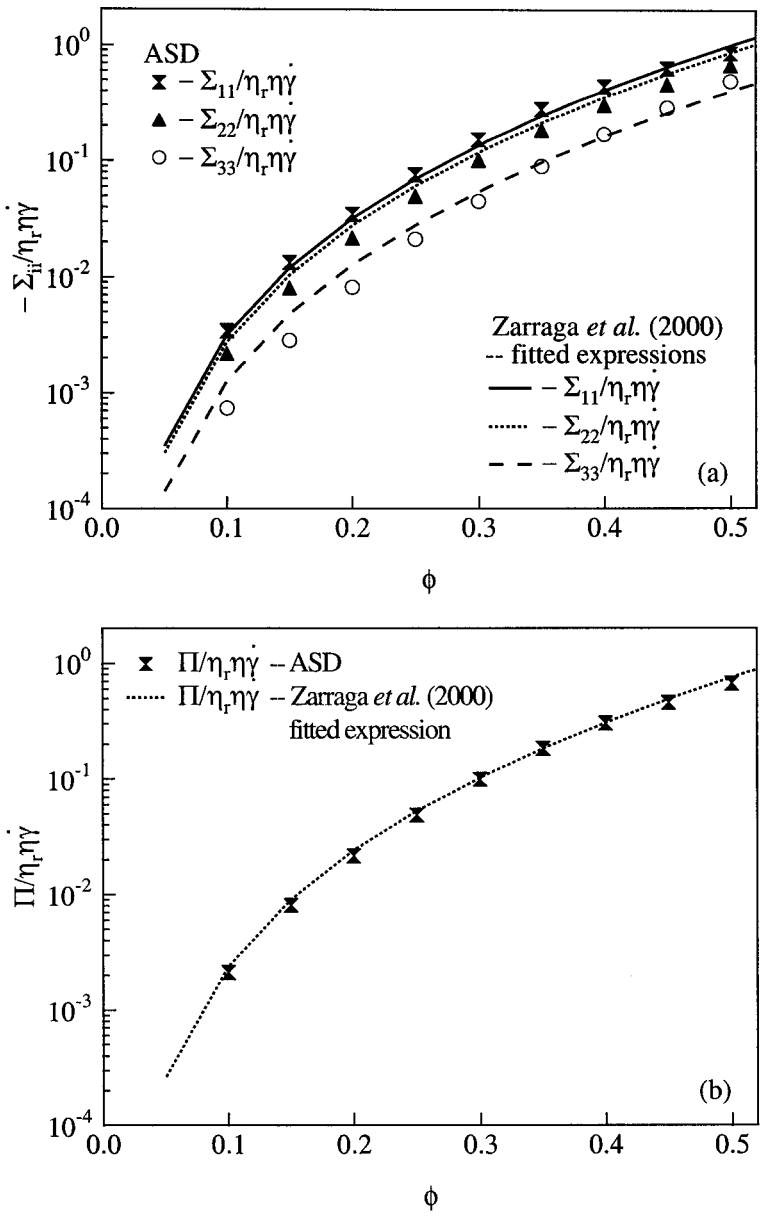

Figure 3.9: The ratios of the suspension normal stresses, Σ_{11}, Σ_{22} and Σ_{33} (a) and particle pressure Π (b) to the shear stress, η_r, are shown as a function of the volume fraction. Accelerated Stokesian Dynamics (ASD) results are for $N = 512$, $\tau = 1000$, $\dot{\gamma}^\star = 1000$. The fitted expressions of Zarraga *et al.* (2000) for the same quantities are also shown.

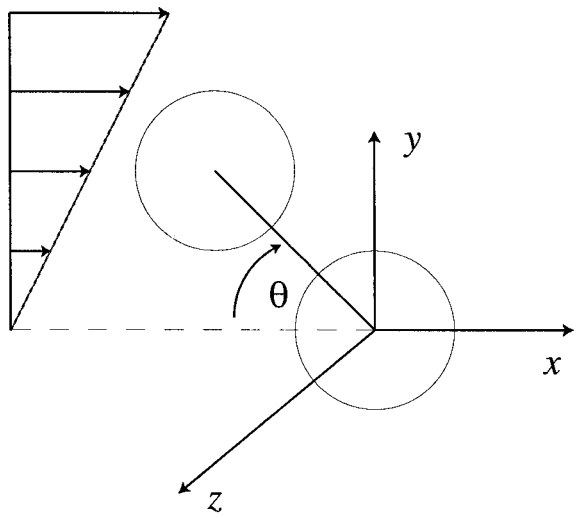

Figure 3.10: The definition of θ for two particles in a shear flow.

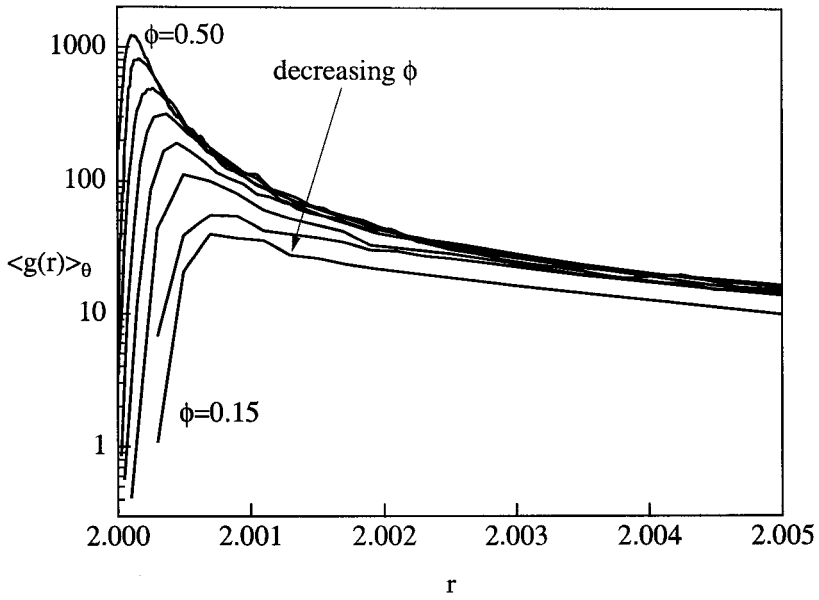

Figure 3.11: The dependence of the angularly averaged pair-distribution function, $\langle g(r)\rangle_\theta$, on the volume fraction. The pair-distribution function is averaged over all orientations and results for $2 < r < 2.005$ are shown. Simulation results are for $N = 512$, $\tau = 1000$, $\dot{\gamma}^\star = 1000$.

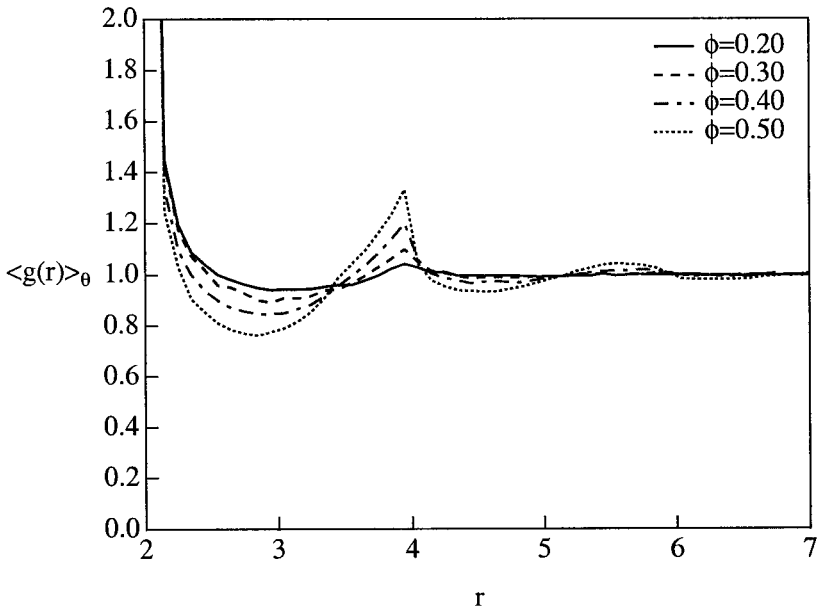

Figure 3.12: The dependence of the angularly averaged pair-distribution function, $\langle g(r)\rangle_\theta$, on the volume fraction. The pair-distribution function is averaged over all orientations and results for $2 < r < 7$ are shown. Simulation results are for $N = 512$, $\tau = 1000$, $\dot{\gamma}^\star = 1000$.

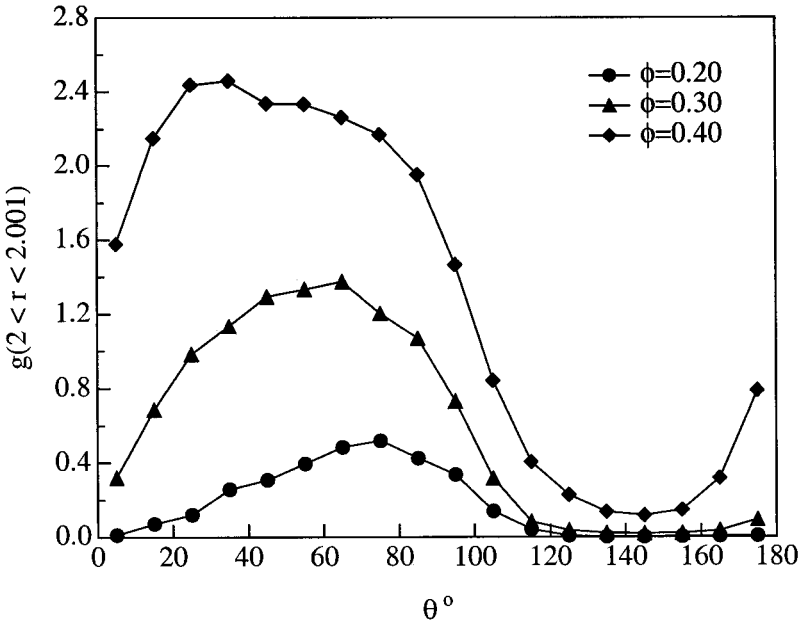

Figure 3.13: The angular dependence of the pair-distribution function, $g(r, \theta)$, for volume fractions of $\phi = 0.20$, 0.30 and 0.40. The angle θ is defined according to figure 3.10 and the pair-distribution function is calculated for $r < 2.001$. Simulation results are for $N = 512$, $\tau = 1000$, $\dot{\gamma}^\star = 1000$.

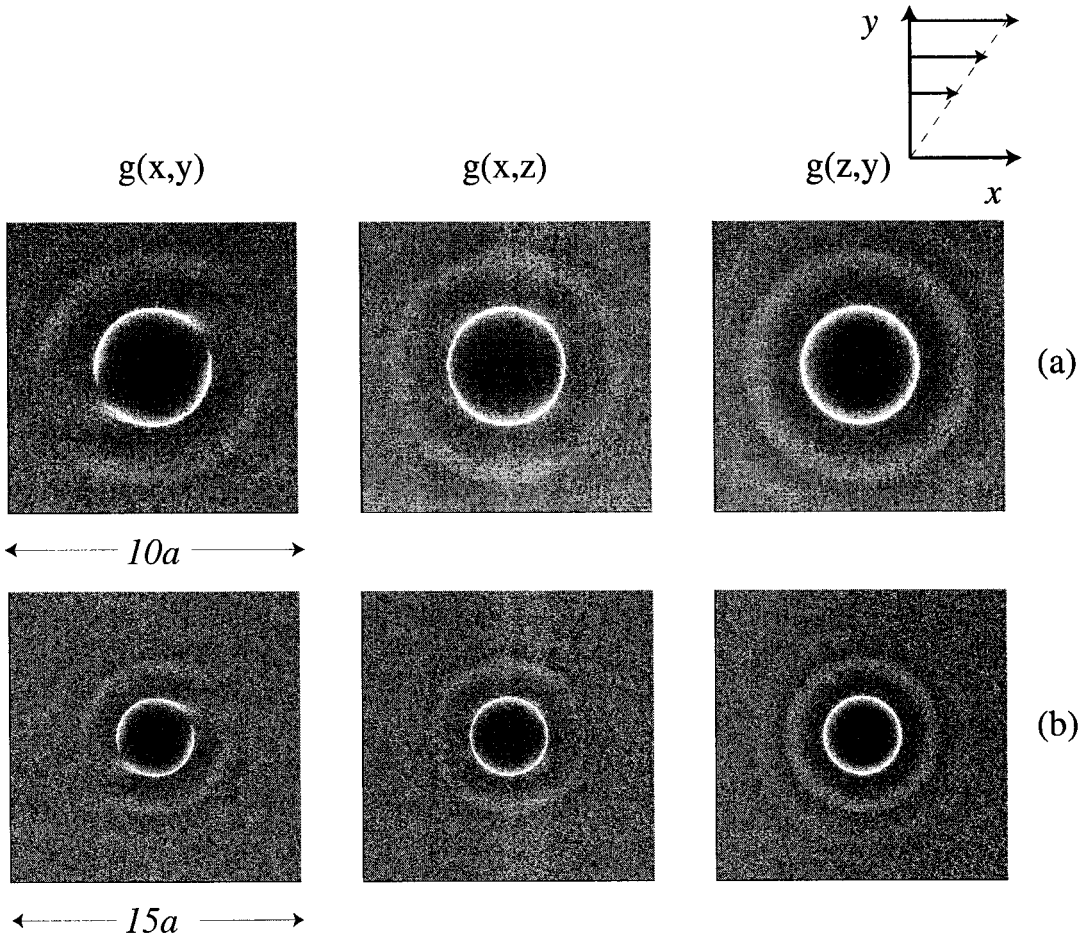

Figure 3.14: The projection of the pair-distribution function onto the xy, xz and zy planes for a system of $N = 512$, $\phi = 0.40$, $\tau = 1000$, $\dot{\gamma}^{\star} = 1000$. The projections are given for an area of $10a \times 10a$ (a) and $15a \times 15a$ (b).

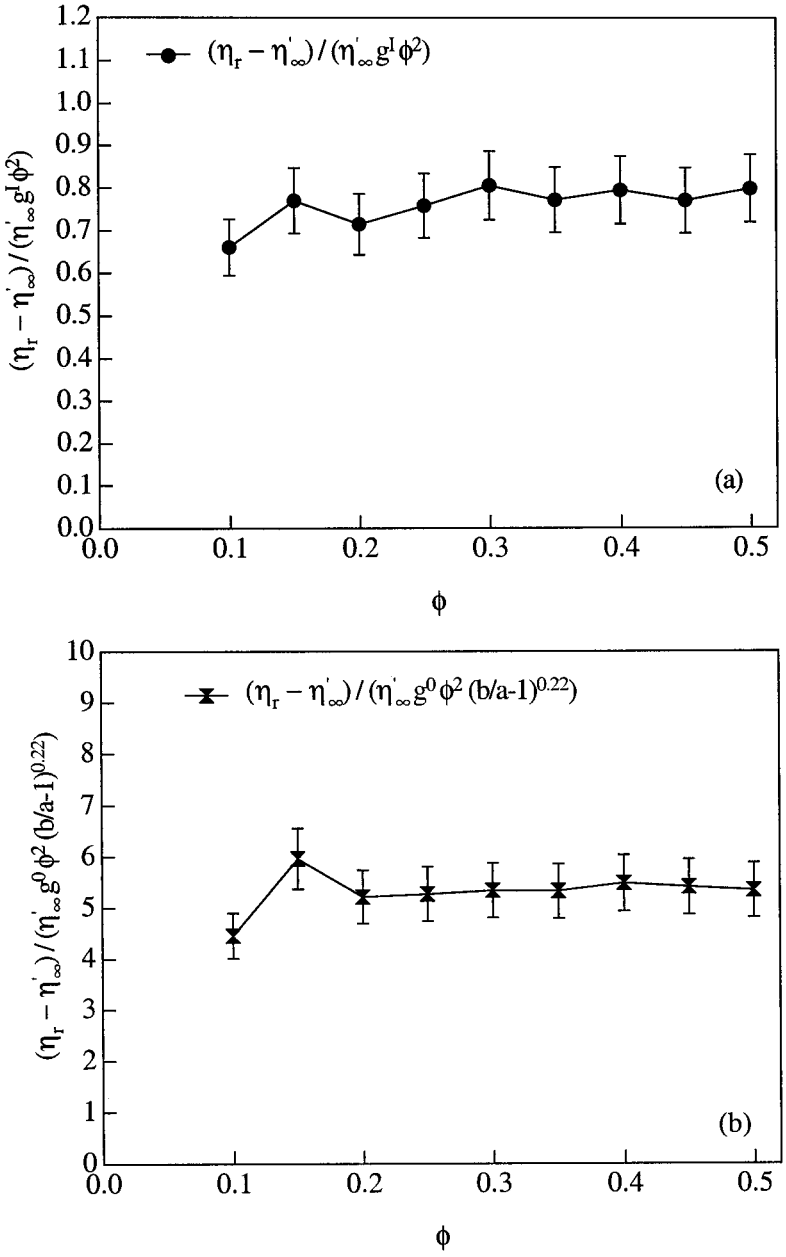

Figure 3.15: The excess viscosity, $\eta_r - \eta'_\infty$, non-dimensionalized with $\eta'_\infty \phi^2 g^I = \eta'_\infty \phi^2 \int_2^{r^\star} g(\boldsymbol{r}) d\boldsymbol{r}$ (a) and $\eta'_\infty g^0(\phi)\phi^2(b/a-1)^{0.22}$ (b), as a function of the volume fraction. Simulation results are for $N = 512$, $\tau = 1000$, $\dot{\gamma}^\star = 1000$.

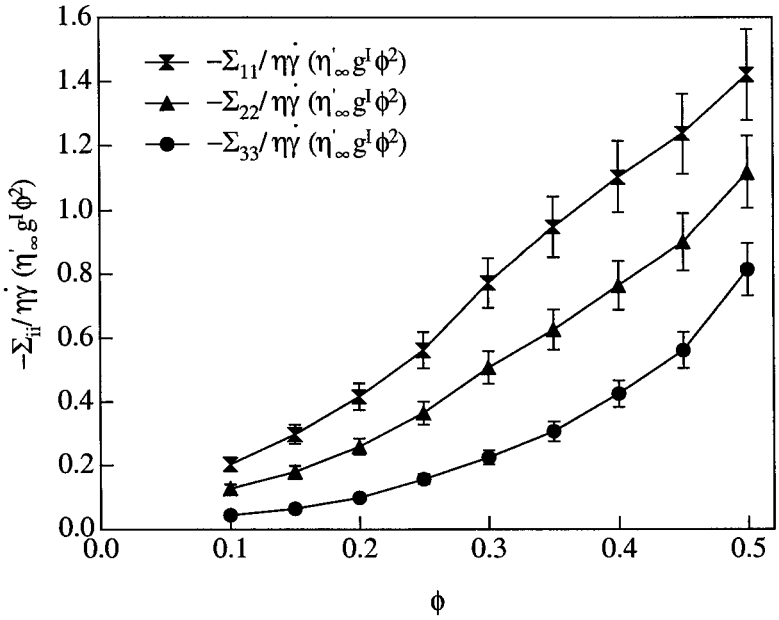

Figure 3.16: The normal stresses, Σ_{11}, Σ_{22}, and Σ_{33}, non-dimensionalized by $\eta\dot{\gamma}\eta'_\infty\phi^2\int_2^{r^\star} g(\boldsymbol{r})d\boldsymbol{r}$, are presented as a function of the volume fraction. Simulation results are for $N = 512$, $\tau = 1000$, $\dot{\gamma}^\star = 1000$.

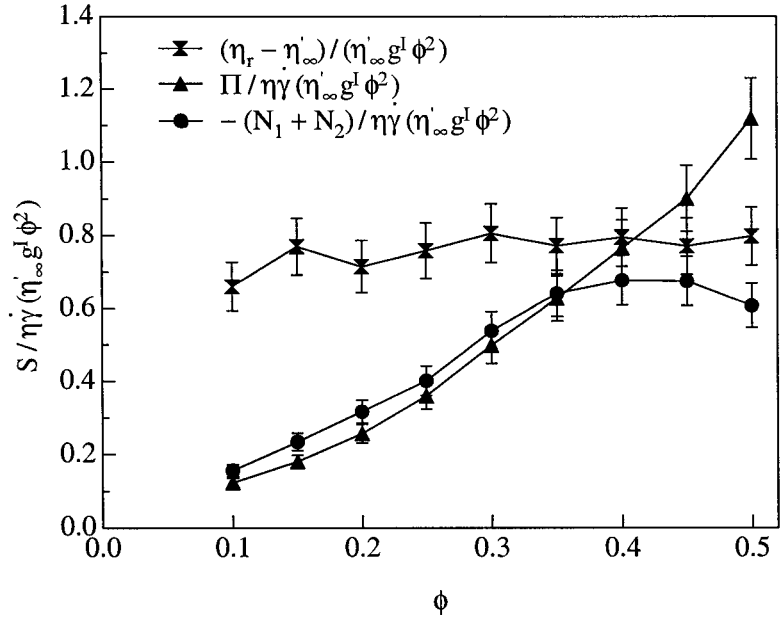

Figure 3.17: The first, N_1, and second, N_2, normal stress differences and the suspension pressure, Π, non-dimensionalized by $\eta'_\infty\phi^2\int_2^{r^\star} g(\boldsymbol{r})d\boldsymbol{r}$, as a function of the volume fraction. The excess viscosity is also shown for comparison. Simulation results are for $N = 512$, $\tau = 1000$, $\dot{\gamma}^\star = 1000$.

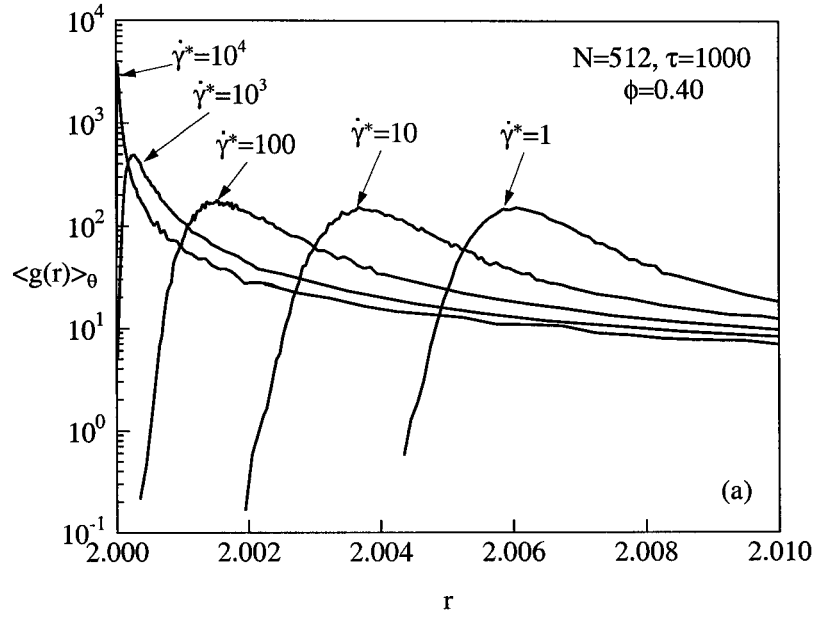

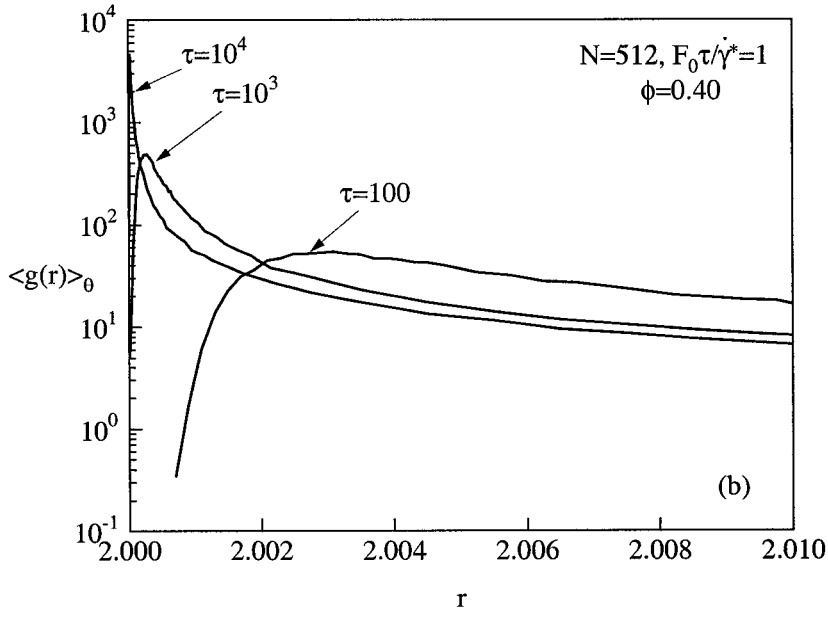

Figure 3.18: The angularly averaged pair-distribution function as a function of the inter-particle force parameters: (a) $\phi = 0.40$, $N = 512$, $\tau = 1000$ and $\dot{\gamma}^\star$ ranging from 1 to 10^4; (b) $\phi = 0.40$, $N = 512$, $F_0\tau/\dot{\gamma}^\star = 1$ and τ ranging from $10^2 - 10^4$.

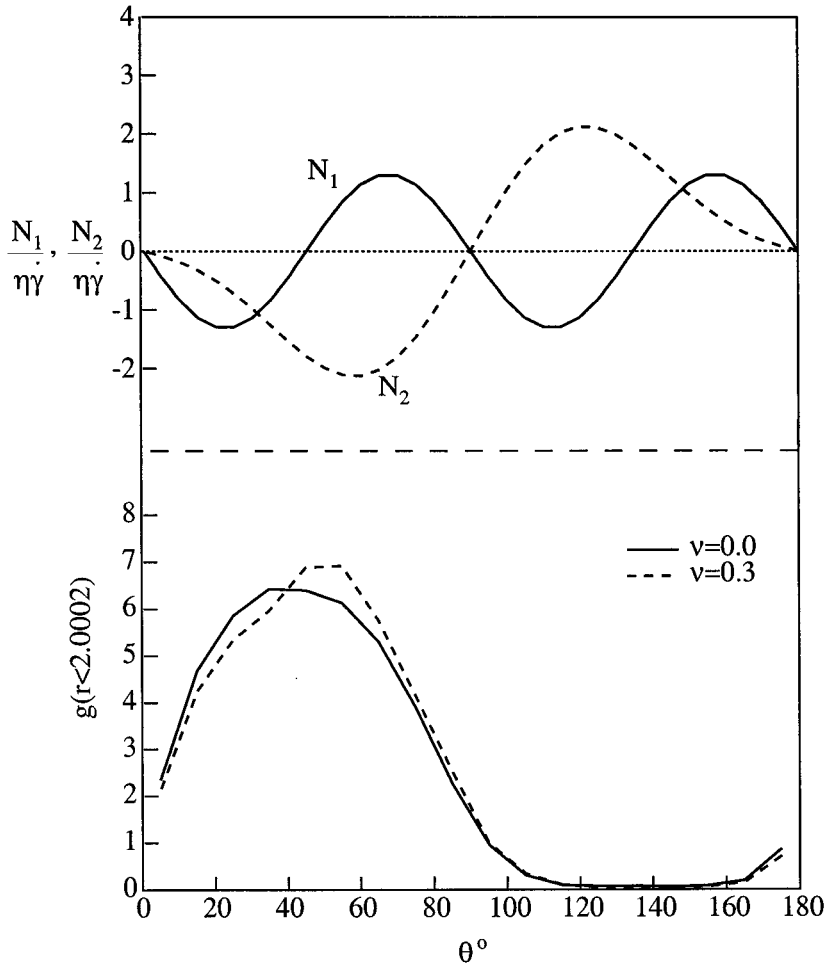

Figure 3.19: The angular dependence of the pair-distribution function for a system with $N = 512$, $\tau = 1000$, $\dot{\gamma}^\star = 1000$ and $\nu = 0.0$ and 0.30. The angular dependence of the normal stress differences for two particles in contact (Acrivos & Nir 1973) is also shown.

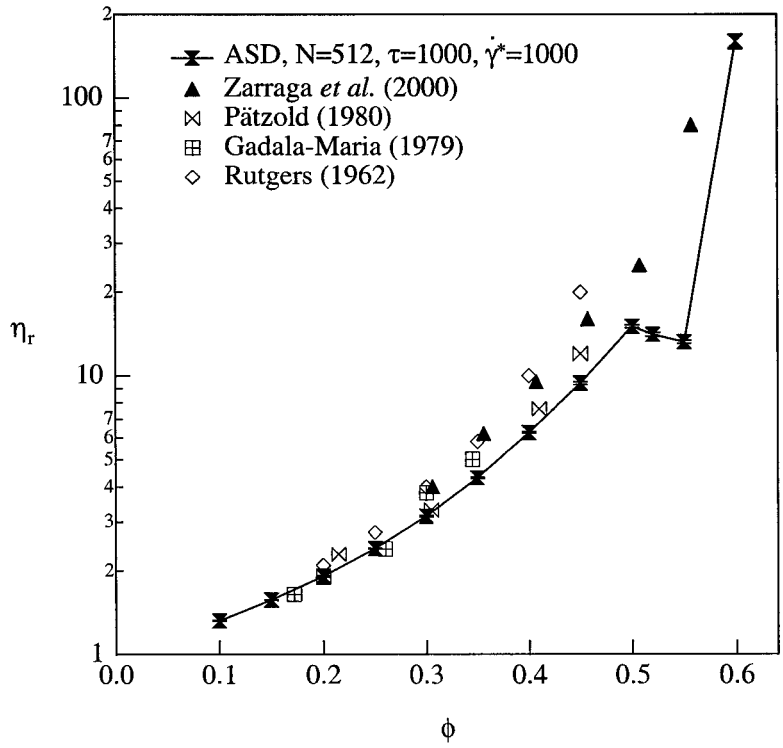

Figure 3.20: The dependence of the relative viscosity, η_r, on the volume fraction for volume fractions up to 0.60.

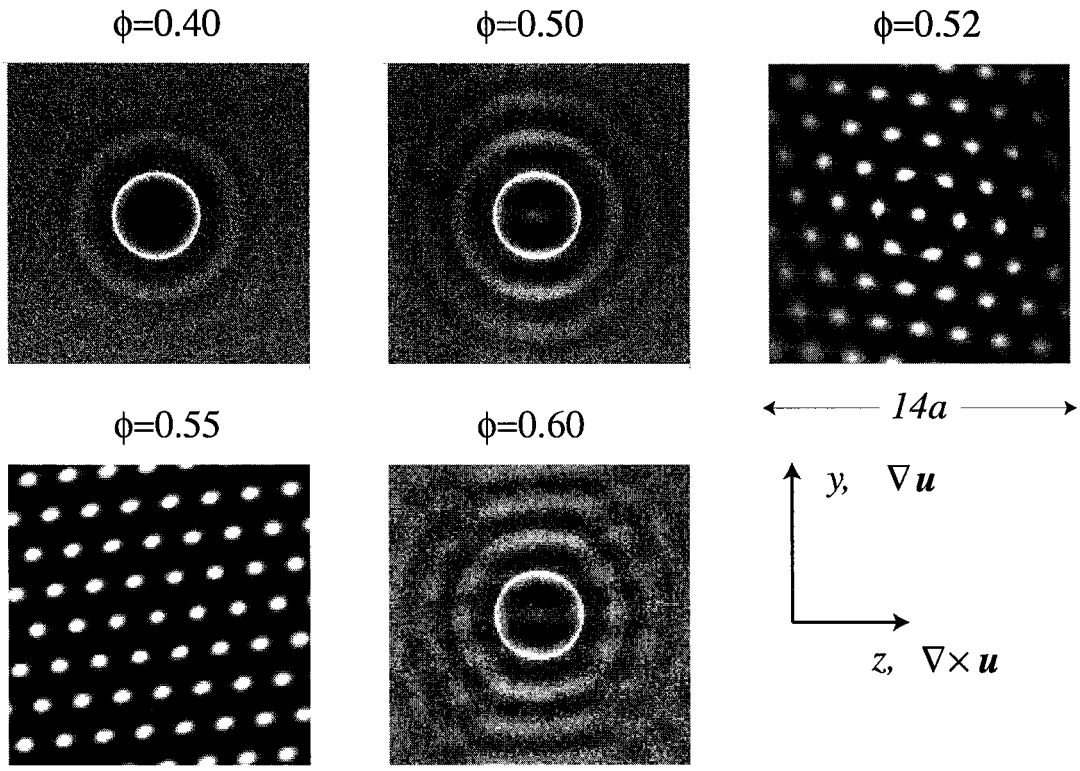

Figure 3.21: The projection of the pair-distribution function onto the zy plane, $g(z, y)$, for volume fractions up to 0.60 and for $N = 512$ and a total strain of 100. The velocity is in the x-direction and the velocity gradient in the y-direction. Shear-induced string ordering occurs for volume fractions above the equilibrium hard-sphere phase boundary at $\phi \approx 0.50$ and below the metastable glassy state at $\phi = 0.58$.

Chapter 4

Shear-Induced Self-Diffusion in Non-Colloidal Suspensions

4.1 Introduction

Shear-induced particle diffusion plays an important role in the behavior of concentrated non-Brownian suspensions and is responsible for a variety of interesting rheological phenomena in such systems. The first direct experimental study of shear-induced diffusion was reported by Eckstein, Bailey & Shapiro (1977); a variation of their experimental technique was later used by Leighton & Acrivos (1987) and Phan & Leighton (1999), followed more recently by the introduction of an alternative experimental method by Breedveld *et al.* (1998, 2001). Most of the aforementioned experiments are limited to the determination of the self-diffusion coefficients only in the velocity gradient and vorticity directions.

Theoretical work on self-diffusion is complicated by the fact that the two-body system in the presence of only hydrodynamic interactions either does not exhibit diffusive behavior (for the motion parallel to the velocity gradient and vorticity directions) or exhibits singular behavior (for the motion parallel to the fluid velocity). Acrivos *et al.* (1992) studied the diffusion coefficient parallel to the fluid velocity by introducing a mechanism (an additional pair of particles) that breaks the resulting singularity, while Wang, Mauri & Acrivos (1996) studied the diffusion perpendicular to the fluid velocity by examining three particle interactions. Da Cuncha & Hinch (1996) studied the two-particle problem in the presence of surface roughness—necessary to create diffusive motion—while Brady &

Morris (1997) introduced residual Brownian motion and a hard-sphere interparticle force to break the symmetry of the two-particle limit. Recently, Marchioro & Acrivos (2001) used Stokesian Dynamics simulations to study shear-induced diffusion in concentrated suspensions and addressed the still unanswered question of whether self-diffusion can be present in a purely deterministic system (e.g., in the absence of any roughness, residual Brownian motion, etc.).

The purpose of this work is to utilize a recently developed algorithm (Sierou & Brady 2001) for the calculation of hydrodynamic interactions among particles that allows the simulation of much larger systems than were previously possible. Although calculation of other rheological properties (e.g., viscosity) has proven to be accurate even with very small systems, the calculation of the self-diffusion coefficient requires significantly larger systems. Access to systems with numbers of particles on the order of 1000 allows accurate calculation of the diffusion coefficient and a study of its dependence on the number of particles and the volume fraction.

The complete diffusion tensor can now be determined and simulation results for both the off-diagonal components and the self-diffusion coefficient parallel to the fluid velocity are presented for the first time for a non-Brownian system. Because the presence of the external velocity field makes the determination of any diffusive displacements in the flow, or longitudinal, direction difficult, only very limited experimental results are available for these components (Breedveld 2000). Foss & Brady (1999) calculated the longitudinal self-diffusion coefficient for a system of Brownian particles at very high Péclet numbers by following the theoretical analysis of Morris & Brady (1996) which suggested that the affine shearing motion could be subtracted directly at each instant in time and the diffusivity could be calculated by taking into account only the non-affine displacements. Unfortunately, as we shall show, this is not correct and the affine displacement couples with the non-affine displacement to give an additional contribution to the longitudinal long-time self-diffusivity. Acrivos *et al.* (1992) theoretically studied the diffusion coefficient in the fluid velocity direction for very dilute suspensions and discovered that the two-particle limit is singular; a singularity that can be resolved with the presence of an additional pair of particles. Although for the volume fractions studied here (above 10%) this singularity

is no longer present, the calculation of the diffusion coefficient in the flow direction still proves to be a formidable task for dilute suspensions, a result of the strong influence of the periodicity on the particle displacements.

In the next section we outline the simulation method and briefly discuss the main details of the new $O(N \ln N)$ algorithm. In §4.3 we discuss how the diffusion coefficients are determined from both the mean-square displacements and the velocity autocorrelation function. In §4.4 results for the diffusivities in the velocity gradient and vorticity direction are presented and compared with experiment. Discrepancies between the simulation and some experimental results can be attributed to the fact that most of the experimental techniques attempt to determine the self-diffusivities for very small strains where the behavior is not yet diffusive; such a case is presented in detail in §4.4.2. In §4.5 the diffusivity in the fluid velocity direction is discussed along with the only non-zero off-diagonal component of the diffusivity tensor. Finally, we conclude in §4.6 with a brief summary and suggestions for future work.

4.2 The Simulation Method

A new implementation of the conventional Stokesian Dynamics (SD) method, called Accelerated Stokesian Dynamics (ASD), is used in our simulations. Since the methodology of ASD has been laid out in a previous work (Sierou & Brady 2001), only a brief account will be presented here. The method utilizes a Particle-Mesh-Ewald summation technique (Darden *et al.* 1993) with an iterative procedure to solve the equations governing the motion of N particles suspended in a viscous fluid at low particle Reynolds number in $O(N \ln N)$ operations. Following the conventional SD method, the hydrodynamic interactions are split into two parts: a far-field many-body part and a pair-wise near-field lubrication part. The near-field interactions can be readily calculated in order N operations—the particles are arranged in a chaining mesh (Hockney & Eastwood, 1986) so that each particle's nearest neighbors are easily identified. Since the near-field interactions are short-ranged, the number of neighboring particles (N_n) is small and the resulting computational cost scales likes $N_n N$. To further reduce both the computational cost and the memory requirements,

the resulting near-field resistance matrices are stored in a sparse form.

The far-field interactions are calculated in an iterative manner and therefore the far-field mobility matrix is never constructed. A resistance formulation is again followed: From assumed values for the hydrodynamic forces, the corresponding fluid velocities are calculated and then with application of Faxéns' laws the initial forces are corrected until convergence. The fluid velocity in the presence of N suspended particles (each particle is represented as a series of force multipoles at the particle's center) is calculated following a Particle-Mesh-Ewald approach, i.e., the resulting infinite sums over all the particles are split into a wave-space and a real-space sum with the introduction of a splitting parameter. The resulting wave-space sum contribution is evaluated on a grid as an inverse Fourier transform, while the real-space sum is calculated analytically. The computational cost of the Fourier sums scales as $N_m^3 \ln N_m$, where N_m is the number of mesh points in each direction (for a 3-D problem), and a careful choice of the splitting parameter allows $N_m \approx N^{1/3}$ with no loss in accuracy. The computational cost for the real-space sum scales as NN_l, where N_l is in general the number of all the particles influencing the velocity of a given particle. However, for sufficiently small values of the splitting parameter, it can be shown that the contribution of particles that are not near-neighbors is very small and can be ignored without significant error. The same chaining mesh procedure is followed for the calculation of the real-space sums as was used for the near-field interactions with an order N cost.

After both the far-field force and the near-field resistance matrices are calculated, the new particle velocities are calculated from the equation of motion:

$$0 = -\boldsymbol{R}_{FU,nf} \cdot (\boldsymbol{U}_p - \boldsymbol{u}^\infty) + \boldsymbol{R}_{FE,nf} : \boldsymbol{E}^\infty + \boldsymbol{F}_p + \boldsymbol{F}_{ff}, \tag{4.1}$$

where $\boldsymbol{U}_p - \boldsymbol{u}^\infty$ is the velocity disturbance at the center of the particle, $\boldsymbol{E}^\infty$ is the externally imposed rate of strain, $\boldsymbol{F}_{ff}$ the far-field contribution to the hydrodynamic force on a particle, $\boldsymbol{F}_p$ is the non-hydrodynamic interparticle force on a particle and $\boldsymbol{R}_{FE,nf}$, $\boldsymbol{R}_{FU,nf}$ are the near-field resistance matrices; note that since only near-field two-body interactions are included, $\boldsymbol{R}_{FU,nf}$ is sparse, symmetric and positive definite. An iterative conjugate

gradient method with an incomplete Cholesky preconditioner is used for the inversion of the sparse near-field resistance matrix. With iterative algorithms the computational time requirement can scale linearly with the matrix size since the sparse matrix multiplications required for an iterative method scale as N. The preconditioner is necessary, however, to keep the number of iterations small. Note that in (4.1) $\boldsymbol{U}_p$ includes the rotational velocities of the particle and $\boldsymbol{F}$ the torques, as there is hydrodynamic coupling between translation and rotation.

We consider the Stokes flow of a suspension of hard spheres in a suspending fluid of viscosity η undergoing simple shear with shear rate $\dot{\gamma}$. As has been demonstrated in the past (Melrose & Ball 1995, Dratler & Schowalter 1996), in the absence of Brownian motion the presence of a repulsive interparticle force is necessary to prevent the formation of infinite clusters that "jam" and result in excessive particle overlaps. Although the choice of this force is somewhat arbitrary, its introduction captures the behavior of a real physical system, since the presence of residual Brownian forces, or particle roughness, would also keep the particles from overlapping. This force was chosen to be of the form (Bossis & Brady 1984)

$$\boldsymbol{F}_{p(\alpha\beta)} = F_0 \frac{\tau \mathrm{e}^{-\tau\epsilon}}{1-\mathrm{e}^{-\tau\epsilon}} \boldsymbol{e}_{(\alpha\beta)}, \tag{4.2}$$

where $6\pi\eta a^2\dot{\gamma}\boldsymbol{F}_{p(\alpha\beta)}$ is the force exerted on sphere α by sphere β, F_0 is a dimensionless constant representing the magnitude of the interparticle force, τ is related to its range, $\epsilon = r-2$ is the spacing between the surfaces of the two spheres and $\boldsymbol{e}_{(\alpha\beta)}$ is the unit vector connecting the centers of the two spheres. In the results reported here the value of τ was set at 1000, while τF_0 was chosen to be unity. Although the exact magnitude and form of this interparticle force can play an important role on the values of some rheological properties (viscosity, normal stress differences), especially for high volume fractions, simulations using other parameters gave very similar results for the case of the self-diffusion tensor. (At very low volume fractions, however, where two particle interactions dominate, $\phi < 0.01$, the range and amplitude of the repulsive force can strongly influence the self-diffusivities.) All lengths are non-dimensionalized by the particle radius a, all times by the characteristic

time $\dot{\gamma}^{-1}$, and the hydrodynamic resistance tensors $\boldsymbol{R}_{FU}$ and $\boldsymbol{R}_{FE}$ by $6\pi\eta a$ and $6\pi\eta a^2$, respectively. The time step used ranged from $\Delta t = 5 \times 10^{-3} - 5 \times 10^{-4}$ depending on the volume fraction (higher volume fractions required smaller time steps). A fourth order Adams-Basforth integration scheme was used to update the particle positions.

4.3 The Self-Diffusivities in the Velocity Gradient (D_{yy}) and Vorticity (D_{zz}) Directions

4.3.1 Theoretical analysis

We now describe in some detail the calculation of the self-diffusion coefficients in the velocity gradient and vorticity directions. (The process of calculating the diffusivity in the fluid velocity direction is subject to further limitations and will be described in the following section.) Dimensional arguments show that the self-diffusivities scale as $\dot{\gamma}a^2$, as these are the only length and time scales in the system (in the absence of interparticle forces). All diffusivities reported are therefore normalized by $\dot{\gamma}a^2$.

Let x, y and z denote the directions of the flow, the velocity gradient and the vorticity, respectively. Then for a suspension undergoing simple shear flow in the x-direction, the mean-square displacements will grow with time according to

$$\langle y(t)y(t)\rangle \sim 2D_{yy}t,$$
$$\langle z(t)z(t)\rangle \sim 2D_{zz}t,$$

at long times after diffusive motion has been established. Here, and hereafter, the angle brackets denote an average over all particles in the system, while D_{yy} and D_{zz} denote the self-diffusivities in the velocity gradient and vorticity directions, respectively. The self-diffusivities are defined as the time rate of change of one half the mean-square dis-

placement:

$$D_{yy} \equiv \lim_{t\to\infty} \frac{1}{2}\frac{d}{dt}\langle y(t)y(t)\rangle\,, \tag{4.3a}$$

$$D_{zz} \equiv \lim_{t\to\infty} \frac{1}{2}\frac{d}{dt}\langle z(t)z(t)\rangle\,. \tag{4.3b}$$

We note here that the main difference between the calculation of the sheared-induced diffusivity and the diffusivity of a Brownian particle is that (4.3) is only valid for long enough times, i.e., times after the diffusive behavior has been established. Since the motion of a non-Brownian particle is purely deterministic, the displacement of a given particle only depends on the external velocity field and its interactions with all other particles in the system. In order for the displacements to change significantly in time and become random, the particle configuration also needs to change. As a result, the initial motion of a non-Brownian particle is not diffusive and relatively long times need to be sampled to determine the diffusion coefficients.

From (4.3) the calculation of the self-diffusivities is straightforward and a number of alternative but equivalent approaches can be used. First, the mean-square displacement curve can be constructed according to (4.3) for a long simulation run. Now that a large number of particles is used, this approach results in a mean-square displacement curve that is linear in time at long times. In addition, as will be demonstrated in the following section, the evaluation of the slope of the mean-square displacement curve can now be done with sufficient accuracy since the system is large.

Second, this same long simulation run can be split into shorter independent runs, and the resulting mean-square displacement curves from each shorter run averaged. This approach has been followed successfully in the past, both in numerical (Foss & Brady 1999; Marchioro & Acrivos 2001) and experimental studies (Breedveld *et al.* 1998, 2001), and has been shown (Foss & Brady 1999; Marchioro & Acrivos 2001) to give results with reduced noise that still capture the diffusive behavior correctly, provided that the shorter runs are long enough for the mean-square displacement to enter the linear regime. Although an infinite time limit is indicated in (4.3), the particle does not necessarily need to travel a very long distance to reach this long-time asymptote; it simply needs to

encounter enough particle-particle interactions to sample the dynamic microstructure and "forget" its initial configuration and velocity. The determination of the minimum time needed for the diffusive behavior to be established is non trivial, however, and, as we shall demonstrate, can be the cause of significant errors.

Finally, the diffusivities can be evaluated from the integral of the velocity autocorrelation function using the well known expression:

$$D_{yy} = \int_0^\infty \lim_{t\to\infty} \langle u_y(\tau + t) u_y(t) \rangle \, d\tau, \tag{4.4}$$

where u_y is replaced by u_z for D_{zz}. The time it takes for the velocity autocorrelation to decay to zero corresponds to the time it takes the mean-square displacement curve to reach the linear regime; for the diffusivities to be evaluated correctly, the integral in (4.4) has to be computed for at least that minimum time.

All three approaches should give identical results since they correspond to the same quantity. In the following section we show the results for all three approaches for a typical case for the calculation of D_{yy} and D_{zz}. (One could also, of course, improve the statistics by averaging over a number of realizations or initial conditions; however, with the large number of particles used and the long simulation times, our results appear to be sufficiently accurate.)

4.3.2 Test case: The long-time self-diffusivity for $\phi = 0.20$, $N = 1000$

We present here in detail the calculation of the long-time self-diffusivity in the velocity gradient, D_{yy}, and vorticity, D_{zz}, directions for the case of a system of $N = 1000$ particles at a volume fraction of $\phi = 0.20$. The interparticle force described by (4.2) is also present.

Figures 4.1(a) and (b) show the mean-square displacement curves, $\langle yy \rangle$ and $\langle zz \rangle$, for strains up to 800 in a linear and a log-log plot, respectively. It is clear from the logarithmic plot that at very short times the mean-square displacement shows a quadratic temporal behavior, while after a strain of about 20 the linear regime sets in and continues until the end of the run. The quadratic behavior corresponds to the regime where the particle velocities are deterministic and still strongly correlated—the diffusive behavior has not

yet been established. It should be noted that, although after a strain of about one the quadratic scaling no longer holds, a transitional region exists up to strains of at least 10 before a clear linear behavior is evident. The slope of the resulting curve for $t > 20$ can be readily evaluated and the resulting diffusivity is given in figure 4.1.

The same trend is evident in figures 4.2(a) and (b) but over a shorter time interval. The long run of the previous case was split into smaller runs of $30-100$ strains, the results averaged and presented again in linear and logarithmic plots. Because of the increased statistical data, the slope of the mean-square displacement curve can be evaluated with greater accuracy than before. The final result for the diffusivity is very close to the value reported in figure 4.1 and within the statistical accuracy of the data. Although the linear behavior of the curves in the short and long runs is identical, the initial transient behavior, as is apparent from the logarithmic plots, can be quantitatively different (qualitatively, a t^2 behavior is apparent for both cases). This is due to the fact that for the shorter runs the sequence of independent configurations are all sampled after the system has reached its steady state configuration, while the beginning of the overall mean-square displacement curve in figure 4.1 corresponds to an initially random configuration. As a result, a different quadratic behavior is seen—the system that starts from a random Monte Carlo configuration has a slower initial quadratic increase of the mean-square displacements. This effect is of no significance for the long-time behavior and the self-diffusivities.

Finally, the non-dimensional velocity autocorrelation function for strains up to 20 is shown in figure 4.3. To further reduce the noise of the calculation, the values of $u(t+\tau)u(t)$ are averaged over all possible time intervals with $\tau = \Delta t$. Again it is clear that although the value of the autocorrelation function drops significantly over the first couple of strains, a relatively long tail persists for strains up to 10 (in agreement with figure 4.2). The diffusivity can be evaluated as the area under the curve of figure 4.3, and it is clear that in order to obtain the correct diffusion coefficients the long-tail must be taken into account, requiring strains of at least 10. It is also worth noting here that, contrary to what has been reported elsewhere, no apparent periodic fluctuations are present in the velocity autocorrelation function (Marchioro & Acrivos 2001). Even if the periodicity of the problem does introduce fluctuations, the velocity autocorrelation function is already

averaged over all possible shapes of the unit cell and therefore the final curve has no periodic dependence. The values for the diffusivities are also given in figure 4.3 and are in excellent agreement with the values calculated from the mean-square displacement curves.

The three approaches to determine the self-diffusivity gave consistent results for all volume fractions studied. The time necessary for the diffusive behavior to be reached is a strong function of the volume fraction, and, as has been reported in the past, increases with decreasing volume fraction. For very dilute suspensions the particle interactions are limited and a larger strain is necessary until the particles have sampled a sufficiently large number of independent collisions and the linear regime is reached. To qualitatively demonstrate this phenomenon, we show in figure 4.4 the velocity autocorrelation function in the y-direction for volume fractions $\phi = 0.10$, 0.30 and 0.50. The increase in the correlation time is apparent and larger times need to be sampled for the more dilute systems. It can also be seen that for the smaller volume fractions the velocity autocorrelation function becomes negative and maintains negative values for longer times.

Before we proceed to the presentation of the majority of our simulation results it is worth mentioning briefly how we define their statistical properties. The values of the diffusivities obtained from the three aforementioned approaches are in all cases in excellent agreement, so their simple average is used as the reported value of the diffusivity. The calculation of the standard deviation, however, needs to be discussed in more detail. The error associated with the calculation of any element of the self-diffusion tensor can result from one (or more) of the following sources: First, errors derived from the solution of the equations of motion—the assumptions used in the development of ASD combined with the 'standard' numerical errors present in any numerical calculation (finite time steps, machine accuracy, etc.)—always lead to a numerical error in the calculation of any property. The statistical nature of the particle displacements and the fact that the magnitude of the numerical error is usually small makes the numerical inaccuracies of very little importance and therefore we shall not consider them further. Second, there is the uncertainty associated with the number of independent mean-square displacement curves available. The mean-square displacement curves shown in figures 4.1 and 4.2 are already averaged over all particles, and for the case of figure 4.2 all the shorter, independent runs

are also averaged. In order to obtain the correct values for the self-diffusion tensor, it must be assured that a sufficient number of mean-square displacement curves have been sampled, or in other words, that all possible particle interactions have been sampled. This can be assured by examining systems with large N, or a large number of configurations of systems with smaller N, as has been suggested in the past. The calculation of the error then corresponds to grouping particles/configurations together and calculating the standard deviation of the resulting measurements. This is the error routinely reported in our results and is calculated either as a temporal average over smaller segments of the mean-square displacement curve for the long runs of figure 4.1, or as an average over different groups of configurations for the case of figure 4.2. (Note that figure 4.2 presents the average mean-square displacement curve over all possible configurations and particles for a given run; only the mean can be calculated from this curve.) Finally, the calculation of the slope of the mean-square displacement curve, or the numerical integration of the velocity autocorrelation function, introduces a numerical error. In addition to any uncertainty associated with the numerical calculation, the most important issue is what is the correct time regime (or strain) over which to determine the diffusivities. Very long tails in the velocity autocorrelation function can be erroneously discarded and visual observation of when the process becomes linear can be misleading and result in large errors. Although we believe that this source of error can be potentially extremely important, we tried to make a conservative estimate in our calculation of the minimum strain needed for diffusive behavior to set in, so we are confident that the error from this source is also insignificant. Therefore, for the remainder of this chapter the error bars denoted correspond to uncertainties associated with simply the volume of the statistical data, uncertainties that for most cases are less that 10%. Finally, the last source of uncertainty, system size and the effect of the periodic unit cell, will be discussed in more detail below.

4.4 Results: The Calculation of D_{yy} and D_{zz}

4.4.1 The dependence on the number of particles N

The introduction of a new, faster methodology allows the calculation of the self-diffusion coefficients for numbers of particles on the order of 10^3, and we can therefore present a more reliable analysis of the dependence of the diffusivities on the number of particles, N. Figure 4.5 and table 4.1 show the dependence of D_{yy} on N, for the case of $\phi = 0.35$ (the interparticle force, defined in (4.2) with the parameters mentioned, is also always present unless otherwise noted). There is a rather sharp increase in the diffusivity for small values of N ($N < 100$), followed by a leveling off. The same trend is apparent for all elements of the self-diffusion tensor. No theoretical expression is available for the N dependence of the long-time self-diffusivity, and so in figure 4.5 we simply present a N^{-1} best fit that seems to describe the data satisfactorily. Plotting the individual mean-square displacements (not shown) for different numbers of particles also verifies that for $N > 100$ all curves are statistically indistinguishable. A possible explanation of this behavior may lie in the fact that after the size of the cell is sufficiently large (or N is sufficiently large), all of the important particle interactions are included and therefore the number of particles plays no role (other than increasing the statistical accuracy, i.e., giving curves that appear smoother). When the number of particles is very small, the corresponding size of the square unit cell is also small (for $N = 27$, $L = 6.86a$ for $\phi = 0.35$). This means that particle interactions for separations greater than L occur through periodic images, which may explain the smaller diffusivities observed for very small number of particles. (As discussed in §4.5.2, a similar, but much more apparent, effect of the size of the unit cell is present in the calculation of D_{xx} for low volume fractions.) For the remainder of this chapter all results will correspond to systems of $N = 1000$ particles and no further corrections to the infinite system limit will be attempted since, as is apparent in figure 4.5, such corrections would be very small and within the statistical accuracy of the calculations.

4.4.2 The dependence on the volume fraction

Figures 4.6 and 4.7 and table 4.2 show the dependence of D_{yy} and D_{zz} on the volume fraction ϕ. Previous experimental and simulation results are also presented. Although qualitatively most sets of experimental or simulation results are in agreement, quantitatively discrepancies are present that need to be explained and examined in more detail. As was mentioned in section 4.3, the notion that the long-time self-diffusivities can be calculated for strains that are not particularly long has been used, and most of the recent experimental and simulation results presented in figures 4.6 and 4.7 are calculated over a large number of configurations but for relatively small strains (Breedveld *et al.* 1998, 2001; Foss & Brady 1999). Unfortunately, as we discuss in detail, the strains used for these studies are too small and therefore do not correspond to the linear regime, as a result they overestimate the diffusivity.

Figure 4.8(a) is adapted from Breedveld *et al.* (2001) and shows the mean-square displacement curve, $\langle yy \rangle$, for $\phi = 0.20$ for strains up to 5. (We choose to examine the case of a relatively small volume fraction in detail because, as is apparent in figure (8) of Breedveld *et al.* (2001), the accuracy in their determination of the mean-square displacement curve seems to be greatly reduced when the volume fraction is increased due to limitations of the experimental technique; this is not observed in the numerical simulations.) The dashed curve represents the 'linear-fit' performed by Breedveld *et al.* (2001); the value of the diffusivity that they obtain is also given. The solid line corresponds to our mean-square displacement for the same volume fraction and for a system of $N = 1000$ particles. The agreement between the two curves is remarkable. Although this is the case for the mean-square displacement curves, the resulting diffusivities are not in good agreement and the value reported by Breedveld *et al.* (2001) is over twice as large as the value we calculate. The reason for this is apparent in figure 4.8(b), where the same mean-square displacement curve is presented but now for strains up to 20. It is now clear that the linear regime has not yet been reached at a strain of 5, and strains of at least 10 need to be sampled for the long-time diffusive behavior to be reached. In figure 4.8(b) we also show the change in slope in the $\langle yy \rangle$ curve and how, if the strain is not sufficiently long, the slope simply corresponds to a transitional regime between the t^2 and t behaviors

and overestimates the diffusivity. The same conclusion is reached by studying the velocity autocorrelation function: the long tail present in the velocity autocorrelation function is not taken into account when short strains are used and, since the velocity autocorrelation function is negative at those strains, the value of the diffusivity is overestimated.

Figure 4.9 presents our simulation results, but now instead of calculating the slope of the displacement curves in the linear regime, we calculate them for the same strains reported by Breedveld (private communication). We now observe a much better agreement between the numerical and experimental data for all volume fractions (although for larger volume fractions, some discrepancies are still present).

Although the limitation on strain in the experiments of Breedveld *et al.* (2001) explains the difference between simulation and experiment, this is not necessarily the case for the other experimental results. Data by Leighton & Acrivos (1987) and Phan & Leighton (1999) are calculated for larger strains, but with a different method of much lower accuracy, and the origin of the differences between these experiments and the simulations is not known.

We also wish to briefly comment here on the data by Foss & Brady (1999). In their approach very small strains were also used, strains that according to figure 4.8(b) should overestimate the resulting mean-square displacement coefficient significantly. As is apparent from figure 4.6, however, this is not the case and our results are in general agreement with the results reported by Foss & Brady (1999). We believe that this is the result of the very small systems used by Foss & Brady (1999); $N = 27$ for all their simulations. As was mentioned in the previous section, a very strong N dependence is present for such a small number of particles and the diffusivities are underestimated significantly. It is the combination of these two sources of error—the very small number of particles and the very small strains used—that cancel each other and lead to a diffusivity of the correct magnitude.

Figure 4.10 presents the zz mean-square displacement curve for $\phi = 0.20$ as given by Breedveld *et al.* (2001) compared with our simulation results; again the agreement is satisfactory. As shown in figure 4.11 the agreement between the short strain simulations and the experimental data is not as good for higher volume fractions as was the case for

D_{yy}. This seems to be a consequence of the different functional dependence on the volume fraction (see below for more detail); in our data D_{zz} is an increasing function of the volume fraction (and as a result so are the values calculated for smaller strains), while Breedveld's data show a very sharp increase followed by a plateau. We have no explanation for this qualitative difference. It seems that although the method developed by Breedveld *et al.* (1998, 2001) has some very attractive characteristics that can reproduce accurate results for small strains, larger strains are needed to capture the long-time diffusive behavior and some adjustments are necessary in the method to allow for larger observation windows.

We now offer a brief discussion of the qualitative behavior of D_{yy} and D_{zz} as a function of volume fraction. For small volume fractions, $\phi < 0.30$, a ϕ^2 behavior is evident for both diffusivities. This is expected since, in the absence of any interparticle force, the interactions between only two particles lead to zero net displacements (the particles always return to their original streamlines), and the presence of a third particle is necessary to generate non-zero displacements leading to a diffusivity of $O(\phi^2)$. As shown by da Cunha & Hinch (1996), in the presence of an interparticle force, however, a net displacement in the velocity-gradient and vorticity directions can be achieved even with only two particles, leading to an $O(\phi)$ correction to the diffusivity. For the range of the interparticle force used here and the minimum separations that result, the size of this $O(\phi)$ correction is extremely small and is overwhelmed by the displacements caused by the presence of a third particle. Evidently, the three-particle effects are significant even at the lowest volume fraction studied ($\phi = 0.10$). Much lower volume fractions would be necessary to capture and verify the order ϕ correction to the diffusivity. We briefly note here that it is not clear whether the presence of an interparticle force is necessary for diffusive motion to appear. It has been suggested in the past (Marchioro & Acrivos 2001) that even in the absence of an interparticle force, diffusive-like characteristics could be present due to the chaotic nature of the many-body hydrodynamic interactions. If that is indeed the case, the order ϕ correction to the diffusivity might not be dominant even for extremely small volume fractions.

As is apparent from figure 4.6, and in qualitative agreement with most experimental results, the diffusivity in the velocity-gradient direction appears to plateau at volume

fractions about $\phi = 0.35 - 0.40$. This is not the case for the diffusivity in the vorticity direction, however, which is seen to increase roughly as ϕ^2 for all volume fractions studied. The possible exception being $\phi = 0.50$, where the increase is less apparent; the experimental results for this case suggest the presence of an earlier plateau in the value of D_{zz}. The presence of such a plateau in either D_{yy} or D_{zz} is interesting and has not been explained theoretically. Brady & Morris (1997) suggested that the diffusivities should be an increasing function of ϕ for all volume fractions, following the increase in the particle-phase stress.

4.5 The Longitudinal (D_{xx}) and Off-Diagonal (D_{xy}) Self-Diffusivities

4.5.1 Theoretical approach

The calculation of the complete diffusivity tensor (including D_{xx} and $D_{xy}[= D_{yx}]$) for a Brownian particle suspended in a fluid undergoing simple shear-flow has been the subject of numerous studies. Elrick (1962) calculated the $\langle xx \rangle$ and $\langle xy \rangle$ mean-square displacements for such a Brownian particle and found them to grow in time according to:

$$\langle xx \rangle = 2D_{xx}t + 2D_{xy}t^2 + \frac{2}{3}D_{yy}t^3, \tag{4.5a}$$

$$\langle xy \rangle = 2D_{xy}t + D_{yy}t^2. \tag{4.5b}$$

Diffusive motion in the y-direction, D_{yy}, couples to the advective flow in the x-direction to give a mean-square displacement in the flow direction that grows cubically in time. In deriving (4.5) it is assumed that all diffusivities are constant in time and that the "random" Brownian step the particle takes is diffusive at all times. Using (4.5) for a system of non-Brownian particles poses further limitations, e.g., the motion in the y-direction is not diffusive at short times and therefore (4.5) can only be valid at very long times where the t^3 (or t^2) behavior will dominate and the linear term ($D_{xx}t$ or $D_{xy}t$) will be difficult to extract. It is therefore desirable to derive an alternative formulation that not only allows the accurate calculation of the diffusivities, but also serves as a proof of the validity

of (4.5) for a system of non-Brownian particles. Following the equations of motion for our system of non-Brownian particles, we show how to calculate the corresponding mean-square displacements and correctly deduce the diffusion coefficients.

In dynamic simulation of particle motion, the position of a given particle (initially at the origin) in the x-direction is given by

$$\begin{aligned} x_i(t) &= \int_0^t U_{x,i}(\tau)d\tau = \int_0^t \left(U^h_{x,i}(\tau) + U^\infty_{x,i}(\tau)\right) d\tau \\ &= X^h + \int_0^t \dot{\gamma} y_i(\tau)d\tau, \end{aligned} \tag{4.6}$$

where $U^h_{x,i}$ and $U^\infty_{x,i}$ correspond to the instantaneous velocities of particle i due to the presence of all the other particles and due to the external velocity field, respectively. For the case of simple shear flow, the external velocity field at the center of the particle is simply $U^\infty_{x,i} = \dot{\gamma} y_i$. In a simulation where the position of each particle is known exactly and the particle velocities are already decomposed into an affine ($\boldsymbol{U}^\infty$) and a non-affine ($\boldsymbol{U}^h$) part, each term of equation (4.6) is known exactly and can be manipulated separately. Foss & Brady (1999) used this decomposition to claim that the long-time self-diffusion coefficient in the x-direction can be calculated from only the non-affine part of the motion (denoted X^h in (4.6)), specifically from:

$$D_{xx} = \lim_{t\to\infty} \frac{1}{2}\frac{d}{dt}\left\langle X^h(t)X^h(t)\right\rangle. \tag{4.7}$$

The theoretical analysis of Morris & Brady (1996) also indicated that such an operation was possible and would result in the correct value of the self-diffusivity for any value of the Péclet number. The approach embodied in (4.7) has been used successfully and correctly in the past for the case of quiescent Brownian suspensions, where now the non-affine part is simply the (many-body) random Brownian displacement.

A fundamental difference between the shear-induced diffusivity of a non-Brownian suspension and the motion of a Brownian particle is the finite (and large) correlation time for the non-affine displacements, as is evident in figure 4.3 for the motion of a particle in the y- and z-directions. In the case of a Brownian particle there exists a time interval small

enough so that the particle position has not changed significantly, but also large enough so that the random component of the particle's velocity is completely uncorrelated with the random component of the velocity at the previous time interval; this time interval is given by the particle momentum relaxation, $\tau_B = m/6\pi\eta a$, which is much smaller than the time scale of configurational changes, a^2/D. Such a time scale does not exist for the case of sheared non-Brownian particles. The hydrodynamic component of the particle velocity, which is what gives rise to diffusive-like motion for sheared suspensions, is only a function of the particle configuration; as a result, in order for this velocity to change significantly (or the velocity autocorrelation function to approach zero), the particle configuration also has to change significantly, and for some cases (e.g., small volume fractions) strains up to 10-20 may be necessary. As was demonstrated in the previous section, this can be a serious limitation for the calculation of D_{yy} and D_{zz} if long enough intervals are not sampled; the consequences are far more apparent, however, for the calculation of D_{xx}, since now one also needs to consider the coupling between the affine and non-affine motions due to the long correlation times.

Starting from the displacement (4.6), the mean-square displacements $\langle xx \rangle$ and $\langle xy \rangle$ can be readily calculated:

$$\langle x(t)x(t) \rangle = \left\langle X^h(t)X^h(t) \right\rangle + \left\langle (\int_0^t \dot{\gamma} y_i(\tau) d\tau)^2 \right\rangle + 2 \left\langle X^h(t) \int_0^t \dot{\gamma} y_i(\tau) d\tau \right\rangle, \tag{4.8}$$

and

$$\langle x(t)y(t) \rangle = \left\langle X^h(t)y(t) \right\rangle + \left\langle y(t) \int_0^t \dot{\gamma} y_i(\tau) d\tau \right\rangle. \tag{4.9}$$

Differentiating with respect to time and using (4.9), we have

$$\frac{d}{dt} \langle x(t)x(t) \rangle = \frac{d}{dt} \left\langle X^h(t)X^h(t) \right\rangle + 2 \langle x(t)y(t) \rangle + 2 \left\langle \frac{dX^h}{dt} \int_0^t \dot{\gamma} y_i(\tau) d\tau \right\rangle, \tag{4.10}$$

and

$$\frac{d}{dt} \langle x(t)y(t) \rangle = \frac{d}{dt} \left\langle X^h(t)y(t) \right\rangle + \langle y(t)y(t) \rangle + \left\langle \frac{dy}{dt} \int_0^t \dot{\gamma} y_i(\tau) d\tau \right\rangle. \tag{4.11}$$

The above equations were derived simply by using the appropriate equations of motion governing the displacement of the particles. Although derived for the case of a sheared non-Brownian suspension, they are also valid for the motion of a Brownian particle, where the hydrodynamic displacements X^h and y are now replaced by the equivalent random Brownian displacements. The fundamental difference between these two cases lies in the calculation of the last terms in equations (4.10) and (4.11). For the case of a Brownian particle, the "diffusive distance" a particle has traveled in the y-direction, represented by the integral $\int_0^t \dot{\gamma} y_i(\tau) d\tau$, is uncorrelated with the particle's instantaneous random velocity (dy/dt or dX^h/dt), since the particle velocities are uncorrelated between time steps on the Brownian relaxation time $\tau_B \ll \Delta t$ (at least within an accuracy $O(\Delta t)$). Unfortunately, this is not the case for the hydrodynamically interacting non-Brownian particles; now the particle positions, or equivalently the distance a particle has traveled in the y-direction, is strongly correlated with the instantaneous velocity of the particle since this velocity is purely a result of a particle's position and only changes significantly when the particle configuration changes significantly. It can be argued that this last term will only introduce a contribution of the order of the correlation time, but now the correlation time is large and scales as $\dot{\gamma}^{-1}$. In addition, the fact that the particle velocities do become uncorrelated after some strain would suggest that the last term in equations (4.10) and (4.11) reaches a constant value for long enough times, contributing a linear term to the total mean-square displacement.

The calculation of $\langle xx \rangle$ as is given in (4.8) or (4.10) accurately describes the particle displacements and is all the information needed if one is interested in the motion of the particles in the flow direction. The calculation of a self-diffusion coefficient—corresponding to a "diffusive"-like term in a master or Fokker-Planck equation—from this mean-square displacement still needs to be addressed, however. It has been suggested (Morris & Brady 1996, Foss & Brady 1999) that the self-diffusion coefficient in the longitudinal direction can simply be calculated by only taking into account the non-affine displacement according to (4.7), or simply the first term in (4.10). The presence of the last term in equation (4.10) or (4.11) makes such a suggestion suspect, and, as will be demonstrated below, the contribution of this term is constant at long times. Note that the second term on

the right-hand-side (rhs) of (4.11) is proportional to $D_{yy}t$ at long times and therefore gives a $D_{xy}(=\frac{1}{2}\frac{d}{dt}\langle xy\rangle)$ growing as t and an $\langle xy\rangle$ growing as t^2 as in (4.5b). Similarly, the $\langle xy\rangle$ term on the rhs of (4.10) gives a t^3 growth for $\langle xx\rangle$. These are the well-known (Elrick, 1962) convectively-enhanced mean-square displacements of a (Brownian) particle and cause no conceptual difficulties. Note also that the only non-zero cross term is xy.

To address the issue of the proper definition of the "diffusivity" in the direction of the shearing motion, we write a master equation for our system as described by (4.6) (van Kampen, 1992):

$$\frac{\partial P}{\partial t} = \left(\frac{1}{2}\frac{d}{dt}\langle xx\rangle\right)\frac{\partial^2 P}{\partial x^2} + \left(\frac{1}{2}\frac{d}{dt}\langle yy\rangle\right)\frac{\partial^2 P}{\partial y^2} + \left(\frac{1}{2}\frac{d}{dt}\langle zz\rangle\right)\frac{\partial^2 P}{\partial z^2} + \left(\frac{1}{2}\frac{d}{dt}\langle xy\rangle\right)\frac{\partial^2 P}{\partial x \partial y}, \tag{4.12}$$

where it has been taken into account that for "macroscopic variables" x, y and z, $\langle x\rangle = \langle y\rangle = \langle z\rangle = 0$, and it has been assumed that the derivatives of the second moments are only functions of time (i.e., they have no spatial dependence). Equation (4.12) simply follows from a second order expansion of the probability distribution of finding a marked particle and is in a very general form valid for a large number of systems. Note that there is no explicit shearing motion, i.e., no convection term in (4.12), because at the macroscopic scale the marked particle has averaged over the microscale shearing flow and wanders "diffusively".

The solution of (4.12) can be written as

$$P = \frac{1}{\Delta^{1/2}}\exp\left(-\frac{x^2}{2\sigma_{x^2}} - \frac{y^2}{2\sigma_{y^2}} - \frac{z^2}{2\sigma_{z^2}} - \frac{2xy}{2\sigma_{xy}}\right), \tag{4.13}$$

where

$$\Delta = \sigma_{z^2}(\sigma_{x^2}\sigma_{y^2} - \sigma_{xy}^2), \tag{4.14a}$$

$$\sigma_{x^2} = B_{11} - B_{12}^2/B_{22}, \tag{4.14b}$$

$$\sigma_{y^2} = B_{22} - B_{12}^2/B_{11}, \tag{4.14c}$$

$$\sigma_{z^2} = B_{33}, \tag{4.14d}$$

$$\sigma_{xy} = B_{12} - (B_{11}B_{22})/B_{12}, \tag{4.14e}$$

and $\boldsymbol{B}$ is the matrix of mean-square displacements

$$B_{11} = \langle xx \rangle , \tag{4.15a}$$

$$B_{22} = \langle yy \rangle , \tag{4.15b}$$

$$B_{33} = \langle zz \rangle , \tag{4.15c}$$

$$B_{12} = \langle xy \rangle . \tag{4.15d}$$

It is straightforward to verify that (4.13) is a solution of (4.12). This is still a very general result since the functional form for the second moments of (4.15) has not yet been specified. Using the functional forms for $d\langle xx \rangle /dt$ and $d\langle xy \rangle /dt$ given by (4.10) and (4.11), equation (4.12) can be rewritten as

$$\frac{\partial P}{\partial t} = -y\frac{\partial P}{\partial x} + D_{xx}(t)\frac{\partial^2 P}{\partial x^2} + D_{yy}(t)\frac{\partial^2 P}{\partial y^2} + D_{zz}(t)\frac{\partial^2 P}{\partial z^2} + 2D_{xy}(t)\frac{\partial^2 P}{\partial x \partial y}, \tag{4.16}$$

where

$$D_{xx}(t) = \frac{1}{2}\frac{d}{dt}\left\langle X^h X^h \right\rangle + \left\langle \frac{dX^h}{dt}\int_0^t \dot{\gamma} y_i(\tau) d\tau \right\rangle , \tag{4.17a}$$

$$D_{yy}(t) = \frac{1}{2}\frac{d}{dt}\langle yy \rangle , \tag{4.17b}$$

$$D_{zz}(t) = \frac{1}{2}\frac{d}{dt}\langle zz \rangle , \tag{4.17c}$$

$$D_{xy}(t) = \frac{1}{2}\frac{d}{dt}\left\langle X^h y \right\rangle + \frac{1}{2}\left\langle \frac{dy}{dt}\int_0^t \dot{\gamma} y_i(\tau) d\tau \right\rangle . \tag{4.17d}$$

Note that the $\langle x(t)y(t)\rangle$ and $\langle y(t)y(t)\rangle$ terms of equations (4.10) and (4.11) (multiplying the second order partial derivatives of P) have been rewritten as the convective flux term $(-y\partial P/\partial x)$ with P given by (4.13). This is a straightforward calculation:

$$
\begin{aligned}
&\frac{1}{2}\frac{\partial^2 P}{\partial x^2}2\langle xy\rangle + \frac{\partial^2 P}{\partial xy}\langle yy\rangle \\
&= P\left(\frac{x^2}{\sigma_{x^2}\sigma_{x^2}} + \frac{y^2}{\sigma_{xy}\sigma_{xy}} + \frac{2xy}{\sigma_{x^2}\sigma_{xy}} - \frac{1}{\sigma_{x^2}}\right)\langle xy\rangle \\
&\quad + P\left(\frac{xy}{\sigma_{x^2}\sigma_{y^2}} + \frac{x^2}{\sigma_{x^2}\sigma_{xy}} + \frac{y^2}{\sigma_{y^2}\sigma_{xy}} + \frac{xy}{\sigma_{xy}\sigma_{xy}}\right)\langle yy\rangle \\
&= P\Bigg(\frac{x^2B_{22}^2B_{12}}{(B_{22}B_{11}-B_{12}^2)^2} + \frac{y^2B_{12}^2B_{12}}{(B_{22}B_{11}-B_{12}^2)^2} - \frac{2xyB_{22}B_{12}^2}{(B_{22}B_{11}-B_{12}^2)^2} \\
&\quad - \frac{B_{22}B_{12}}{(B_{22}B_{11}-B_{12}^2)} + \frac{xyB_{22}^2B_{11}}{(B_{22}B_{11}-B_{12}^2)^2} - \frac{x^2B_{22}^2B_{12}}{(B_{22}B_{11}-B_{12}^2)^2} \\
&\quad - \frac{y^2B_{11}B_{12}B_{22}}{(B_{22}B_{11}-B_{12}^2)^2} + \frac{xyB_{12}^2B_{22}}{(B_{22}B_{11}-B_{12}^2)^2} + \frac{B_{22}B_{12}}{(B_{22}B_{11}-B_{12}^2)}\Bigg) \\
&= P\frac{-y^2B_{12}+xyB_{22}}{(B_{22}B_{11}-B_{12}^2)},
\end{aligned}
$$

and

$$
-y\frac{\partial P}{\partial x} = P\left(\frac{xy}{\sigma_{x^2}} + \frac{y^2}{\sigma_{xy}}\right) = P\frac{-y^2B_{12}+xyB_{22}}{(B_{22}B_{11}-B_{12}^2)}.
$$

We have denoted the diffusivities as functions of time so that (4.16) and (4.17) are valid at each instant in time, and not only for very long-times when the motion becomes truly diffusive. As has been mentioned, at long times both contributions to D_{xx} and D_{xy} become constant with time—it is those values of the diffusivity that we wish to calculate.

From the master equation (4.12) describing the macroscopic behavior of our system, we have derived the conventional convection-diffusion equation (4.16) where, by construction, the diffusion coefficients are given by equations (4.17). It is these diffusion coefficients that we wish to calculate, and it is now apparent that in order to calculate the diffusivity in the x-direction one needs more information than simply the non-affine displacements. The theoretical analysis of Morris & Brady (1996) also agrees with the above conclusion; unfortunately, an error in their earlier calculation, which has been corrected (Brady 2001),

led to the omission of the last terms of equation (4.17) for the calculation of D_{xx} and D_{xy}.

For simplicity of notation we rewrite (4.17) as:

$$D_{xx}(t) = D^{\star}_{xx}(t) + D^{corr}_{xx}(t), \tag{4.18a}$$

$$D_{xy}(t) = D^{\star}_{xy}(t) + D^{corr}_{xy}(t), \tag{4.18b}$$

where

$$D^{\star}_{xx}(t) = \frac{1}{2}\frac{d}{dt}\left\langle X^h X^h \right\rangle, \tag{4.19a}$$

$$D^{\star}_{xy}(t) = \frac{1}{2}\frac{d}{dt}\left\langle X^h y \right\rangle, \tag{4.19b}$$

and

$$D^{corr}_{xx}(t) = \left\langle \frac{dX^h}{dt}\int_0^t \dot{\gamma} y_i(\tau)\delta\tau \right\rangle, \tag{4.20a}$$

$$D^{corr}_{xy}(t) = \frac{1}{2}\left\langle \frac{dy}{dt}\int_0^t \dot{\gamma} y_i(\tau)\delta\tau \right\rangle. \tag{4.20b}$$

We refer to the term omitted by the previous authors as a "correction" simply for clarity—both terms can be equally important for the shear-induced diffusivity. It can also be seen as a correction compared to the Brownian case where such a term is absent.

Calculating the self-diffusivities from (4.17) is now straightforward for any simulation. We chose to express these diffusivities as functions of the non-affine displacement because we wanted to stress the importance of the missing term in the calculations of Morris & Brady (1996) and Foss & Brady (1999). It is also straightforward to calculate the diffusivities directly from equations (4.10) and (4.11):

$$\begin{aligned} D_{xx}(t) &= \frac{1}{2}\frac{d}{dt}\left\langle X^h X^h \right\rangle + \left\langle \frac{dX^h}{dt}\int_0^t \dot{\gamma} y_i(\tau)d\tau \right\rangle \\ &= \frac{1}{2}\frac{d}{dt}\left\langle x(t)x(t) \right\rangle - \left\langle x(t)y(t) \right\rangle, \end{aligned} \tag{4.21}$$

and

$$D_{xy}(t) = \frac{1}{2}\frac{d}{dt}\left\langle X^h y \right\rangle + \frac{1}{2}\left\langle \frac{dy}{dt}\int_0^t \dot{\gamma} y_i(\tau) d\tau \right\rangle$$
$$= \frac{1}{2}\frac{d}{dt}\left\langle x(t)y(t) \right\rangle - \frac{1}{2}\left\langle y(t)y(t) \right\rangle . \qquad (4.22)$$

In other words, all the information needed for the calculation of the diffusivities is simply the overall mean-square displacements $\langle xx \rangle$, $\langle xy \rangle$ and $\langle yy \rangle$. This approach is equivalent to using (4.5), which is, however, only valid at long times. Also using a constant value for the diffusivity (D_{yy}) can result in large errors when trying to determine D_{xx} and D_{xy} at intermediate times. On the other hand, using (4.5) at truly long times to extract D_{xx} and D_{xy} can result in very low accuracy since the t^3 (or t^2) behavior will dominate the total displacement and the linear term would be all but impossible to determine. In an experimental set-up equations (4.17) or (4.21) and (4.22) can be used without further modifications. The only requirement is that the particle trajectories need to be followed closely enough so that the derivatives and integrals of the mean-square displacements are calculated with sufficient accuracy.

Figure 4.12 shows the resulting D_{xx} self-diffusivity (as calculated by either (4.17) or (4.21)—in a simulation where the exact positions are known at each instant in time the two approaches are identical) as a function of time for a system of $N = 1000$ particles and a volume fraction of 0.35. The curve has been averaged over all particles and over 30 independent configurations. The two separate contributions to the diffusivity, (4.18a), are also shown. Both contributions become constant after the correlation time, verifying that they both should be included in the calculation of the self-diffusivity. The same behavior is seen in figure 4.13, this time for D_{xy}. Both corrections to D_{xx} and D_{xy} are negative, resulting in a smaller absolute value of the D_{xx} diffusivity and a larger absolute value of the D_{xy} diffusivity since, as is discussed in Foss & Brady (1999), the non-affine term, $D^{\star}_{xy}$, is also negative. For this relatively high volume fraction the effect of the correction to the value of D_{xx} is small. The effect on the value of D_{xy} is rather significant, however, since the non-affine contribution, $D^{\star}_{xy}$, is relatively small. The correction to the diffusivities for a much lower volume fraction of $\phi = 0.15$ is shown in figure 4.14. The absolute values of

both the correction to the xx and xy diffusivities are now significantly larger, in agreement with the fact that it now takes a much longer time for the particle velocities to become uncorrelated, increasing the time limit for the integrals in D_{xx}^{corr} and D_{xy}^{corr}; it is also apparent that it takes a longer time for the corrective term to reach a constant value.

It is also worth noting that it is the presence of D_{xx}^{corr} that results in the singular behavior for the two-particle limit studied by Acrivos *et al.* (1992). It can be shown that for the two-particle case the non-affine term of the mean-square displacement is well behaved and gives a finite contribution to the diffusivity. Hence, the contribution of D^{corr}, especially for small volume fractions, can be very important and can dominate the overall behavior of the mean-square displacement. Figure 4.15 shows the "correction" to the self-diffusivity as a function of the volume fraction. (Note again that the term correction is used for simplicity—this part of the diffusivity is as important as the non-affine part, and it is only calculated separately to emphasize its omission from previous studies). Both corrections are increasing (in magnitude) functions of the volume fraction for small volume fractions, and decreasing (in magnitude) functions of ϕ as the volume fraction is further increased. This behavior can be explained from the functional form (4.20) of the correction: The correlation time is a monotonically decreasing function of the volume fraction since it depends directly on the number of collisions between particles. Therefore, the time over which the integrals of (4.20) are calculated decreases as ϕ increases. On the other hand, for low volume fractions, the particle's non-affine y displacement, upon which the corrections to the diffusivity directly depend, are smaller—D_{yy} is small for small volume fractions. The combination of those two factors results in the observed non-monotonic behavior for the corrective contribution to the self-diffusivity.

4.5.2 The volume fraction dependence

Before presenting the results for D_{xx} we shall briefly discuss some limitations concerning the calculation of the diffusivity in the x-direction for small volume fractions. It has been shown that in the two-particle limit the behavior of the mean-square displacement in the x-direction is singular and the presence of more particles need to be invoked to remove this singularity. Even when the singularity is not present, however, as is the case in our

simulations (the singularity is a result of particles coming from infinity interacting with a test particle—in a periodic system the finite size of the simulation cell introduces a cut-off), the resulting x-displacement for a given two-body interaction can be large. For the diffusive regime to be established each particle must sample a randomly distributed number of different displacements with a zero average. In a dilute periodic system this implies that each particle, after it interacts with a given second particle and before it again interacts with this particle's image, must sample a sufficient number of interactions with other, third particles. This can give a strict condition on the minimum size of the unit cell, and thus on the size of the system simulated. Although the same condition must be satisfied for concentrated systems, the magnitude of each individual displacement is significantly smaller and their frequency significantly larger at high ϕ.

To demonstrate the severity of this limitation, consider two particles suspended in a periodic unit cell of finite length L, initially at positions with relative displacements ΔX_0, ΔY_0, and for simplicity $\Delta Z_0 = 0$ (as shown in figure 4.16). If initially in positions with different y-coordinates the two particles will interact and at the end of the interaction will return at the same y-positions, but there will be a net displacement in the x-direction (Acrivos *et al.* 1992). After the end of the interaction the particles will continue moving undisturbed until the "faster" particle reaches the end of the periodic domain, at which time it will reenter the cell on the opposite face. For a periodic domain the maximum distance between two particles has to be less than L, so eventually (the time will depend both on L and the difference in the affine undisturbed velocities between the two particles, which is proportional to ΔY_0) the two particles will interact again. This second interaction will be identical to the first, since the particles' vertical positions did not change as a result of the first interaction. This behavior will continue indefinitely and at each "collision" the displacement of each particle is always exactly the same. It is clear that such a scenario would never evolve into diffusive-like motion, even at infinite time, since only one displacement is sampled for each particle, and of course $\langle \Delta X \rangle \neq 0$.

In a dilute system the same problem is present: a given particle, after interacting with an initial second particle, has a very high probability not to collide with any third particles until it exits the periodic cell and interacts with the same particle for the second time.

Such a behavior leads to particle velocities that are strongly correlated for aphysically long times and mean-square displacements that exhibit quadratic behavior for very long times. Figure 4.17 shows the non-affine term (X^h of equation (4.6)) of the x-displacement for one of the particles of such a pair initially displaced $\Delta X_0 = -10a$ and $\Delta Y_0 = 0.5a$ relative to the reference particle in a unit cell of three different lengths ($L = 20a$, $40a$ and $60a$). Each "step" corresponds to a repeated interaction between the pair of particles resulting in a displacement that appears linear. Increasing the size of the cell simply changes the frequency of each step, resulting in a linear behavior with a different coefficient. The mean-square displacement corresponding to the displacement for $L = 20a$ of figure 4.17 is plotted in figure 4.18 (we choose to only present the non-affine piece of the displacement, since, as will be shown later, the coupled term has a much more favorable behavior for non-zero volume fractions). The quadratic behavior is clear, verifying that such a system of two particles would never reach the diffusive regime. The case studied in figures 4.17 and 4.18 corresponds to a given initial lateral displacement between the two particles. Increasing the initial ΔY_0 does not improve the situation because, although each individual step is smaller in magnitude, the frequency is increased significantly; particles that have large ΔY_0 have very different affine velocities and, as a result, approach and interact with each other more frequently. It should be noted that the $\langle yy \rangle$ and $\langle zz \rangle$ mean-square displacements do not suffer from this problem because the net y or z displacements from an encounter are zero, and thus only the "diffusive" displacements remain. Figure 4.18 also shows the non-affine term ($\langle X^h X^h \rangle$) of the mean-square displacement curve for the case of a suspension of $N = 1000$ at $\phi = 0.10$. The quadratic behavior is again evident, making it impossible to calculate a diffusion coefficient.

The obvious way to overcome the effect of periodicity is to use a large periodic unit cell. However, this can place a severe requirement on the number of particles needed, especially at low ϕ. What is necessary is that by the time a particle has crossed the unit cell, its position and velocity should be uncorrelated with its initial position and velocity. Since the particle motion is deterministic, it is the stochastic or shear-induced "diffusive" motion that results in the loss of correlation. Thus, to loose correlation a particle must diffuse a distance say l in the y-direction before it is convected through the unit cell,

i.e., $l^2/D_{yy} \ll L/a\dot{\gamma}$, or $L/a \gg \dot{\gamma}l^2/D_{yy}$, where L is the length of the unit cell in the x-direction. The correlation distance l must be at least of the order of the particle size a, and $D_{yy} = \dot{\gamma}a^2 d_{yy}(\phi)$, so that the simulation cell must satisfy $L/a \gg 1/d_{yy}(\phi)$. For small ϕ, $d_{yy} \sim 10^{-3}$, giving $L/a \sim 10^3$ or $N \sim 10^9$ for a square unit cell. (Attempts to use an elongated, non-square, unit cell experienced numerical difficulties associated with shearing a very anisotropic cell.) Even with a fast algorithm, such large-scale simulations are not currently feasible.

In order to get meaningful results without using an extremely large system, we followed an alternative approach. We generated a large number of independent configurations of particles and calculated the individual displacements for each individual particle. As has been mentioned, because of the periodicity the mean displacement for each particle, even after long strains, will not average to zero since particles keep interacting with the same images. In order to get the correct behavior, we combine the particles into groups (chosen randomly from different initial configurations) and calculate the mean-square displacements of the resulting groups. If enough particles are in each group, the average displacement for a group fluctuates around zero. (We combine particles from different initial configurations for our averages. Particles from the same configuration could also be used but there is an upper limit above which the statistics are no longer sampled correctly; e.g., since the suspension is force free, if all the particles are grouped together one gets not only $\langle x \rangle = 0$ but also $\langle xx \rangle = 0$). For the new groups, we calculate the mean-square displacements in all directions and identify a linear regime for the x-direction. The times for these simulations are kept relatively short, but long enough to reach, we believe, the diffusive regime. This is done both to reduce the computational cost since now hundreds of configurations of thousands of particles are used, and to ensure that a linear regime is identified. In order for the diffusive behavior to be seen, the groups must include enough configurations so that their average displacement is zero. If that is not the case, then as time elapses the systematic error will increase since the individual particle square displacements continue to grow in time. Ideally, one should try to identify a time scale where the diffusion process has started and the particles have not yet left the periodic cell. In order for the diffusion process to be evident, however, many collisions need to occur and

therefore the "grouped" particles need to travel a significant distance, which for the system sizes we are now studying means going through the periodic cell a number of times.

While such a procedure works, it can be subject to large errors, since on the one hand grouping of the particles reduces their statistical accuracy (i.e., 10 groups of 1000 particles have the same statistical accuracy of just 10 particles), and on the other hand it is not always clear when the motion becomes diffusive, or even whether the grouping, although it improves the behavior, completely eliminates the problem. Figure 4.19(a) shows the derivative of the affine term of the mean-square displacements as a function of time for $\phi = 0.15$. A number of independent initial configurations (100) of $N = 1000$ particles is used and the results averaged. It is apparent that for a time of order 5-10 strains the behavior of the mean-square displacement changes dramatically, even without the particle grouping. While the diffusive regime is almost reached, the effect of the periodicity becomes apparent and the diffusivity without grouping becomes linear in time (corresponding to a quadratic behavior for the mean-square displacement).

Groups of 500 particles are consequently formed (5 particles from each of the independent configurations), and the mean-square displacement of the resulting groups of particles is calculated. Since now the statistics only correspond to the statistics of 200 independent particles, a number (50) of random groupings of the particles are generated and averaged. The effect of the grouping is to transform the linear diffusivity regime into a constant one—as is suggested over the last 10 strains of figure 4.19(a). Again, there is significant uncertainty as a result of the loss of statistics and the uncertainty associated with the beginning of the linear regime, making it hard to make solid quantitative estimates. Figure 4.19(b) shows the non-affine mean-square displacement, $\langle X^h X^h \rangle$, for the two cases described above for strains between 20 and 30. A linear curve is also shown. It is apparent that the non-grouped curve deviates from the linear behavior, while the grouped curve seems to follow it for all strains shown. It can also be seen, however, that the difference between the two curves is not dramatic. Despite these limitations, we nevertheless proceed with the calculation of the diffusivities, noting that our results for the smaller volume fractions may be subject to large errors. We note here that it is $D^{\star}_{xx}$ that has this very strong dependence on periodicity. The other term, D^{corr}_{xx}, plotted in figure

4.14 for $\phi = 0.15$ becomes linear in time. This is due to the coupling with the motion in the y-direction, a motion that does not suffer from the same limitations because, even for low volume fractions, the diffusive motion in the y-direction is a result of interaction between at least 3 particles. The calculation of $\langle xy \rangle$ is also not nearly as problematic as $\langle xx \rangle$, again due to the coupling with the motion in the y-direction, and the grouping is not necessary.

Figure 4.20 and table 4.3 present D_{xx} as a function of the volume fraction, along with the values of $D^{\star}_{xx}$, although as has already been mentioned $D^{\star}_{xx}$ does not correspond to the self-diffusivity. The diffusivity is expected to be an increasing function of the volume fraction for very dilute systems according to the dilute limit theoretical predictions of Acrivos et al. (1992); this is in agreement with our calculated values between $\phi = 0.10$ and $\phi = 0.15$. As the volume fraction is increased further, the interactions between particle pairs become more frequent, while at the same time the displacement resulting from a given interaction is expected to decrease in magnitude. The values seem to plateau at higher volume fractions, at least within the accuracy of our calculations. The volume fraction behavior of D_{xy}, shown in figure 4.21 and table 4.4, is dominated by the behavior of the corrective term, leading to an initially increasing volume fraction dependence followed by a decreasing one—the value of the non-affine term on the other hand seems to be an increasing function of the volume fraction, reaching a plateau at about the same values where the D_{yy} component also reaches a plateau. It is interesting to note that other than D_{zz} the remaining components of the diffusivity tensor have a similar behavior at high volume fractions—reaching apparent plateaus. This can be expected since there is strong coupling between these three self-diffusivities. It is also interesting to note that the anisotropy between the values of D_{xx}, D_{yy} and D_{zz} decreases with increasing volume fraction—the values of D_{yy} and D_{zz} are very close for $\phi = 0.50$, while the value of D_{xx} is less than twice as large. The only other available numerical results for the calculation of these two properties are the results by Foss & Brady (1999), which are also presented in figures 4.20 and 4.21. Unfortunately, as was already mentioned, the strains used for their study are not sufficiently long and only the $D^{\star}$ term of the diffusivities is calculated in their simulations, making comparisons difficult. To our knowledge the only experimental

results available for D_{xx} and D_{xy} are the results of Breedveld (2000). The limitation to very small strains before the diffusive behavior has been established is still present in his results as was the case for the calculation of D_{yy} and D_{zz}. In addition, it is not clear from his analysis whether the correct self-diffusivity, as opposed to $D^{\star}$ or a different combination of the non-affine and affine displacements, is determined. The use of formulae (4.21) and (4.22) should help in the experimental measurement of the diffusivities.

4.6 Conclusions

The calculation of the complete tensor of the shear-induced diffusivities through numerical simulation has been presented. The availability of a faster algorithm allows routine simulations of much larger systems, significantly improving the accuracy of the results and diminishing system size effects. The self-diffusivities in the velocity gradient and vorticity directions, D_{yy} and D_{zz}, were calculated as a function of the volume fraction for $\phi = 0.10 - 0.50$ and compared with existing experimental results. While both appear to be increasing functions of the volume fraction for small to intermediate ϕ, D_{yy} plateaus at high ϕ, in agreement with a number of previous experiments. The quantitative agreement between our simulation results and experiment was not always satisfactory and we suggest that one of the reasons for this difference is the difficulty associated with correctly identifying the diffusive-regime. The presence of a long correlation time during which the mean-square displacements show first a quadratic and then a transitional behavior is a main difference between the behavior of a non-Brownian particle diffusing under the influence of shear and a Brownian particle. This difference is further manifest in the calculation of the self-diffusivity in the flow direction, D_{xx}, and the off-diagonal self-diffusivity, D_{xy}. Previous work had suggested that the diffusion in the x-direction can be simply calculated by taking into account only the non-affine contributions to the particle velocity (or particle displacement), as would be appropriate for a single Brownian particle. Careful construction of the convection diffusion equation for the system of sheared non-Brownian particles demonstrated that a coupled term (in addition to the term arising from the non-affine displacements) is present, a term that was erroneously omitted in previous studies. The

correct longitudinal self-diffusivities were determined and their dependence on the volume fraction studied. An additional limitation is present when calculating the longitudinal diffusion coefficient for low volume fractions; the effect of the periodicity is extremely severe leading to an artificial quadratic behavior of the mean-square displacements. Although an attempt was made to decrease the effect of the periodicity without further increasing the size of the system, the accuracy of the results was not always satisfactory pointing to the need for either studying larger systems or devising an alternative approach. A very small number of experimental data is available for the longitudinal self-diffusivity, and we hope that we have provided a better understanding of how this property can be calculated which would allow meaningful comparisons with experiment in the future.

Acknowledgement

This work was supported in part by grant NAG8-1661 from NASA and by a Dow graduate fellowship to AS. Access to an Alpha-based Beowulf cluster at the California Institute of Technology was provided by the Center for Advanced Computing Research.

References

ACRIVOS, A., BATCHELOR, G. K., HINCH, E. J., KOCH, D. L. & MAURI, R. 1992 The longitudinal shear-induced diffusion of spheres in a dilute suspension. *J. Fluid Mech.* **240**, 651.

BOSSIS, G. & BRADY, J. F. 1984 Dynamic simulation of sheared suspensions. I.General method. *J. Chem. Phys.* **80**, 5141.

BRADY, J. F. 2001 (private communication).

BRADY, J. F. & MORRIS, J. F. 1997 Microstructure of strongly sheared suspensions and its impact on rheology and diffusion. *J Fluid Mech.* **348**, 103.

BREEDVELD, L. V. A. 2000 Shear-induced self-diffusion in concentrated suspensions. PhD thesis, University of Twente, The Netherlands.

BREEDVELD, V., VAN DEN ENDE, D., TRIPATHI, A. & ACRIVOS, A. 1998 The measurement of the shear-induced particle and fluid tracer diffusivities by a novel method. *J Fluid Mech.* **375**, 297.

BREEDVELD, V., VAN DEN ENDE, D., BOSSCHER, M., JONGSCHAAP, R. J. J. & MELLEMA, J. 2001 Measuring shear-induced self-diffusion in a counter-rotating geometry. *Phys. Rev. E* **63**, 1403.

DA CUNHA, F. R. & HINCH, E. J. 1996 Shear-induced dispersion in a dilute suspension of rough spheres. *J. Fluid Mech.* **309**, 211.

DARDEN, T., YORK, D. & PEDERSEN, L. 1993 Particle Mesh Ewald: An $n\log(n)$ method for Ewald sums in large systems. *J. Chem. Phys.* **98**, 10089.

DRATLER, D. I. & SCHOWALTER, W. R. 1996 Dynamic simulations of suspensions of non-Brownian hard spheres. *J. Fluid Mech.*, **325**, 53.

ELRICK, D. E. 1962 Source functions for diffusion in uniform shear flow. *Austral. J. Phys.* **15**, 283.

ECKSTEIN, E. C., BAILEY, D. G. & SHAPIRO, A. H. 1977 Self-diffusion of particles in shear-flow of a suspension. *J. Fluid Mech.* **79**, 191.

FOSS, D. R. & BRADY, J. F. 1999 Self-diffusion in sheared suspensions by dynamic simulation. *J. Fluid Mech.* **401**, 243.

HOCKNEY, R. W. & EASTWOOD, J. W. 1982 Computer simulation using particles. Kluwer, New York.

LEIGHTON, D. & ACRIVOS, A. 1987 Measurement of shear-induced migration of particles in concentrated suspensions. *J. Fluid Mech.* **177**, 109.

MARCHIORO, M. & ACRIVOS, A. 2001 Shear-induced particle diffusivities from numerical simulations. *J. Fluid Mech.* (to appear).

MELROSE, J. R. & BALL, R. C. 1995 The pathological behavior of sheared hard-spheres with hydrodynamic interactions. *Europhys. Lett.* **32**, 535.

MORRIS, J. F. & BRADY, J. F. 1996 Self-diffusion in sheared suspensions *J. Fluid Mech.* **312**, 223.

PHAN, S. E. & LEIGHTON, D. 1999 Measurement of the shear-induced tracer diffusivity in concentrated suspensions. *J. Fluid Mech.* (submitted).

SIEROU, A. & BRADY, J. F. 2001 Accelerated Stokesian Dynamics Simulations. *J. Fluid Mech.* (to appear).

VAN KAMPEN, N. G. 1992 Stochastic processes in physics and chemistry. Rev. and enl. ed., Elsevier Science Publishers, Amsterdam.

WANG, Y., MAURI, R. & ACRIVOS, A. 1996 Transverse shear-induced liquid and particle tracer diffusivities of a dilute suspension of spheres undergoing a simple shear flow. *J. Fluid Mech.* **327**, 255.

N	D_{yy}	D_{zz}
SD		
16	0.019 ± 0.003	0.009 ± 0.002
27	0.027 ± 0.003	0.012 ± 0.003
54	0.037 ± 0.007	0.014 ± 0.005
64	0.038 ± 0.007	0.015 ± 0.005
ASD		
64	0.0360 ± 0.006	0.0140 ± 0.004
125	0.0408 ± 0.006	0.0157 ± 0.004
256	0.0432 ± 0.005	0.0170 ± 0.003
512	0.0450 ± 0.004	0.0177 ± 0.003
1000	0.0462 ± 0.004	0.0185 ± 0.003

Table 4.1: The dependence of D_{yy} and D_{zz} on the number of particles N, with N ranging from $16 - 1000$ for $\phi = 0.35$.

ϕ	D_{yy}	D_{zz}
0.10	0.0017 ± 0.0003	0.0011 ± 0.0002
0.15	0.0045 ± 0.0006	0.0024 ± 0.0004
0.20	0.0084 ± 0.0010	0.0040 ± 0.0006
0.25	0.0171 ± 0.0020	0.0070 ± 0.0007
0.30	0.0310 ± 0.0040	0.0117 ± 0.0010
0.35	0.0460 ± 0.0050	0.0185 ± 0.0020
0.40	0.0620 ± 0.0060	0.0290 ± 0.0030
0.45	0.0583 ± 0.0070	0.0450 ± 0.0040
0.50	0.0580 ± 0.0070	0.0520 ± 0.0050

Table 4.2: The dependence of D_{yy} and D_{zz} on the volume fraction ϕ for $N = 1000$.

ϕ	D_{xx}	$D^{\star}_{xx}$	D^{corr}_{xx}
0.10	0.1086 ± 0.020	0.190	-0.0814
0.15	0.1566 ± 0.030	0.254	-0.0974
0.20	0.0980 ± 0.020	0.190	-0.0920
0.25	0.0660 ± 0.015	0.159	-0.0880
0.30	0.0610 ± 0.012	0.141	-0.0800
0.35	0.0737 ± 0.013	0.127	-0.0533
0.40	0.0829 ± 0.010	0.113	-0.0300
0.45	0.0998 ± 0.010	0.107	-0.0073
0.50	0.0837 ± 0.010	0.087	-0.0035

Table 4.3: The dependence of D_{xx}, $D^{\star}_{xx}$ and D^{corr}_{xx} on the volume fraction ϕ for $N = 1000$.

ϕ	D_{xy}	$D^{\star}_{xy}$	D^{corr}_{xy}
0.10	-0.0390 ± 0.004	-0.0013	-0.0376
0.15	-0.0534 ± 0.005	-0.0052	-0.0487
0.20	-0.0640 ± 0.007	-0.0077	-0.0564
0.25	-0.0717 ± 0.009	-0.0124	-0.0593
0.30	-0.0746 ± 0.010	-0.0180	-0.0566
0.35	-0.0758 ± 0.009	-0.0214	-0.0544
0.40	-0.0725 ± 0.007	-0.0293	-0.0432
0.45	-0.0594 ± 0.007	-0.0336	-0.0258
0.50	-0.0430 ± 0.006	-0.0297	-0.0133

Table 4.4: The dependence of D_{xy}, $D^{\star}_{xy}$ and D^{corr}_{xy} on the volume fraction ϕ for $N = 1000$.

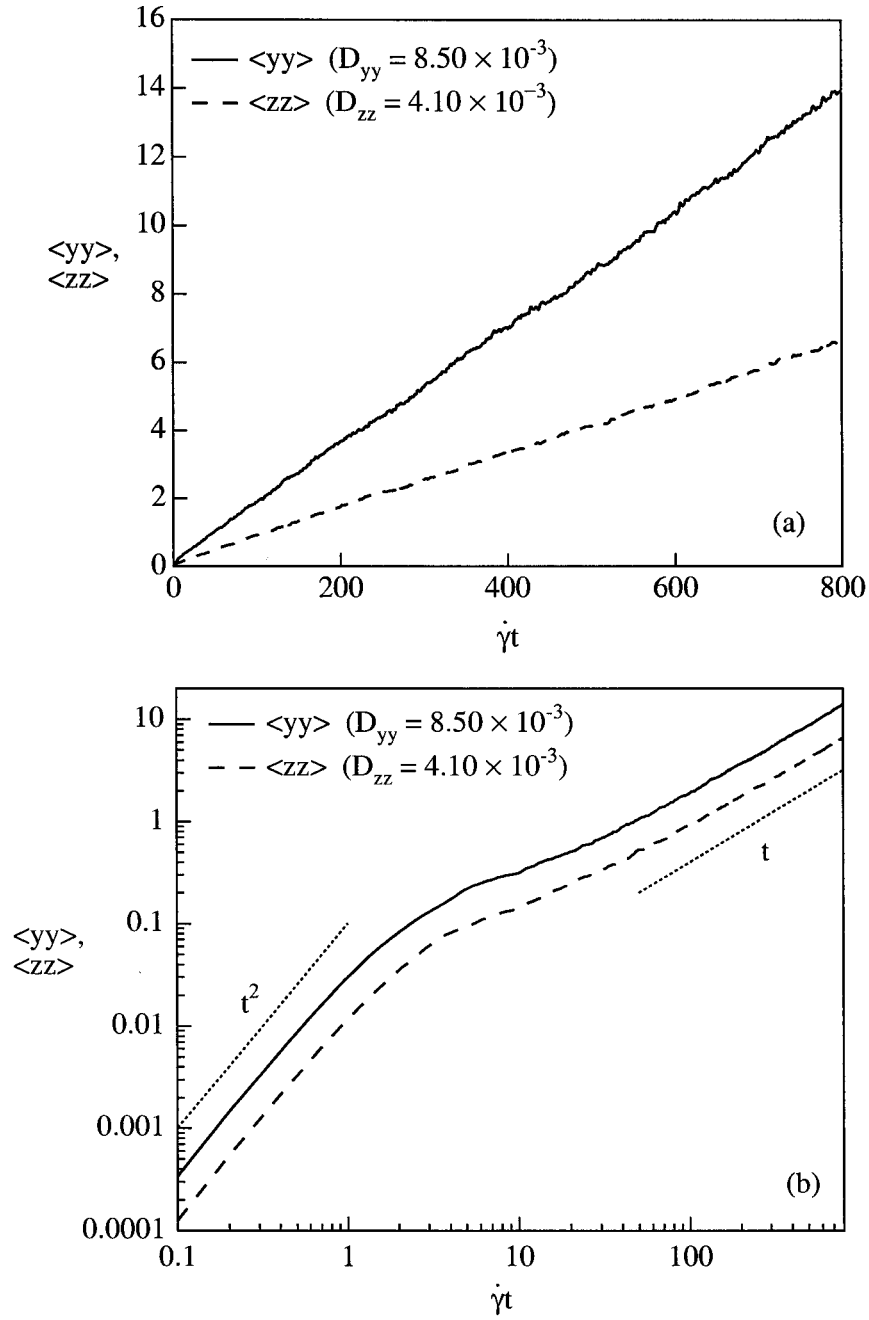

Figure 4.1: The mean-square displacement curves $\langle yy \rangle$ and $\langle zz \rangle$ as a function of time (or strain) $\dot{\gamma}t$ for a system of $N = 1000$, $\phi = 0.20$ for strains up to 800, plotted in a linear (a) and log-log (b) plot. The values of the resulting diffusivities are also given. In this and subsequent figures, all mean-square displacements are in units of a^2, and all diffusivities in units of $\dot{\gamma}a^2$.

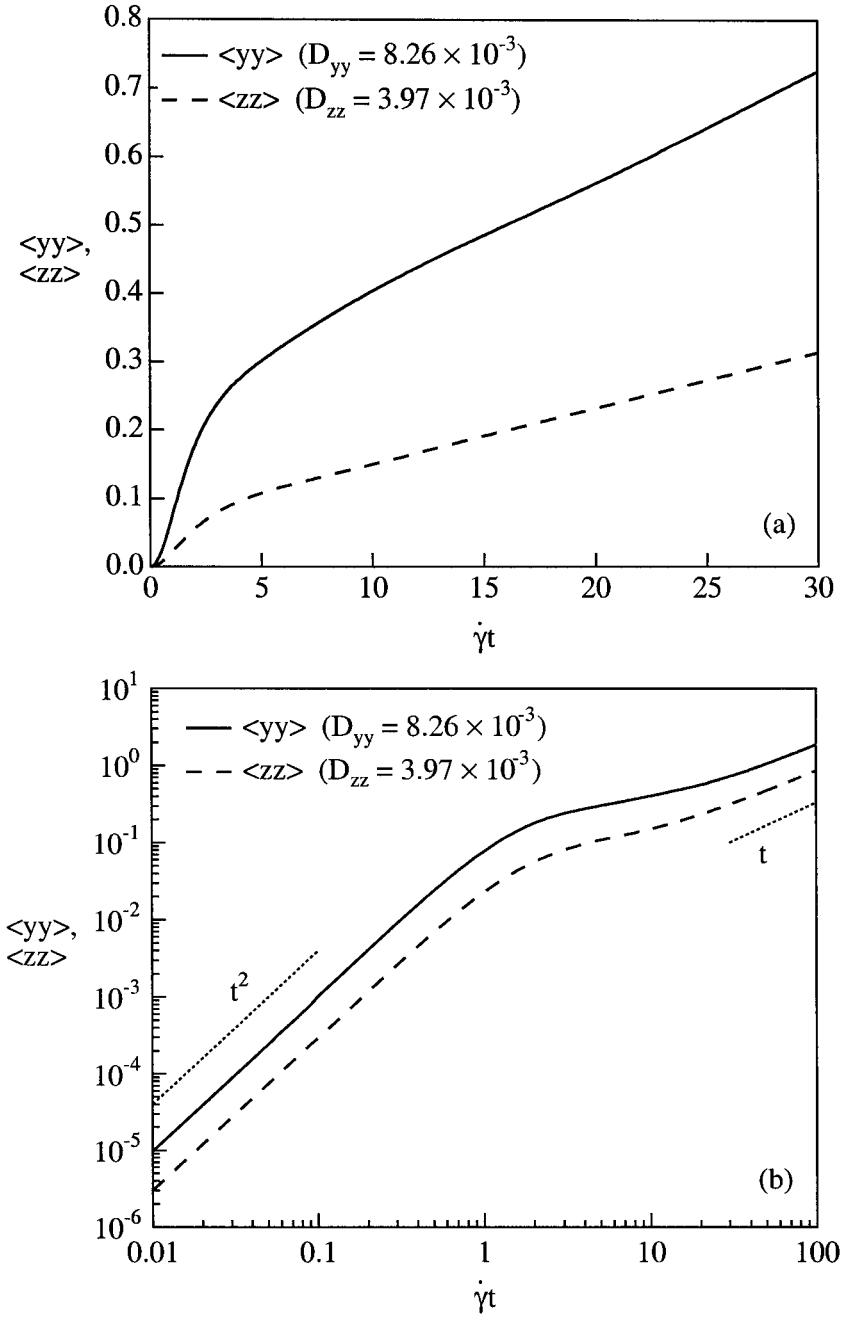

Figure 4.2: The mean-square displacement curves $\langle yy \rangle$ and $\langle zz \rangle$ as a function of time (or strain) $\dot{\gamma}t$ for a system of $N = 1000$, $\phi = 0.20$ averaged over total strain of 30 in (a) and of 100 in (b). The values of the resulting diffusivities are also given.

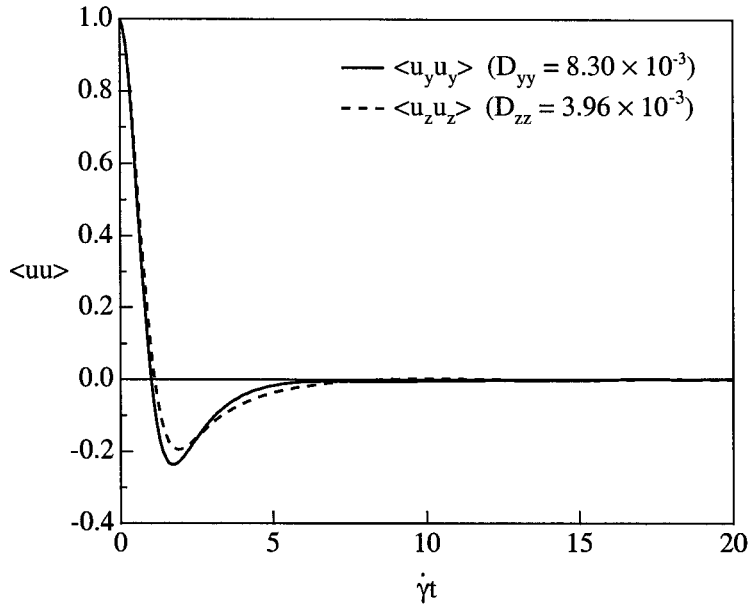

Figure 4.3: The velocity autocorrelation functions $\langle u_y u_y \rangle$ and $\langle u_z u_z \rangle$ for a system of $N = 1000$, $\phi = 0.20$ plotted over a total strain of 20. The values are non-dimensionalized with the value of the autocorrelation function at time zero. The values of the diffusivities are given by the areas under the curves. In this and the following figure the velocities have been normalized by $\dot{\gamma} a$.

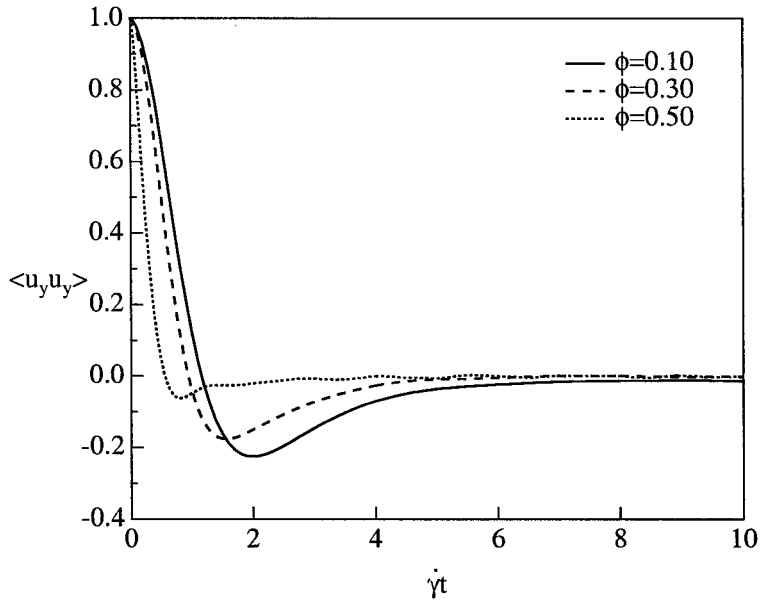

Figure 4.4: The velocity autocorrelation function $\langle u_y u_y \rangle$ for a system of $N = 1000$ and $\phi = 0.10$, $\phi = 0.30$ and $\phi = 0.50$ plotted over total strain of 10. The values are non-dimensionalized with the value of the autocorrelation function at time zero.

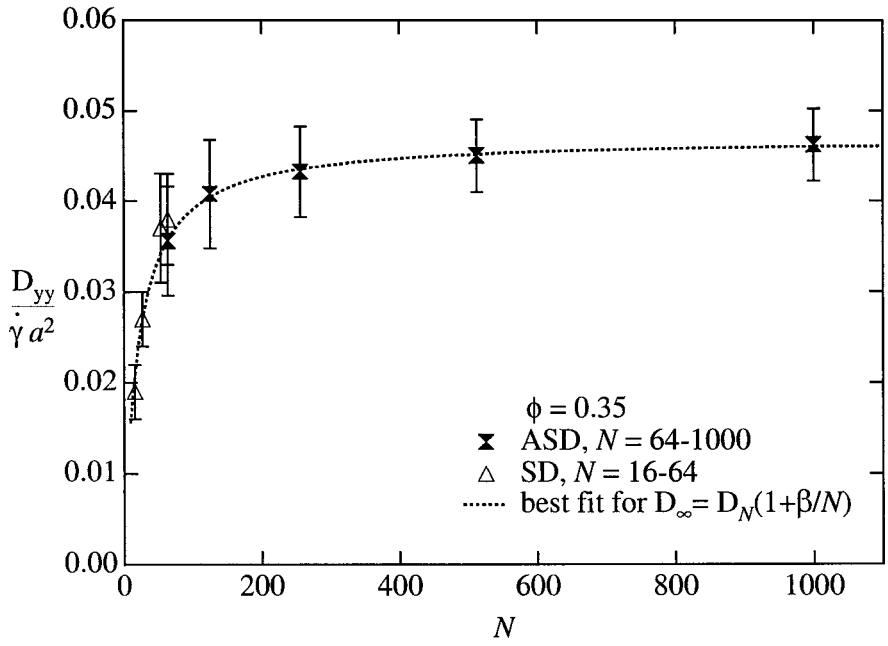

Figure 4.5: The dependence of D_{yy} on the number of particles N, with N ranging from $16 - 1000$, for $\phi = 0.35$. A very sharp increase is observed for small volume fractions, followed by a relatively constant value.

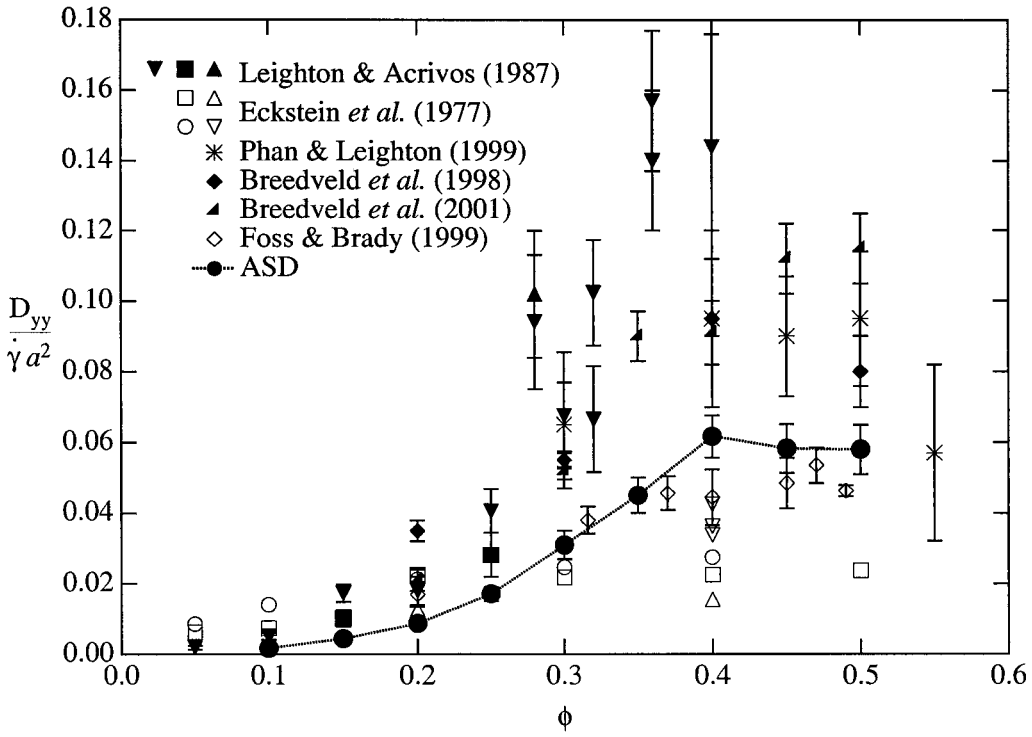

Figure 4.6: The dependence of D_{yy} on the volume fraction ϕ. Accelerated Stokesian Dynamics results (ASD) are calculated for a system of $N = 1000$ and compared with a number of experimental and simulation results.

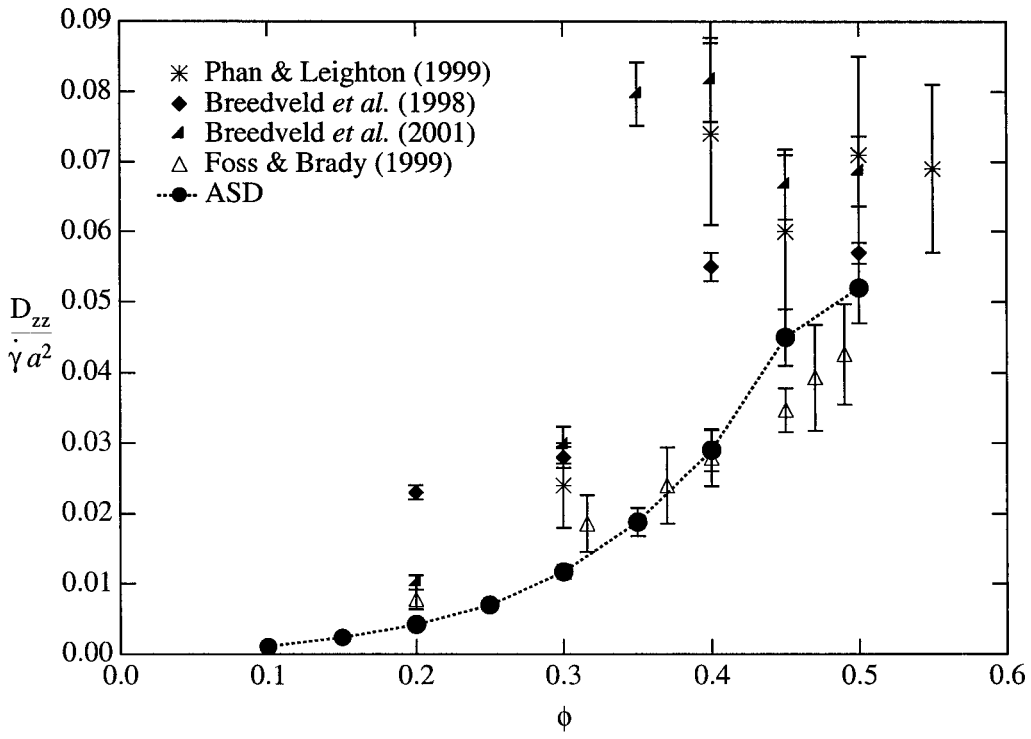

Figure 4.7: The dependence of D_{zz} on the volume fraction ϕ. Accelerated Stokesian Dynamics results (ASD) are calculated for a system of $N = 1000$ and compared with a number of experimental and simulation results.

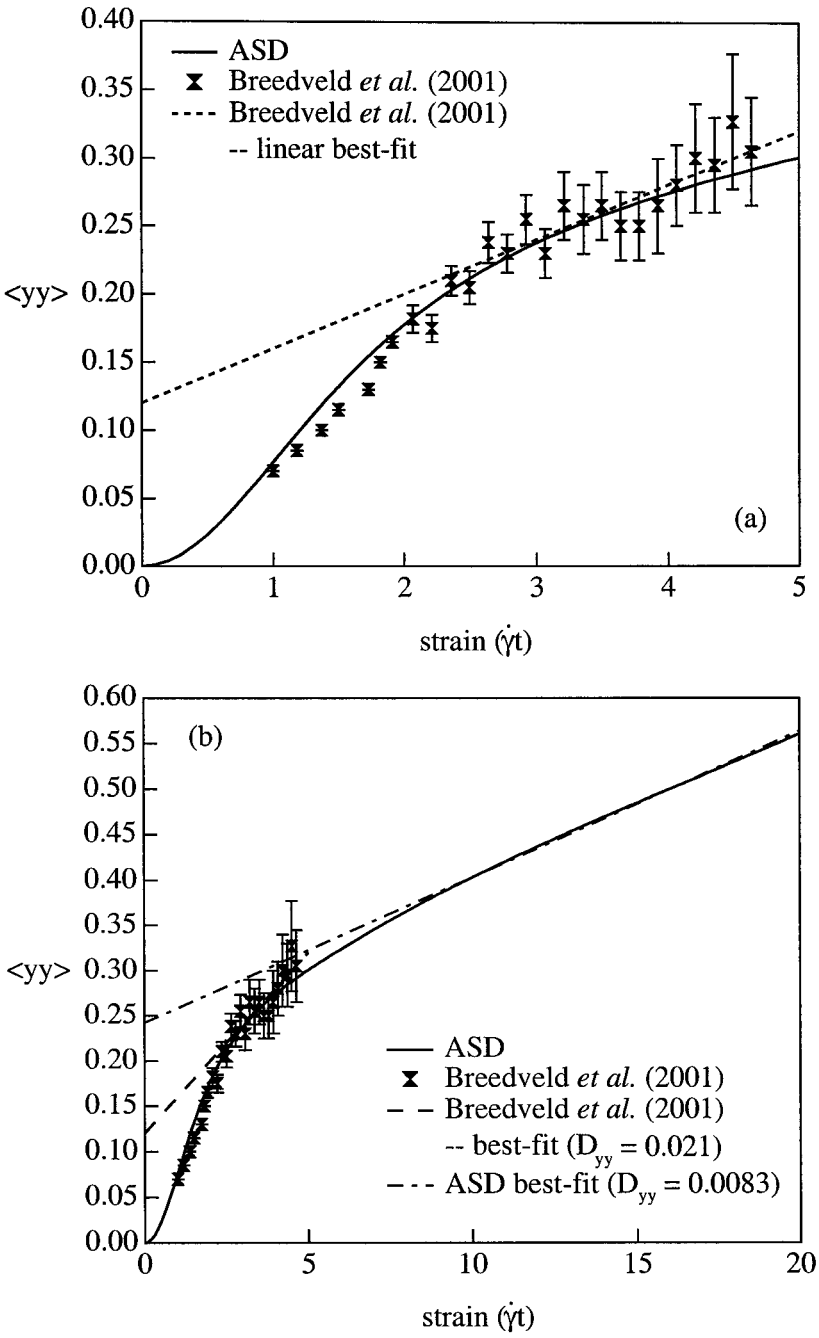

Figure 4.8: The mean-square displacement $\langle yy \rangle$ as calculated from ASD simulations for $\phi = 0.20$, $N = 1000$, is compared with the equivalent results given by Breedveld *et al.* (2001) for strains of 5 (a) and 20 (b). The resulting diffusivities and slopes of the mean-square displacement curve are also shown.

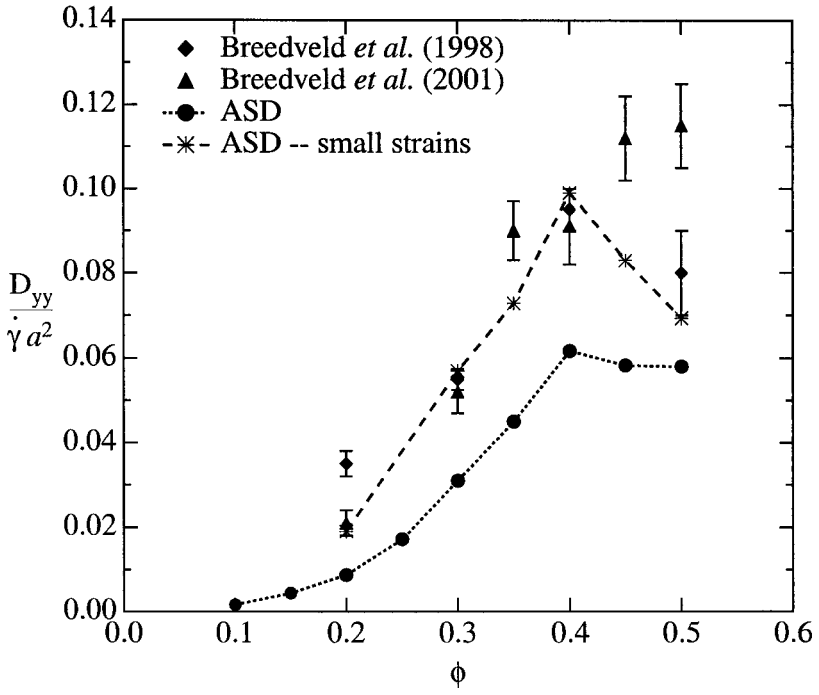

Figure 4.9: The self-diffusion coefficient D_{yy} as calculated from ASD for long strains, short strains and compared with the experimental results (corresponding to the same short strains) given by Breedveld *et al.* (2001).

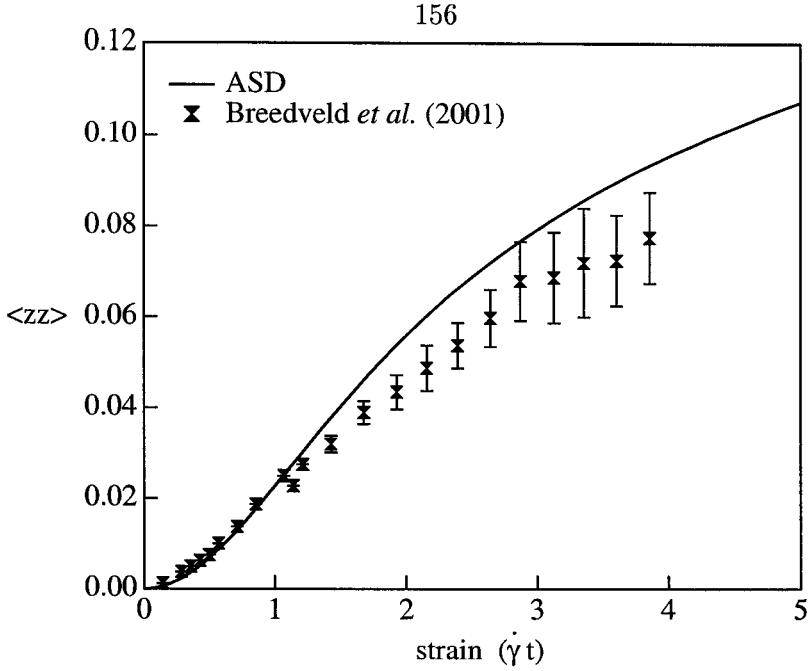

Figure 4.10: The mean-square displacement $\langle zz \rangle$ as calculated from ASD simulations for $\phi = 0.20$, $N = 1000$, is compared with the equivalent results given by Breedveld *et al.* (2001) for strains of 5.

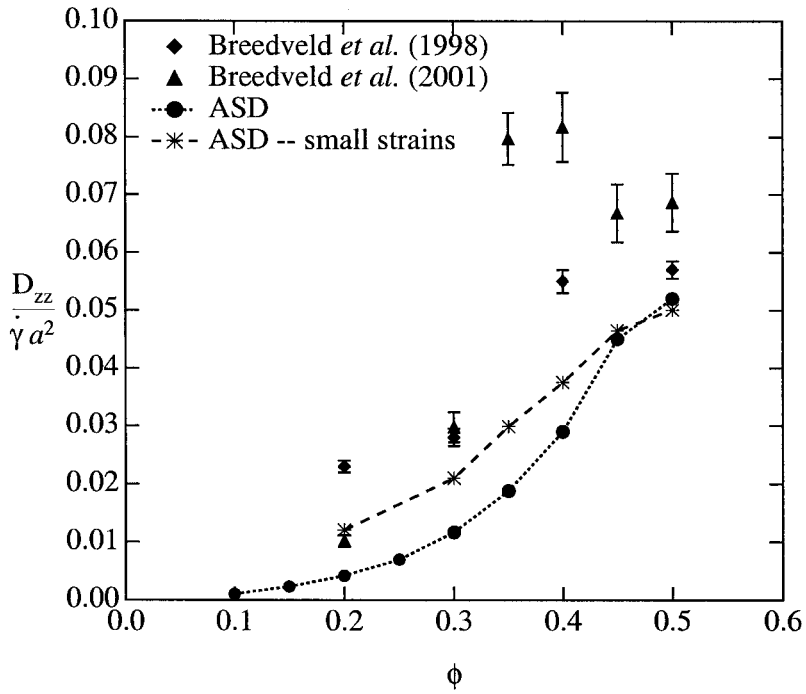

Figure 4.11: The self-diffusion coefficient D_{zz} as calculated from ASD for long strains, short strains and compared with the experimental results (corresponding to the same short strains) given by Breedveld *et al.* (2001).

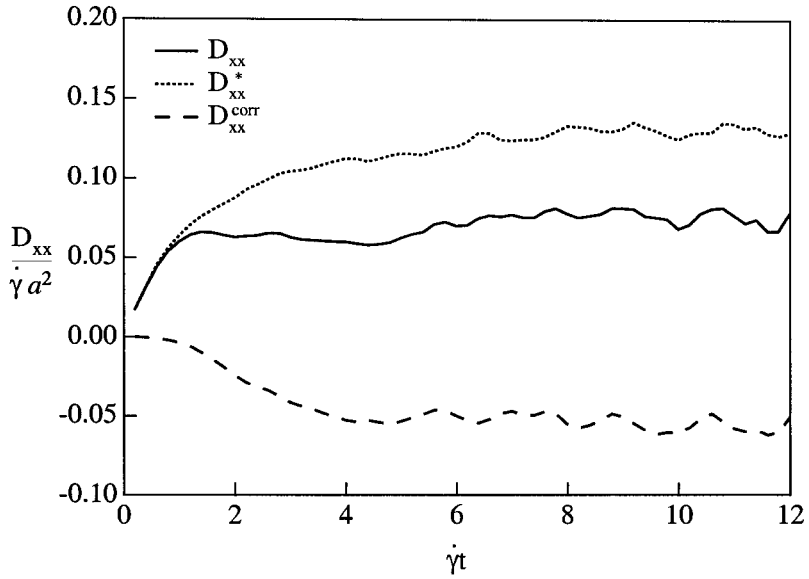

Figure 4.12: The self-diffusivity in the longitudinal direction, D_{xx}, is plotted as a function of strain for a system of $N = 1000$, $\phi = 0.35$. The values of the two terms contributing to D_{xx} according to (4.18a) are also given.

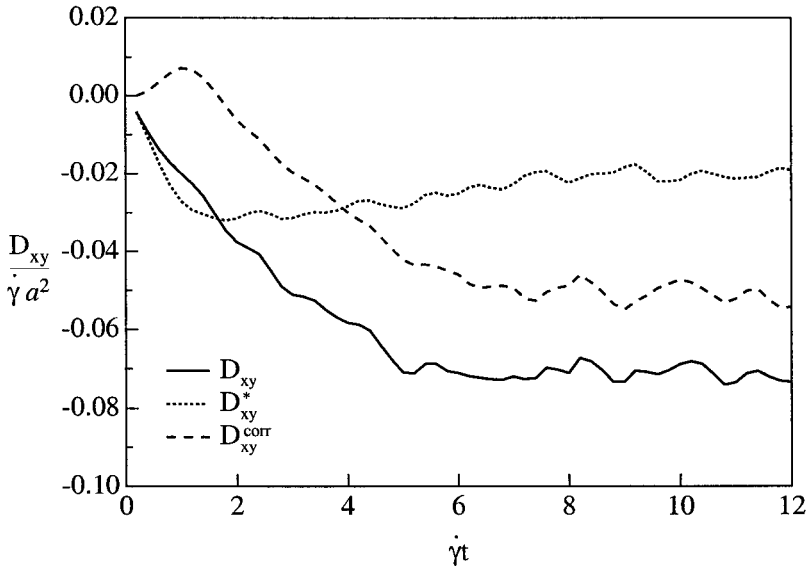

Figure 4.13: The cross diffusivity, D_{xy}, is plotted as a function of strain for a system of $N = 1000$, $\phi = 0.35$. The values of the two terms contributing to D_{xy} according to (4.18b) are also given.

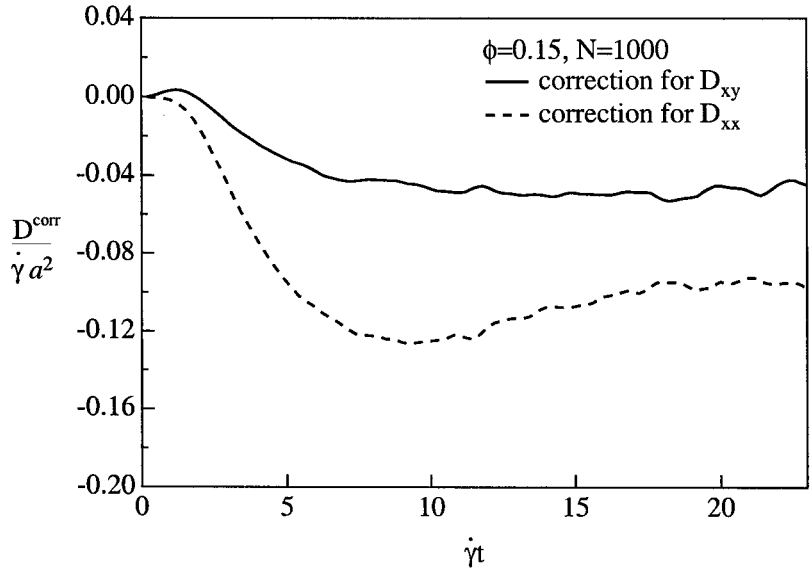

Figure 4.14: The corrective terms, D_{xx}^{corr} and D_{xy}^{corr}, for a system of $N = 1000$ and a relatively small volume fraction $\phi = 0.15$ are plotted as a function of strain.

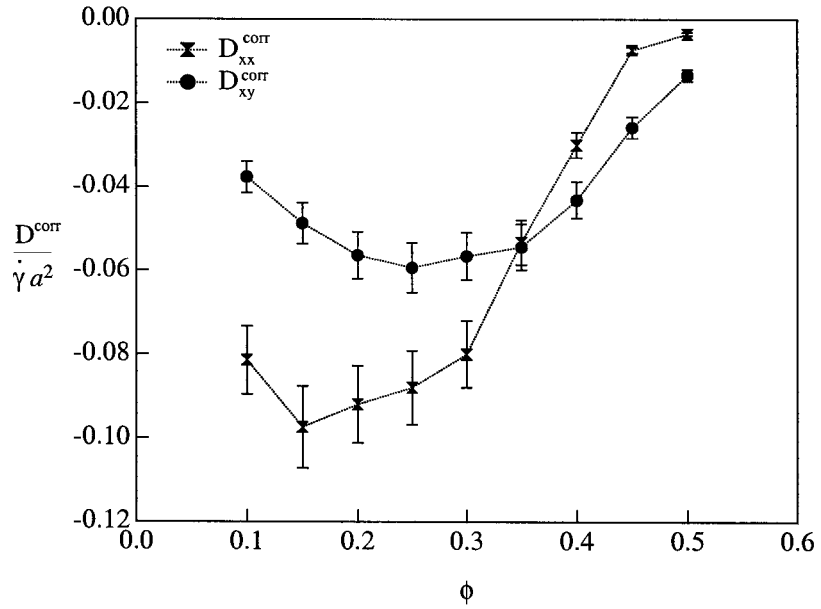

Figure 4.15: The corrective terms, D_{xx}^{corr} and D_{xy}^{corr}, for a system of $N = 1000$ are plotted as a function of the volume fraction.

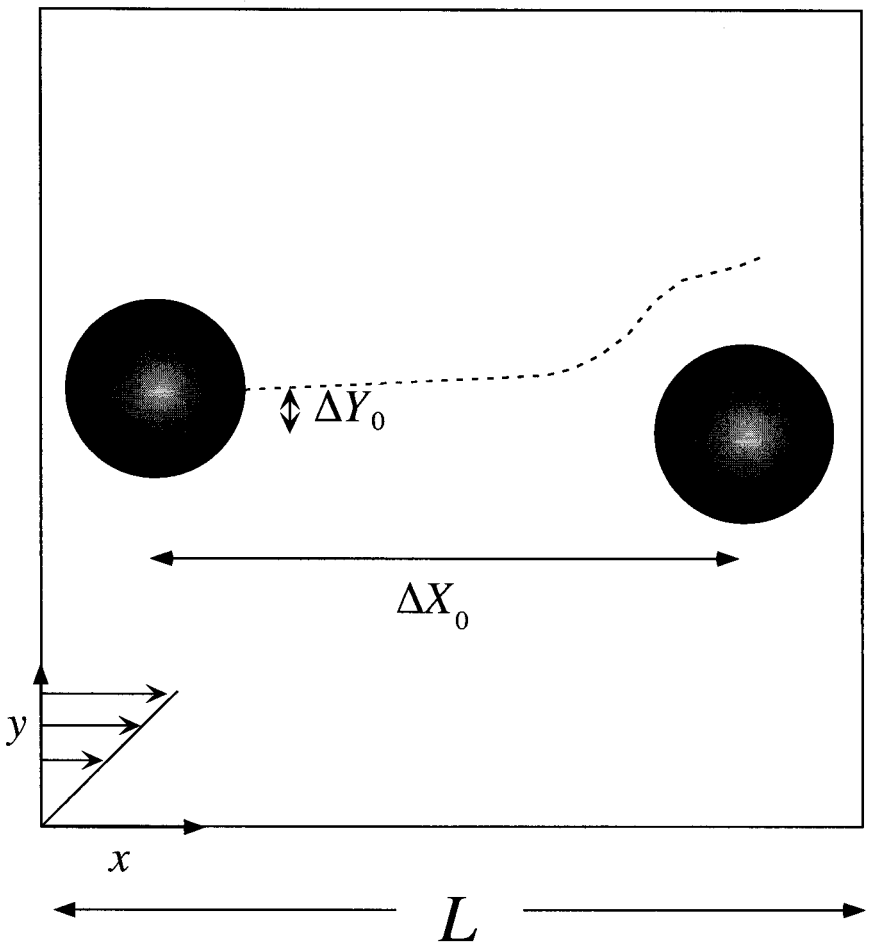

Figure 4.16: Two particles undergoing simple shear flow in a periodic cell of length L—the other two dimensions of the periodic cell are assumed infinite, so that the two particles do not interact with their mirror images in the y and z directions. The two particles are initially placed at distance $\Delta X_0 = -10a$, $\Delta Y_0 = 0.5a$ and $\Delta Z_0 = 0$, independently of the value of L.

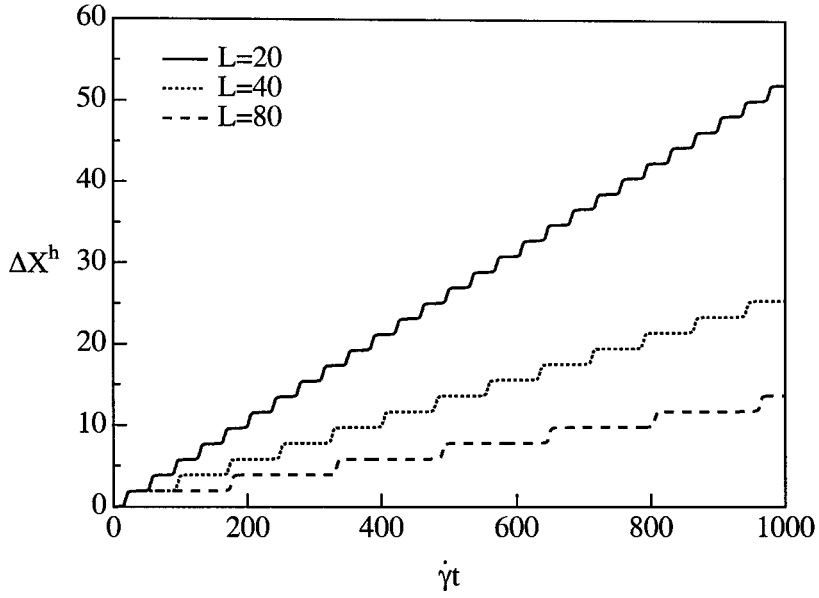

Figure 4.17: The net non-affine displacement X^h for one of a pair of particles subject to shear flow is plotted as a function of strain for different values of $L = 20a$, $40a$ and $80a$.

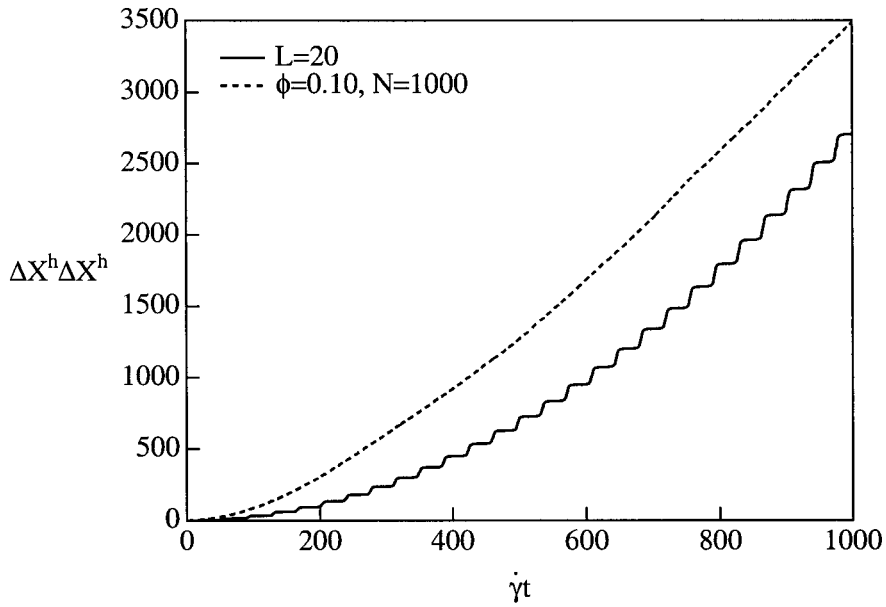

Figure 4.18: The square non-affine displacement $X^h X^h$ corresponding to the $L = 20a$ case of the previous figure. The mean-square displacement for a system of 1000 particles at $\phi = 0.10$ is also shown.

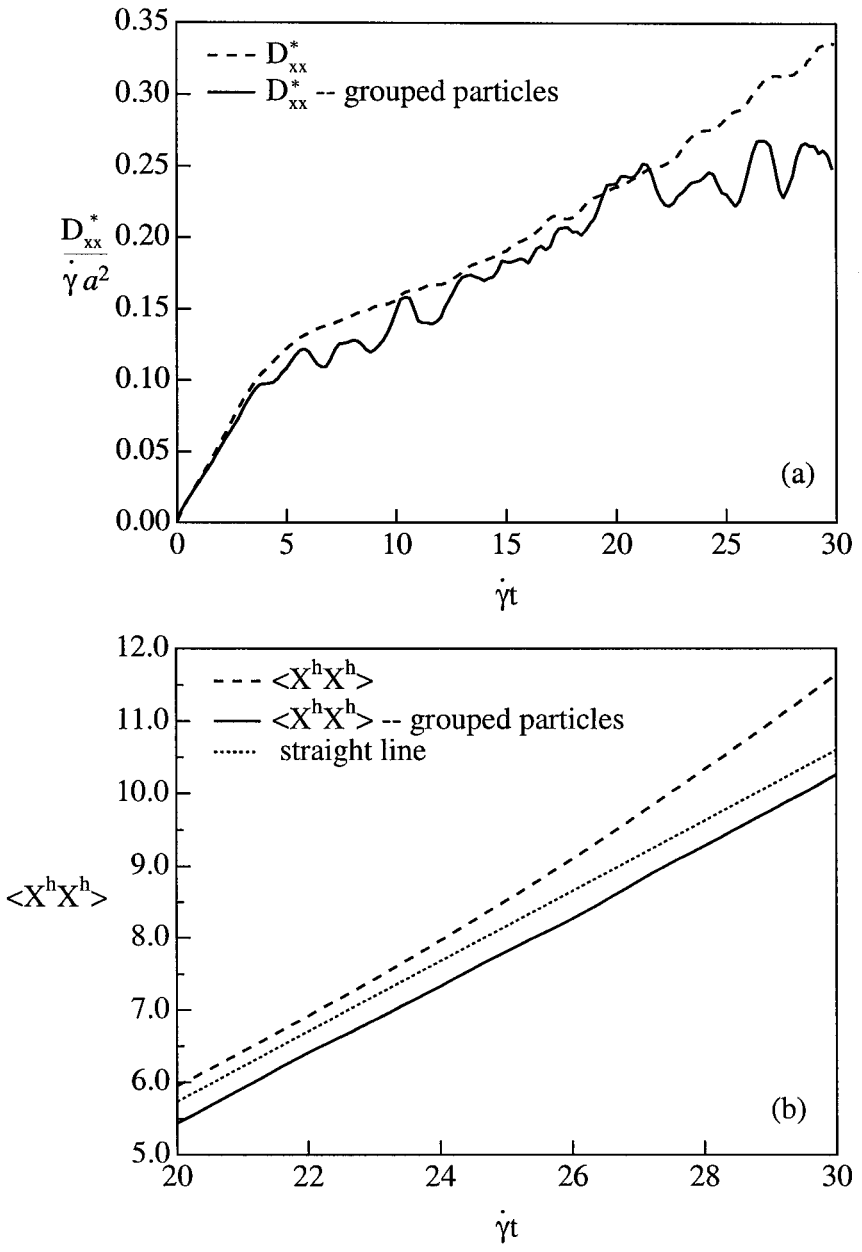

Figure 4.19: The effect of the particle grouping on the calculation of the non-affine diffusivity $D^{\star}_{xx}$. (a) The values of $D^{\star}_{xx}$ are presented as a function of strain for a system of 100 configurations of $N = 1000$ at $\phi = 0.15$, and compared with the same diffusivity when the particles are first arranged in groups of 500 particles. (b) The corresponding mean-square displacements for these two cases are also presented and compared.

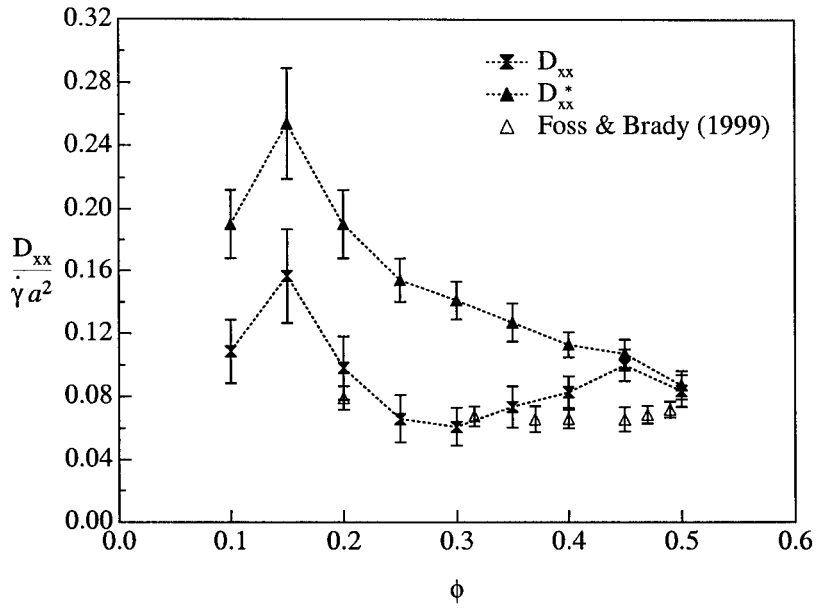

Figure 4.20: The self-diffusion coefficient D_{xx} plotted as a function of the volume fraction. The values of $D^{\star}_{xx}$ are also presented and compared with the simulation results of Foss & Brady (1999).

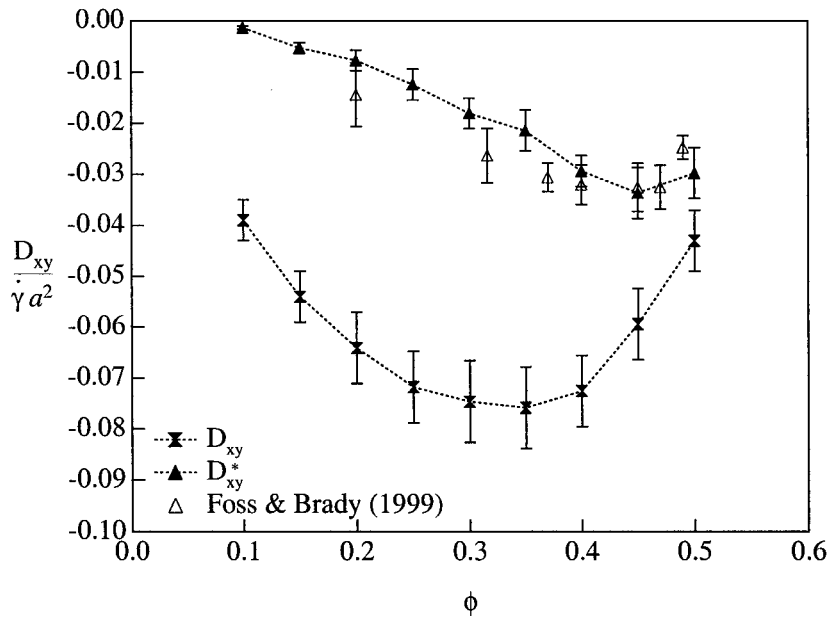

Figure 4.21: The self-diffusion coefficient D_{xy} plotted as a function of the volume fraction. The values of $D^{\star}_{xy}$ are also presented and compared with the simulation results of Foss & Brady (1999).

Chapter 5

Conclusions

We have developed a new method for calculating the hydrodynamic interactions among particles in a suspension at small Reynolds number, based on the Stokesian Dynamics method but with a significantly more favorable computational cost of $N \ln N$. This new method, referred to as Accelerated Stokesian Dynamics (ASD), avoids the expensive calculation of the far-field mobility matrix in favor of the direct calculation of the far-field hydrodynamic force, and uses a carefully chosen preconditioning scheme to dramatically reduce the computational cost of any iterative matrix inversions. ASD was first validated through test problems in the rheology of both structured and random suspensions, and accurate results were obtained with much larger numbers of particles (typically on the order of 1000). With access to larger systems, the high-frequency dynamic viscosities and short-time self-diffusivities of random suspensions for volume fractions above the freezing point were studied.

The method was then applied to the study of sheared non-Brownian suspensions. The relative viscosity, first and second normal stress differences and particle pressure were determined as a function of the volume fraction and were found to be in satisfactory agreement with experiment. The ratio of the normal to shear stress and the ratio of normal to "excess" shear stress (defined as the suspension viscosity minus the high-frequency dynamic viscosity) were also determined and it was found that the normal stresses were better, but not perfectly, correlated with the excess shear stress, pointing to the fact that the origin of both is the deformed microstructure. The pair-distribution function

determined from our simulations clearly showed anisotropy in the microstructure, leading to non-Newtonian rheological behavior. Using the theoretical arguments of Brady & Morris (1997), the dominant contribution to the stress was attributed to pairs of particles near contact, and an appropriate rescaled shear-stress was thus constructed. This simple scaling successfully captured the microstructural and volume fraction dependence and reduced the scaled shear stress to a constant. Access to larger systems also allowed the study of denser suspensions—with volume fractions up to 0.60. For volume fractions above 0.50 the system ordered into strings, while surprisingly at even higher volume fractions ($\phi = 0.60$) the system was again disordered. This behavior is reminiscent of molecular dynamics simulations of hard-spheres in the metastable regime (above the freezing point $\phi \approx 0.494$ and below the glass transition $\phi \approx 0.58$) where it is impossible to equilibrate the system for long times without partial order.

Shear-induced diffusion was subsequently studied and the complete diffusivity tensor was calculated. The diffusivities in the velocity gradient and vorticity directions, D_{yy} and D_{zz}, were determined as a function of the volume fraction and compared with available experimental results. While both appear to be increasing functions of the volume fraction for small to intermediate ϕ, D_{yy} plateaus at high ϕ, in agreement with previous experiments. The quantitative agreement between experiment and simulation, however, was not always satisfactory and it is suggested that the difference is associated with correctly identifying the diffusive regime. The presence of a long correlation time during which the mean-square displacements show first a quadratic and then a transitional behavior was identified as a main difference between sheared-induced diffusion of non-Brownian particles and diffusion of Brownian particles. The longitudinal and cross diffusivities were also presented as a function of volume fraction. Careful construction of the convection-diffusion equation demonstrated that a coupled term, coupling the non-affine and affine displacements, is present; a term that was erroneously omitted in previous studies. The corrected longitudinal and cross diffusivities were thus calculated and an additional limitation, caused by the finite size of the simulation cell, was discussed.

The ASD methodology opens up an entire new class of suspension problems that can be routinely investigated and its power was demonstrated with the study of diffusion

and rheology in non-Brownian suspensions. Its extension to particles of different sizes or particles of non-spherical shape should be relatively straightforward. The effect of polydispersity can thus be studied and its impact on the rheology and structure of concentrated suspensions can be addressed. The main principles of the method can also be applied to a broader field of particle flow problems, e.g., it can be modified to include particle and fluid inertia. The inclusion of fluid inertia (finite Reynolds number) adds further complications since the governing equations are no longer linear, but existing fast spectral methods can potentially replace the fast PME algorithm used here and allow the extension of the method to at least moderate Reynolds numbers. It is our hope that a wide range of problems can and will be addressed with ASD in the future.

Appendix A

The ASD Method: Instructions and General Considerations

A.1 General Description

The general idea is to construct an order N algorithm that maintains most characteristics of the conventional Stokesian Dynamics (SD) algorithm. There are two main differences between this version and conventional SD. First, is the calculation of the far-field hydrodynamic force. The calculation of this force is generally an order (N^2) operation since the contributions of all particle pairs can be of importance (disturbances decay very slowly). In order to accelerate this procedure, the Ewald sums are rewritten in a slightly different form and it is observed that by changing the value of the splitting parameter α (corresponding to ξ in SD), the real-sum contribution can be evaluated accurately by using only the nearest neighbors contributions (order $N\times$small number of nearest neighbors). The wave-space sum on the other hand, can also be evaluated accurately by rewriting it as a Fast Fourier sum and calculating it with a conventional FFT method. The number of operations for this procedure depends on the number of FFT points, and by careful balancing, it can be reduced to order N. This new calculation of the far-field contribution is combined with an iteration procedure and application of Faxén's laws to give the far-field force (and not the resistance matrix). The second difference lies in the inversion of the resistance matrix, which is now done iteratively. By using the incomplete Cholesky factor as a preconditioner, the number of iterations required is small and therefore the

matrix inversion is also reduced to an order N procedure. The motivation and theoretical background for this new algorithm is presented in chapter 2. Here we present an overview and flow chart and, in addition, give some details and practical considerations about the code itself.

A.2 Flow Chart

The flow-chart of the algorithm is presented in figure A.1 and is described in some detail below. This procedure corresponds to one time-step of the algorithm, where the initial positions and velocities of the particles are known.

Step 1:

An initial guess is made for the far-field hydrodynamic force/torque/etc. on each particle. The values of the far-field hydrodynamic force at the previous time step are used as this initial guess for every time-step but the very first one. For the very first time-step the initial guess is arbitrary, and its choice only affects the rate of convergence of the algorithm for this given time step.

Step 2:

For the given hydrodynamic force/torque/etc. on each particle, the hydrodynamic contributions to the fluid velocity (and its derivatives) are calculated. These contributions are expressed as a wave- and real-space sum over all N particles. The real-space part is calculated analytically in a pairwise fashion (formulae are given in appendix C). Although this is an $O(N^2)$ operation as it includes contributions from all particles, an appropriate choice of the splitting parameter allows the truncation of the sum to include only neighboring particles and thus become an $O(N)$ operation. The wave-space sum is calculated as a Fast Fourier sum on a fixed grid. Standard FFT routines are used and the manner in which the force is distributed from the center of the particle to the grid is presented in appendix B. A simple Lagrangian interpolation is further used to calculate the fluid velocity at each particle's center from the velocity on neighboring grid points.

Step 3:

From the fluid velocity at the center of the particle, the hydrodynamic force on the particle is calculated utilizing Faxén's laws. This completes the first iteration loop, since from an initial guess for the hydrodynamic force (Step 1), a new value is obtained. Two different approaches can be used to guarantee convergence: A simple underrelaxation scheme that repeats the calculation with the new value of the hydrodynamic force, or a standard iterative inversion package (GMRES is used here). The underrelaxation scheme has a much slower convergence rate when the initial guess is not very good, which is the case for the first time step and for very dense suspensions, where strong lubrication interactions change the forces on the particles significantly from one time-step to the next. On the other hand, it behaves favorably for low volume fractions when the hydrodynamic force changes very slowly. GMRES generally converges faster to a solution of a given accuracy, regardless of the initial guess. Because of the minimum residuals used, however, the solution is approached from "different directions" and as a result is not as smooth as a function of iteration (unless a sufficiently small convergence criterion is used). This can have an effect when calculating properties for very low volume fractions, where some properties have values that are close to zero, and the use of a strict convergence criterion is then recommended (or the underrelaxation scheme). At the end of this iterative procedure the far-field hydrodynamic force/torque/etc. on a particle are known to the desired accuracy for a given set of particle velocities. (Note that by using Faxén's laws to calculate the new hydrodynamic force, the particle velocities are assumed known, since in principle $\boldsymbol{R}_{FU,ff} \cdot \boldsymbol{U}_p$ is calculated.) It is also noted that contrary to conventional SD the calculation of the far-field interactions is now repeated for every time step. Since the far-field force is calculated directly (using the current particle velocity), it is not possible to retain the same mobility (or resistance) tensor until the particle configuration changes significantly.

Step 4:

A sparse version of the near-field resistance matrix is constructed by taking into account only the nearest neighbors and by storing them appropriately. This is a straightforward calculation very similar to the SD calculation of the near-field lubrication matrix. The only difference is that a chaining-mesh is introduced to identify the nearest neighbors and store the resulting matrices in $O(N)$.

Step 5:

The system:

$$0 = \boldsymbol{R}_{FU,nf} \cdot (\boldsymbol{U}_p - \boldsymbol{u}^{\infty}) + \boldsymbol{F}_{ff} + \boldsymbol{F}_{ext} \tag{A.1}$$

is solved (for the case of simple shear flow the term $\boldsymbol{R}_{FE,nf} : \boldsymbol{E}^{\infty}$ is also included in the rhs of the equation of motion). First, an incomplete Cholesky preconditioner is constructed for $\boldsymbol{R}_{FU,nf}$ and is multiplied with both sides of A.1. The purpose of the preconditioner is to improve the convergence of the iterative procedure, since the near-field resistance matrix can be very ill-conditioned and expensive to invert, especially when studying shearing flows where the particle minimum separations are very small. A standard conjugate gradient iterative procedure is then followed and the new particle velocities are calculated. We note again that in this procedure the far-field force is calculated with the velocity of the previous time step; this can be regarded as simply a semi-explicit approach (since the resistance matrix is also calculated for the previous positions) and seems to work well for all problems studied. Alternatively, an additional iteration loop can be introduced which allows the use of the current velocity for the far-field calculation.

Step 6:

The particles are moved to their new positions and the procedure is repeated from step one. A fourth order Adams-Basforth scheme is used to obtain the new particle positions, as in conventional SD.

An additional note:

As was already mentioned, for a given configuration of particles the exact particle velocities and far-field forces can be calculated. Without changing the particle positions, one can converge both the far-field force (inner loop, steps 1-3) and the resulting velocities in an outer loop (by simply repeating the whole process with the particle positions fixed). Although GMRES is guaranteed to converge for the calculation of the far-field force in the inner loop, this straightforward iteration scheme for the velocity is not. In other words, when solving

$$0 = -\boldsymbol{R}_{nf}\boldsymbol{U}(t + \Delta t) + \boldsymbol{F}_{ff}(\boldsymbol{U}(t)),$$

the resulting velocities do not always converge (especially when the initial guess for $\boldsymbol{U}$ is not very good). This problem is easily addressed by relaxing the equation of motion to

$$0 = -(\boldsymbol{R}_{nf} + \boldsymbol{I}\beta)\boldsymbol{U}(t + \Delta t) + \boldsymbol{F}_{ff}(\boldsymbol{U}(t)) + \boldsymbol{I}\beta\boldsymbol{U}(t),$$

where β is an adjustable parameter. (We note here that even in the absence of convergence problems, $\beta = 1$ is necessary for the near-field matrix to be positive definite.) Typically values of $\beta = 2 - 4$ may be needed for the velocity scheme to be convergent. When the underrelaxation scheme is used for the calculation of the far-field force, the introduction of additional relaxation for the velocity is not necessary and $\beta = 1$ should be used. (The slower convergence for $\boldsymbol{F}_{ff}$ is sufficient to allow convergence of the velocities as well.)

A.3 Variables

NUMPART: Number of particles. The value of *NLIM* in the two header files should agree with the value of *NUMPART* in the input file.

*IN*3, *IN*5, *IN*6: Three, five and six times the number of particles—used for setting the dimensions of different property arrays.

MMAX: Maximum number of linked cells in each direction. The linked cells correspond to the "chaining mesh" (see chapter 2, Hockney & Eastwood, 1986) and their purpose is to group the particles in smaller sets so that the nearest neighbors can be located in order N.

MLINK: Actual number of linked cells in each direction (note: *MLINK* must be greater or equal to 3).

NNEIGH: Maximum number of closest (near-field) neighbors for any particle. The value of this variable defines the size of the near-field resistance matrix arrays and a very large value (combined with a large *NLIM*) can cause memory limitations. Its value is in close connection with *RCELLNF* (see below). Typical values for a 3-D dense system are ≈ 50, which is usually a conservative estimate—only for volume fractions

near close packing the number of neighbors approaches this value.

NBCELL: Maximum number of total neighbors—its value is generally larger than *NNEIGH* since it also includes the real sum neighbors.

NN2: Maximum number of all neighboring pairs. Again this value depends on *NBCELL* and it is the absolutely maximum number of pairs—before any cut-off procedure is applied.

NSQ1: Actual number of all neighboring pairs—its value depends on the cut-off radius *RCELLRS*.

NNX: Maximum number of near-neighboring pairs. This value now depends on *NNEIGH*.

NSQ1NF: Actual number of near-neighboring pairs—its value depends on the cut-off radius *RCELLNF*.

RCELLNF: The cut-off radius for the near-field interactions. In agreement with conventional SD the value 4.0 is used (but it can be easily relaxed to ≈ 3.5 to reduce the computational cost).

RCELLRS: The cut-off radius for the real-sum (far-field) interactions. Its value also depends on *MLINK*. For a linked cell with length of about $3 - 3.5$, the cut-off is usually $6.0 - 8.0$.

ITMAX: Maximum number of iterations for the inversion of $\boldsymbol{R}_{FU,nf}$.

TOL: Required tolerance for the inversion of $\boldsymbol{R}_{FU,nf}$ (corresponds to the accuracy of the residual calculation).

NCELL: Actual number of linked cells ($MLINK^3$).

OMEGA1: Relaxation parameter for the Faxén's iteration. For large dense systems a small value is necessary (typical values can be as low as 0.01). When GMRES is used this parameter is always 1.

$TOLFMAX$: The tolerance for the calculation of the far-field force. When using the relaxation parameter the actual tolerance is $TOLFMAX/OMEGA1$. When using GMRES this tolerance corresponds to a standard convergence criterion.

$ALPHA$: The splitting parameter for the calculation of the far-field interactions. Recommended values: Choose $MLINK$ so that $(XCELL/MLINK)$ is between $3.5 - 4$. Then use $ALPHA$ approximately equal to $\alpha = 10 - 12$, and $1 - 2$ FFT points per particle radius. Since the value of the splitting parameter is only important for the far-field calculation some of these conditions can be relaxed when using denser systems (where the relative error in the far-field calculation corresponds to a much smaller error to the overall calculation).

$FP(NLIM)$: Array of the interparticle force on each particle. To these values the external and the far-field force are eventually added.

$DIS(4, NN2)$: Array that keeps DX, DY, DZ and DR, for each pair of particles (for particles with $DR < RCELLRS$).

$ID(2, NN2)$: Identities of the 2 particles consisting each pair (again following $RCELLRS$).

$DISNF(4, NN2)$: Same as DIS, but now only particles with $DR < RCELLNF$ are included (near-field distances).

$IDNF(2, NN2)$: Same as ID, but following $RCELLNF$.

$LIST(IN3)$: Linked-List Array.

$IHEAD(MMAXCU)$ Head particle in each cell $(MMAXCU = MMAX^3)$.

$MAP(MMAX26)$ Map of neighboring cells for use in the linked list calculation $(MMAX26 = 26MMAX)$.

$NLIST(NLIM, NNEIGH)$: List of structure for the sparse version of the resistance matrix: $NLIST(I, 1) = J$ means that particle J is the first neighbor of particle I, $NLIST(I, 2) = J$ means that particle J is the 2nd neighbor of particle I, etc.

$NALOC(NLIM)$: The actual number of neighbors (near-field) of each particle (note: $NALOC(I)$ must be less than $NNEIGH$).

$IDL(2, NNX)$: Matrix that maps ID-pairs into the sparse matrix structure. $IDL(1, KK) = II$, means that for the first particle of the pair KK the second particle of the pair is neighbor numbered II (equivalently $IDL(2, KK) = JJ$).

$IORDER(NLIM)$: The ordered array of particles (according to reverse Cuthill-McKee ordering): $IORDER(I) = J$ means that the order of particle I—after the re-ordering—is J.

$IODINV(NLIM)$: The inverse of the re-ordering array, such that:

$IODINV(IORDER(I)) = I$

$XCELL$, $YCELL$, $ZCELL$: The dimensions of the unit cell (in particle radii).

$XC12$, $YC12$, $ZC12$: Half of the dimensions of the unit cell.

$GAMMA$: The shear-rate $\dot{\gamma}$.

$GAMT$: The total strain ($\dot{\gamma}dt$)—when the cell is returned to its undistorted shape (at $t = 1$) $GAMT$ is set again to zero (just as in conventional SD).

HGT: $YCELL \times GAMT$

EPS: The cell distortion: $HGT/YCELL$ (values between 0 and 1).

$FACVISC$: Corresponds to β (see description for subroutine calvelo.f) and is part of the input file. Value of 1.0 is used for the underrelaxation scheme—larger values (up to ≈ 4) are needed when GMRES is used. For some sedimentation problems (e.g., dense cubic arrays) a large value MUST be used or the far-field does not converge (roughly $FACVISC >$ 1/sedimentation velocity, so values up to 100 may be needed). This is a special case where $R_{nf} = 0$ and as a result the "outer-loop" (mentioned in the additional note of the flow-chart) is not guaranteed to converge. (However, for this special case the sedimentation velocity can be calculated directly and no iteration

procedure is actually necessary—it is simply mentioned here to draw attention to the some limitations of the convergence scheme.)

$LDIS(IN6)$: Array that keeps track of how many times the particles leave and return into the unit cell (for positions) and of how many times the particles have completed a full 2π rotation (for angular positions).

$VELJ(IN6)$: Initial guess and solution for the particle disturbance velocities: $\boldsymbol{U}_p - \boldsymbol{u}^\infty$ (including angular velocities).

$U(IN6)$: Particle total velocities.

$UDIFF(IN6)$: Particle disturbance velocities.

$UOLD(IN6, 4)$: The last four values of the particle velocities.

$X(IN6)$: Particle positions (and angular positions).

$XOLD(IN6, 4)$: The last four values of the particle positions.

$F(IN3)$: The far-field hydrodynamic forces (only forces!).

$T(IN3)$: The far-field hydrodynamic torques.

$S(IN5)$: The far-field hydrodynamic stresslets.

$Ursum1(IN3)$: The real-space contribution to the fluid velocity (note: only 3 components for fluid velocity).

$delUrsum1(IN3 \times 3)$: The real-space contribution to the first derivative of the fluid velocity (9 components for each particle).

$del2Ursum1(IN3)$: The real-space contribution to the ∇^2 of the fluid velocity (3 components for each particle).

$del3Ursum1(IN3 \times 3)$: The real-space contribution to the ∇^2 of the first velocity derivative (9 components).

Lx, $Lxmax$: Actual and maximum number of FFT points in the x-direction of the unit cell (note: needs to be a power of 2! Choose so that there are 1-2 FFT points per particle radius). They must also have the same value in the input file and the program subroutines.

Ly, $Lymax$, Lz, $Lzmax$: Same for y- and z- directions.

$ux(Lx, Ly, Lz)$: The x-component of the wave-space part of the fluid velocity on the FFT grid.

$uy(Lx, Ly, Lz)$, $uz(Lx, Ly, Lz)$: Same for y and z components.

$fx(Lx, Ly, Lz)$: The x-component of the force distribution on the FFT grid.

$fy(Lx, Ly, Lz)$, $fz(Lx, Ly, Lz)$: Same for y and z components.

$uff(IN3)$: The wave-space far-field contribution to the fluid velocity at the center of each particle.

$del3uff(IN3 \times 3)$: The wave-space far-field contribution to the first derivative of the fluid velocity at the center of each particle.

$del2uff(IN3)$, $del3uff(IN3 \times 3)$: Remaining derivatives.

$RFU(IN6, N6NBR)$: The near-field sparse version of the resistance matrix. Its dimensions are not $6N \times 6N$ as in conventional SD—now only the non-zero values are taken into account and the matrix is arranged in a $6N \times 6NNEIGH$ array.

$RFE(IN6, N5NBR)$: The similarly arranged near-field sparse version of $\boldsymbol{R}_{FE,nf}$ (now, $N5NBR = 5NNEIGH$).

$RSE(IN5, N5NBR)$: Same for $\boldsymbol{R}_{SE,nf}$.

A.4 Subroutines

adlub3d.f: Calculates the near-field (lubrication) contribution. The near-field matrices RFU, RFE and RSE are calculated by calling subroutine rlub for each pair of

neighboring particles (very similar to conventional SD). Difference: An "arbitrary" number is added to the diagonal of RFU (and subtracted from the force balance) so that the matrix can be inverted (and convergence is guaranteed—see above).

caldist3d.f: Calculates the distances between pairs of particles and checks for overlaps. Again very similar to old version. Difference: It rearranges the particle pairs in two distance arrays (DIS, $DISNF$), keeping only the ones with distances less than the respective cut-off radii ($RCELLRS$, $RCELLNF$).

calstrs3d.f: Calculates the particle stress: $RSU \cdot U + RSE : E$. Now this corresponds to the near-field particle stress (since RSU, RSE are the near-field matrices) and the far field stresslet (S) is added to that value to give the total stress.

calvelo3d.f: This is the subroutine where the new particle velocities are calculated. This part of the code has been changed significantly.

$$0 = -\left(\boldsymbol{R}_{FU,nf}(t) + \beta \boldsymbol{I}\right) \cdot \left(\boldsymbol{U}_p - \boldsymbol{u}^{\infty}\right)(t + \Delta t) + \boldsymbol{F}_{ff}(t) + \boldsymbol{F}_{ext} + \beta \left(\boldsymbol{U}_p - \boldsymbol{u}^{\infty}\right)(t)$$

is now solved. $\boldsymbol{F}_{ff}$ is calculated independently and just added as an external force. The term β is added to the diagonal of RFU so that inversion is possible (otherwise RFU can have very small values on the diagonal and/or not be positive definite). RFU is then inverted following an iterative procedure (see linbcg for inverting procedure).

fastlongrandom.f: Controls the calculation of the Fourier space part of the far-field velocities and their derivatives. It controls the following subroutines:

offlinedistr.f: Distributes the force, torque, stresslet from each particle to a 3-D grid set on the unit cell. The distribution preserves the force balances and for each particle a mesh of $5 \times 5 \times 5$ grid points—centered at the nearest grid point—is used.

fft.f: This subroutine is a typical FFT-solver—it solves for the velocities on a grid when the forces on the same grid are known (note: you need to change $Lmax$

before each compilation).

interpolate.f: Interpolates from the grid velocities to the velocities at the center of each particle using simple Lagrangian interpolation.

setrealsum.f Controls the calculation of the real-space part of the particle velocities. For each pair of particles it calculates analytically (through subroutine realsum.f) the contribution to each particle's velocity and velocity's higher derivatives.

genrcm.f: Finds the reverse Cuthill-Mckee ordering and returns the values of array *IORDER* (uses subroutines rcm.f, roots.f and fnroot.f).

linbcg.f: Performs the iterative procedure for the calculation of the new particle velocities (is called from calvelo). It controls the following subroutine:

inchol.f: Calculates the incomplete Cholesky preconditioner. When the incomplete Cholesky breaks down, a sufficiently large number is added to the diagonal of *RFU* until no breakdowns occur.

prog20.f: Constructs the chain-linked lists.

sdmainlink3d.f: Main program.

traject3d.f: Calculates the new positions of the particles (4th order scheme—exactly as in conventional SD).

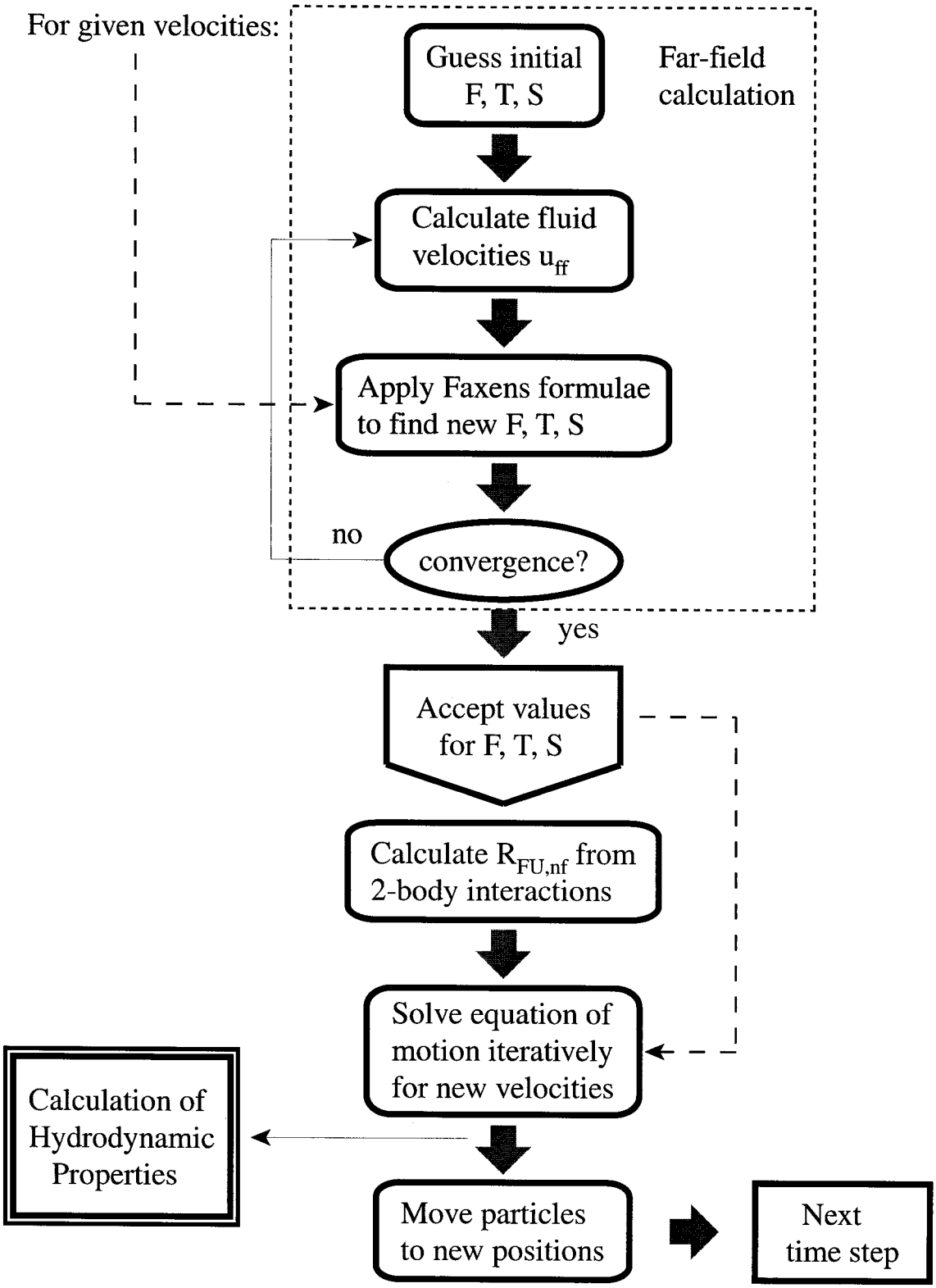

Figure A.1: The ASD method flowchart.

Appendix B

The Force Distribution on the Grid

We briefly describe the process of distributing a force/torque/etc. from the particle's center to a grid located around the particle. As was mentioned in chapter 2, the starting point is a truncated version of the Taylor series expansion of the force. Thus, the net force (and higher force moments) are conserved when transferred from the particle's center to a fixed grid. To schematically demonstrate this procedure, assume a particle located at position (x, y, z) with a simple point force F^0 acting on its center. A grid, with grid distances, dx, dy and dz, is also surrounding the particle (figure B.1). If the position of the particle coincides with a grid point, the point force is simply applied to the corresponding grid point. Since the force remains at the actual center of the particle, all net moments are distributed correctly by construction. In a more general case, however, the center of the particle will not coincide with a grid point and the force distribution will not be as simple. For the particle of figure B.1 it is assumed that its z-coordinate coincides with a grid point (z^0) while its x and y coordinates do not. The nearest grid points can thus be identified as x^0, y^0. Assigning all the force to the nearest grid point (x^0, y^0, z^0) satisfies only the net-force balance ($O(1)$ approach—as demonstrated in figure B.1a). Extending the assignment to more grid points allows both the net-force balance and the balance of higher force moments to be satisfied. This procedure is demonstrated in figure B.1(b)-(d). The distance from the nearest point (0) is denoted as dx^0 and dy^0. Figure B.1(a) simply presents the transfer of the net force to the nearest grid point. Figures B.1(b) and (c) present the additional force assignments that maintain the correct first moment (xF^0

and yF^0 for the two-dimensional case). Such a distribution is not unique (since for this case only 3 equations are satisfied with up to 25 unknowns). Symmetry considerations significantly reduce the number of equations, and, in addition, where possible, a one-dimensional finite difference approximation is used. It is thus assured that the "correction" of a given moment does not introduce any lower moments. The approximation of figure B.1 is truncated at the first-moment level. The force distribution presented in B.1(d) satisfies the net-force and net-first-force-moment balance, but has a non-zero second and higher moments. The level of approximation used in the algorithm maintains moments up to the third; for a given component of the grid force then, and the full 3D case, 20 equations can be formulated: one of zeroth order, 3 of first order (x, y and z), 6 of second order (x^2, y^2, z^2, xy, xz, yz) and 10 of third order (x^3, y^3, z^3, x^2y, x^2z, xyz, y^2x, y^2z, z^2y, z^2x). We will now present the form of these 20 equations for the distribution of a point-force and a doublet.

Force: F_i

The basic equation for the distribution from the particle to the grid is

$$F_i^0 e^{-2\pi \mathrm{i}(\boldsymbol{k}\cdot\boldsymbol{r}^0)} = \sum_{nodes_\gamma} f_i^\gamma e^{-2\pi \mathrm{i}(\boldsymbol{k}\cdot\boldsymbol{r}^\gamma)},$$

where $\boldsymbol{r}^0 = (x^0, y^0, z^0)$ is the position of a particle's center, $\boldsymbol{r}^\gamma = (x^\gamma, y^\gamma, z^\gamma)$ the grid-point positions and F_i^0, f_i^γ, the i-component of the particle and grid-distributed force respectively. Expanding the exponential terms in Taylor series about $\boldsymbol{r}^0$ on the left and $\boldsymbol{r}^\gamma$ on the right, we get:

$$\begin{aligned} &F_i^0 \left(1 + 2\pi \mathrm{i} k_l x_l^0 - 2\pi^2 k_l k_m x_l^0 x_m^0 + ..\right) \\ &= \sum_{nodes\gamma} f_i^\gamma \left(1 + 2\pi \mathrm{i} k_l x_l^\gamma - 2\pi^2 k_l k_m x_l^\gamma x_m^\gamma + ..\right). \end{aligned}$$

By matching terms, up to order $O(k^3)$ the following equations are obtained:

$$F_i^0 = \sum_\gamma f_i^\gamma,$$

$$x^0 F_i^0 = \sum_\gamma x^\gamma f_i^\gamma,$$

$$y^0 F_i^0 = \sum_\gamma y^\gamma f_i^\gamma,$$

$$z^0 F_i^0 = \sum_\gamma z^\gamma f_i^\gamma,$$

$$\left(x^0\right)^2 F_i^0 = \sum_\gamma \left(x^\gamma\right)^2 f_i^\gamma,$$

$$\left(y^0\right)^2 F_i^0 = \sum_\gamma \left(y^\gamma\right)^2 f_i^\gamma,$$

$$\left(z^0\right)^2 F_i^0 = \sum_\gamma \left(z^\gamma\right)^2 f_i^\gamma,$$

$$x^0 y^0 F_i^0 = \sum_\gamma x^\gamma y^\gamma f_i^\gamma,$$

$$x^0 z^0 F_i^0 = \sum_\gamma x^\gamma z^\gamma f_i^\gamma,$$

$$y^0 z^0 F_i^0 = \sum_\gamma y^\gamma z^\gamma f_i^\gamma,$$

$$\left(x^0\right)^3 F_i^0 = \sum_\gamma \left(x^\gamma\right)^3 f_i^\gamma,$$

$$\left(y^0\right)^3 F_i^0 = \sum_\gamma \left(y^\gamma\right)^3 f_i^\gamma,$$

$$\left(z^0\right)^3 F_i^0 = \sum_\gamma \left(z^\gamma\right)^3 f_i^\gamma,$$

$$\left(x^0\right)^2 y^0 F_i^0 = \sum_\gamma \left(x^\gamma\right)^2 y^\gamma f_i^\gamma,$$

$$\left(x^0\right)^2 z^0 F_i^0 = \sum_\gamma \left(x^\gamma\right)^2 z^\gamma f_i^\gamma,$$

$$\left(y^0\right)^2 x^0 F_i^0 = \sum_\gamma \left(y^\gamma\right)^2 x^\gamma f_i^\gamma,$$

$$\left(y^0\right)^2 z^0 F_i^0 = \sum_\gamma \left(y^\gamma\right)^2 z^\gamma f_i^\gamma,$$

$$\left(z^0\right)^2 x^0 F_i^0 = \sum_\gamma \left(z^\gamma\right)^2 x^\gamma f_i^\gamma,$$

$$\left(z^0\right)^2 y^0 F_i^0 = \sum_\gamma \left(z^\gamma\right)^2 y^\gamma f_i^\gamma,$$

$$x^0 y^0 z^0 F_i^0 = \sum_\gamma x^\gamma y^\gamma z^\gamma f_i^\gamma.$$

The first Moment: Doublet D_{ij}

The force distribution is based on the following equation:

$$-2\pi k_j D_{ij}^0 e^{-2\pi \mathrm{i}\left(\boldsymbol{k}\cdot\boldsymbol{r}^0\right)} = \sum_\gamma f_i^\gamma e^{-2\pi \mathrm{i}\left(\boldsymbol{k}\cdot\boldsymbol{r}^\gamma\right)}$$

Expanding again in Taylor series, we obtain:

$$\begin{aligned} &-2\pi k_j D_{ij}^0 \left(1 + 2\pi \mathrm{i} k_l x_l^0 - 2\pi^2 k_l k_m x_l^0 x_m^0 + ..\right) \\ &= \sum_\gamma f_i^\gamma \left(1 + 2\pi \mathrm{i} k_l x_l^\gamma - 2\pi^2 k_l k_m x_l^\gamma x_m^\gamma + ..\right). \end{aligned}$$

By matching terms, up to order $O(k^3)$, we obtain:

$$0 = \sum_\gamma f_i^\gamma$$

$$-D_{i1}^0 = \sum_\gamma x^\gamma f_i^\gamma,$$

$$-D_{i2}^0 = \sum_\gamma y^\gamma f_i^\gamma,$$

$$-D_{i3}^0 = \sum_\gamma z^\gamma f_i^\gamma,$$

$$-2x^0 D_{i1}^0 = \sum_\gamma \left(x^\gamma\right)^2 f_i^\gamma,$$

$$-2y^0 D_{i2}^0 = \sum_\gamma \left(y^\gamma\right)^2 f_i^\gamma,$$

$$-2z^0 D_{i3}^0 = \sum_\gamma \left(z^\gamma\right)^2 f_i^\gamma,$$

$$-\left(x^0 D^0_{i2} + y^0 D^0_{i1}\right) = \sum_\gamma x^\gamma y^\gamma f^\gamma_i,$$

$$-\left(x^0 D^0_{i3} + z^0 D^0_{i1}\right) = \sum_\gamma x^\gamma z^\gamma f^\gamma_i,$$

$$-\left(y^0 D^0_{i3} + z^0 D^0_{i2}\right) = \sum_\gamma y^\gamma z^\gamma f^\gamma_i,$$

$$-3\left(x^0\right)^2 D^0_{i1} = \sum_\gamma \left(x^\gamma\right)^3 f^\gamma_i,$$

$$-3\left(y^0\right)^2 D^0_{i2} = \sum_\gamma \left(y^\gamma\right)^3 f^\gamma_i,$$

$$-3\left(z^0\right)^2 D^0_{i3} = \sum_\gamma \left(z^\gamma\right)^3 f^\gamma_i,$$

$$-\left(\left(x^0\right)^2 D^0_{i2} + 2x^0 y^0 D^0_{i1}\right) = \sum_\gamma \left(x^\gamma\right)^2 y^\gamma f^\gamma_i,$$

$$-\left(\left(x^0\right)^2 D^0_{i3} + 2x^0 z^0 D^0_{i1}\right) = \sum_\gamma \left(x^\gamma\right)^2 z^\gamma f^\gamma_i,$$

$$-\left(\left(y^0\right)^2 D^0_{i1} + 2y^0 x^0 D^0_{i2}\right) = \sum_\gamma \left(y^\gamma\right)^2 x^\gamma f^\gamma_i,$$

$$-\left(\left(y^0\right)^2 D^0_{i3} + 2y^0 z^0 D^0_{i2}\right) = \sum_\gamma \left(y^\gamma\right)^2 z^\gamma f^\gamma_i,$$

$$-\left(\left(z^0\right)^2 D^0_{i1} + 2z^0 x^0 D^0_{i3}\right) = \sum_\gamma \left(z^\gamma\right)^2 x^\gamma f^\gamma_i,$$

$$-\left(\left(z^0\right)^2 D^0_{i2} + 2z^0 y^0 D^0_{i3}\right) = \sum_\gamma \left(z^\gamma\right)^2 y^\gamma f^\gamma_i,$$

$$-\left(x^0 y^0 D^0_{i3} + x^0 z^0 D^0_{i2} + y^0 z^0 D^0_{i1}\right) = \sum_\gamma x^\gamma y^\gamma z^\gamma f^\gamma_i.$$

This procedure can be applied to the potential dipole and higher moments in a very similar manner. The net-force is distributed with a leading error of $O(dx^4)$, the doublet with a leading error of $O(dx^3)$, while the potential quadrupole (highest moment maintained) with a leading error of $O(dx)$. If higher accuracy is desired a larger number of constrains (> 20) is necessary, corresponding to a larger number of grid points per particle. A $5 \times 5 \times 5$ set of grid points (centered around the grid-point nearest to the particle's center) is used here.

As was already mentioned, the distribution scheme is not unique but follows an efficient and general method based on one-dimension finite difference formulae. As is apparent from the matched-series expansion equations, force contributions obtained from different sources (e.g., the fact that the point force is not on the grid and a net doublet) can be combined. These combined forces are then distributed on the grid following a prespecified pattern which is maintaining the overall moments to the desired accuracy. Assuming that node (i, j, k) is the one closest to the center of the particle, the tables below present this prespecified pattern. Note that since the cell is sheared (and therefore the grid is sheared) a distortion parameter e ($\tan\theta = e$, with θ the angle between the y-side of the undistorted cell and the y-side of the distorted one; θ takes values between 0 and $\pi/4$ and e between 0 and 1) is also introduced and that all quantities have been normalized.

$$\sum_{\gamma} f^{\gamma} = 1$$

node	i, j, k
	1

$$\sum_{\gamma} x^{\gamma} f^{\gamma} = 1$$

node	$i-2$	$i-1$	i	$i+1$	$i+2$
	$\frac{1}{12dx}$	$-\frac{8}{12dx}$	0	$\frac{8}{12dx}$	$-\frac{1}{12dx}$

$$\sum_{\gamma} y^{\gamma} f^{\gamma} = 1$$

node	$j-2$	$j-1$	j	$j+1$	$j+2$
$i-2$	0	0	0	0	$-\frac{1}{12dx}e$
$i-1$	0	0	0	$\frac{8}{12dx}e$	0
i	$\frac{1}{12dy}$ $-\frac{1}{12dx}e$	$-\frac{8}{12dy}$ $+\frac{8}{12dx}e$	0	$\frac{8}{12dy}$ $-\frac{8}{12dx}e$	$-\frac{1}{12dy}$ $+\frac{1}{12dx}e$
$i+1$	0	$-\frac{8}{12dx}e$	0	0	0
$i+2$	$\frac{1}{12dx}e$	0	0	0	0

$$\sum_{\gamma} z^{\gamma} f^{\gamma} = 1$$

node	$k-2$	$k-1$	k	$k+1$	$k+2$
	$\frac{1}{12dz}$	$-\frac{8}{12dz}$	0	$\frac{8}{12dz}$	$-\frac{1}{12dz}$

$$\sum_{\gamma} (x^{\gamma})^2 f^{\gamma} = 1$$

node	$i-1$	i	$i+1$
	$\frac{1}{2dx^2}$	$-\frac{2}{2dx^2}$	$\frac{1}{2dx^2}$

$$\sum_{\gamma}(y^{\gamma})^2 f^{\gamma} = 1$$

node	$j-1$	j	$j+1$
$i-1$	$\frac{1}{4dx^2}e^2$ $-\frac{1}{4dxdy}e$	0	$\frac{1}{4dx^2}e^2$ $+\frac{1}{4dxdy}e$
i	$\frac{1}{2dy^2}$ $-\frac{1}{2dx^2}e^2$	$-\frac{2}{2dy^2}$	$\frac{1}{2dy^2}$ $-\frac{1}{2dx^2}e^2$
$i+1$	$\frac{1}{4dx^2}e^2$ $+\frac{1}{4dxdy}e$	0	$\frac{1}{4dx^2}e^2$ $-\frac{1}{4dxdy}e$

$$\sum_{\gamma}(z^{\gamma})^2 f^{\gamma} = 1$$

node	$k-1$	k	$k+1$
	$\frac{1}{2dz^2}$	$-\frac{2}{2dz^2}$	$\frac{1}{2dz^2}$

$$\sum_{\gamma} x^{\gamma} y^{\gamma} f^{\gamma} = 1$$

node	$i-2$	$i-1$	i	$i+1$	$i+2$
$j-1$	0	$\frac{1}{4dxdy}$ $-\frac{1}{4dx^2}e$	$\frac{1}{4dx^2}e$	$-\frac{1}{4dxdy}$ $+\frac{1}{4dx^2}e$	$-\frac{1}{4dx^2}e$
j	0	0	0	0	0
$j+1$	$-\frac{1}{4dx^2}e$	$-\frac{1}{4dxdy}$ $+\frac{1}{4dx^2}e$	$\frac{1}{4dx^2}e$	$\frac{1}{4dxdy}$ $-\frac{1}{4dx^2}e$	0

$$\sum_{\gamma} x^{\gamma} z^{\gamma} f^{\gamma} = 1$$

node	$i-1$	i	$i+1$
$k-1$	$\frac{1}{4dxdy}$	0	$-\frac{1}{4dxdz}$
k	0	0	0
$k+1$	$-\frac{1}{4dxdz}$	0	$\frac{1}{4dxdy}$

$$\sum_{\gamma} y^{\gamma} z^{\gamma} f^{\gamma} = 1$$

for i

node	$j-1$	j	$j+1$
$k-1$	$\frac{1}{4dydz} - \frac{1}{4dxdz}e$	0	$-\frac{1}{4dydz} + \frac{1}{4dxdz}e$
k	0	0	0
$k+1$	$-\frac{1}{4dydz} + \frac{1}{4dxdz}e$	0	$\frac{1}{4dydz} - \frac{1}{4dxdz}e$

and for $i-1$, $j+1$

node	$k-1$	k	$k+1$
	$-\frac{1}{4dxdz}e$	0	$\frac{1}{4dxdz}e$

and for $i+1$, $j-1$

node	$k-1$	k	$k+1$
	$\frac{1}{4dxdz}e$	0	$-\frac{1}{4dxdz}e$

$$\sum_{\gamma} (x^{\gamma})^3 f^{\gamma} = 1$$

node	$i-2$	$i-1$	i	$i+1$	$i+2$
	$-\frac{1}{12dx^3}$	$\frac{2}{12dx^3}$	0	$-\frac{2}{12dx^3}$	$\frac{1}{12dx^3}$

$$\sum_{\gamma}(y^{\gamma})^3 f^{\gamma} = 1$$

node	$j-2$	$j-1$	j	$j+1$	$j+2$
$i-2$	0	0	0	$-\frac{1}{12dy^2dx}e$ $+\frac{1}{12dx^3}e^3$	$\frac{1}{12dy^2dx}e$
$i-1$	0	$\frac{2}{12dy^2dx}e$ $+\frac{1}{12dx^3}e^3-\frac{1}{4dx^2dy}e^2$	0	$-\frac{2}{12dy^2dx}e$ $-\frac{1}{4dx^3}e^3+\frac{1}{4dx^2dy}e^2$	0
i	$-\frac{1}{12dy^3}$ $+\frac{1}{12dy^2dx}e$	$\frac{2}{12dy^3}-\frac{5}{12dy^2dx}e$ $-\frac{1}{4dx^3}e^3+\frac{1}{2dx^2dy}e^2$	0	$-\frac{2}{12dy^3}+\frac{5}{12dy^2dx}e$ $\frac{1}{4dx^2dy}e^2-\frac{1}{2dx^2dy}e^2$	$\frac{1}{12dy^3}$ $-\frac{1}{12dy^2dx}e$
$i+1$	0	$\frac{2}{12dy^2dx}e$ $+\frac{1}{4dx^3}e^3-\frac{1}{4dx^2dy}e^2$	0	$-\frac{2}{12dy^2dx}e$ $-\frac{1}{12dx^3}e^3+\frac{1}{4dx^2dy}e^2$	0
$i+2$	$-\frac{1}{12dy^2dx}e$	$-\frac{1}{12dy^2dx}e$ $-\frac{1}{12dx^3}e^3$	0	0	0

$$\sum_{\gamma}(z^{\gamma})^3 f^{\gamma} = 1$$

node	$k-2$	$k-1$	k	$k+1$	$k+2$
	$-\frac{1}{12dz^3}$	$\frac{2}{12dz^3}$	0	$-\frac{2}{12dz^3}$	$\frac{1}{12dz^3}$

$$\sum_{\gamma}(x^{\gamma})^2 y^{\gamma} f^{\gamma} = 1$$

node	$i-2$	$i-1$	i	$i+1$	$i+2$
$j-1$	0	$-\frac{1}{4dx^2dy}$ $+\frac{1}{4dx^3}e$	$\frac{2}{4dx^2dy}$ $-\frac{3}{4dx^3}e$	$-\frac{1}{4dx^2dy}$ $\frac{3}{4dx^3}e$	$-\frac{1}{4dx^3}e$
j	0	0	0	0	0
$j+1$	$\frac{1}{4dx^3}e$	$\frac{1}{4dx^2dy}$ $-\frac{3}{4dx^3}e$	$-\frac{2}{4dx^2dy}$ $+\frac{3}{4dx^3}e$	$\frac{1}{4dx^2dy}$ $-\frac{1}{4dx^3}e$	0

$$\sum_{\gamma}(x^{\gamma})^2 z^{\gamma} f^{\gamma} = 1$$

node	$i-1$	i	$i+1$
$k-1$	$-\frac{1}{4dx^2dz}$	$\frac{2}{4dx^2dz}$	$-\frac{1}{4dx^2dz}$
k	0	0	0
$k+1$	$\frac{1}{4dx^2dz}$	$-\frac{2}{4dx^2dz}$	$\frac{1}{4dx^2dz}$

$$\sum_{\gamma} x^{\gamma}(y^{\gamma})^2 f^{\gamma} = 1$$

node	$i-2$	$i-1$	i	$i+1$	$i+2$
$j-1$	0	$-\frac{1}{4dxdy^2}$ $+\frac{1}{2dx^2dy}e-\frac{1}{4dx^3}e^2$	$-\frac{1}{4dx^2dy}e$ $+\frac{3}{4dx^3}e^2$	$\frac{1}{4dxdy^2}$ $+\frac{1}{2dx^2dy}e-\frac{3}{4dx^3}e^2$	$\frac{1}{4dx^3}e^2$
j	0	$\frac{2}{4dxdy^2}$	0	$-\frac{2}{4dxdy^2}$	0
$j+1$	$-\frac{1}{4dx^3}e^2$	$-\frac{1}{4dxdy^2}$ $-\frac{1}{2dx^2dy}e+\frac{3}{4dx^3}e^2$	$\frac{1}{4dx^2dy}e$ $-\frac{3}{4dx^3}e^2$	$\frac{1}{4dxdy^2}$ $-\frac{1}{2dx^2dy}e+\frac{1}{4dx^3}e^2$	0

$$\sum_{\gamma}(y^{\gamma})^2 z^{\gamma} f^{\gamma} = 1$$

for i

node	$k-1$	k	$k+1$
$j-1$	$-\frac{1}{4dy^2dz}$ $+\frac{1}{8dxdydz}e+\frac{1}{8dx^2dz}e^2$	0	$\frac{1}{4dy^2dz}$ $\frac{1}{8dxdydz}e-\frac{1}{8dx^2dz}e^2$
j	$\frac{2}{4dy^2dz}$	0	$-\frac{2}{4dy^2dz}$
$j+1$	$-\frac{1}{4dy^2dz}$ $+\frac{1}{8dxdydz}e+\frac{1}{8dx^2dz}e^2$	0	$\frac{1}{4dy^2dz}$ $\frac{1}{8dxdydz}e-\frac{1}{8dx^2dz}e^2$

for $i-2$, $j+1$

node	$k-1$	k	$k+1$
	$\frac{1}{24dxdydz}e$ $-\frac{1}{24dx^2dz}e^2$	0	$-\frac{1}{24dxdydz}e$ $+\frac{1}{24dx^2dz}e^2$

for $i-1$

node	$k-1$	k	$k+1$
$j-1$	$\frac{1}{12dxdydz}e$ $-\frac{1}{12dx^2dz}e^2$	0	$-\frac{1}{12dxdydz}e$ $+\frac{1}{12dx^2dz}e^2$
j	0	0	0
$j+1$	$-\frac{1}{4dxdydz}e$	0	$\frac{1}{4dxdydz}e$

for $i+1$

node	$k-1$	k	$k+1$
$j-1$	$-\frac{1}{4dxdydz}e$	0	$\frac{1}{4dxdydz}e$
j	0	0	0
$j+1$	$\frac{1}{12dxdydz}e$ $-\frac{1}{12dx^2dz}e^2$	0	$-\frac{1}{12dxdydz}e$ $+\frac{1}{12dx^2dz}e^2$

for $i+2$, $j-1$

node	$k-1$	k	$k+1$
	$\frac{1}{24dxdydz}e$ $-\frac{1}{24dx^2dz}e^2$	0	$-\frac{1}{24dxdydz}e$ $+\frac{1}{24dx^2dz}e^2$

$$\sum_{\gamma}(z^{\gamma})^2 x^{\gamma} f^{\gamma} = 1$$

node	$k-1$	k	$k+1$
$i-1$	$-\frac{1}{4dz^2dx}$	$\frac{2}{4dz^2dx}$	$-\frac{1}{4dz^2dx}$
i	0	0	0
$i+1$	$\frac{1}{4dz^2dx}$	$-\frac{2}{4dz^2dx}$	$\frac{1}{4dz^2dx}$

$$\sum_{\gamma}(z^{\gamma})^2 y^{\gamma} f^{\gamma} = 1$$

for i

node	$k-1$	k	$k+1$
$j-1$	$-\frac{1}{4dz^2dy}$ $+\frac{1}{4dz^2dx}e$	$\frac{2}{4dz^2dy}$ $-\frac{2}{4dz^2dx}e$	$-\frac{1}{4dx^2dy}$ $+\frac{1}{4dz^2dx}e$
j	0	0	0
$j+1$	$\frac{1}{4dz^2dy}$ $-\frac{1}{4dz^2dx}e$	$-\frac{2}{4dz^2dy}$ $+\frac{2}{4dz^2dx}e$	$\frac{1}{4dz^2dy}$ $-\frac{1}{4dz^2dx}e$

for $i-1$, $j+1$

node	$k-1$	k	$k+1$
	$\frac{1}{4dz^2dx}e$	$-\frac{2}{4dz^2dx}e$	$\frac{1}{4dz^2dx}e$

for $i+1$, $j-1$

node	$k-1$	k	$k+1$
	$-\frac{1}{4dz^2dx}e$	$\frac{2}{4dz^2dx}e$	$-\frac{1}{4dz^2dx}e$

$$\sum_{\gamma} x^{\gamma} y^{\gamma} z^{\gamma} f^{\gamma} = 1$$

for $k-1$

node	$i-2$	$i-1$	i	$i+1$	$i+2$
$j-1$	0	$-\frac{1}{8dxdydz} + \frac{1}{8dx^2dz}e$	$-\frac{1}{8dx^2dz}e$	$\frac{1}{8dxdydz} - \frac{1}{8dx^2dz}e$	$\frac{1}{8dx^2dz}e$
j	0	0	0	0	0
$j+1$	$\frac{1}{8dx^2dz}e$	$\frac{1}{8dxdydz} - \frac{1}{8dx^2dz}e$	$-\frac{1}{8dx^2dz}e$	$-\frac{1}{8dxdydz} + \frac{1}{8dx^2dz}e$	

for $k+1$

node	$i-2$	$i-1$	i	$i+1$	$i+2$
$j-1$	0	$\frac{1}{8dxdydz} - \frac{1}{8dx^2dz}e$	$\frac{1}{8dx^2dz}e$	$-\frac{1}{8dxdydz} + \frac{1}{8dx^2dz}e$	$-\frac{1}{8dx^2dz}e$
j	0	0	0	0	0
$j+1$	$-\frac{1}{8dx^2dz}e$	$-\frac{1}{8dxdydz} + \frac{1}{8dx^2dz}e$	$\frac{1}{8dx^2dz}e$	$\frac{1}{8dxdydz} - \frac{1}{8dx^2dz}e$	

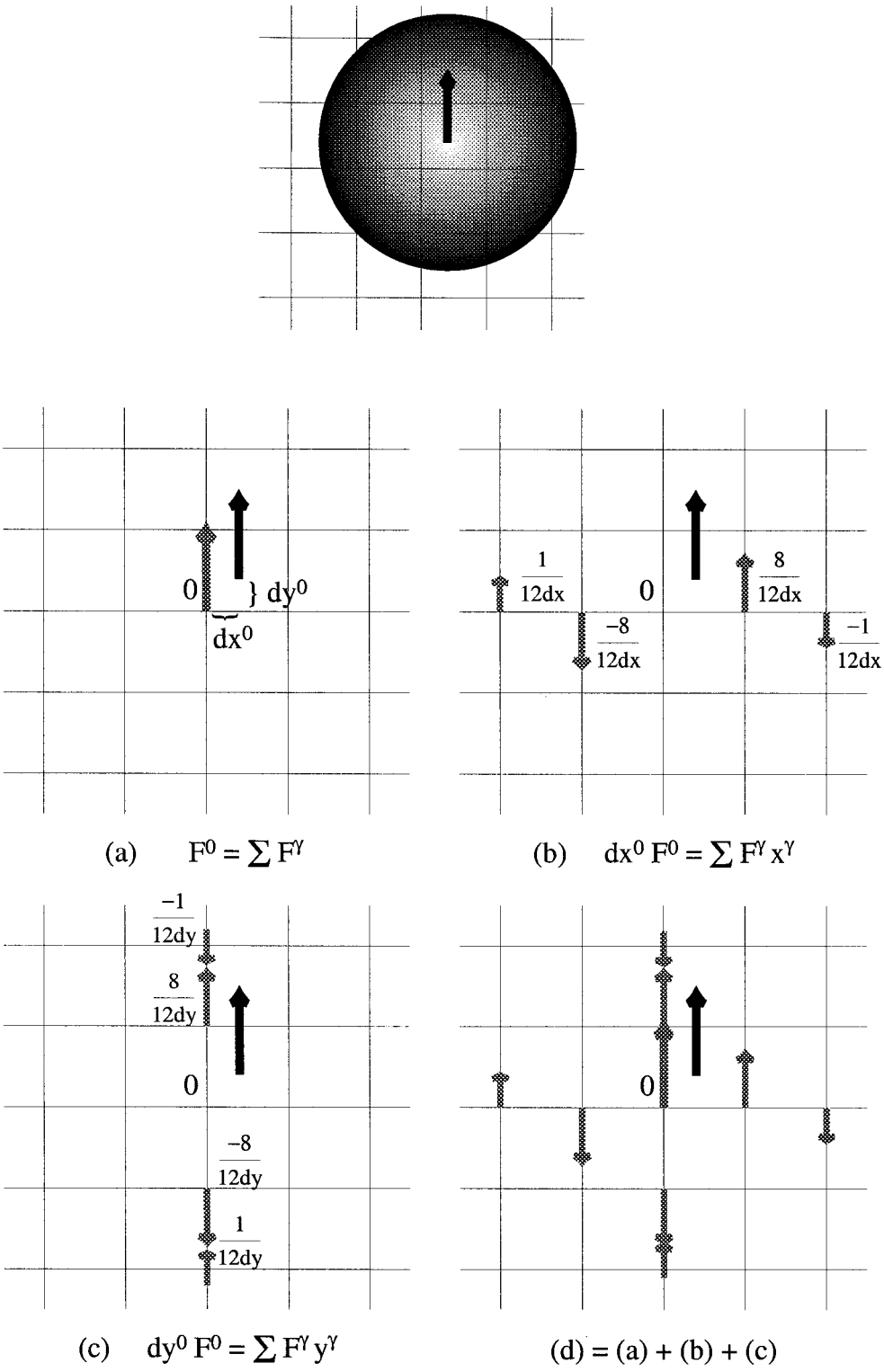

Figure B.1: The force distribution from the center of a particle to a fixed grid.

Appendix C

One Term Real Sums

The one term, real-space part of the Ewald summation is presented here. Formulae are presented for corrections to the velocity, velocity gradient, velocity Laplacian, gradient of the velocity Laplacian and pressure. The fluid velocity at the center of any particle (or at any other point in the fluid) can be calculated analytically by simply adding the contributions given below for all neighboring particles. It is again noted that a self term (corresponding to $\boldsymbol{x} = 0$) must always be added when the fluid velocity is calculated at the center of a particle.

C.1 Force: $\boldsymbol{F_i}$

The j-component of the net force F_j acting on a particle generates a disturbance velocity (velocity gradient and higher derivatives of the velocity) and disturbance pressure in the fluid given by:

Velocity

for $\boldsymbol{x} \neq 0$:

$$u_i = -\frac{1}{4\pi\eta}\left[-\phi_{\frac{1}{2}}\left(\frac{\pi}{\alpha^{\frac{3}{2}}}\right) r^2\delta_{ij} + \alpha^{-\frac{1}{2}}\phi_{-\frac{1}{2}}\delta_{ij} + \pi\alpha^{-\frac{3}{2}}\phi_{\frac{1}{2}}x_i x_j\right] F_j,$$

and for $\boldsymbol{x} = 0$:

$$u_i = -\frac{1}{4\pi\eta}\left(-\frac{2}{\alpha^{\frac{1}{2}}}\right) F_i.$$

(Note: F_i corresponds to the hydrodynamic force on the particle; the hydrodynamic force on the fluid has the opposite sign.)

Velocity Gradient

for $\boldsymbol{x} \neq 0$:

$$\frac{\partial u_i}{\partial x_k} = -\frac{1}{4\pi\eta}\left[-\frac{\pi}{\alpha^{\frac{3}{2}}}\left(4\delta_{ij}x_k - \delta_{jk}x_i - \delta_{ik}x_j\right)\phi_{\frac{1}{2}} + \frac{2\pi^2}{\alpha^{\frac{5}{2}}}\left(r^2\delta_{ij}x_k - x_i x_j x_k\right)\phi_{\frac{3}{2}}\right]F_j,$$

and for $\boldsymbol{x} = 0$:

$$\frac{\partial u_i}{\partial x_k} = 0.$$

Velocity Laplacian

for $\boldsymbol{x} \neq 0$:

$$\nabla^2 u_i = -\frac{1}{4\pi\eta}\left[-\frac{4\pi^3}{\alpha^{\frac{7}{2}}}\left(r^4\delta_{ij} - r^2 x_i x_j\right)\phi_{\frac{5}{2}} + \frac{2\pi^2}{\alpha^{\frac{5}{2}}}\left(9r^2\delta_{ij} - 7x_i x_j\right)\phi_{\frac{3}{2}} - \frac{10\pi}{\alpha^{\frac{3}{2}}}\delta_{ij}\phi_{\frac{1}{2}}\right]F_j,$$

and for $\boldsymbol{x} = 0$:

$$\nabla^2 u_i = -\frac{1}{4\pi\eta}\left(\frac{20}{3}\frac{\pi}{\alpha^{\frac{3}{2}}}\right)F_i.$$

Gradient of Velocity Laplacian

for $\boldsymbol{x} \neq 0$:

$$\begin{aligned}\frac{\partial \nabla^2 u_i}{\partial x_l} = -\frac{1}{4\pi\eta}\Bigg[&\frac{8\pi^4}{\alpha^{\frac{9}{2}}}\left(r^4 x_l\delta_{ij} - r^2 x_i x_j x_l\right)\phi_{\frac{7}{2}} \\ &-\frac{4\pi^3}{\alpha^{\frac{7}{2}}}\left(13r^2 x_l\delta_{ij} - 9x_i x_j x_l - r^2\delta_{il}x_j - r^2\delta_{jl}x_i\right)\phi_{\frac{5}{2}} \\ &+\frac{2\pi^2}{\alpha^{\frac{5}{2}}}\left(28\delta_{ij}x_l - 7\delta_{il}x_j - 7\delta_{jl}x_i\right)\phi_{\frac{3}{2}}\Bigg]F_j,\end{aligned}$$

and for $\boldsymbol{x} = 0$:

$$\frac{\partial \nabla^2 u_i}{\partial x_l} = 0.$$

Pressure

$$P = -\frac{1}{4\pi\eta}\left[-\frac{2\pi^2}{\alpha^{\frac{5}{2}}}r^2\phi_{\frac{3}{2}} + \frac{5\pi}{\alpha^{\frac{3}{2}}}\phi_{\frac{1}{2}}\right]x_j F_j.$$

C.2 First Force Moment: Doublet D_{ij}

The ij-component of the first force moment tensor, corresponding to the particle stresslet and torque, produces a disturbance in the fluid velocity and pressure given by:

Velocity

for $\boldsymbol{x} \neq 0$:

$$u_i = -\frac{1}{4\pi\eta}\left[-\frac{\pi}{\alpha^{\frac{3}{2}}}\left(4\delta_{ij}x_k - \delta_{jk}x_i - \delta_{ik}x_j\right)\phi_{\frac{1}{2}} + \frac{2\pi^2}{\alpha^{\frac{5}{2}}}\left(r^2\delta_{ij}x_k - x_i x_j x_k\right)\phi_{\frac{3}{2}}\right]D_{jk},$$

and for $\boldsymbol{x} = 0$:

$$u_i = 0.$$

Velocity Gradient

for $\boldsymbol{x} \neq 0$:

$$\begin{aligned}\frac{\partial u_i}{\partial x_l} = &-\frac{1}{4\pi\eta}\left[-\frac{4\pi^3}{\alpha^{\frac{7}{2}}}\left(r^2\delta_{ij}x_k x_l - x_i x_j x_k x_l\right)\phi_{\frac{5}{2}}\right. \\ &+\frac{2\pi^2}{\alpha^{\frac{5}{2}}}\left(6\delta_{ij}x_l x_k + r^2\delta_{ij}\delta_{kl} - \delta_{jk}x_i x_l - \delta_{ik}x_l x_j\right. \\ &\left.-\delta_{il}x_j x_k - \delta_{jl}x_i x_k - \delta_{kl}x_i x_j\right)\phi_{\frac{3}{2}} \\ &\left.-\frac{\pi}{\alpha^{\frac{3}{2}}}\left(4\delta_{ij}\delta_{kl} - \delta_{jk}\delta_{il} - \delta_{ik}\delta_{jl}\right)\phi_{\frac{1}{2}}\right]D_{jk},\end{aligned}$$

and for $\boldsymbol{x} = 0$:

$$\frac{\partial u_i}{\partial x_l} = -\frac{1}{4\pi\eta}\frac{2\pi}{3\alpha^{\frac{3}{2}}}\left(4D_{il} - D_{li} - \delta_{il}D_{jj}\right).$$

Velocity Laplacian

for $\boldsymbol{x} \neq 0$:

$$\begin{aligned}\nabla^2 u_i(\boldsymbol{x}) = &-\frac{1}{4\pi\eta}\left[\frac{8\pi^4}{\alpha^{\frac{9}{2}}}\left(r^4 x_k\delta_{ij} - r^2 x_i x_j x_k\right)\phi_{\frac{7}{2}}\right.\\ &-\frac{4\pi^3}{\alpha^{\frac{7}{2}}}\left(13r^2 x_k\delta_{ij} - 9x_i x_j x_k - r^2\delta_{ik}x_j - r^2\delta_{jk}x_i\right)\phi_{\frac{5}{2}}\\ &\left.+\frac{2\pi^2}{\alpha^{\frac{5}{2}}}\left(28\delta_{ij}x_k - 7\delta_{ik}x_j - 7\delta_{jk}x_i\right)\phi_{\frac{3}{2}}\right] D_{jk},\end{aligned}$$

and for $\boldsymbol{x} = 0$:

$$\nabla^2 u_i = 0.$$

Gradient of Velocity Laplacian

for $\boldsymbol{x} \neq 0$:

$$\begin{aligned}\frac{\partial\nabla^2 u_i}{\partial x_l} = &-\frac{1}{4\pi\eta}\left[-\frac{16\pi^5}{\alpha^{\frac{11}{2}}}\left(r^4\delta_{ij}x_k x_l - r^2 x_i x_j x_k x_l\right)\phi_{\frac{9}{2}}\right.\\ &+\frac{8\pi^4}{\alpha^{\frac{9}{2}}}\left(17r^2\delta_{ij}x_l x_k - 11x_i x_j x_l x_k + r^4\delta_{ij}\delta_{kl} - r^2\delta_{il}x_j x_k\right.\\ &\left.-r^2\delta_{jl}x_i x_k - r^2\delta_{kl}x_i x_j - r^2\delta_{jk}x_i x_l - r^2\delta_{ik}x_j x_l\right)\phi_{\frac{7}{2}}\\ &-\frac{4\pi^3}{\alpha^{\frac{7}{2}}}\left(54\delta_{ij}x_k x_l + 13r^2\delta_{ij}\delta_{kl} - r^2\delta_{jk}\delta_{il} - r^2\delta_{ik}\delta_{jl}\right.\\ &\left.-9\delta_{il}x_j x_k - 9\delta_{jl}x_i x_k - 9\delta_{kl}x_i x_j - 9\delta_{jk}x_i x_l - 9\delta_{ik}x_j x_l\right)\phi_{\frac{5}{2}}\\ &\left.+\frac{2\pi^2}{\alpha^{\frac{5}{2}}}\left(28\delta_{ij}\delta_{kl} - 7\delta_{ik}\delta_{jl} - 7\delta_{jk}\delta_{il}\right)\phi_{\frac{3}{2}}\right] D_{jk},\end{aligned}$$

and for $\boldsymbol{x} = 0$:

$$\frac{\partial\nabla^2 u_i}{\partial x_l} = -\frac{1}{4\pi\eta}\left[-\frac{28}{5}\frac{\pi^2}{\alpha^{\frac{5}{2}}}\left(4D_{il} - D_{li} - \delta_{il}D_{jj}\right)\right].$$

Pressure

$$P = -\frac{1}{4\pi\eta}\left[\frac{2\pi^3}{\alpha^{\frac{7}{2}}}r^2 x_j x_k\phi_{\frac{5}{2}} - \frac{2\pi^2}{\alpha^{\frac{5}{2}}}\left(r^2\delta_{jk} + 7x_j x_k\right)\phi_{\frac{3}{2}} + \frac{5\pi}{\alpha^{\frac{3}{2}}}\delta_{jk}\phi_{\frac{1}{2}}\right] D_{jk}.$$

C.3 Second Force Moment: d_i

The i-component of the second force moment generates a velocity and pressure disturbance given by:

Velocity

for $\boldsymbol{x} \neq 0$:

$$u_i = -\frac{1}{4\pi\eta}\left[\frac{2\pi^3}{\alpha^{\frac{7}{2}}}\left(r^4\delta_{ij} - r^2 x_i x_j\right)\phi_{\frac{5}{2}} - \frac{\pi^2}{\alpha^{\frac{5}{2}}}\left(9r^2\delta_{ij} - 7x_i x_j\right)\phi_{\frac{3}{2}} + \frac{5\pi}{\alpha^{\frac{3}{2}}}\delta_{ij}\phi_{\frac{1}{2}}\right] d_j,$$

and for $\boldsymbol{x} = 0$:

$$\nabla^2 u_i = -\frac{1}{4\pi\eta}\left(-\frac{10}{3}\frac{\pi}{\alpha^{\frac{3}{2}}}\right) d_i.$$

Velocity gradient

for $\boldsymbol{x} \neq 0$:

$$\begin{aligned}\frac{\partial u_i}{\partial x_k} = &-\frac{1}{4\pi\eta}\left[-\frac{4\pi^4}{\alpha^{\frac{9}{2}}}\left(r^4 x_k\delta_{ij} - r^2 x_i x_j x_k\right)\phi_{\frac{7}{2}}\right. \\ &+\frac{2\pi^3}{\alpha^{\frac{7}{2}}}\left(13r^2 x_k\delta_{ij} - 9x_i x_j x_k - r^2\delta_{ik}x_j - r^2\delta_{jk}x_i\right)\phi_{\frac{5}{2}} \\ &\left.-\frac{\pi^2}{\alpha^{\frac{5}{2}}}\left(28\delta_{ij}x_k - 7\delta_{ik}x_j - 7\delta_{jk}x_i\right)\phi_{\frac{3}{2}}\right] d_j,\end{aligned}$$

and for $\boldsymbol{x} = 0$:

$$\frac{\partial u_i}{\partial x_k} = 0.$$

Velocity Laplacian

for $\boldsymbol{x} \neq 0$:

$$\nabla^2 u_i = -\frac{1}{4\pi\eta}\left[\frac{8\pi^5}{\alpha^{\frac{11}{2}}}\left(r^6\delta_{ij} - r^4 x_i x_j\right)\phi_{\frac{9}{2}} - \frac{4\pi^4}{\alpha^{\frac{9}{2}}}\left(20r^4\delta_{ij} - 18r^2 x_i x_j\right)\phi_{\frac{7}{2}} + \frac{2\pi^3}{\alpha^{\frac{7}{2}}}\left(91r^2\delta_{ij} - 63x_i x_j\right)\phi_{\frac{5}{2}} - \frac{\pi^2}{\alpha^{\frac{5}{2}}}\left(70\delta_{ij}\right)\right] d_j,$$

and for $\boldsymbol{x} = 0$:

$$\nabla^2 u_i = -\frac{1}{4\pi\eta}\left(\frac{28\pi^2}{\alpha^{\frac{5}{2}}} d_i\right).$$

Gradient of Velocity Laplacian

for $\boldsymbol{x} \neq 0$:

$$\begin{aligned}\frac{\partial \nabla^2 u_i}{\partial x_l} = -\frac{1}{4\pi\eta}\Bigg[&-\frac{16\pi^6}{\alpha^{\frac{13}{2}}}\left(r^6\delta_{ij}x_l - r^4 x_l x_i x_j\right)\phi_{\frac{11}{2}} \\ &+\frac{8\pi^5}{\alpha^{\frac{11}{2}}}\left(26r^4\delta_{ij}x_l - 22r^2 x_i x_j x_l - r^4\delta_{il}x_j - r^4\delta_{jl}x_i\right)\phi_{\frac{9}{2}} \\ &-\frac{4\pi^4}{\alpha^{\frac{9}{2}}}\left(171r^2\delta_{ij}x_l - 99x_i x_j x_l - 18r^2\delta_{il}x_j - 18r^2\delta_{jl}x_i\right)\phi_{\frac{7}{2}} \\ &+\frac{2\pi^3}{\alpha^{\frac{7}{2}}}\left(252\delta_{ij}x_l - 63\delta_{il}x_j - 63\delta_{jl}x_i\right)\phi_{\frac{5}{2}}\Bigg] d_j,\end{aligned}$$

and for $\boldsymbol{x} = 0$:

$$\frac{\partial \nabla^2 u_i}{\partial x_l} = 0.$$

Pressure

$$P = -\frac{1}{4\pi\eta}\left[\frac{4\pi^4}{\alpha^{\frac{9}{2}}} r^4 x_j \phi_{\frac{7}{2}} - \frac{2\pi^3}{\alpha^{\frac{7}{2}}} 14 r^2 x_j \phi_{\frac{5}{2}} + \frac{35\pi^2}{\alpha^{\frac{5}{2}}} x_j \phi_{\frac{3}{2}}\right] d_j.$$

C.4 Third Force Moment: L_{ij}

The ij-component of the third force moment generates a velocity and pressure disturbance in the fluid given by:

Velocity

for $\boldsymbol{x} \neq 0$:

$$\begin{aligned} u_i = &- \frac{1}{4\pi\eta} \left[\frac{8\pi^4}{\alpha^{\frac{9}{2}}} \left(r^4 x_k \delta_{ij} - r^2 x_i x_j x_k \right) \phi_{\frac{7}{2}} \right. \\ &- \frac{4\pi^3}{\alpha^{\frac{7}{2}}} \left(13 r^2 x_k \delta_{ij} - 9 x_i x_j x_k - r^2 \delta_{ik} x_j - r^2 \delta_{jk} x_i \right) \phi_{\frac{5}{2}} \\ &\left. + \frac{2\pi^2}{\alpha^{\frac{5}{2}}} \left(28 \delta_{ij} x_k - 7 \delta_{ik} x_j - 7 \delta_{jk} x_i \right) \phi_{\frac{3}{2}} \right] L_{jk}, \end{aligned}$$

and for $\boldsymbol{x} = 0$:

$$u_i = 0.$$

Velocity gradient

for $\boldsymbol{x} \neq 0$:

$$\begin{aligned} \frac{\partial u_i}{\partial x_l} = &- \frac{1}{4\pi\eta} \left[- \frac{16\pi^5}{\alpha^{\frac{11}{2}}} \left(r^4 \delta_{ij} x_k x_l - r^2 x_i x_j x_k x_l \right) \phi_{\frac{9}{2}} \right. \\ &+ \frac{8\pi^4}{\alpha^{\frac{9}{2}}} \left(17 r^2 \delta_{ij} x_k x_l + r^4 \delta_{ij} \delta_{kl} - 11 x_i x_j x_k x_l - r^2 \delta_{il} x_j x_k \right. \\ &\left. - r^2 \delta_{jl} x_i x_k - r^2 \delta_{kl} x_i x_j - r^2 \delta_{jk} x_i x_l - r^2 \delta_{ik} x_j x_l \right) \phi_{\frac{7}{2}} \\ &- \frac{4\pi^3}{\alpha^{\frac{7}{2}}} \left(54 \delta_{ij} x_k x_l + 13 r^2 \delta_{ij} \delta_{kl} - 9 \delta_{jk} x_i x_l - 9 \delta_{ik} x_j x_l \right. \\ &\left. - 9 \delta_{il} x_j x_k - 9 \delta_{jl} x_i x_k - 9 \delta_{kl} x_i x_j - r^2 \delta_{jk} \delta_{il} - r^2 \delta_{ik} \delta_{jl} \right) \phi_{\frac{5}{2}} \\ &\left. + \frac{2\pi^2}{\alpha^{\frac{5}{2}}} \left(28 \delta_{ij} \delta_{kl} - 7 \delta_{ik} \delta_{jl} - 7 \delta_{jk} \delta_{il} \right) \phi_{\frac{3}{2}} \right] L_{jk}, \end{aligned}$$

and for $\boldsymbol{x} = 0$:

$$\frac{\partial u_i}{\partial x_l} = - \frac{1}{4\pi\eta} \left[\frac{28\pi^2}{5\alpha^{\frac{5}{2}}} \left(4 L_{il} - L_{li} - \delta_{il} L_{jj} \right) \right].$$

Velocity Laplacian

for $\boldsymbol{x} \neq 0$:

$$\begin{aligned}\nabla^2 u_i = &-\frac{1}{4\pi\eta}\left[\frac{32\pi^6}{\alpha^{\frac{13}{2}}}\left(r^6\delta_{ij}x_k - r^4 x_i x_j x_k\right)\phi_{\frac{11}{2}}\right.\\
&-\frac{16\pi^5}{\alpha^{\frac{9}{2}}}\left(26r^4\delta_{ij}x_k - 22r^2 x_i x_j x_k - r^4\delta_{jk}x_i - r^4\delta_{ik}x_j\right)\phi_{\frac{9}{2}}\\
&+\frac{8\pi^4}{\alpha^{\frac{9}{2}}}\left(171r^2\delta_{ij}x_k - 99x_i x_j x_k - 18r^2\delta_{ik}x_j - 18r^2\delta_{jk}x_i\right)\phi_{\frac{7}{2}}\\
&\left.-\frac{4\pi^3}{\alpha^{\frac{7}{2}}}\left(252\delta_{ij}x_k - 63\delta_{jk}x_i - 63\delta_{ik}x_j\right)\phi_{\frac{5}{2}}\right]L_{jk},\end{aligned}$$

and for $\boldsymbol{x} = 0$:

$$\nabla^2 u_i = 0.$$

Gradient of Velocity Laplacian

for $\boldsymbol{x} \neq 0$:

$$\begin{aligned}\frac{\partial u_i}{\partial x_l} = &-\frac{1}{4\pi\eta}\left[-\frac{64\pi^7}{\alpha^{\frac{15}{2}}}\left(r^6\delta_{ij}x_k x_l - r^4 x_i x_j x_k x_l\right)\phi_{\frac{13}{2}}\right.\\
&+\frac{32\pi^6}{\alpha^{\frac{13}{2}}}\left(32r^4\delta_{ij}x_k x_l + r^6\delta_{ij}\delta_{kl} - 26r^2 x_i x_j x_k x_l - r^4\delta_{il}x_j x_k\right.\\
&\left.-r^4\delta_{jl}x_i x_k - r^4\delta_{kl}x_i x_j - r^4\delta_{jk}x_i x_l - r^4\delta_{ik}x_j x_l\right)\phi_{\frac{11}{2}}\\
&-\frac{16\pi^5}{\alpha^{\frac{11}{2}}}\left(275r^2\delta_{ij}x_k x_l + 26r^4\delta_{ij}\delta_{kl} - 143x_i x_j x_k x_l - 22r^2\delta_{jk}x_i x_l - 22r^2\delta_{ik}x_j x_l\right.\\
&\left.-22r^2\delta_{il}x_j x_k - 22r^2\delta_{jl}x_i x_k - 22r^2\delta_{kl}x_i x_j - r^4\delta_{jk}\delta_{il} - r^4\delta_{ik}\delta_{jl}\right)\phi_{\frac{9}{2}}\\
&+\frac{8\pi^4}{\alpha^{\frac{9}{2}}}\left(594\delta_{ij}x_k x_l + 171r^2\delta_{ij}\delta_{kl} - 99\delta_{il}x_j x_k - 99\delta_{jl}x_i x_k\right.\\
&\left.-99\delta_{kl}x_i x_j - 99\delta_{ik}x_l x_j - 99\delta_{jk}x_l x_i - 18r^2\delta_{jl}\delta_{ik} - 18r^2\delta_{il}\delta_{jk}\right)\phi_{\frac{7}{2}}\\
&\left.-\frac{4\pi^3}{a^{\frac{7}{2}}}\left(252\delta_{ij}\delta_{kl} - 63\delta_{jk}\delta_{il} - 63\delta_{ik}\delta_{jl}\right)\phi_{\frac{5}{2}}\right]L_{jk},\end{aligned}$$

and for $\boldsymbol{x} = 0$:

$$\frac{\partial\nabla^2 u_i}{\partial x_l} = -\frac{1}{4\pi\eta}\left[\frac{72\pi^3}{\alpha^{\frac{7}{2}}}\left(4L_{il} - L_{li} - \delta_{il}L_{jj}\right)\right].$$

Pressure

$$P = -\frac{1}{4\pi\eta}\left[\frac{16\pi^5}{\alpha^{\frac{11}{2}}}r^4 x_j x_k \phi_{\frac{9}{2}} - \frac{8\pi^4}{\alpha^{\frac{9}{2}}}\left(18r^2 x_j x_k + r^4\delta_{jk}\right)\phi_{\frac{7}{2}} + \frac{4\pi^3}{\alpha^{\frac{7}{2}}}\left(14r^2\delta_{jk} + 63x_j x_k\right)\phi_{\frac{5}{2}} - \frac{70\pi^2}{\alpha^{\frac{5}{2}}}\delta_{jk}\phi_{\frac{3}{2}}\right] L_{jk}.$$